International Journal of Antennas and Propagation

Radio Wave Propagation and Wireless Channel Modeling

Guest Editors: Ai Bo, Thomas Kürner, César Briso Rodríguez, and Hsiao-Chun Wu

Radio Wave Propagation and Wireless Channel Modeling

International Journal of Antennas and Propagation

Radio Wave Propagation and Wireless Channel Modeling

Guest Editors: Ai Bo, Thomas Kürner, César Briso Rodríguez, and Hsiao-Chun Wu

Editorial Board

Contents

Hindawi Publishing Corporation
International Journal of Antennas and Propagation
Volume 2013, Article ID 835160, 3 pages
http://dx.doi.org/10.1155/2013/835160

Editorial

Radio Wave Propagation and Wireless Channel Modeling

Ai Bo,[1] Thomas Kürner,[2] César Briso Rodríguez,[3] and Hsiao-Chun Wu[4]

[1] *State Key Laboratory of Rail Traffic Control and Safety, Beijing Jiaotong University, Beijing 100044, China*
[2] *Technische Universität Braunschweig, Braunschweig 38106, Germany*
[3] *Universidad Politecnica de Madrid, Madrid 28031, Spain*
[4] *Louisiana State University, LA 70803, USA*

Correspondence should be addressed to Ai Bo; aibo@ieee.org

Received 25 November 2012; Accepted 25 November 2012

Mechanisms about radio wave propagation are the basis for wireless channel modeling. Typical wireless channel models for typical scenarios are of great importance to the physical layer techniques such as synchronization, channel estimation, and equalization. Nowadays, many channel models concerned with either large-scale modeling and small-scale fast fading models have been established. However, with the development of some new techniques such as multiuser MIMO systems, vehicle-to-vehicle technique, wireless relay technique, and short-distance or short-range technique, novel wireless channel models should be developed to cater for these new applications. As for this special issue, we cordially invite some researchers to contribute papers that will stimulate the continuing efforts to understand the mechanisms about radio wave propagations and wireless channel models under variant scenarios. This special issue provides the state-of-the-art research in mobile wireless channels.

As we know, scene partitioning is the premise and basis for wireless channel modeling. The paper titled "*Radio wave propagation scene partitioning for high-speed rails*" discusses the scene partitioning for high-speed rail (HSR) scenarios. Based on the measurements along HSR lines with 300 km/h operation speed in China, the authors partitioned the HSR scene into twelve scenarios. Further work based on theoretical analysis of radio wave propagation mechanisms, such as reflection and diffraction, may lead to develop the standard of radio wave propagation scene partitioning for HSR.

The paper "*Quantification of scenario distance within generic WINNER channel model*" deals with the topic on the scenario comparisons on the basis of the fundamental theory that a generic WINNER model uses the same set of parameters for representing different scenarios. It approximates the WINNER scenarios with multivariate normal distributions and then uses the mean Kullback-Leibler divergence to quantify the divergence. The results show that the WINNER scenario groups (A, B, C, D) or propagation classes (LoS, NLoS) do not necessarily ensure minimum separation within the groups/classes. The computation of the divergence of the actual measurements and WINNER scenarios confirms that the parameters of the C2 scenario in WINNER series are a proper reference for a large variety of urban macrocell environments.

The paper "*Fading analysis for the high speed railway viaduct and terrain cutting scenarios*" provides a good understanding of fading characteristics in HSR environment based on the measurements taken in both high-speed viaduct and terrain cutting scenarios using track side base stations. Kolmogorov-Smirnov (K-S) test has been first introduced in the statistical analysis to find out the most appropriate model for the small-scale fading envelope. Some important conclusions are drawn: though both Rice and Nakagami distributions provide a good fit to the first-order envelope data in both scenarios, only the Rice model generally fits the second-order statistics data accurately. For the viaduct scenario, higher Rice K factor can be observed. The change tendency of the K factor as a function of distance in the two scenarios is completely different.

The paper "*Propagation mechanism modeling in the near-region of arbitrary cross-sectional tunnels*" talks about the modeling of the propagation mechanisms and their dividing point in the near-region of arbitrary cross-sectional tunnels. By conjunctively employing the propagation theory and the three-dimensional solid geometry, it presents a general model for the dividing point between two propagation mechanisms.

Furthermore, the general dividing point model is specified in rectangular, circular, and arched tunnels, respectively. Five groups of measurements are used to justify the model in different tunnels at different frequencies. The results could help to deepen the insight into the propagation mechanisms in tunnels.

A key characteristic of train-to-train (T2T) communication, a recently proposed novel technique for HSR, is to avoid accidents conducted among trains without any aid of infrastructure. The paper "*A novel train-to-train communication model design based on multihop in high-speed railway*" provides a novel T2T communication model in a physical layer based on multihop and cooperation technique. The mechanism of this model lies in the idea that a source train uses trains on other tracks as relays to transmit signals to destination train on the same track. The paper titled "*Outage analysis of train-to-train communication model over Nakagami-m channel in high-speed railway*" analyzes the end-to-end outage performance of T2T communication model in HSR over independent identical and nonidentical Nakagami-m channels. It presents a novel closed form for the sum of squared independent Nakagami-m variates and then derives an expression for the outage probability of the identical and nonidentical Nakagami-m channels. Numerical analysis indicates that the derived analytical results are reasonable and the outage performance is better over Nakagami-m channel in HSR scenarios.

The above-mentioned papers are for HSR communication wireless channel models. There are also some papers dealing with the channel models for satellites, ships, human bodies, and vehicle-to-vehicle communications.

The paper "*State modeling of the land mobile propagation channel with multiple satellites*" evaluates a novel approach for multisatellite state modeling: the Master-Slave approach and its corresponding realization method named Conditional Assembling Method. The primary concept is that slave satellites are modeled according to an existing master state sequence, whereas the correlation between multiple slaves is omitted. For modeling two satellites (one master and one slave), the "Conditional Assembling Method" enables an accurate resimulation of the correlation coefficient between the satellites, the single satellite state probabilities, and the combined state probabilities of master and slave. The probability of the "all bad-" state resulting from master-slave is compared with an analytically estimated "all bad-" state probability from measurements. Master-slave has a high probability error in case of a high correlation between the slave satellites. Furthermore, a master satellite with a high elevation provides a lower probability error compared to a master with low elevation.

The improvement of maritime radio links often requires an increase of emitted power or receiver sensitivity. Another way is to replace the poor antenna gains of traditional surface ship whips by novel antenna structures with directive properties. The paper "*Impact of ship motions on maritime radio links*" developed a tool for modeling the impact of ship motions on the antenna structures. The tool includes a deterministic two-ray model for radio-wave propagation over the sea surface.

The paper "*Statistical modeling of ultrawideband body-centric wireless channels considering room volume*" presents the results of a statistical modeling of on-body ultrawideband (UWB) radio channels for wireless body area network (WBAN) applications. A measured delay profile can be divided into two domains: in the first domain there is either a direct (for line of sight) or diffracted (for nonline of sight) wave which is dependent on the propagation distance along the perimeter of the body, but essentially unrelated to room volume; and the second domain has multipath components that are dominant and dependent on room volume. The first domain was modeled with a conventional power decay law model and the second domain with a modified Saleh-Valenzuela model considering the room volume. Realizations of the impulse responses are presented based on the composite model and compared with the measured average power delay profiles.

The paper titled "*On the statistical properties of Nakagami-hoyt vehicle-to-vehicle fading channel under nonisotropic scattering*" argues the statistical properties of vehicle-to-vehicle Nakagami-Hoyt (Nakagami-q) channel model under non-isotropic condition. The spatial-time correlation function (STCF), the power spectral density (PSD), squared time autocorrelation function (SQCF), level crossing rate (LCR), and the average duration of fade (ADF) of the Nakagami-Hoyt channel have been derived under the assumption that both the transmitter and receiver are nonstationary with nonomnidirectional antennas. A simulator utilizing the inverse-fast-fourier-transform- (IFFT-) based computation method is designed for the model.

The paper "*NECOP propagation experiment: rain-rate distributions observations and prediction model comparisons*" talks about the empirical distribution functions for the evaluation of rain-rate based on the observed data. The empirical distribution functions were compared with cumulative distribution functions generated using four different rain-rate distribution models. It is found that although each of the models shows similar qualitative features at lower exceedance of time, the characteristics at higher time percentages show quantitative difference from the experimental data except the improved version of Moupfouma model. The results further show that the rain-fall rate and the microwave propagation characteristics in the observed region are out of accord with International Telecommunication Union predictions. This information is vital for predicting rain fading cumulative probability distributions.

The paper "*Influence of training set selection in artificial neural network-based propagation path loss predictions*" utilizes the artificial neural networks (ANNs) and ray-tracing technique for predicting the received power/path loss in both outdoor and indoor links. A complete description of the process for creating and training an ANN-based model is presented with special emphasis on the training process. The optimum selection of the training set is discussed. A quantitative analysis based on results from two narrowband measurement campaigns is also presented.

The following fours papers are related with multi-input and multioutput (MIMO) techniques. The paper "*A tradeoff*

between rich multipath and high receive power in MIMO capacity" presents a discussion of rich multipath (in NLOS) or signal-to-noise ratio (SNR) (usually in LOS) effects on MIMO channel capacity. It is investigated by performing simulations using simple circle scatterer and WINNER II channel model. The simulation results show that these two factors behave differently as the channel conditions vary. When the scatterer number in channel is low, the high receive SNR is more important than capacity. The multipath richness will get the upper bound when the scatterer number is beyond a certain threshold. However, the channel capacity will not change much as the scatterers continue to increase.

The paper "*Construction and capacity analysis of high-rank LoS MIMO channels in high speed railway scenarios*" talks about the validity of the maximum capacity criterion applied to realize high-rank LoS MIMO channels for HSR scenarios. Performance is evaluated by ergodic capacity. Numerical results demonstrate that, by simply adjusting antenna spacing according to the maximum capacity criterion, significant capacity gains are achievable. Two proposals are presented to reconfigure antenna arrays so as to maximize LoS MIMO capacity in the HSR scenarios. The paper "*Geometry-based stochastic modeling for MIMO channel in high-speed mobile scenario*" discusses the geometry-based stochastic channel models for the terrain cutting, suburb, and urban scenarios in HSR. The space time correlation functions in analytical form are obtained in suburb and urban scenarios. The comparisons of the space correlation characteristics under three scenarios are made.

The paper "*Performance evaluation of closed-loop spatial multiplexing codebook based on indoor MIMO channel measurement*" discusses closed-loop MIMO technique standardized for long-term evolution (LTE) system. Based on the wideband MIMO channel measurement in a typical indoor scenario, capacity loss (CL) of the limited size codebook relative to perfect precoding is studied in two extreme channel conditions. The results show that current codebook design for single-layer transmission is nearly capacity lossless and the CL will increase with the number of transmitted layers. Furthermore, the capacity improvement of better codebook selection criterions is very limited compared to CL. To survey the effect of frequency domain channel variation on MIMO-OFDM system, a function is defined to measure the fluctuation levels of the key channel metrics within a subband and to reveal the inherent relationship between them.

Ai Bo
Thomas Kürner
César Briso Rodríguez
Hsiao-Chun Wu

Hindawi Publishing Corporation
International Journal of Antennas and Propagation
Volume 2013, Article ID 176704, 17 pages
http://dx.doi.org/10.1155/2013/176704

Research Article

Quantification of Scenario Distance within Generic WINNER Channel Model

Milan Narandžić,[1] Christian Schneider,[2] Wim Kotterman,[3] and Reiner S. Thomä[2]

[1] *Department for Power, Electronic and Communication Engineering, Faculty of Technical Sciences, Trg D. Obradovića 6, 2100 Novi Sad, Serbia*
[2] *Electronic Measurement Research Lab, Ilmenau University of Technology, PSF 100565, 98684 Ilmenau, Germany*
[3] *Digital Broadcasting Research Laboratory, Ilmenau University of Technology, PSF 100565, 98684 Ilmenau, Germany*

Correspondence should be addressed to Milan Narandžić; orange@uns.ac.rs

Received 27 July 2012; Revised 29 October 2012; Accepted 1 November 2012

Academic Editor: Ai Bo

Starting from the premise that stochastic properties of a radio environment can be abstracted by defining scenarios, a generic MIMO channel model is built by the WINNER project. The parameter space of the WINNER model is, among others, described by normal probability distributions and correlation coefficients that provide a suitable space for scenario comparison. The possibility to quantify the distance between reference scenarios and measurements enables objective comparison and classification of measurements into scenario classes. In this paper we approximate the WINNER scenarios with multivariate normal distributions and then use the mean Kullback-Leibler divergence to quantify their divergence. The results show that the WINNER scenario groups (A, B, C, and D) or propagation classes (LoS, OLoS, and NLoS) do not necessarily ensure minimum separation within the groups/classes. Instead, the following grouping minimizes intragroup distances: (i) indoor-to-outdoor and outdoor-to-indoor scenarios (A2, B4, and C4), (ii) macrocell configurations for suburban, urban, and rural scenarios (C1, C2, and D1), and (iii) indoor/hotspot/microcellular scenarios (A1, B3, and B1). The computation of the divergence between Ilmenau and Dresden measurements and WINNER scenarios confirms that the parameters of the C2 scenario are a proper reference for a large variety of urban macrocell environments.

1. Introduction

In order to maximize transmission efficiency, wireless communication systems are forced to exploit the spatial and temporal dimensions of the radio channel to the full. The design and performance analysis of such system requires the channel model to reflect all relevant propagation aspects, which imposes serious constraints on the minimal complexity of the model.

This paper concentrates on the class of geometry-based stochastic channel models (GSCMs) that offer good trade-off between complexity and performance (realism). These models deal with physical ray propagation and therefore implicitly or explicitly include the geometry of the propagation environment. The flexible structure of GSCMs enables the representation of different propagation environments by simple adjustment of model parameters, which is referred to as *generic* property. The generic models introduce abstract classes called *scenarios* that act as stochastic equivalents for many similar radio environments. As discussed in [1] these scenarios are not necessarily distinguished by the quantification of parametric space, but they represent a convenient terminology to designate typical deployment and propagation conditions. From history, it was COST207 [2] that started classifying environments based on the type of dispersion (delay spread and delay window), so some intuitive consideration of the (rather limited) parameter space was involved. But, these types of differences have (almost) never been sought later on, when defining new scenarios, especially following deployment schemes.

Nowadays we can distinguish between two major classes of generic models: COST 259/273/2100 ([3–5], resp.) and 3GPP SCM [6]/WINNER [7, 8]. The first one defines spatial regions where interacting objects become "visible,"

that is, contributing to the total received field. The second class offers an abstraction of the environment in parametric space by using delay and angular spreads, cross-polarization, shadowing, K-factor, and so forth. These generic models have been made by joint effort of many institutions; otherwise provision of parameters for different scenarios would be unattainable. Despite different model structures, significant overlap of propagation scenario definitions exists between SCM/WINNER and COST models [9].

The need for generic models follows from the ever growing concept of heterogeneous networks, requiring simultaneous representation of multiple scenarios or transitions between scenarios. For this purpose scenarios of generic models provide a uniform modeling approach and decrease the perceived complexity of handling different environments.

A reduction of the number of scenarios in generic models also reduces the necessary time and effort for design and performance evaluation of communication systems. Since every environment is specific, the classification of propagation environments into the different (reference) scenarios is not a simple task: how many classes suffice and how much divergence within a class should be tolerated? Obviously, a meaningful answer can be provided only if we have a metric to quantify the similarity between propagation environments. Providing such a metric is the main goal of this paper.

In absence of a scenario distance metric, reference scenarios are typically formed as a combination of system deployment schemes, mobility assumptions, and narrative description of environments, as illustrated in Section 2 for the WINNER reference propagation scenarios. The structure of the WINNER channel model and an approximation of its parametric space with multivariate normal distribution are given in Section 3. Section 4 describes measurement experiments used for the validation of the proposed distance metric and WINNER scenario parameters. The mean Kullback-Leibler divergence is introduced in Section 5 and is exploited to quantify the similarity between the approximated WINNER scenarios. Necessary modifications of the WINNER correlation coefficients are explained in the same section. Section 6 presents the results of measurement classification based on the introduced divergence measure, and Section 7 concludes the paper.

2. WINNER Reference Propagation Scenarios

The WINNER (Wireless World Initiative New Radio) project [10] was conducted in three phases (I, II, and +) from 2004 until 2010, with the aim to define a single ubiquitous radio access system concept, scalable and adaptable to different short range and wide area scenarios. The effects of the radio-propagation on the overall system design are abstracted by the introduction of Reference Propagation Scenarios (RPSs). RPSs are related to WINNER system-deployment schemes, being suitably selected to represent different coverage ranges: wide area (WA), metropolitan area (MA), and local area (LA), and each deployment scheme was described by as few propagation scenarios as possible. The outcome is that the WINNER scenarios cover some typical cases, without the intent to encounter all possible propagation environments.

The WINNER reference propagation scenarios [7] are determined by the aspects that have immediate impact on the radio-signal propagation:

(i) propagation environment,

  (a) LoS/NLoS condition,
  (b) limited distance range,

(ii) terminal positions (heights) with respect to environment,

(iii) mobility model (terminal speed),

(iv) carrier frequency range/bandwidth.

Due to different propagation mechanisms under LoS and NLoS conditions, they are distinguished and separately characterized in all applicable physical environments.

All WINNER reference propagation scenarios are represented by generic channel model. This model, called WINNER channel Model (WIM), has been developed within the 3GPP Spatial Channel Model (SCM) framework. By its nature, these models are representing the wideband MIMO channels in static environments for nonstationary users. The MATLAB implementations of SCM and WIM are publicly available through the project website [10]. At the end of the phase II, WIM was parameterized for 12 different scenarios, being listed in Table 1. The full set of WIM RPS parameters can be found in Sections 4.3 and 4.4 of the WINNER deliverable D1.1.2 [7]. Relations between WINNER reference propagation scenarios and WIM parameters are illustrated in Figure 1.

The characterization of the reference propagation scenarios and parametrization of the generic model are based on channel sounding results. In order to collect relevant data, a large number of measurement campaigns have been carried out during the project. However, the realization of large-scale campaigns and the subsequent processing of the results are both complex and time consuming. As a consequence, the WINNER "scenario" is formed on the basis of measurement results that are gathered by different institutions and are individually projected on the parameter set of WINNER model. These measurements were conducted in radio environments providing the best possible match with defined reference scenarios. For that purpose, the position and movement of communication terminals were chosen according to the typical usage pattern. The resulting scenario-specific model parameters sometimes also include results found in the literature, in order to come up with the most typical representatives for a targeted scenario.

3. Structure of the WINNER Channel Model

WIM is a double-directional [11] geometry-based stochastic channel model, in which a time-variable channel impulse response is constructed as a finite sum of Multi-Path Components (MPCs). The MPCs are conveniently grouped into clusters, whose positions in multidimensional space are

Table 1: WINNER reference propagation scenarios.

Scenario	Definition	LoS/NLoS	Mob. [km/h]	AP ht [m]	UE ht [m]	Distance range [m]	Coverage
A1 (In building)	Indoor small office/residential	LoS/NLoS	0–5	1–2.5	1–2.5	3–100	LA
A2	Indoor-to-outdoor	LoS/NLoS	0–5	2–5 + floor height	1-2	3–1000	LA
B1 (Hotspot)	Typical urban microcell	LoS/NLoS	0–70	Below RT (3–20)	1-2	10–5000	LA, MA
B2	Bad urban microcell	LoS/NLoS	0–70	Below RT	1-2	10–5000	MA
B3 (Hotspot)	Large indoor hall	LoS	0–5	2–6	1-2	5–100	LA
B4	Outdoor-to-indoor	LoS/NLoS	0–5	Below RT	1-2	3–1000	MA
B5a (Hotspot, Metropol)	LoS stat. feeder, rooftop to rooftop	LoS	0	Above RT	Above RT	30–8000	MA
B5b/C5b (Hotspot, Metropol)	LoS stat. feeder, street level to street level	LoS	0	3–5	3–5	20–400	MA
B5c (Hotspot, Metropol)	LoS stat. feeder, below rooftop to street level	LoS	0	Below RT, for example, 10	3–5	20–1000	MA
B5d (Hotspot, Metropol)	NLoS stat. feeder, above rooftop to street level	NLoS	0	Above RT, for example, 32	3–5	35–3000	MA
B5f	Feeder link BS $\rightarrow$ FRS. Approximately RT to RT level	LoS/OLoS/NLoS	0	RT, for example, 25	RT, for example, 15	30–1500	WA
C1 (Metropol)	Suburban	LoS/NLoS	0–120	Above RT, 10–40	1-2	30–5000	MA, WA
C2 (Metropol)	Typical urban macrocell	NLoS	0–120	Above RT, for example, 32	1-2	10–5000	MA, WA
C3	Bad urban macrocell	LoS/NLoS	0–70	Above RT	1-2	50–5000	—
C4	Outdoor-to-indoor	LoS/NLoS	0–5	Above RT	1-2 + floor height	50–5000	MA
D1 (Rural)	Rural macrocell	LoS/NLoS	0–200	Above RT, for example, 45	1-2	35–10000	WA
D2a	Moving networks: BS—MRS, rural	LoS	0–350	20–50	2.5–5	30–3000	WA
D2b	Moving networks: MRS—MS, rural	LoS/OLoS/NLoS	0–5	>2.5	1-2	3–100	WA

Table 2: Large-scale parameters of WINNER model.

LSP Name	Acronym	Power distribution
Shadow fading	SF	Around mean transmission loss
Delay spread	DS	Over delay domain
Angular spread	ASD/ASA ESD/ESA	Over angular domain: (i) at Departure and Arrival (ii) over Azimuth and Elevation, "Azimuth/Elevation"
Narrowband K-factor	K	Betw. LoS and NLoS clusters
CROSS polar. ratio	XPR	Betw. co- and cross-polar MPCs

determined by Large-Scale Parameter (LSP) realizations. LSPs are controlling the distribution of the power (spreading) over the individual dimensions of the channel, as indicated in Table 2.

Within the modeling context LSPs are exploited to govern the evolution of the synthesized channel. The entire process of WIM parameter synthesis can be done in three hierarchy levels [9].

(1) On top level, large-scale parameters listed in Table 2 are drawn randomly from tabulated log-normal Probability Density Functions (PDFs). With the exception of XPR, all other LSPs are generated as *correlated* random variables.

(2) On the second level, cluster parameters are determined. For the sake of the simplicity this level of freedom is reduced in SCM/WIM, since all clusters share the same (scenario dependent) intra-Cluster Angular Spread (CAS).

(3) In order to further simplify cluster characterization, SCM/WIM does not deal with random placement of MPCs in delay or angular domains. Instead, the same, simple internal structure of the cluster is used and MPC parameters are calculated in a deterministic manner.

Following the given WIM approximations the LSPs become the most important for the particular scenario characterization. We would therefore ignore the lower hierarchy levels when computing a scenario divergence in Section 5.

3.1. Transformed LSP Domain. The WINNER model investigates LSP distributions and their correlations in transformed domain [6] where normal distributions for all transformed LSPs are assumed. For log-normally distributed LSPs (delay and angular spreads) the mapping $\tilde{s} = g(s) = \log_{10}(s)$ is applied (Figure 2). The remaining LSPs (SF, XPR, and K-factor) have Gaussian distributions when expressed in (dB). The WINNER tables specify marginal (per-dimension) TLSP distributions with mean and variance parameters $(\mu_i, \sigma_i)_{i=1,\dots,k}$ and matrix of correlation coefficients $\boldsymbol{\rho} = [\rho_{i,j}]_{i=1,\dots,k;\, j=1,\dots,k}$. The entries of this matrix express pairwise correlations of the LSPs x_i and x_j in the form of the correlation coefficient:

$$\rho_{i,j} = \frac{\mathrm{Cov}\left[x_i, x_j\right]}{\sqrt{\mathrm{Cov}\left[x_i, x_i\right]\mathrm{Cov}\left[x_j, x_j\right]}} = \frac{\sigma_{i,j}^2}{\sigma_i \sigma_j}, \quad (1)$$

where $\sigma_{i,j} = \mathrm{Cov}[x_i, x_j] = E[(x_i - E[x_i])(x_j - E[x_j])]$. Figure 3 shows marginal distributions of delay spread in transformed domain for all WIM reference scenarios having NLoS propagation and additionally includes the maximum likelihood estimate of normal distributions for Ilmenau and Dresden measurements, which will be discussed in the following sections.

3.1.1. Multivariate Normal Distribution of TLSPs. The multivariate normal probability density function of a k-dimensional random vector $\mathbf{x} = [x_1, x_2, \dots, x_k]^T : \mathcal{N}(\boldsymbol{\mu}, \boldsymbol{\Sigma})$ can be expressed as [12]

$$f(\mathbf{x}) = \frac{1}{(2\pi)^{k/2}|\boldsymbol{\Sigma}|^{1/2}} \exp\left(-\frac{1}{2}(\mathbf{x} - \boldsymbol{\mu})^T \boldsymbol{\Sigma}^{-1}(\mathbf{x} - \boldsymbol{\mu})\right), \quad (2)$$

where

$$\boldsymbol{\mu} = E[\mathbf{x}] \in \mathbb{R}^k \quad (3)$$

is k-dimensional mean vector and $k \times k$ covariance matrix is

$$\boldsymbol{\Sigma} = \mathrm{Cov}[\mathbf{x}, \mathbf{x}] = E\left[(\mathbf{x} - E[\mathbf{x}])(\mathbf{x} - E[\mathbf{x}])^T\right] \in \mathbb{R}^{k \times k}. \quad (4)$$

Although the structuring of the WIM TLSP distribution parameters is slightly different, they basically represent maximum-likelihood estimates of a multivariate normal (MVN) distribution parameters (3) and (4). (The random variables showing very specific dependence are not jointly normally distributed even if their marginal distributions are normal. Since only dependence between continuous WIM LSPs is expressed by the correlation coefficient (1), we assume without explicit proof that the vector of LSPs will have jointly normal distribution.) It is therefore possible to reconstruct the full covariance matrix of MVN by the following scaling:

$$\boldsymbol{\Sigma} = \boldsymbol{\Sigma}_0^{1/2} \boldsymbol{\rho} \boldsymbol{\Sigma}_0^{1/2}, \quad (5)$$

where

$$\boldsymbol{\Sigma}_0 = \mathrm{diag}\left(\sigma_1^2, \sigma_2^2, \dots, \sigma_k^2\right) \quad (6)$$

represents the diagonal covariance matrix of the uncorrelated LSPs. Accordingly, every WINNER scenario can be abstracted with (up to) 8-dimensional normally distributed random process where relevant dimensions describe different large-scale parameters listed in Table 2. In a given case, the multivariate normal process offers a straightforward approximation of WINNER scenario since the majority of them have identical cluster structure.

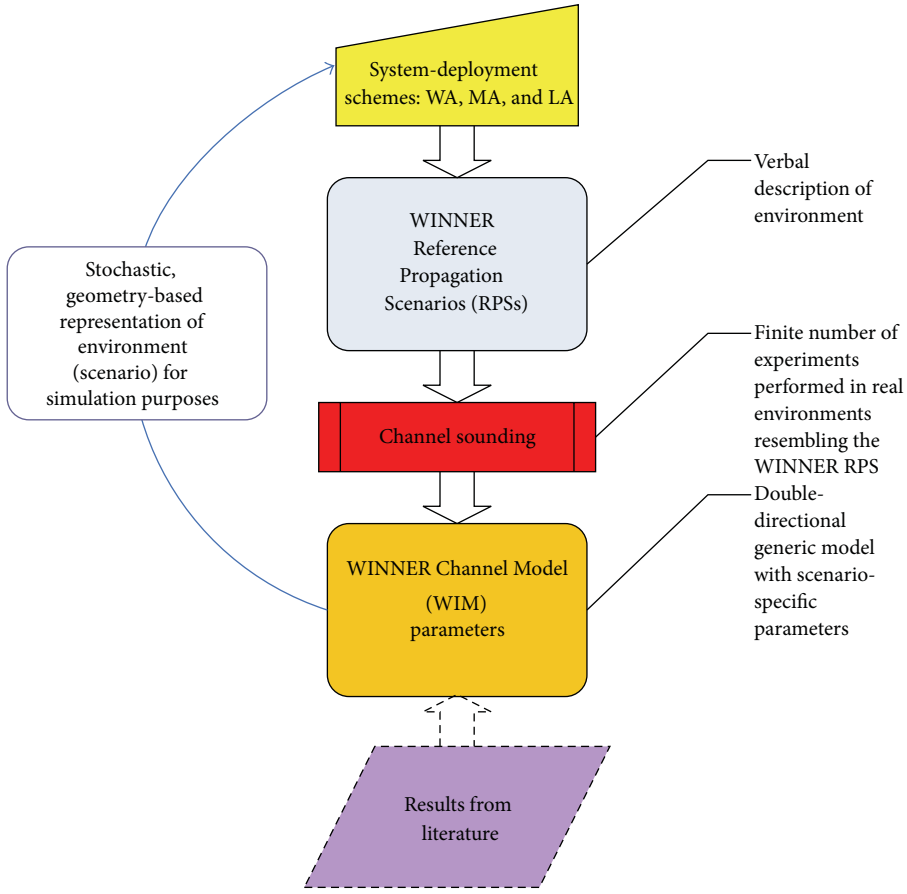

Figure 1: Genesis and representation of WINNER reference propagation scenarios [9].

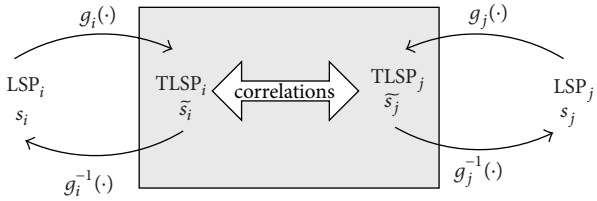

Figure 2: LSP are characterized and synthetized in transformed domain.

3.2. Terminal Separation. Although WIM describes the propagation environment implicitly within LSP parametric space, it is still using distance to govern transmission loss and spatial variations of LSP realizations.

Local stationarity region represents a larger area where multipath structure of physical propagation channel does not change significantly ("local region of stationarity" [13], "drop" [6], and "channel segment" [7]), and it is therefore characterized by a single realization from multidimensional LSP distribution. In WINNER model it is conveniently assumed that the extent of local stationarity region can be represented by the scenario-dependent constant (*decorrelation distance*) that is independent from the LSP cross-correlations.

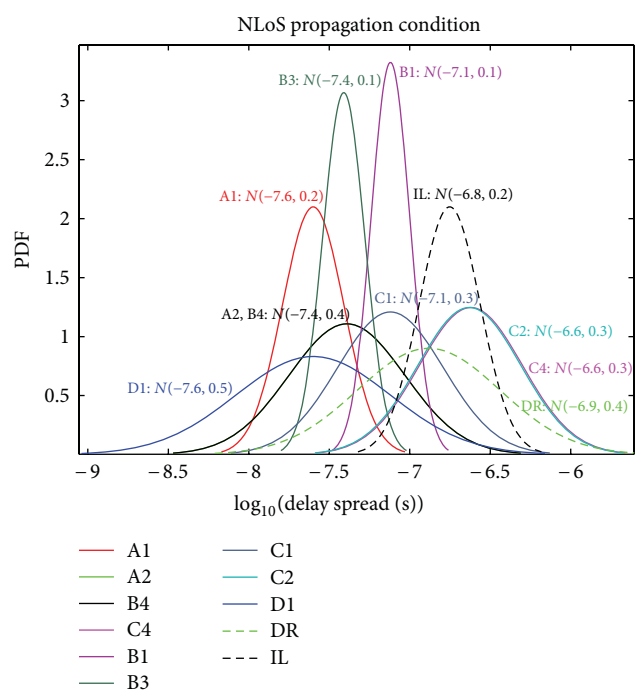

Figure 3: Delay spread PDFs in transformed domain.

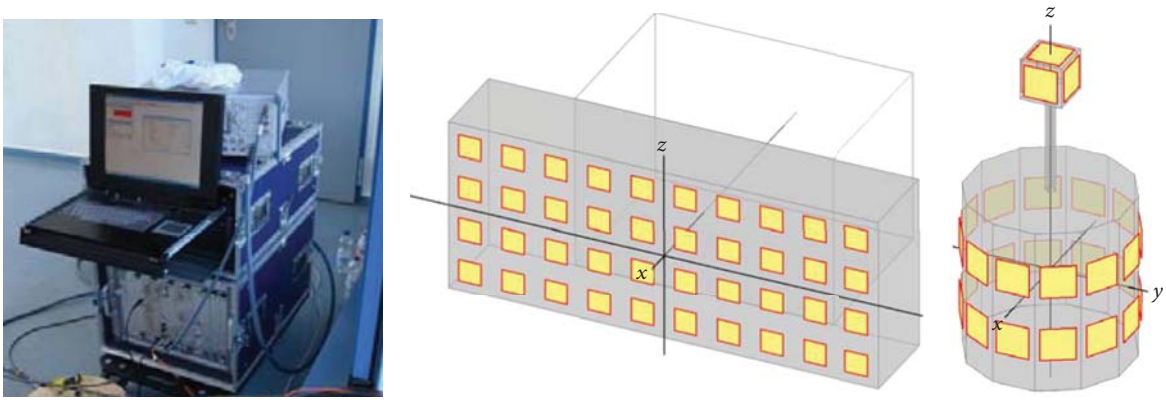

(a) (b) (c)

Figure 4: Measurement equipment: RUSK sounder (Tx) and antenna arrays—PULA8 (Tx) and SPUCA12 + MIMO-Cube (Rx).

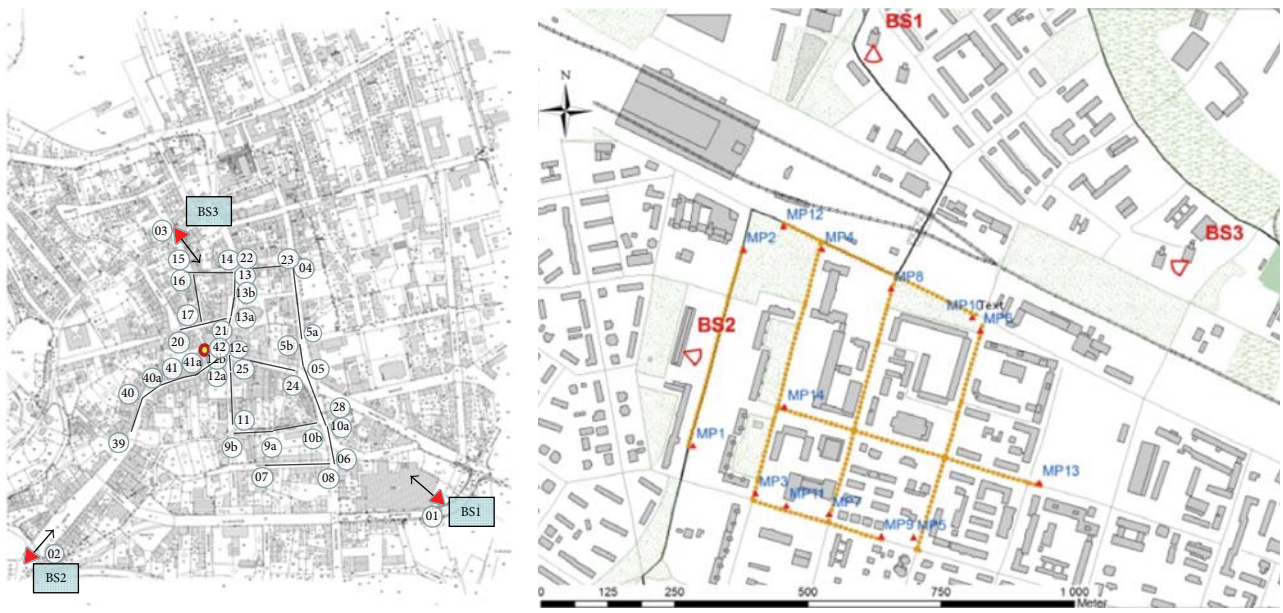

(a) (b)

Figure 5: BS locations and measurement tracks in Ilmenau and Dresden.

Both transmission loss and decorrelation distance are deterministic features in WIM. They do not impact MVN distribution of TLSPs and could be analyzed independently. Therefore, we investigate MVN process as joint model for WINNER LSP marginal distributions and cross-correlation coefficients. This representation of multidimensional channel, on the scenario scale, can be considered as a generalization of the 1D small-scale fading channel approach, where stochastic properties of instantaneous envelope are characterized by PDF.

4. Representation of Measurements in WINNER Parametric Space

The multidimensional sounding enables the investigation of the complete spatiotemporal structure of a radio channel that, additionally to the temporal delay of incoming waves, includes their angular directions at transmission and at reception as well as their polarizations. This can be achieved by the specialized estimation algorithms as RIMAX [14] when calibration data of double-polarized measurement antenna

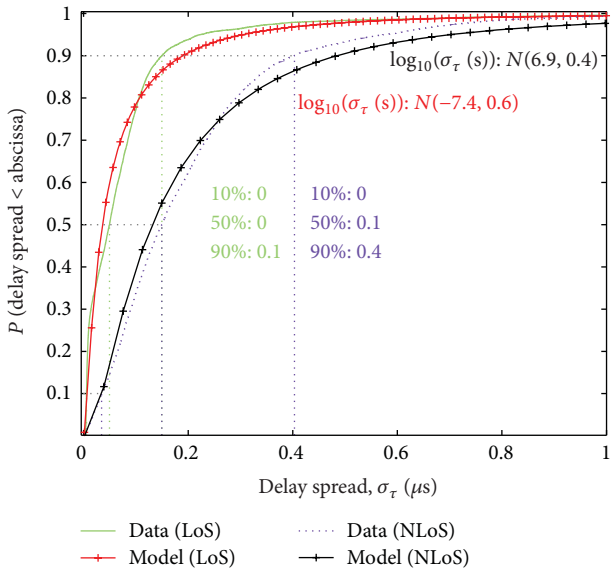

Figure 6: Distributions of delay spreads in Dresden measurement.

array is available [15, 16]. The multidimensional sounding is performed by dedicated RF equipment that sequentially transmits and measures channel responses between multiple antennas on transmitter and receiver sides. This approach requires high reliability of the time referencing of measurement data on both sides of radiolink, which is typically achieved by highly stable rubidium or cesium clocks.

4.1. Measurement Campaigns. In this paper data from two measurement experiments will be exploited: the first one is performed in Ilmenau, Germany, in 2008 and the second in Dresden, Germany in 2009. In the rest of the paper they will be conveniently labeled as IL and DR, respectively. Both measurements are performed with Medav RUSK channel sounder [17] at 2.53 GHz using frequency bandwidth of 100 MHz. To allow high-resolution parameter estimations of multipath structure, dedicated antenna arrays at transmit and receive sides are used, providing a total of 928 MIMO subchannels (Figure 4). The time necessary to record the responses of all wideband MIMO sub-channels, T_S, was 12.1 ms for Ilmenau and 24.2 ms for Dresden measurement. This limits the maximally allowed speed between the measurement vehicle and other interacting objects, $v \leq \lambda/2T_S$, to 17.6 km/h and 8.8 km/h, respectively ($\lambda \approx 12$ cm denotes the wavelength of the carrier). Under these conditions channels are properly sampled in space-time.

In both campaigns, three well-separated base station locations within city centers are used (Figure 5), and mobile terminal is positioned on the rooftop of the car. The same macrocell measurement setup, including the configuration of the measurement equipment, provides the proper base for comparison of Ilmenau and Dresden propagation environments. Ilmenau is a small city compared to Dresden: whereas Ilmenau is characterized by 3-4 floor buildings, Dresden has buildings with 6–8 floors. Subsequently the base station height at Dresden (~50 m) was almost doubled compared to Ilmenau (~25 m).

4.2. Estimated MVN Distribution Parameters. Data from both measurement locations is used to estimate the parameters of WINNER model. The parameters of marginal LSPs and corresponding correlation coefficients estimated from Ilmenau and Dresden measurements are given in Tables 8 and 9 together with parameters describing WINNER reference propagation scenarios. Additional details regarding Ilmenau and Dresden measurements and analysis can be found in [18, 19], respectively.

According to the description of WINNER reference propagation scenarios, both measurements should be assigned to the typical urban macrocell scenario, C2. Since both measurements are conducted after the publication of WIM-C2 parameters, they provide a proper test set for the validation of reported WIM parameters.

4.2.1. Normality of Estimated LSPs in Transformed Domain. Figure 6 shows maximum likelihood fit of the empirical delay spread CDF from Dresden measurement with WINNER-like log-normal distribution. Although this approximation seems reasonable, the null hypothesis, that collected and transformed DS samples coming from normal distribution, is rejected by both Lilliefors [20] and Jarque-Bera [21] normality tests. In contrast to the one-sample Kolmogorov-Smirnov test, these tests are suitable when parameters of null distribution are unknown and must be estimated. The normality hypothesis is also rejected for other large-scale parameters estimated from Ilmenau and Dresden data, for both LoS and NLoS conditions. Therefore the representation of measurements in WINNER parametric space can be considered as maximum-likelihood approximation of empirical multivariate distribution with MVN process.

5. Quantification of Scenario Distance

As showed in Section 3.1.1, the parameter set of WINNER model is equivalent to the parameters of the multivariate normal distribution. Therefore, all measurement projections and reference scenarios share the same parameter set and could be treated as multivariate probability distributions. This enables the introduction of a metric to quantify the divergence (distance) between different projections of measurements on the parameter set of the model, including the representatives of different reference scenarios. In order to illustrate the (dis)similarity between B3 and C2 WINNER scenarios under LoS and NLoS propagation, joint 2D PDFs of delay spread and shadow fading are presented in Figure 7. We can observe that these scenarios have differences, but some kind of similarity measure will be useful. Having in mind that we want to quantify the distance between two

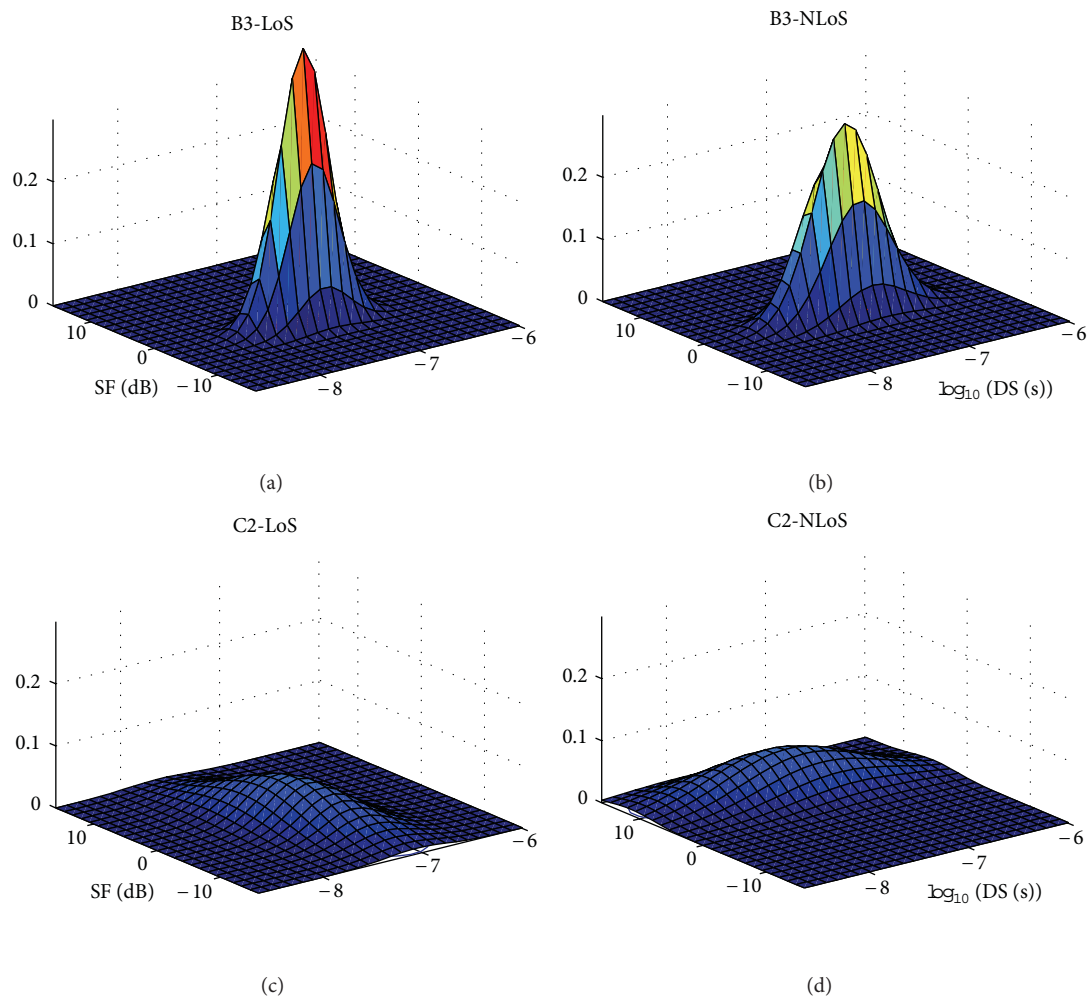

Figure 7: Comparison of joint (DS and SF) PDFs for B3 and C2 WINNER scenarios, for LoS and NLoS propagation.

distributions P and Q, it is possible to apply some form of relative entropy, for example, Kullback-Leibler (KL) divergence [22]:

$$D_{\mathrm{KL}}(P\|Q) = \int_{\mathbf{x}\in\mathbb{R}^k} p(\mathbf{x}) \log_2 \frac{p(\mathbf{x})}{q(\mathbf{x})} d\mathbf{x}, \tag{7}$$

where p and q denote the densities of P and Q. The computation of the KL divergence according to (7) would require multidimensional mapping of the $\mathbb{R}^k$ subset into two PDFs: p and q. This approach may become impractical for a large number of dimensions: in the case of WINNER it is necessary to consider up to 8 dimensions (although the XPR is not correlated with other LSPs). The marginal PDFs of K-factor are given only for scenarios with LoS propagation what reduces the dimensionality of MVN distribution for NLoS propagation for 1.

In a special case when considering divergence between two MVN distributions it is possible to construct an analytical expression that depends solely on distribution parameters. The Kullback-Leibler divergence from $\mathcal{N}_0(\mu_0, \Sigma_0)$ to $\mathcal{N}_1(\mu_1, \Sigma_1)$, for nonsingular matrices Σ_0 and $\Sigma_1 \in \mathbb{R}^{k\times k}$, is [23]

$$\begin{aligned} D_{\mathrm{KL}}(\mathcal{N}_0\|\mathcal{N}_1) &= \frac{1}{2\log_e 2}\cdot\left[\log_e\left(\frac{\det(\Sigma_1)}{\det(\Sigma_0)}\right)\right. \\ &\quad \left. + \operatorname{tr}\left(\Sigma_1^{-1}\Sigma_0\right) + (\mu_1-\mu_0)^{\top}\Sigma_1^{-1}(\mu_1-\mu_0) - k\right]. \end{aligned} \tag{8}$$

This metric enables a simple comparison of reference WINNER scenarios. Therefore we found that the original form of KL metric (7) is more suitable for this particular problem than its symmetrized form, the Jansen-Shannon divergence [24]. Since KL divergence is not symmetric, it is necessary to define some other symmetrized extension to obtain proper distance metric. We propose to use mean KL divergence:

$$D_{\overline{\mathrm{KL}}}(P\|Q) = \frac{1}{2}\left[D_{\mathrm{KL}}(P\|Q) + D_{\mathrm{KL}}(Q\|P)\right]. \tag{9}$$

5.1. Negative Definite Covariance Matrices. In some cases negative or complex values are obtained for KL divergence, indicating that the matrix of correlation coefficients ($\boldsymbol{\rho}$) is not positive semidefinite, that is, $\boldsymbol{\rho} < 0$. The problem is manifesting only for scenarios with resolved elevation angles (Table 3) where the dimensionality of the MVN distribution is increased from 6 (LoS)/5 (NLoS) to 7/6 or 8/7. The problem is, however, not related to the number of dimensions or elevation parameters themselves since simple removal of elevation dimension(s) does not resolve it. This means that correlation coefficients between WINNER LSPs analyzed jointly do not form a proper correlation matrix (CM)—not even without elevations.

It is observed that the number of decimal places used for representation of CM elements cannot be arbitrarily reduced since the resulting matrix may become negative definite. Since individual coefficients in WINNER parameter tables are expressed using only one decimal place, it is possible that this lack of precision causes negative definite CM for scenarios with an increased number of dimensions.

In order to enable the comparison of problematic scenarios their correlation coefficients have to be slightly modified to form positive definite CM. The "real" correlation matrix is computed using alternate projections method (APM) [25, 26]. For a given symmetric matrix $\boldsymbol{\rho} \in \mathbb{R}^{kxk}$ this method finds the nearest correlation matrix $\widehat{\boldsymbol{\rho}}$, that is, (semi) definite, and has units along the main diagonal. The solution is found in the intersection of the following sets of symmetric matrices $S = \{Y = Y^T \in \mathbb{R}^{kxk} \mid Y \geq 0\}$ and $U = \{Y = Y^T \in \mathbb{R}^{kxk} \mid y_{ii} = 1,\ i = 1, \ldots, k\}$. The iterative procedure in nth step applies updated Dykstra's correction ΔS_{n-1} and subsequently projects intermediate result to both matrix sets, using projections P_S and P_U:

$$\begin{aligned}
&\Delta \mathbf{S}_0 = 0, \qquad \mathbf{Y}_0 = \boldsymbol{\rho}, \qquad n = 0 \\
&\text{do} \\
&\quad n = n + 1 \\
&\quad \mathbf{R}_n = \mathbf{Y}_{n-1} - \Delta \mathbf{S}_{n-1} \\
&\quad \mathbf{X}_n = P_S(\mathbf{R}_n) \\
&\quad \Delta \mathbf{S}_{n-1} = \mathbf{X}_n - \mathbf{R}_n \\
&\quad \mathbf{Y}_n = P_U(\mathbf{X}_n) \\
&\text{while } \left\|\mathbf{Y}_n - \mathbf{Y}_{n-1}\right\|_F < tol.
\end{aligned} \tag{10}$$

The projection P_S replaces all negative eigenvalues of the matrix with a small positive constant ϵ, and P_U forces ones along the main diagonal. The procedure stops when Frobenius distance $\|\cdot\|_F$ between Y_n projections from two consecutive iterations drops below a predefined tolerance tol. Note, however, that the small tolerance parameter does not insure that Frobenius distance (FD) from the original matrix is equally small.

The positive definite approximation $\widehat{\boldsymbol{\rho}}$ obtained by APM will depend on the selected parameters ϵ and tol [27]: for $tol = 10^{-10}$, the effect of eigenvalue ϵ on Frobenius distance FD $= \|\boldsymbol{\rho} - \widehat{\boldsymbol{\rho}}\|_F$ is illustrated in Table 3. The results show that FD decreases when a smaller value of ϵ is used to substitute originally negative eigenvalues. However, the selection of small ϵ will proportionally increase the eigenvalues and coefficients of the inverse correlation matrix, $\widehat{\boldsymbol{\rho}}^{-1}$. This will consequently increase the KL divergence (7) to all other scenarios. As a compromise, the new WINNER correlation coefficients corresponding to positive definite matrix are recomputed for $\epsilon = 10^{-2}$ and $tol = 10^{-10}$ and given in Table 9. The maximal absolute modification of original correlation coefficients per scenario, $\max\{|\Delta\rho_{i,j}|\}$, where $\Delta\rho_{i,j} = \rho_{i,j} - \widehat{\rho}_{i,j}$, is given in Table 3. The highest absolute correction $\Delta\rho = 0.13$ is applied to C2-NLoS scenario.

The minimum number of decimal places required to keep $\widehat{\boldsymbol{\rho}}$ positive definite is determined for different values of ϵ and listed in Table 3. The results show that smaller Frobenius distance requires higher precision for saving coefficients. For $\epsilon = 10^{-2}$ two decimal places are sufficient to express correlation coefficients for all scenarios (Table 9).

5.2. Mean KL Divergence. In order to enable comparisons between LoS and NLoS scenarios where K-factor is missing under NLoS, as well as other scenarios where certain parameters (dimensions) are missing, the reduction of dimensionality was necessary: only those dimensions existing in both scenarios are used to calculate the mean KL divergence. This means that scenarios with lower number of resolved dimensions could exhibit more similarity as a consequence of incomplete representation. A fair comparison would be possible only if all scenarios have the same number of dimensions. The respective mean KL divergences between all WINNER scenarios, including Ilmenau and Dresden measurements, are given in Table 4 (for WINNER scenarios that give two sets of LoS parameters, mean KL distances are computed for LoS parameters before breakpoint distance of transmission loss).

In order to simplify the analysis of obtained results, for each (scenario, propagation) combination the closest match is found and listed in Table 5. Divergences within the same WINNER scenario group, or having same propagation conditions, are not minimum as may have been expected. Table 5 shows that only 5 among 16 WINNER scenarios have the closest match within the same WINNER group (A, B, C, and D). This comes as consequence of subjective classification of similar environments, without previously introduced metric. The minimum distances from Table 5, $D_{\overline{\mathrm{KL}}} = 0.1$, confirm some expectations: B4-NLoS (outdoor-to-indoor) is closest to A2-NLoS (indoor-to-outdoor) because these are reciprocal scenarios. Also, microcell and macrocell versions of outdoor-to-indoor (B4 and C4) are the closest although not belonging to the same group. Mean KL divergences from Table 5 suggest that there is a better way to group available scenarios.

The average distances between all scenarios from one WINNER group to all scenarios in the other groups are given in Table 6. If all groups gather the most similar scenarios, an average distance between any two groups will be higher than the average distance within a single group. From Table 6 we can see that this applies to groups A and D, which

Table 3: Frobenius distance (FD) between empirical corr. matrix ρ and its positive definite approximation $\widehat{\rho}$, the required number of decimal places (DP) in $\widehat{\rho}$, and maximal correction of original correlation coefficients $\max\{|\Delta\rho_{i,j}|\}$, as functions of the substituting eigenvalue ϵ in APM for $tol = 10^{-10}$.

		10^{-1}			10^{-2}			10^{-3}			10^{-6}		
Scenario	Propagation	$\lVert\cdot\rVert$	DP	max( )	$\lVert\cdot\rVert$	DP	max( )	$\lVert\cdot\rVert$	DP	max( )	$\lVert\cdot\rVert$	DP	max( )
A1	LoS	0.245	1	0.1	0.123	2	0.04	0.108	2	0.03	0.108	2	0.03
B4	NLoS	0.316	1	0.1	0.241	2	0.1	0.227	3	0.091	0.226	4	0.091
B1	LoS	0.374	1	0.1	0.269	2	0.09	0.257	3	0.085	0.255	3	0.085
B1	NLoS	0.2	1	0.1	0.066	2	0.02	0.056	3	0.019	0.055	3	0.019
C1	LoS	0.346	1	0.1	0.203	2	0.07	0.191	3	0.065	0.19	4	0.064
C1	OLoS	0.346	1	0.1	0.203	2	0.07	0.191	3	0.065	0.19	4	0.064
C1	NLoS	0.245	1	0.1	0.245	1	0.1	0.245	1	0.1	0.245	1	0.1
C2	LoS	0.374	1	0.1	0.193	2	0.06	0.174	3	0.058	0.173	6	0.058
C2	OLoS	0.374	1	0.1	0.193	2	0.06	0.174	3	0.058	0.173	6	0.058
C2	NLoS	0.548	1	0.2	0.338	2	0.13	0.333	3	0.129	0.332	5	0.129
DR	LoS	0.168	1	0.048	0.168	1	0.048	0.168	1	0.048	0.168	1	0.048
DR	NLoS	0.116	1	0.046	0.116	1	0.046	0.116	1	0.046	0.116	1	0.046
IL	LoS	0.133	1	0.043	0.133	1	0.043	0.133	1	0.043	0.133	1	0.043
IL	NLoS	0.144	1	0.047	0.144	1	0.047	0.144	1	0.047	0.144	1	0.047

Table 4: Mean KL divergence between WINNER scenarios and Ilmenau and Dresden measurements.

Scen.		A1	A1	A2	B1	B1	B3	B3	B4	C1	C1	C2	C2	C4	D1	D1	D2a	IL	IL	
	Prop.	LoS	NLoS	NLoS	LoS	NLoS	LoS	NLoS	NLoS	LoS	NLoS	LoS	NLoS	NLoS	LoS	NLoS	LoS	LoS	NLoS	LoS
A1	NLoS	19.6																		
A2	NLoS	11.0	15.4																	
B1	LoS	78.1	44.5	57.1																
B1	NLoS	52.3	51.1	27.0	20.6															
B3	LoS	14.1	8.3	21.7	23.6	15.4														
B3	NLoS	12.3	9.9	32.9	16.2	10.1	5.4													
B4	NLoS	45.2	26.8	0.1	138.5	67.1	21.1	31.5												
C1	LoS	120.9	119.2	60.7	101.6	57.4	33.1	15.5	170.8											
C1	NLoS	224.2	262.4	29.4	86.4	98.3	17.7	9.8	280.1	54.7										
C2	LoS	55.5	41.7	27.8	48.6	55.5	23.2	10.1	72.1	23.5	103.4									
C2	NLoS	117.1	134.3	50.3	121.5	141.7	40.3	20.7	163.4	28.9	33.2	54.2								
C4	NLoS	36.4	41.3	11.4	56.1	31.5	49.4	49.5	9.8	55.3	26.8	31.1	38.5							
D1	LoS	25.1	35.8	29.5	14.2	44.2	28.2	31.5	27.0	5.9	14.1	12.9	19.1	31.2						
D1	NLoS	14.3	14.4	19.9	11.2	23.9	11.5	11.4	17.5	14.6	4.8	5.6	11.5	23.7	6.7					
D2a	LoS	15.6	18.8	30.1	6.1	11.2	13.6	9.7	25.9	7.4	8.7	9.9	15.9	31.7	6.7	5.4				
IL	LoS	84.6	64.8	149.9	51.8	45.9	49.4	24.9	145.2	32.5	23.4	35.7	16.9	130.1	55.9	24.8	36.1			
IL	NLoS	87.3	74.1	116.9	105.5	53.7	46.7	26.2	154.0	25.8	25.6	36.4	15.3	89.7	41.8	24.4	22.8	2.8		
DR	LoS	96.6	94.3	128.9	43.8	49.7	44.0	22.5	130.4	11.6	20.3	23.9	16.0	128.9	14.0	23.0	12.7	38.3	32.0	
DR	NLoS	119.2	104.8	140.8	48.2	48.8	45.1	24.4	142.3	8.6	22.0	27.4	11.0	126.9	16.5	25.2	14.4	30.1	22.8	2.7

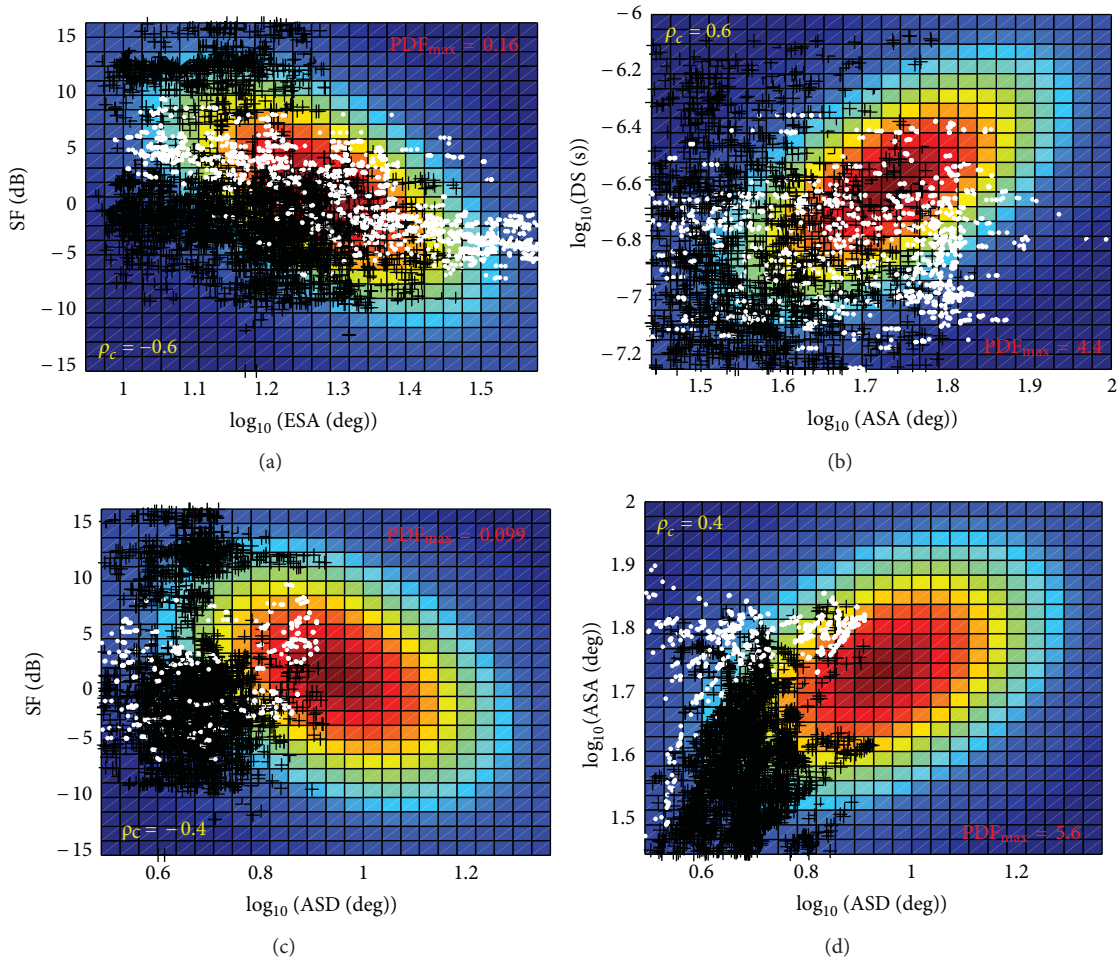

Figure 8: Comparison of joint WINNER C2 2D PDFs with the LSP realizations from Ilmenau (black pluses) and Dresden (white dots), for NLoS propagation.

are, according to average intergroup distance, closest to themselves. This indicates that subjective WINNER grouping can be partially supported by mean KL distance. However, the deviations are observable for groups B and C where other groups appear to be closer (at a lower average distance) than other scenarios from the same group. This situation is possibly caused by inappropriate assignment of distant scenarios, outdoor-to-indoor microcell scenario B4-NLoS and suburban C1-NLoS, to the corresponding groups.

An inspection of Table 3 reveals that the majority of scenarios with increased dimensionality (resolved elevations) come from groups B and C. This means that larger intra-group distance may appear due to increased dimensionality. Additionally, their correlation matrices have been modified by APM method, so that the parameter ϵ impacts the absolute value of the mean KL distance. The joint effect of these phenomena is illustrated by mean KL distances along the main diagonal of Table 6: they are proportional to the number of modified group members that are listed in Table 3: $\#_D = 0$, $\#_A = 1$, $\#_B = 3$, $\#_C = 6$.

Table 5: Closest (scenario, propagation) pairs according to mean KL divergence.

Scen.1	Prop.1	Scen.2	Prop.2	$\overline{KL}$
A1	LoS	A2	NLoS	11.0
A1	NLoS	B3	LoS	8.3
A2	NLoS	B4	NLoS	0.1
B1	LoS	D2a	LoS	6.1
B1	NLoS	B3	NLoS	10.1
B3	LoS	B3	NLoS	5.4
B3	NLoS	B3	LoS	5.4
B4	NLoS	A2	NLoS	0.1
C1	LoS	D1	LoS	5.9
C1	NLoS	D1	NLoS	4.8
C2	LoS	D1	NLoS	5.6
C2	NLoS	DR	NLoS	11.0
C4	NLoS	B4	NLoS	9.8
D1	LoS	C1	LoS	5.9
D1	NLoS	C1	NLoS	4.8
D2a	LoS	D1	NLoS	5.4
IL	LoS	IL	NLoS	2.8
IL	NLoS	IL	LoS	2.8
DR	LoS	DR	NLoS	2.7
DR	NLoS	DR	LoS	2.7

Table 6: Average distance between WINNER scenario groups: A, B, C, and D.

	A	B	C	D
A	15.3			
B	32.1	35.0		
C	88.8	70.6	45.0	
D	22.6	19.1	14.5	6.3

Table 7: Average distance between WINNER LoS and NLoS propagation conditions.

	LoS	NLoS
LoS	31.8	
NLoS	42.1	50.9

For 6 out of 16 (scenario, propagation) pairs the best match has the opposite propagation condition (LoS, instead of NLoS, and vice versa), indicating that WINNER LoS and NLoS parameters do not form disjunctive sets (Table 5). Calculation of the mean distance between all LoS and NLoS scenarios in Table 7 shows that lower average distance can be expected between scenarios having LoS propagation condition (they are more similar than different scenarios with NLoS propagation).

6. Classification of Measurements

The same criterion, KL divergence, can be applied to classify measurements as well. For this purpose even empirical distributions of LSPs can be used since KL metric (7) supports that. However, the extraction of the corresponding WINNER parameters simplifies the comparison since analytical expression (8) can be applied. Therefore we use the latter approach to compare Ilmenau and Dresden measurements with other WINNER scenarios.

Since both measurements have been performed in urban environments with macrocell setup (antennas were elevated above rooftops), it is expected that the closest scenario will be WINNER C2, which represents typical urban macrocells. These expectations are met for Ilmenau measurements, where WINNER C2-NLoS is the closest scenario for both LoS and NLoS conditions, with minimal distances $D_{\overline{\mathrm{KL}}} = 16.9$ and $D_{\overline{\mathrm{KL}}} = 15.3$ (Table 4). In the case of Dresden measurements minimal mean KL divergences (8.6 and 11.6) indicate that the closest WIM scenario is C1-LoS, for both LoS and NLoS propagation conditions. This resemblance of Dresden measurements to suburban propagation (WINNER C1) may come from dominant height of BS positions with respect to environment.

Figure 8 shows the 2D PDFs of the reference WINNER C2-NLoS scenario together with joint LSP realizations from Ilmenau and Dresden measurements. For the NLoS propagation condition Ilmenau and Dresden measurements are quite close to C2: C2-NLoS is the best match for Ilmenau-NLoS ($D_{\overline{\mathrm{KL}}} = 16.3$) and the second best match for Dresden-NLoS data ($D_{\overline{\mathrm{KL}}} = 11$). Additionally, among all results presented in Table 4 the closest match of WIM C2-NLoS is just Dresden-NLoS (row showed in red).

For LoS conditions, distances from WINNER C2 and Ilmenau and Dresden measurements are larger (35.7 and 23.9) which classifies Ilmenau-LoS to C2-NLoS ($D_{\overline{\mathrm{KL}}} = 16.9$) and Dresden-LoS into C1-LoS ($D_{\overline{\mathrm{KL}}} = 11.6$). Table 5 shows the increased similarity between LoS and NLoS propagation conditions in Ilmenau and Dresden measurements. This occurs also for WINNER B3, while other WINNER scenarios do not show this property. One possible interpretation comes from the data segmentation into LoS and NLoS classes: the actual propagation conditions for the LoS or NLoS-labeled data may actually correspond to, for example, obstructed line of sight (OLoS). The previous analysis demonstrates that mean KL divergence, additionally to the comparison of different measurements, enables the quantification of complex relations between different data segments of the same measurement, as long as they use the same LSP space representation.

The mean KL distances between Ilmenau and Dresden measurements (38.3-LoS and 22.8-NLoS) are higher than corresponding distances from these measurements to the reference WINNER-C2 scenario. This confirms that WINNER C2 parameters provide appropriate representation for a wide class of urban macro-cell environments.

7. Conclusions

The paper presents the scenario concept of WINNER and proposes its abstraction to a multivariate normal distribution of large-scale parameters. Disregarding transmission loss and decorrelation distance removes the spatial extent from scenario definitions.

The generic property of the model is exploited to compare the large-scale parameters that describe different scenarios. For this purpose, a symmetrized extension of the Kullback-Leibler divergence is proposed. This enables the comparison of parameters between reference scenarios and measurements, as well as a direct comparison of empirical LSP distributions (measured or synthesized by channel model). The given approach can be also applied to other generic stochastic models if appropriate metrics are chosen that reflect models' specifics.

The presented results indicate that, according to the mean Kullback-Leibler divergence, WINNER scenario groups or propagation classes do not ensure the minimum separation within the group/class. It appears that other criteria, for example, coverage range, were more significant for the WINNER taxonomy. Judged from the mean Kullback-Leibler divergence large similarity exists between the indoor-to-outdoor and outdoor-to-indoor scenarios (A2, B4, and C4), between macro-cell configurations for suburban, urban, and rural scenarios (C1, C2, and D1), and between the indoor/hotspot/microcellular scenarios (A1, B3, and B1).

It is demonstrated that the results of measurements could be associated with the closest WINNER scenario. As expected, typical urban macro-cell scenario C2 was the one closest to the Ilmenau measurements. For the Dresden

Table 8: LSP marginal PDF parameters.

LSP	Scen. Prop.	A1 LoS	A1 NLoS	A2 NLoS	B4 NLoS	C4 NLoS	B1 LoS	B1 NLoS	B3 LoS	B3 NLoS	C1 LoS	C1 NLoS	C2 LoS	C2 NLoS	D1 LoS	D1 NLoS	D2a LoS	DR LoS	DR NLoS	IL LoS	IL NLoS
DS		−7.4	−7.6	−7.4	−7.4	−6.6	−7.4	−7.1	−7.5	−7.4	−7.2	−7.1	−7.4	−6.6	−7.8	−7.6	−7.4	−7.4	−6.9	−6.9	−6.8
DS		0.3	0.2	0.4	0.4	0.3	0.3	0.1	0.1	0.1	0.5	0.3	0.6	0.3	0.6	0.5	0.2	0.6	0.4	0.2	0.2
ASD		1.6	1.7	1.8	1.8	1.8	0.4	1.2	1.2	1.1	0.8	0.9	1.0	0.9	0.8	1.0	0.7	0.7	0.7	0.2	0.4
ASD		0.3	0.2	0.2	0.2	0.2	0.4	0.2	0.2	0.2	0.1	0.4	0.3	0.2	0.2	0.5	0.3	0.1	0.1	0.3	0.4
ASA		1.6	1.7	1.3	1.3	1.3	1.4	1.6	1.6	1.7	1.5	1.6	1.7	1.7	1.2	1.5	1.5	1.5	1.6	1.6	1.6
ASA		0.3	0.1	0.4	0.4	0.4	0.2	0.2	0.2	0.1	0.2	0.3	0.2	0.1	0.2	0.3	0.2	0.1	0.1	0.2	0.2
ESD		0.9	1.1	N/A	0.9	N/A	0.4	0.6	N/A	N/A	0.7	0.9	0.7	0.9	N/A	N/A	N/A	N/A	N/A	N/A	N/A
ESD		0.3	0.2	N/A	0.3	N/A	0.2	0.2	N/A	N/A	0.2	0.2	0.2	0.2	N/A	N/A	N/A	N/A	N/A	N/A	N/A
ESA		0.9	1.1	N/A	1.0	N/A	0.6	0.9	N/A	N/A	1.1	1.0	0.9	1.3	N/A	N/A	N/A	1.2	1.2	1.3	1.3
ESA		0.3	0.2	N/A	0.4	N/A	0.2	0.2	N/A	N/A	0.2	0.2	0.2	0.2	N/A	N/A	N/A	0.1	0.1	0.2	0.2
SF		0.0	0.0	0.0	0.0	0.0	0.0	0.0	0.0	0.0	0.0	0.0	0.0	0.0	0.0	0.0	0.0	0.0	0.0	−0.0	0.0
SF		3.0	4.0	7.0	7.0	7.0	3.0	4.0	3.0	4.0	4.0	8.0	4.0	8.0	4.0	8.0	4.0	8.3	5.3	4.0	3.6
K		7.0	N/A	N/A	N/A	N/A	9.0	N/A	2.0	N/A	9.0	N/A	7.0	N/A	7.0	N/A	7.0	9.8	N/A	5.9	N/A
K		6.0	N/A	N/A	N/A	N/A	6.0	N/A	3.0	N/A	7.0	N/A	3.0	N/A	6.0	N/A	6.0	7.8	N/A	7.1	N/A
XPR		11.0	10.0	9.0	9.0	9.0	9.0	8.0	9.0	6.0	8.0	4.0	8.0	7.0	12.0	7.0	12.0	9.7	7.0	7.3	6.2
XPR		4.0	4.0	11.0	11.0	11.0	3.0	3.0	4.0	3.0	4.0	3.0	4.0	3.0	8.0	4.0	8.0	3.6	4.1	1.2	2.2

Table 9: LSP correlation coefficients.

		LSP1	DS	DS	DS	DS	DS	DS	ASD	ASD	ASD	ASD	ASD	ASA	ASA	ASA	ASA	ESD	ESD	ESD	ESA	ESA	SF
Scen.	Prop.	LSP2	ASD	ASA	ESD	ESA	SF	K	ASA	ESD	ESA	SF	K	ESD	ESA	SF	K	ESA	SF	K	SF	K	K
A1	LoS		0.7	0.8	0.5	0.7	−0.6	−0.6	0.6	0.5	0.0	−0.5	−0.6	0.0	0.5	−0.5	−0.6	0.4	−0.4	0.0	0.0	0.0	0.4
A1	LoS		0.67	0.82	0.52	0.66	−0.58	−0.59		0.48	0.03	−0.52	−0.61	0.01	0.48	−0.49	−0.60	0.38	−0.39	0.00	−0.02	−0.01	0.40
A1	NLoS		−0.1	0.3	−0.6	0.0	−0.5	N/A	−0.3	0.5	0.0	0.0	N/A	0.0	0.5	−0.4	N/A	0.5	0.0	N/A	0.0	N/A	N/A
A2	NLoS		0.4	0.4	N/A	N/A	−0.5	N/A	0.0	N/A	N/A	0.0	N/A	N/A	N/A	0.2	N/A	N/A	N/A	N/A	N/A	N/A	N/A
B1	LoS		0.5	0.8	−0.5	0.0	−0.4	−0.7	0.4	0.5	0.5	−0.5	−0.3	0.0	0.0	−0.5	−0.3	0.0	0.0	0.0	0.0	0.0	0.5
B1	LoS		0.41	0.74	−0.41	0.03	−0.43	−0.65	0.44	0.44	0.48	−0.48	−0.33	−0.04	−0.01	−0.48	−0.32	0.02	−0.02	0.04	−0.01	0.01	0.49
B1	NLoS		0.2	0.4	−0.5	0.0	−0.7	N/A	0.1	0.5	0.5	0.0	N/A	0.0	0.0	−0.4	N/A	0.0	0.0	N/A	0.0	N/A	N/A
B1	NLoS		0.18	0.40	−0.48	0.01	−0.68	N/A	0.10	0.48	0.49	−0.01	N/A	−0.00	−0.00	−0.40	N/A	0.01	0.01	N/A	0.01	N/A	N/A
B3	LoS		−0.3	−0.4	N/A	N/A	−0.1	−0.3	0.3	N/A	N/A	0.3	0.2	N/A	N/A	−0.4	−0.1	N/A	N/A	N/A	N/A	N/A	0.6
B3	NLoS		−0.1	0.0	N/A	N/A	−0.2	N/A	−0.3	N/A	N/A	−0.3	N/A	N/A	N/A	0.2	N/A	N/A	N/A	N/A	N/A	N/A	N/A
B4	NLoS		0.4	0.4	−0.6	0.0	−0.5	N/A	0.0	0.5	0.0	0.0	N/A	0.0	0.5	0.2	N/A	0.5	0.0	N/A	0.0	N/A	N/A
B4	NLoS		0.33	0.37	−0.50	−0.03	−0.45	N/A	0.02	0.43	0.02	−0.03	N/A	−0.03	0.51	0.19	N/A	0.48	0.04	N/A	−0.01	N/A	N/A
C1	LoS		0.2	0.8	−0.5	0.0	−0.6	−0.2	0.1	0.5	0.0	−0.5	0.2	0.0	0.4	−0.5	−0.2	0.0	0.0	0.0	−0.8	0.0	0.0
C1	LoS		0.20	0.75	−0.46	0.06	−0.53	−0.19	0.10	0.50	0.00	−0.50	0.20	−0.02	0.36	−0.54	−0.20	0.03	0.03	0.00	−0.75	0.00	0.00
C1	NLoS		0.3	0.7	−0.5	0.0	−0.4	N/A	0.3	0.5	−0.4	−0.4	N/A	0.0	0.0	−0.3	N/A	0.0	0.0	N/A	−0.8	N/A	N/A
C1	NLoS		0.3	0.7	−0.5	−0.0	−0.4	N/A	0.3	0.5	−0.3	−0.3	N/A	−0.0	0.0	−0.3	N/A	−0.0	−0.0	N/A	−0.7	N/A	N/A
C2	LoS		0.4	0.8	−0.5	0.0	−0.4	−0.4	0.3	0.5	0.0	−0.5	0.1	0.0	0.4	−0.5	−0.2	0.0	0.0	0.0	−0.8	0.0	0.3
C2	LoS		0.35	0.74	−0.44	0.01	−0.41	−0.37	0.33	0.46	0.01	−0.47	0.08	−0.04	0.39	−0.50	−0.22	0.00	−0.02	0.02	−0.77	−0.01	0.29
C2	NLoS		0.4	0.6	−0.5	0.0	−0.4	N/A	0.4	0.5	−0.4	−0.6	N/A	0.0	0.0	−0.3	N/A	0.0	0.0	N/A	−0.8	N/A	N/A
C2	NLoS		0.38	0.60	−0.49	−0.02	−0.42	N/A	0.40	0.45	−0.28	−0.47	N/A	0.00	−0.00	−0.30	N/A	−0.05	−0.05	N/A	−0.67	N/A	N/A
C4	NLoS		0.4	0.4	N/A	N/A	−0.5	N/A	0.0	N/A	N/A	0.0	N/A	N/A	N/A	0.2	N/A	N/A	N/A	N/A	N/A	N/A	N/A
D1	LoS		−0.1	0.2	N/A	N/A	−0.5	0.0	−0.3	N/A	N/A	0.2	0.0	N/A	N/A	−0.2	0.1	N/A	N/A	N/A	N/A	N/A	0.0
D1	NLoS		−0.4	0.1	N/A	N/A	−0.5	N/A	−0.2	N/A	N/A	0.6	N/A	N/A	N/A	0.1	N/A	N/A	N/A	N/A	N/A	N/A	N/A
D2a	LoS		−0.1	0.2	N/A	N/A	−0.5	0.0	−0.3	N/A	N/A	0.2	0.0	N/A	N/A	−0.2	0.1	N/A	N/A	N/A	N/A	N/A	0.0
DR	LoS		−0.07	−0.03	N/A	0.06	−0.62	−0.65	0.42	N/A	0.08	−0.08	−0.06	N/A	0.25	−0.13	−0.10	N/A	N/A	N/A	−0.43	−0.27	0.73
DR	LoS		−0.1	−0.0	N/A	0.1	−0.6	−0.7	0.4	N/A	0.1	−0.1	−0.1	N/A	0.3	−0.1	−0.1	N/A	N/A	N/A	−0.4	−0.3	0.7
DR	NLoS		−0.11	−0.21	N/A	−0.29	−0.49	N/A	0.40	N/A	0.05	0.06	N/A	N/A	0.27	0.12	N/A	N/A	N/A	N/A	−0.26	N/A	N/A
DR	NLoS		−0.1	−0.2	N/A	−0.3	−0.5	N/A	0.4	N/A	0.1	0.1	N/A	N/A	0.3	0.1	N/A	N/A	N/A	N/A	−0.3	N/A	N/A
IL	LoS		−0.10	−0.12	N/A	−0.03	−0.04	−0.38	0.58	N/A	−0.34	0.17	0.03	N/A	0.42	−0.50	−0.21	N/A	N/A	N/A	−0.77	−0.29	0.52
IL	LoS		−0.1	−0.1	N/A	−0.0	−0.0	−0.4	0.6	N/A	−0.3	0.2	0.0	N/A	0.4	−0.5	−0.2	N/A	N/A	N/A	−0.8	−0.3	0.5
IL	NLoS		0.08	−0.04	N/A	−0.16	0.02	N/A	0.65	N/A	−0.36	0.18	N/A	N/A	0.30	−0.34	N/A	N/A	N/A	N/A	−0.77	N/A	N/A
IL	NLoS		0.1	−0.0	N/A	−0.2	0.0	N/A	0.7	N/A	−0.4	0.2	N/A	N/A	0.3	−0.3	N/A	N/A	N/A	N/A	−0.8	N/A	N/A

measurements, suburban LSP distributions of C1 were closest. This measurement, however, appears to be at minimum distance from C2-NLoS, indicating a validity of assumed macro-cell measurement setup. The proper choice of WINNER C2 parameters for representation of the whole class of urban macrocells is confirmed by the Ilmenau and Dresden measurements: these measurements are closer to the C2 reference than to each other.

For those scenarios/measurements where the correlation coefficients form a negative definite symmetric matrix, the alternating projection method is exploited to determine the closest correlation matrix. Therefore, the paper also introduces the modified WINNER scenario parameters that enable a quantification of scenario divergence.

Appendix

Parameters of WINNER Channel Model Describing MVN Distributions

In order to ensure the traceability of the presented divergences, the relevant subset of WINNER parameters is given in Tables 8 and 9. They also include the MVN distribution parameters estimated from Ilmenau and Dresden measurements. Additionally, Table 9 contains the modified correlation coefficients $\widehat{\rho}$ that form positive definite correlation matrices. They are used for scenario representation instead of original coefficients.

Acknowledgment

The authors would like to acknowledge the contributions of their colleagues from EASY-C project during the conduction and analysis of measurements, especially to Carsten Jandura, Actix GmbH.

References

[1] A. F. Molisch, H. Asplund, R. Heddergott, M. Steinbauer, and T. Zwick, "The COST259 directional channel model-part I: overview and methodology," *IEEE Transactions on Wireless Communications*, vol. 5, no. 12, pp. 3421–3433, 2006.

[2] "Digital land mobile radio communications," Tech. Rep. COST207, 1989.

[3] L. Correia, Ed., *Wireless Flexible Personalised Communications: COST 259, European Co-Operation in Mobile Radio Research*, Wiley, 2001.

[4] L. Correia, "Mobile broadband multimedia networks—techniques, models and tools for 4G," Final Report COST 273, Elsevier, Oxford, UK, 2006.

[5] R. Verdone and A. Zanella, *Pervasive Mobile and Ambient Wireless Communications*, Signals and Communication Technology, Springer, London, UK, 2012.

[6] 3GPP TR25.996 V9.0.0, Spatial channel model for MIMO simulations,Third Generation Partnership Project (3GPP), Tech. Rep., December 2009, http://www.3gpp.org/.

[7] P. Kyösti, J. Meinilä, L. Hentilä et al., "IST-4-027756 WINNER II Deliverable 1.1.2. v.1.2, WINNER II Channel Models," Tech. Rep. IST-WINNERII, 2007.

[8] Guidelines for evaluation of radio interface technologies for IMTAdvanced, Report ITU-R M.2135-1, International Telecommunication Union, Radiocommunication Sector (ITU-R), 2009, http://www.itu.int/pub/R-REP-M.2135-1-.

[9] M. Narandžić, C. Schneider, and R. S. Thomä, "WINNER wideband MIMO system-level channel model, comparison with other reference models," in *Proceedings of the Internationales Wissenschartliches Kolloquium (IWK '09)*, vol. 54, Ilmenau, Germany, 2009.

[10] WINNER (Wireless world INitiative NEw Radio), http://projects.celtic-initiative.org/winner+/.

[11] M. Steinbauer, A. F. Molisch, and E. Bonek, "The double-directional radio channel," *IEEE Antennas and Propagation Magazine*, vol. 43, no. 4, pp. 51–63, 2001.

[12] "Multivariate normal distribution," http://en.wikipedia.org/wiki/Multivariate_normal_distribution.

[13] A. Gehring, M. Steinbauer, I. Gaspard, and M. Grigat, "Empirical channel stationarity in urban environments," in *Proceedings of the European Personal Mobile Communications Conference (EPMCC '01)*, Vienna, Austria, February 2001.

[14] R. Thomä, M. Landmann, and A. Richter, "RIMAX—a maximum likelihood framework for parameter estimation in multidimensional channel sounding," in *Proceedings of the International Symposium on Antennas and Propagation*, Sendai, Japan, August 2004.

[15] M. Landman, M. Narandžić, and R. S. Thomä, "Limits of experimental channel characterization related to antenna calibration," in *Proceedings of the 29th General Assembly of the International Union of Radio Science (URSI '08)*, Chicago, Ill, USA, August 2008.

[16] M. Landmann, M. Käske, and R. S. Thomä, "Impact of incomplete and inaccurate data models on high resolution parameter estimation in multidimensional channel sounding," *IEEE Transactions on Antennas and Propagation*, vol. 60, no. 2, pp. 557–573, 2012.

[17] Rusk channel sounder, http://www.channelsounder.de/.

[18] C. Schneider, M. Narandžić, M. Käske, G. Sommerkorn, and R. S. Thomä, "Large Scale parameter for the WINNER II channel model at 2. 53 GHz in urban macro cell," in *Proceedings of the IEEE 71st Vehicular Technology Conference (VTC '10)*, Taipei, Taiwan, May 2010.

[19] M. Narandžić, C. Schneider, M. Käske, S. Jäckel, G. Sommerkorn, and R. S. Thomä, "Large-scale parameters of wideband MIMO channel in urban multi-cell scenario," in *Proceedings of the 5th European Conference on Antennas and Propagation (EUCAP '11)*, pp. 3759–3763, Rome, Italy, April 2011.

[20] H. W. Lilliefors, "On the Kolmogorov-Smirnov test for normality with mean and variance unknown," *Journal of the American Statistical Association*, vol. 62, no. 318, pp. 399–402, 1967.

[21] C. M. Jarque and A. K. Bera, "A test for normality of observations and regression residuals," *International Statistical Review*, vol. 55, no. 2, pp. 163–172, 1987.

[22] S. Kullback and R. A. Leibler, "On information and sufficiency," *The Annals of Mathematical Statistics*, vol. 22, no. 1, pp. 79–86, 1951.

[23] W. D. Penny and S. J. Roberts, "Variational bayes for generalised autoregressive models," Tech. Rep. PARG-00-12, Department of Engineering Science, Oxford University, 2000.

[24] B. Fuglede and F. Topsøe, "Jensen-Shannon Divergence and Hilbert space embedding," http://www.math.ku.dk/~topsoe/ISIT2004JSD.pdf.

[25] J. P. Boyle and R. L. Dykstra, "A method for finding projections onto the intersection of convex sets in Hilbert spaces," *Advances in Order Restricted Inference*, vol. 37, pp. 28–47, 1986.

[26] N. J. Higham, "Computing the nearest correlation matrix—a problem from finance," *IMA Journal of Numerical Analysis*, vol. 22, no. 3, pp. 329–343, 2002.

[27] A. P. García Ariza, J. F. Monserrat, and L. Rubio, "Alternating projection method applied to indefinite correlation matrices for generation of synthetic MIMO channels," *International Journal of Electronics and Communications*, vol. 64, no. 1, pp. 1–7, 2010.

Hindawi Publishing Corporation
International Journal of Antennas and Propagation
Volume 2013, Article ID 864641, 7 pages
http://dx.doi.org/10.1155/2013/864641

Research Article

A Tradeoff between Rich Multipath and High Receive Power in MIMO Capacity

Zimu Cheng, Binghao Chen, and Zhangdui Zhong

State Key Laboratory of Rail Traffic Control and Safety, Beijing Jiaotong University, Beijing 100044, China

Correspondence should be addressed to Zimu Cheng; 10120073@bjtu.edu.cn

Received 27 July 2012; Accepted 24 November 2012

Academic Editor: Ai Bo

A discussion about which of the two factors, rich multipath (in NLOS) or signal-to-noise ratio (SNR) (usually in LOS), affects the Multiple-Input Multiple-Output (MIMO) channel capacity more is presented in this paper. This interesting discussion is investigated by performing simulations using simple circle scatterer model and WINNER II channel model. And the simulation shows that these two factors behave differently as the channel condition varyies. When the scatterer number in channel is low, the high receive SNR is more important to capacity. The multipath richness will have greater influence when the scatterer number exceeds a certain threshold. However, the channel capacity will not change much as the scatterers continue to increase.

1. Introduction

Multiple-Input Multiple-Output (MIMO) is a hot research topic that has always attracted much attention in recent decades. When multiple antennas are deployed at both transmit side and receive side, the performance of communication system can be enhanced significantly.

The MIMO performance highly depends on the propagation environments and channel model structures. Two channel conditions, that is, NLOS (Non-line-of-sight) and LOS (Line-of-sight), are commonly used in propagation research. In general, if a strong LOS path exists in environment, it is called the Ricean channel. If there is no LOS path, the receive signal will follow Rayleigh distribution. In Rayleigh assumption, the multipath is scattered by the rich scatterers uniformly distributed around the receiver. And the multipath richness is important for MIMO system, for it will provide a large number of eigenvalues of MIMO channel. While in LOS scenario, generally the LOS path is stronger than scattering components and leads to a high receive SNR which will also contribute to MIMO capacity. But a high SNR associated with LOS often implies a low degree of scattering which, however, will cause the capacity loss again. This paper is going to talk about whether the rich multipath or high receive SNR is more important to MIMO capacity.

The discussions about which of these two factors is more important have started in the literature. Wallace and Jensen discuss the MIMO capacity variation with SNR and multipath richness using full-wave indoor finite-difference time domain (FDTD) simulations [1]. The relationship of SNR, effective degrees of freedom (EDOF), and capacity is studied. Also a slight change of multipath richness is observed only in the indoor environment. Malik studies MIMO capacity and multipath scaling in ultrawideband (UWB) channels [2]. It is found that in a rich scattering environment, the indoor UWB system capacity can be dramatically increased by using MIMO array. Matthaiou et al. investigates the impact of sparse multipath on MIMO channel performance [3]. According to the indoor measurement data, it shows that physical nature of scattering environment has a noticeable impact on the degree of freedom afforded by a sparse multipath MIMO channel. The ergodic capacity has strong dependency on the sparse multipath environment. Koch and Lapidoth research the high-SNR behavior of the capacity of noncoherent multipath fading channels [4]. At high SNR, if the number of path is finite, the capacity grows to double logarithmically with the SNR. Meanwhile, the high-SNR behavior of the capacity of multipath fading channels depends critically on the assumed channel model. A slight change in the channel model might lead to completely different capacity

results. Saad et al. focus on the relationship between channel correlation, eigenvalues, and capacity [5]. They draw the conclusion that the eigenmodes of channel are independent of the SNR, but depend on channel correlation. And the maximum eigenmode of MIMO channel increases with the channel correlation while all other eigenmodes decrease. Knopp et al. investigate the impact of sparse multipath components on the LOS MIMO channel capacity using in-room measurements [6]. It is found that single but strong deterministic multipath signal distinctly enhances the channel capacity in low-rank LOS channel, while no significant capacity change occurs in high-rank LOS channel due to the reflected waves. However, most of the measurements above are taken indoors and the corresponding simulations and theoretical analysis are considered in the indoor environment only. More general channel models are used in this paper, and the relationship between the number of scatterers and eigenvalues is analyzed.

To avoid the Rayleigh channel model limitation that the scatterers' distribution is ideal and does not agree well with the real case, the circle scatterer model and WINNER II channel models are used in this paper, for they can be manipulated flexibly and are much closer to the real case that the multipath is a kind of sparse in real channel. Although a general geometry-based stochastic model, consisting of two-ring and ellipse scatterers with single-bounce and double-bounce paths, is proposed in [7–9], the circle scatterer model and WINNER II model used in this paper can also cover most of the scenarios. More importantly, it is easy to change the number of scatterers or clusters in these two models, which will make us concentrate on the relationship between scatterer number and channel capacity. Besides the discussion, the effect of scatterer number on MIMO channel structure, that is, the eigenvalues for all subchannels, is analyzed as well. The discussion is based on mobile scenario. For the high velocity of receiver, the channel information is unknown at the transmitter. So equal power allocation strategy is applied, which will be described in details later.

The paper is organized as follows. In Section 2, circle scatterer model and WINNER II channel model are introduced. MIMO channel capacity will be derived and developed in Section 3. Section 4 is devoted to the simulation result and the conclusions are drawn in Section 5.

2. MIMO Channel Model

2.1. Circle Scatterer Model. This model is aimed at generating multiple-point scatterers around the receiver. The scatterers can be placed in a circle with the receiver in the center. The receive signal consists of the waves scattered once by each point scatterer. The basic simulation idea is to calculate the complex envelop for each possible combination of transmit and receive antennas, like what Figure 1 shows. Then, the ensemble of complex envelop constitutes the channel transmission matrix. From there, singular value decomposition (SVD) of H is performed for assessing the available capacity [10].

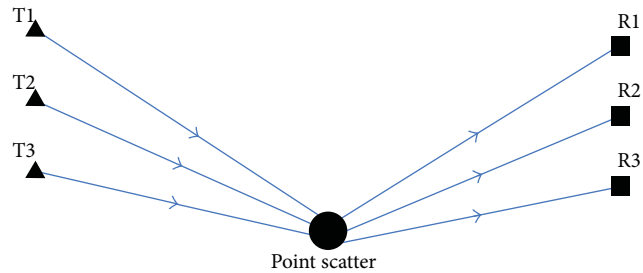

Figure 1: Circle scatterer model.

The general representation of the complex envelop received at antenna j from transmit antenna i is given by

$$r^{ij} = \sum_{n=1}^{N} a_n \exp\left(-jk_c d_n^{ij} + j\Phi_n^{ij}\right), \tag{1}$$

where coefficients ij indicate Tx-Rx antenna pair, n indicates the scatterer number, N indicates the total number of scatterers (paths), and a_n indicates the transmit power of the path, while d_n^{ij} and Φ_n^{ij} are the distance of Tx-scatterer-Rx and the phase of the received wave, respectively. k_c is the propagation constant.

2.2. WINNER II Channel Model. The WINNER II channel model is a geometry-based stochastic channel model, which can generate an arbitrary MIMO channel matrix for defined scenarios. It is ray-based double directional multilink and antenna-independent model for MIMO systems. The statistical distributions of channel parameters such as AoA (Angle of Arrival), DoA (Angle of Departure), delay spread, and delay values are obtained from channel measurements. In the simulation, the parameters are determined stochastically from the distributions for each channel sample. Fixed 20 rays compose a cluster, which is considered as a propagation path diffused in space domain. The channel impulse response coefficients are generated by combining contributions of all rays which are characterized by small scale parameters.

One single link of the WINNER II channel model is illustrated in Figure 2 [11], in which the parameters for generation of channel matrix are also illustrated. Each circle with several dots represents scattering region causing one cluster. The number of clusters varies from 8 to 20 depending on different scenarios.

φ and ϕ are the AoA and AoD, respectively, τ is the cluster delay, and σ is the delay spread. $\bar{v}$ is the speed of MS. So the channel matrix of WINNER II MIMO channel model is given by [11]

$$H(t;\tau) = \sum_{n=1}^{N} H_n(t;\tau), \tag{2}$$

where

$$H_n(t;\tau) = \iint F_{rx}(\varphi)\, h_n(t;\tau,\phi,\varphi)\, F_{tx}^{T}(\phi)\, d\phi\, d\varphi, \tag{3}$$

where N is the total number of paths, and F_{tx} and F_{rx} refer to antenna array response matrices for the transmitter and

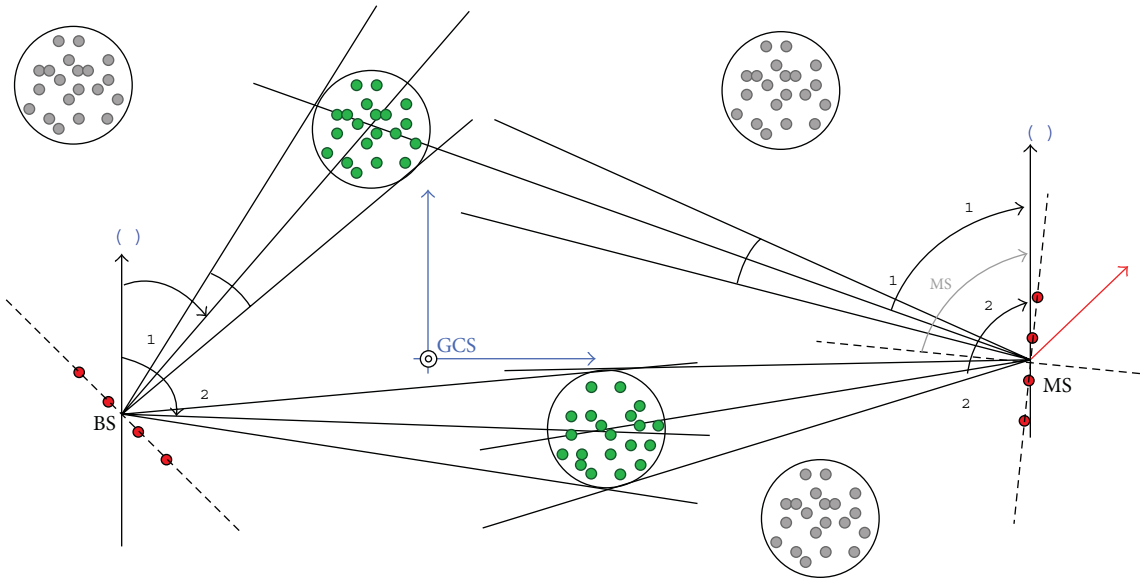

Figure 2: WINNER II channel model.

receiver, respectively. h_n is the propagation channel response matrix for cluster n.

The channel response for cluster n from transmitter antenna elements s to receiver transmitter elements u is given by [11]

$$\begin{aligned} H_{u,s,n}(t;\tau) &= \sum_{m=1}^{M} \begin{bmatrix} F_{rx,u,V}(\varphi_{n,m}) \\ F_{rx,u,H}(\varphi_{n,m}) \end{bmatrix}^T \begin{bmatrix} \alpha_{n,m,VV} & \alpha_{n,m,VH} \\ \alpha_{n,m,HV} & \alpha_{n,m,HH} \end{bmatrix} \\ &\quad \times \begin{bmatrix} F_{tx,s,V}(\phi_{n,m}) \\ F_{tx,s,H}(\phi_{n,m}) \end{bmatrix} \\ &\quad \times \exp\left(j2\pi\lambda_0^{-1}\left(\overline{\varphi}_{n,m}\cdot\overline{r}_{rx,u}\right)\right) \\ &\quad \times \exp\left(j2\pi\lambda_0^{-1}\left(\overline{\phi}_{n,m}\cdot\overline{r}_{tx,s}\right)\right) \\ &\quad \times \exp\left(j2\pi\upsilon_{n,m}t\right)\delta\left(\tau-\tau_{n,m}\right), \end{aligned} \tag{4}$$

where $F_{tx,u,H}$ and $F_{rx,u,V}$ represent the antenna element u field patterns for horizontal and vertical polarizations. $\alpha_{n,m,HH}$ and $\alpha_{n,m,HV}$ represent the complex gains of horizontalto-horizontal and horizontal-to-vertical polarization of ray n, m. And λ_0 is the wave length of carrier frequency. Meanwhile, $\overline{\varphi}_{n,m}$ is AoA unit vector, and $\overline{\phi}_{n,m}$ is AoD unit vector. $\overline{r}_{rx,u}$ and $\overline{r}_{tx,s}$ represent the location vector of elements u and s respectively. $\upsilon_{n,m}$ refers to the Doppler shift component of ray n, m. And the superscript $(\cdot)^T$ means transposition. All the small scale parameters mentioned above are time variant for the reason that the radio channel is modeled dynamically. More details about parameters generation in WINNER II model can be found in [11].

3. MIMO Channel Capacity

A MIMO system model can be expressed as

$$y = Hx + n, \tag{5}$$

where x and y are the vectors of transmitted and received signals at one sample time, respectively, and n is the addictive white Gaussian noise (AWGN). If it is considered that the transmitter has n_t antennas while the receiver has n_r antennas, then H should be an $n_r \times n_t$ matrix.

According to the information theory, the ergodic capacity is given by [12]

$$C = \mathrm{E}\left[\log\det\left(I_{n_r} + \frac{\mathrm{SNR}}{n_t}HH^*\right)\right], \tag{6}$$

where I_{n_r} is an n_r rank unit matrix and $\mathrm{SNR} = P/N_0$ is the signal-to-noise ratio at receiver.

The channel also can be divided into several parallel independent subchannels by the method of SVD. The number of subchannels is the same as the number of singular values and the gains of these subchannels are related to the value of the singular values. Hence, the total channel capacity can be obtained by summing the capacities of all the subchannels. In that case, the ergodic capacity can be expressed as follows [12]:

$$C = \sum_{i=1}^{n_{\min}} \log\left(1 + \frac{\mathrm{SNR}}{n_t}\lambda_i^2\right), \tag{7}$$

where $n_{\min} = \min\{n_t, n_r\}$, λ_i are singular values of channel matrix. For the reason that λ_i is nonnegative, the equation above can be concluded as

$$\begin{aligned} C &= \log \prod_{i=1}^{n_{\min}} \left(1 + \frac{\mathrm{SNR}}{n_t}\lambda_i^2\right) \\ &\le \log \left(\frac{\sum_{i=1}^{n_{\min}} \left(1 + (\mathrm{SNR}/n_t)\lambda_i^2\right)}{n_{\min}}\right)^2 \\ &= 2\log \left(\frac{\sum_{i=1}^{n_{\min}} \left(1 + (\mathrm{SNR}/n_t)\lambda_i^2\right)}{n_{\min}}\right) \\ &= 2\log \left(1 + \frac{\mathrm{SNR}}{n_t n_{\min}} \sum_{i=1}^{n_{\min}} \lambda_i^2\right). \end{aligned} \tag{8}$$

If the sum of λ_i is a constant number, then the MIMO channel capacity could reach the maximum in a given scenario when all λ_i are equal.

The power allocation strategy also affects the capacities of the subchannels. There are two strategies in common use, waterfilling algorithm and equal power allocation scheme [12]. A lot of researches adopt waterfilling algorithm since they assume that the transmitter learns the channel state information (CSI) before it transmits the data vector. However, there are some environments that the transmitter could not obtain the CSI, like in high speed moving time-variant scenario. Hence, in this paper, equal power allocation strategy is used in these particular situations.

4. Simulation Result

In this section, based on the formula described above, the performance of MIMO capacity with different scatterer number, that is, different multipath richness, is investigated in simulations. Meanwhile, the effect of scatterer number on MIMO channel structure is shown as well.

4.1. Circle Scatterer Model. The simulation of this model is depicted in Figure 3. The BS is located 500 m away from the MS. The velocity of the MS is 10 m/s. The scatterers are placed randomly on the circle around MS with the radius of 200 m. The carrier frequency is 900 MHz and the wavelength is 0.33 m. The total transmit power is set to 0 dBm and SNR is set to 20 dB as well. 5 × 5 antennas are used and they are separated by one wavelength at each side. A direct link between BS and MS is considered as the LOS component in this scenario. The simulation has run 400 times to get a mean value at each data point. In the simulation, the power of all scattering components is almost the same. And the Ricean K factor is introduced to control the LOS path energy.

The effects of NLOS and LOS with different Ricean K factors on ergodic channel capacity changing with scatterer number are given in Figure 4. If there are more than 5 scatterers, it can be noticed that the NLOS case provides more capacity than the LOS case with the same number of scatterers. In order to accomplish the same capacity as NLOS case, more scatterers are needed in LOS scenario. For example, when the channel capacity is around 23 bit/s/Hz, the scatterer number for NLOS scenario is about 5, while 5 more scatterers, that is, about 10 scatterers in total, are required in LOS scenario. When the scatterers are less than 5, the enhanced receive power brought by LOS path is more important to capacity. And among those three LOS cases, the smaller the Ricean K factor is, the better performance the system could offer. Meanwhile, when the number of scatterers reaches 25, the system is already in rich multipath environment. In this situation, there is a little increase in capacity no matter how many scatterers are added.

The reason of MIMO capacity change is that multipath richness and LOS power (also Ricean K factor) will affect the eigenvalues distribution. Figures 5 and 6 show the change of eigenvalues with the scatterer number in NLOS and LOS-8 dB scenarios, respectively. In NLOS scenario, the first eigenvalue λ_1 is quite big and the others are quite small

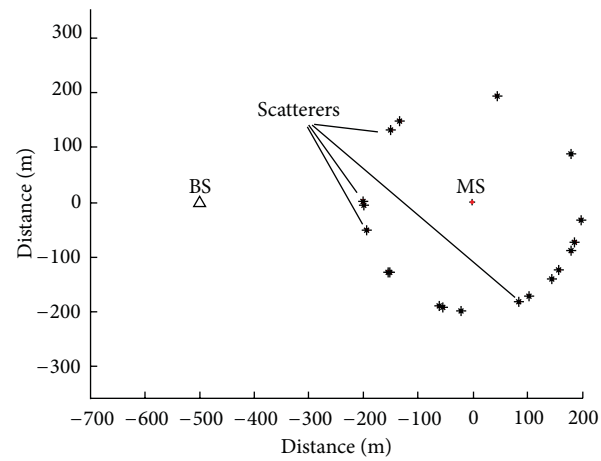

Figure 3: Circle scatterer model setup.

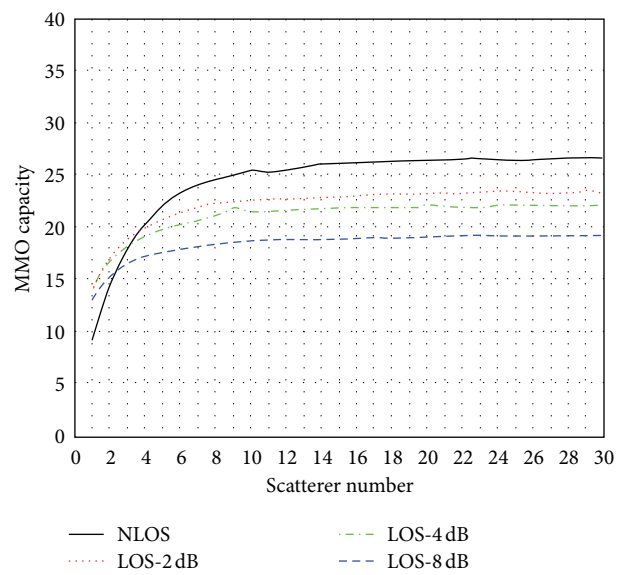

Figure 4: MIMO capacity comparison.

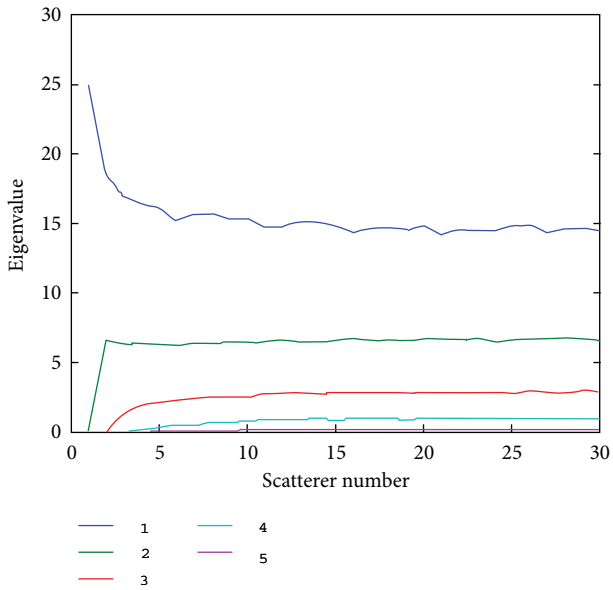

Figure 5: Eigenvalues comparison in NLOS.

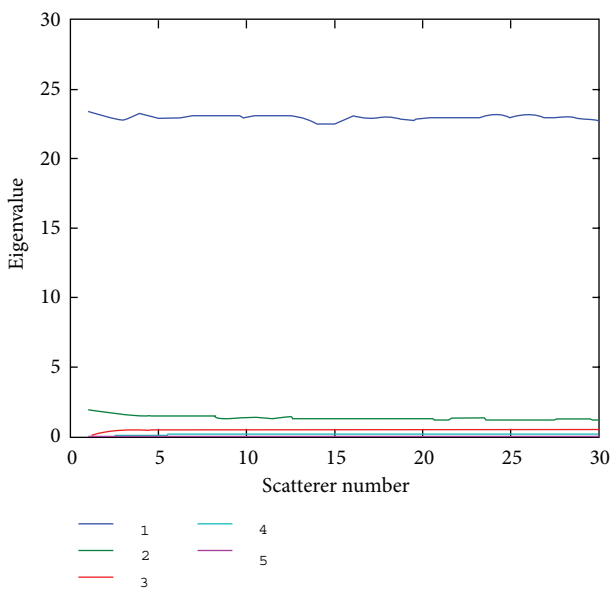

Figure 6: Eigenvalues comparison in LOS.

initially. However, with the increase of the scatterer number, λ_1 decreases to a lower level, while the others increase at the same time. More scatterers are helpful in NLOS scenario to reduce the gap between different eigenvalues, which is much closer to the ideal case given by expression (8). However, this case only happens in a certain scatterer number range. When the scatterer number is from 2 to 8, the eigenvalues of all subchannels vary significantly. It shows that the eigenvalues will converge in NLOS scenario as the scatterers increase. Then, the scatterer number will not affect the MIMO channel structure much. According to Figure 6, it can be seen that, due to the LOS component, λ_1 always stays at a high level. λ_2 to λ_5 are so small that the channel matrix could not achieve full-rank. It seems that the eigenvalue λ_1 is much higher than the other eigenvalues. In order to increase the third or fourth eigenvalue, adding scatterers only works in a short range and the effect is limited.

4.2. WINNER II Channel Model. D2 scenario (rural moving networks) is used in the simulation. It represents radio propagation in environments where both the access point and the receiver are moving at very high speed in a rural area. A typical example of this scenario occurs in carriages of high-speed trains where wireless coverage is provided by the so-called moving relay stations (MRSs). Hence, There are two parts in D2 scenario: D2a (BS-MRS) and D2b (MRS-MS). WINNER II defines D2a as LOS case which has 8 clusters. The parameters in D2b scenario are not defined in WINNER II but it recommends using the parameters in D1 scenario (rural macrocell) instead. So, D2b is typically seen as NLOS case with 10 clusters. In the simulation, the distance between BS and MS is 500 m, and the height of BS and MS is 32 m and 1.5 m, respectively. The velocity of MS is limited at 55.56 m/s in LOS and 10 m/s in NLOS. The carrier frequency is 5.25 GHz and the wavelength is 0.057 m. The SNR is set to 20 dB as well. 4×4 antennas are used and they are separated by 1 cm at each side. In this scenario, Ricean K factor in LOS situation is 7 dB. 100 samples are taken in one simulation, and 500-time simulations are run for one cluster number.

Figure 7 shows the MIMO capacity of LOS and NLOS in D2 scenario. It can be seen that at the beginning, the capacity is increasing for the reason that the clusters could offer some DOF. However, the capacity has a slight decrease when the cluster number continues increasing. This is because WINNER II normalizes the total power to one and allocates the cluster power according to their delays. When the number of cluster increases, the power allocated to each cluster would decline. Some of the clusters get quite small power that the signal even could not reach the receiver through the channel fading. In that case, the total power received gets smaller. Meanwhile, when there is only one cluster, LOS case has an advantage. When the number is 2, the capacity of NLOS and LOS are almost equal. Then, the capacity of NLOS becomes bigger. But it is also shown that the influence of the capacity decrease affects NLOS more. That is because in LOS case, most of the power would allocate to the LOS component; multipath is not the crucial factor.

Figures 8 and 9 illustrate the eigenvalues in LOS and NLOS situation, respectively. There is little change during the cluster number increasing. Comparing these two cases, λ_1 is a little higher in LOS than in NLOS scenario, while in NLOS, the second eigenvalue λ_2 has a bigger value.

Hence, in this WINNER channel model simulation, the path number (cluster number) does not affect the capacity as much as the former model.

5. Conclusion

In this paper, the effect of rich multipath and high receive power on MIMO channel capacity is investigated. A simple circle scatterer model and WINNER II channel model are used to simulate the channel matrix. From the simulation

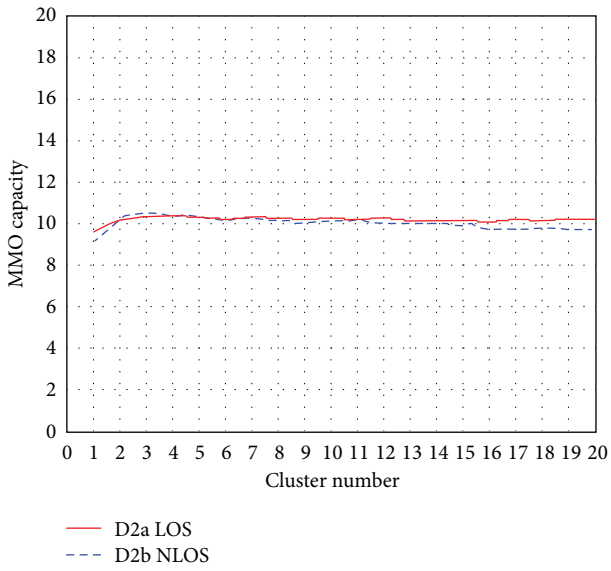

Figure 7: MIMO capacity comparison.

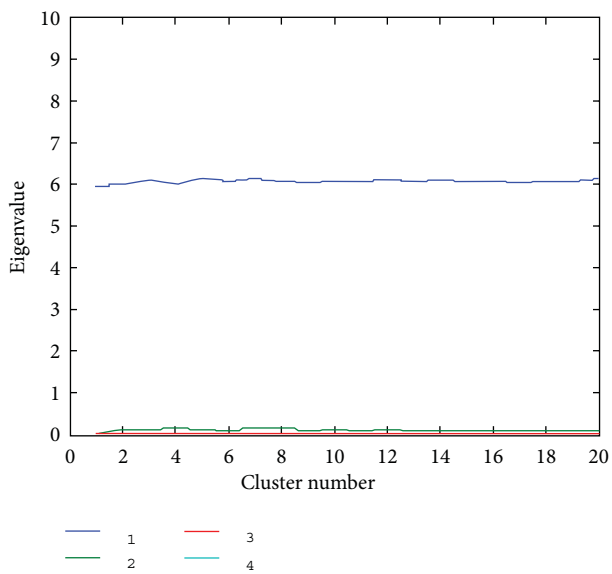

Figure 8: Eigenvalues comparison in LOS.

results, it can be seen when the scatterer number exceeds a certain threshold, the multipath richness prevails over the high receive SNR. When the scatterers are few, the high receive SNR is more important. However, the multipath richness will have little influence on capacity as the scatterers continue to increase.

Acknowledgments

The project is supported by the Program for New Century Excellent Talents under Grant NCET-09-0206, the National Natural Science Foundation of China under Grant 60830001, the Key Project of State Key Laboratory of Rail Traffic Control and Safety under Grants RCS2008ZZ006 and RCS2011ZZ008, Program for Changjiang Scholars and Innovative Research Team under Grant no. IRT0949, the Project of State Key Laboratory of Rail Traffic Control and Safety under Grants RCS2008ZT005 and RCS2010ZT012, Beijing Natural Science Foundation (4112048), and "the Fundamental Research Funds for the Central Universities" under Grants nos. 2010JBZ008 and 2011YJS010.

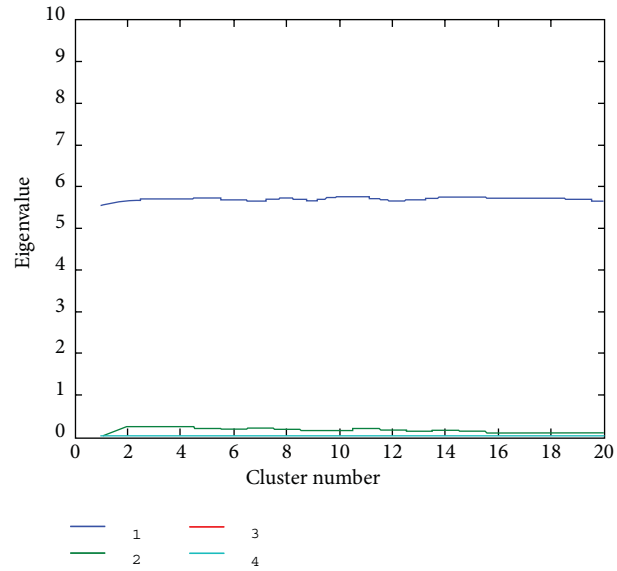

Figure 9: Eigenvalues comparison in NLOS.

References

[1] J. W. Wallace and M. A. Jensen, "MIMO capacity variation with SNR and multipath richness from full-wave indoor FDTD simulations," in *Proceedings of the IEEE International Antennas and Propagation Symposium and USNC/CNC/URSI North American Radio Science Meeting*, vol. 2, pp. 523–526, June 2003.

[2] W. Q. Malik, "MIMO capacity and multipath scaling in ultra-wideband channels," *Electronics Letters*, vol. 44, no. 6, pp. 427–428, 2008.

[3] M. Matthaiou, A. M. Sayeed, and J. A. Nossek, "Sparse multipath MIMO channels: performance implications based on measurement data," in *Proceedings of the IEEE 10th Workshop on Signal Processing Advances in Wireless Communications (SPAWC '09)*, pp. 364–368, June 2009.

[4] T. Koch and A. Lapidoth, "On multipath fading channels at high SNR," *IEEE Transactions on Information Theory*, vol. 56, no. 12, pp. 5945–5957, 2010.

[5] A. Saad, M. Ismail, and N. Misran, "Rayleigh multiple input multiple," in *Proceeding of the International Multi Conference of Engineers and Computer Scientists*, vol. 2, 2009.

[6] A. Knopp, R. T. Schwarz, C. A. Hofmann, M. Chouayakh, and B. Lankl, "Measurements on the impact of sparse multipath components on the LOS MIMO channel capacity," in *Proceedings of the 4th IEEE International Symposium on Wireless Communication Systems (ISWCS '07)*, pp. 55–60, October 2007.

[7] X. Cheng, C. X. Wang, H. Wang et al., "Cooperative MIMO channel modeling and multi-link spatial correlation properties,"

IEEE Journal on Selected Areas in Communications, vol. 30, no. 2, pp. 388–396, 2012.

[8] C.-X. Wang, X. Cheng, and D. I. Laurenson, "Vehicle-to-vehicle channel modeling and measurements: recent advances and future challenges," *IEEE Communications Magazine*, vol. 47, no. 11, pp. 96–103, 2009.

[9] X. Cheng, C.-X. Wang, D. I. Laurenson, S. Salous, and A. V. Vasilakos, "An adaptive geometry-based stochastic model for non-isotropic MIMO mobile-to-mobile channels," *IEEE Transactions on Wireless Communications*, vol. 8, no. 9, pp. 4824–4835, 2009.

[10] F. Perez Fontan and P. Marino Espineria, *Modeling the Wireless Propagation Channel-A Simulation Approach With MATLAB*, John Willey & Sons, 2008.

[11] P. Kyosti et al., "WINNER II Channel Models," IST-WINNER D1.1.2v1.2, Sep. 2007.

[12] D. Tse and P. Viswanath, *Fundamntal of Wireless Communication*, Cabridge University Press, Cambridge, UK, 2005.

Hindawi Publishing Corporation
International Journal of Antennas and Propagation
Volume 2013, Article ID 617895, 10 pages
http://dx.doi.org/10.1155/2013/617895

Research Article

Outage Analysis of Train-to-Train Communication Model over Nakagami-*m* Channel in High-Speed Railway

Pengyu Liu,[1] Xiaojuan Zhou,[2] and Zhangdui Zhong[1]

[1] *State Key Laboratory of Rail Traffic Control and Safety, Beijing Jiaotong University, Beijing 100044, China*
[2] *Department of Telecommunication Engineering, University of Armed Police Force Engineering, Xian 710086, China*

Correspondence should be addressed to Pengyu Liu; 11111034@bjtu.edu.cn

Received 22 July 2012; Accepted 5 October 2012

Academic Editor: Ai Bo

This paper analyzes the end-to-end outage performance of high-speed-railway train-to-train communication model in high-speed railway over independent identical and nonidentical Nakagami-*m* channels. The train-to-train communication is inter-train communication without an aid of infrastructure (for base station). Source train uses trains on other rail tracks as relays to transmit signals to destination train on the same track. The mechanism of such communication among trains can be divided into three cases based on occurrence of possible-occurrence relay trains. We first present a new closed form for the sum of squared independent Nakagami-*m* variates and then derive an expression for the outage probability of the identical and non-identical Nakagami-*m* channels in three cases. In particular, the problem is improved by the proposed formulation that statistic for sum of squared Nakagami-*m* variates with identical *m* tends to be infinite. Numerical analysis indicates that the derived analytic results are reasonable and the outage performance is better over Nakagami-*m* channel in high-speed railway scenarios.

1. Introduction

Railway has played a significant role in helping transport passengers and goods. Accidents in railway always result in loss of lives and property. Safety issues have drawn increasing research attention due to the personal and property security.

A part of railway accidents is brought by malfunction of control center system. The train-to-train communication will serve as an assisting role which coordinates operations among trains based on multihop, when control center system is broken. It aims at detecting a potential collision and then broadcasting prewarning messages concerning this emergency to other trains on the same and neighboring tracks.

The multihop train-to-train communication model in physical layer lies in the thoughts that the source train uses the trains operating on other tracks as relays to transmit signals to destination train on the same track. Such mechanism can be divided into three cases based on occurrence of other relay trains. These relay trains occur following the Poisson Process [1], and therefore the arrival procedure follows the distribution of negative exponent. The proposed train-to-train communication model, introducing OFDM and MIMO technique, realizes the intertrain adhoc communication based on the Poisson Process in high-speed railway scenarios.

Since 2006, train-to-train communication has been researched by several organizations, such as the German Aerospace Center (DLR). Reference [2] discusses the RCAS approach consisting only of mobile adhoc components without the necessity of extensions of the railway infrastructure, while [3] describes an overview of the state of the art in collision avoidance related with transportation systems for maritime transportation, aircraft, and road transportation, and the RCAS is introduced. Reference [4] proposes a channel model for direct train-to-train communication appropriate for the 400 MHz band, and [5] presents an infrastructure-less cross-layer train-to-train communication system exploiting all characteristics of a pervasive computing system, like direct communication in mobile adhoc networks. Reference [6] designs an infrastructure-less adhoc inter-vehicle communication system that fulfills these

requirements with respect to the boundary conditions in the railway environment. Reference [7] presents analysis and results of a comprehensive measurement campaign investigating the propagation channel in case of direct communication between railway vehicles.

Despite that the fact the RCAS designed by the DLR has progressed tremendously in physical layer, it only work well for the train operation velocity lower than 200 Km/h, which is not able to function in the high-speed railway. Generally speaking, the velocity of high-speed railway train is up to 360 Km/h. In this case, safety distance among trains is 10 Km [8]. The proposed train-to-train communication model in physical layer has been evaluated by BER previously. In this paper, we continue to analyze the proposed multihop train-to-train communication model using outage probability. We first present a new closed-form for the sum of squared independent Nakagami-m variates with identical m [9], the proposed formulation improves the problem that statistic for sum of squared Nakagami-m variables with identical m is infinite. Then we derive an expression for the outage probability of the identical m ($m = 1$ or $m = 2$) and nonidentical Nakagami-m channels [10] in three cases. Such outage analysis is first applied to the multihop train-to-train communication model. The previous research indicates that the BER of train-to-train communication model reaches 10^{-6} when receiving SNR is 10 dB, which meets the requirements of the *International Union of Railway* (UIC). Therefore the threshold should be set to 10 dB. If the receiving signal SNR is below that value, the signal quality at receiver cannot realize normal communication among trains and the train-to-train communication is regarded as outage. The maximum distance of train-to-train communication is set to 6 Km and it is probable that m value of Nakagami-m channel in two receiving path at receiver is different, for example, one path is $m = 1$ and the other path is $m = 2$. This paper considers the Nakagami-m channel not only with identical m but also with nonidentical m in receiver's receiving path.

The rest of this paper is organized as follows. Section 2 gives a description of the proposed train-to-train communication model based on multihop. Section 3 derives expressions for the outage probability of three conditions. Section 4 shows the outage probability simulation results of this model. In Section 5, this paper is concluded.

2. Proposed Train-to-Train Communication Model

In this section, three cases of train-to-train communication model are presented in Figures 1, 2, and 3, where the S, R1, and D represent source terminal, fixed-occurring relay terminal, and destination terminal, respectively. The R1 is the train that meets S on another rail track, and the R2 and R3 represent the first possible-occurring relay terminal and the third possible-occurring relay terminal. The average operating velocities of the R1 and R2 are 100 m/s, and those of D and R3 are −100 m/s. The rail 1, rail 2, rail 3, and rail 4 stand for four parallel rail tracks. These cases are described below.

2.1. Case I. The S transmits signals to the R1 on different rail tracks when they meet each other. At the same time, the S searches the potential relay R2 on a neighboring rail track 1. If the R2 is not found, R1 will keep broadcasting messages within its communication coverage (6 Km), and if it receives the response of D, their communication link will be held on and the transmission between them is performed.

2.2. Case II. If the R2 is searched, the S and R1 simultaneously transmit the signals to the R2. The R2 also performs the search of the potential relay R3. If the R3 does not exist, it will operate for some seconds until the distance between R2 and D is within a communication range. Finally, the R2 and R1, acting as two relays of the source, will transmit the signals to the destination terminal.

2.3. Case III. If the R3 exists, it will receive the signals from the R2 and R1 and then combine them. Finally, the R3, R2, and R1, as three relays of the source, will forward the signals to the destination terminal.

Under these cases, this paper respectively analyzes the outage probability of the train-to-train communication model.

3. Outage Analysis of Train-to-Train Communication Model

$\{X_n, n = 1, \ldots, M\}$ is M independent Nakagami-m distributed RVs, with PDF expressed as [11]

$$f_{Xl}(x) = \frac{2x^{2m_n-1} m_n^{m_n}}{\overline{x}_n^{m_n}(m-1)!} \exp\left(-\frac{m_n x^2}{\overline{x}_n}\right), \tag{1}$$

where m_n denotes the Nakagami-m fading parameter and $\overline{x}_n$ is expectation of X_n^2.

Furthermore, let $Y_n = X_n^2$, the PDF given by

$$f_{Yl}(x) = \frac{x^{m_n-1} m_n^{m_n}}{\overline{x}_n^{m_n}(m-1)!} \exp\left(-\frac{m_n x}{\overline{x}_n}\right) \tag{2}$$

and CDF [9]

$$F_{Yl}(x) = 1 - \exp\left(-\frac{m_n x}{\overline{x}_n}\right) \sum_{l}^{m_n-1} \left(\frac{x m_n}{\overline{x}_n}\right)^l. \tag{3}$$

Before analyzing the outage probability of train-to-train communication model, we first give the close-form of the sum of squared Nakagami-m variates with identical m and nonidentical m.

Theorem 1 (PDF of the Sum of Squared Nakgami-m RVs with identical m). *Let $\{Y_n, n = 1, \ldots, M\}$ be a set of RVs following the PDF presented in* (2), *with $\overline{x}_i - \overline{x}_j = o(x)$, $i \neq j$ and $m_1 = m_2 = \cdots = m_M = m$. The PDF of the sum*

$$Z_M = \sum_{i=1}^{M} Y_i \tag{4}$$

is given by

$$f_{Z_M}(z) = \left(\frac{m}{\overline{z}}\right)^{(M-1)m} \frac{\Gamma(m)}{\Gamma(Mm)} z^{(M-1)m} \times \frac{z^{m-1} m^m}{\overline{z}_M^m (m-1)!} \exp\left(-\frac{mz}{\overline{z}_M}\right). \quad (5)$$

Proof. Step 1. For $M = 2$, the PDF of $Z_2 = Y_1 + Y_2$ can be evaluated as

$$f_{Z_2}(z) = \int_0^z f_{Y_1}(x; m_1, \overline{x}_1) f_{Y_2}(z - x; m_2, \overline{x}_2)\, dx. \quad (6)$$

Insert (2) into (6) and use [12, equation (3.383.1)], (6) can be derived as

$$f_{Z_2}(z) = \frac{B(m_1, m_2)}{\overline{z}_1^{m_1} \overline{z}_2^{m_2} \Gamma(m_1)\Gamma(m_2)} z^{-1+m_1+m_2} \exp\left(-\frac{m_2 z}{\overline{z}_2}\right) * F_1\left(m_1; m_1 + m_2; -\left(\frac{m_1}{\overline{z}_1} - \frac{m_2}{\overline{z}_2}\right) z\right). \quad (7)$$

Since $m_1/z_1 - m_2/\overline{z}_2 = o(x)$ and using [12, equation (9.210.1)]

$$F_1\left(m_1; m_1 + m_2; -\left(\frac{m_1}{\overline{x}_1} - \frac{m_2}{\overline{x}_2}\right) z\right) = \sum_{k=0}^{+\infty} \frac{z^k}{k!} \frac{(m_1 + k - 1)! / (m_1 - 1)!}{(m_2 + m_1 + k - 1)! / (m_1 + m_2 - 1)!} \times \left[-\left(\frac{m_1}{\overline{z}_1} - \frac{m_2}{\overline{z}_2}\right) z\right]^k, \quad (8)$$

where $[-(m_1/z_1 - m_2/\overline{z}_2)z]^k|_{k=0} = 1$ and $[-(m_1/\overline{z}_1 - m_2/\overline{z}_2) z]^k|_{k \neq 0} = 0$, (7) can be denoted as

$$\begin{aligned} f_{Z_2}(z) &= \frac{B(m_1, m_2)}{\overline{x}_1^{m_1} \overline{x}_2^{m_2} \Gamma(m_1)\Gamma(m_2)} z^{-1+m_1+m_2} \exp\left(-\frac{m_2 z}{\overline{z}_2}\right) \\ &= \left(\frac{m_1}{\overline{z}}\right)^{m_1} \left(\frac{m_2}{\overline{z}}\right)^{m_2} \frac{\Gamma(m_2)}{\Gamma(m_2 + m_1)} \times z^{m_1} \frac{z^{m_2-1} m_2^{m_2}}{\overline{z}_n^{m_2} (m_2 - 1)!} \exp\left(-\frac{m_2 z}{\overline{z}_2}\right) \\ &= \left(\frac{m_1}{\overline{z}}\right)^{m_1} \left(\frac{m_2}{\overline{z}}\right)^{m_2} \frac{\Gamma(m_2)}{\Gamma(m_2 + m_1)} z^{m_1} f_{Y_2}(z). \end{aligned} \quad (9)$$

Step 2. For $M = 3$, the PDF of Z_3 can be efficiently expressed as

$$f_{Z_3}(z) = \int_0^z f_{Z_2}(x; m_1, \overline{x}_1) f_{Y_3}(z - x; m_3, \overline{x}_3)\, dx. \quad (10)$$

Following Step 1 of PDF calculation of Z_2, the PDF of Z_3 can be denoted as:

$$f_{Z_2}(z) = \left(\frac{m_1}{\overline{z}}\right)^{m_1} \left(\frac{m_2}{\overline{z}}\right)^{m_2} \left(\frac{m_3}{\overline{z}}\right)^{m_3} \times \frac{\Gamma(m_3)}{\Gamma(m_2 + m_1 + m_3)} z^{m_1+m_2} f_{Y_3}(z). \quad (11)$$

Step 3. According to the same procedure as Steps 1 and 3, the sum of M Nakagami-m RVs can be expressed as

$$f_{Z_M}(z) = \left(\frac{mz}{\overline{Y}_1}\right)^{m(M-1)} \frac{\Gamma(m)}{\Gamma(Mm)} f_{Y_M}(z). \quad (12)$$

□

Corollary 2 (PDF of the sum of Squared Nakagami-m RVs with identical m). *The CDF of Z_M is given by*

$$F_M(Z) = \left(\frac{mz}{\overline{Y}_1}\right)^{m(M-1)} \frac{\Gamma(m)}{\Gamma(Mm)} \times \left[\frac{((M-1)m - 1)!}{(m/\overline{z}_M)^{Mm}} - e^{-(m/\overline{z}_M)z} \times \sum_{k=0}^{Mm-1} \frac{((M-1)m - 1)!}{k!} \frac{z^k}{(m/\overline{z}_M)^{Mm-k}}\right]. \quad (13)$$

Theorem 3 (PDF of the Sum of Squared Nakgami-m RVs with nonidentical m). *Let $\{Y_n, n = 1, \ldots, M\}$ be a set of RVs following the PDF presented in (2), with $m_1 \neq m_2 \neq \cdots \neq m_M \neq m$. The PDF of the sum is given by [11]*

$$\begin{aligned} f_{Z_M}(z) &= \sum_{i=1}^{M} \sum_{k=1}^{m_i} \frac{\overline{y}_i^{m_i} m_h^{m_h}}{\prod_{h=1}^{M} \overline{y}_h^{m_h} m_i^{m_i}} \times \prod_{j=1, j\neq i}^{M} \left(\frac{m_j}{\overline{y}_j} - \frac{m_i}{\overline{y}_i}\right)^{-m_j} \frac{z^{m_i-1} m_i^{m_i}}{\overline{y}_i^{m_i} (m-1)!} \exp\left(-\frac{m_i z}{\overline{y}_i}\right) \\ &= \sum_{i=1}^{M} \sum_{k=1}^{m_i} \frac{\overline{z}_i^{m_i}}{\prod_{h=1}^{M} \overline{y}_h^{m_h}} \prod_{j=1, j\neq i}^{M} \left(\frac{1}{\overline{y}_j} - \frac{1}{\overline{y}_i}\right)^{-m_j} F_{Yl}(x_i). \end{aligned} \quad (14)$$

Corollary 4 (PDF of the sum of Squared Nakagami-m RVs with nonidentical m). *The CDF of Z_M is given by [13]*

$$\begin{aligned} F_M(Z) &= \sum_{i=1}^{M} \sum_{k=1}^{m_i} \frac{\overline{y}_i^{m_i} m_h^{m_h}}{\prod_{h=1}^{M} \overline{y}_h^{m_h} m_i^{m_i}} \prod_{j=1, j\neq i}^{M} \left(\frac{m_j}{\overline{y}_j} - \frac{m_i}{\overline{y}_i}\right)^{-m_j} \times \left(1 - \exp\left(-\frac{m_n z}{\overline{y}_n}\right) \sum_{l}^{m_n-1} \left(\frac{z m_n}{\overline{y}_n}\right)^l\right) \\ &= \sum_{i=1}^{M} \sum_{k=1}^{m_i} \frac{\overline{y}_i^{m_i}}{\prod_{h=1}^{M} \overline{y}_h^{m_h}} \prod_{j=1, j\neq i}^{M} \left(\frac{1}{\overline{y}_j} - \frac{1}{\overline{y}_i}\right)^{-m_j} F_{Yl}(xi). \end{aligned} \quad (15)$$

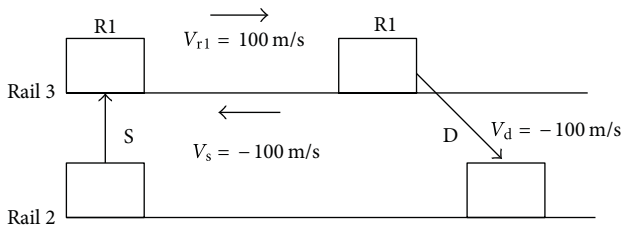

Figure 1: Train-to-train communication model of case I.

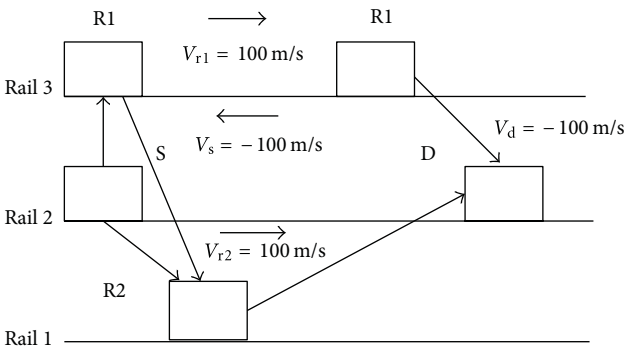

Figure 2: Train-to-train communication model of case II.

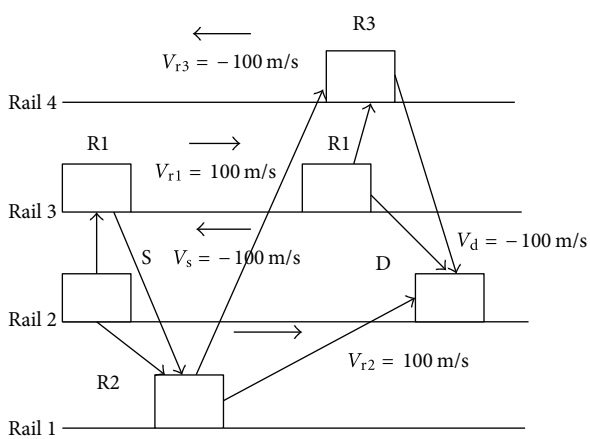

Figure 3: Communication model of case III.

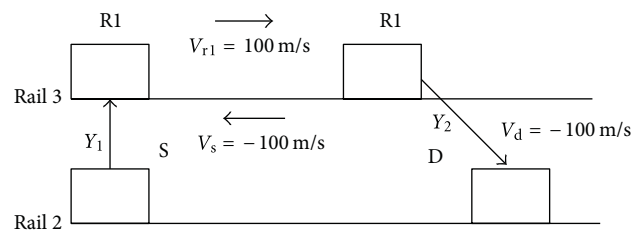

Figure 4: Communication model of case I.

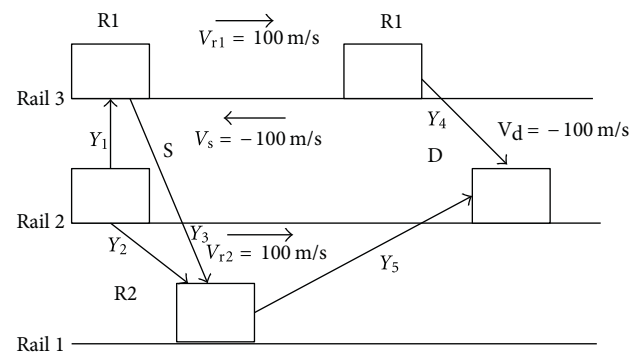

Figure 5: Communication model of case II.

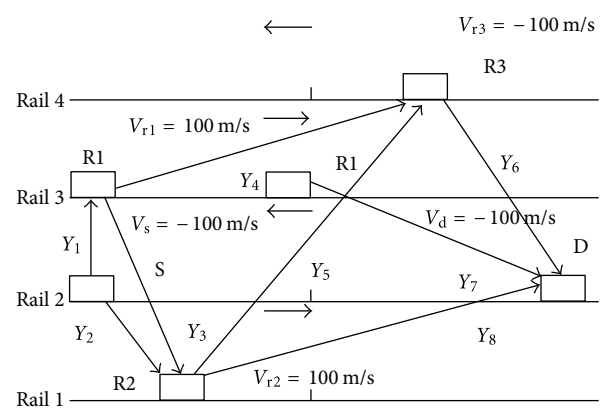

Figure 6: Communication model of case III.

The outage event happens when the Y falls below given threshold Y_0 under Nakagami-m channel and its probability is defined as

$$P_{\text{out}}(Y) = \text{Prob}\left[Y < Y_0\right] = 1 - \exp\left(-\frac{m_n Y_0}{\overline{y}}\right) \sum_{l}^{m_n - 1} \left(\frac{Y_0 m_n}{\overline{y}}\right)^l, \quad (16)$$

where $\overline{Y}$ is average receiving signal-to-noise ratio.

Next the outage probabilities of train-to-train communication model under three cases are analyzed.

3.1. Case I. In Figure 4, Y_1 and Y_2 are SNR of receiving signal at R1 and D, respectively. Since each node applies $2*2$ MIMO, Y_1 and Y_2 are sum of 4 squared Nakagami-m variables at receiver.

The outage probability F_{outI} of case I is expressed as

$$F_{\text{outI}} = \text{Prob}\left[Y_1 < Y_0\right] + \text{Prob}\left[Y_1 > Y_0\right] * \text{Prob}\left[Y_2 < Y_0\right]. \quad (17)$$

Y_0 is the threshold SNR.

Inserting (13) or (15) into (17), the F_{outI} under Nakagami-m channel with identical m and nonidentical m can be written as follows.

(1) Identical-m:

$$\begin{aligned}F_{\text{out I}} &= \left(\frac{mz}{\overline{Y}_1}\right)^{3m}\frac{\Gamma(m)}{\Gamma(3m)}\\ &\times\left[\frac{(3m-1)!}{\left(m/\overline{Y}_1\right)^{3m}}-\exp\left(-\left(\frac{m}{\overline{Y}_1}\right)Y_0^k\right)\right.\\ &\left.\times\sum_{k=0}^{3m-1}\frac{(3m-1)!}{k!}\frac{Y_0^k}{\left(m/\overline{Y}_1\right)^{4m-k}}\right]\\ &+\left(\frac{mz}{\overline{Y}_2}\right)^{3m}\frac{\Gamma(m)}{\Gamma(3m)}\\ &\times\left[\frac{(3m-1)!}{\left(m/\overline{Y}_2\right)^{3m}}-\exp\left(-\left(\frac{m}{\overline{Y}_2}\right)Y_0^k\right)\right.\\ &\left.\times\sum_{k=0}^{3m-1}\frac{(3m-1)!}{k!}\frac{Y_0^k}{\left(m/\overline{Y}_2\right)^{4m-k}}\right]\\ &*\left[1-\left(\frac{mz}{\overline{Y}_1}\right)^{3m}\frac{\Gamma(m)}{\Gamma(3m)}\right.\\ &\times\left[\frac{(3m-1)!}{\left(m/\overline{Y}_1\right)^{3m}}-\exp\left(-\left(\frac{m}{\overline{Y}_1}\right)Y_0^k\right)\right.\\ &\left.\left.\times\sum_{k=0}^{3m-1}\frac{(3m-1)!}{k!}\frac{Y_0^k}{\left(m/\overline{Y}_1\right)^{4m-k}}\right]\right].\end{aligned} \tag{18}$$

(2) Nonidentical m:

$$\begin{aligned}F_{\text{out I}} &= \sum_{i=1}^{4}\sum_{k=1}^{m_i}\frac{\overline{Y}_1^{m_i}}{\prod_{h=1}^{M}\overline{Y}_1^{m_h}}\prod_{j=1,j\neq i}^{4}\left(\frac{1}{\overline{Y}_j}-\frac{1}{\overline{Y}_i}\right)^{-m_j}F_{Yl}(Y_0)\\ &+\left[1-\sum_{i=1}^{4}\sum_{k=1}^{m_i}\frac{\overline{Y}_1^{m_i}}{\prod_{h=1}^{4}\overline{Y}_1^{m_h}}\right.\\ &\left.\times\prod_{j=1,j\neq i}^{4}\left(\frac{1}{\overline{Y}_j}-\frac{1}{\overline{Y}_i}\right)^{-m_j}F_{Yl}(Y_0)\right]\\ &*\sum_{i=1}^{4}\sum_{k=1}^{m_i}\frac{\overline{Y}_2^{m_i}}{\prod_{h=1}^{4}\overline{Y}_2^{m_h}}\prod_{j=1,j\neq i}^{4}\left(\frac{1}{\overline{Y}_j}-\frac{1}{\overline{Y}_i}\right)^{-m_j}F_{Yl}(Y_0).\end{aligned} \tag{19}$$

3.2. Case II. In Figure 5, Y_1 are SNR of receiving signal at R1, Y_2, Y_3 are SNR of receiving signal at R2, and Y_4, Y_5 are receiving signal SNR at D.

The outage probability F_{outI} of case I is expressed as

$$\begin{aligned}F_{\text{out II}} &= \text{Prob}\left[Y_1<Y_0\right]+\text{Prob}\left[Y_1>Y_0\right]\\ &*\text{Prob}\left[Y_2+Y_3<Y_0\right]+\text{Prob}\left[Y_1>Y_0\right]\\ &*\text{Prob}\left[Y_2+Y_3>Y_0\right]*\text{Prob}\left[Y_4+Y_5<Y_0\right].\end{aligned} \tag{20}$$

Inserting (13) or (15) into (20), the F_{outII} under Nakagami-m channel with identical m and nonidentical m can be written as follows.

(1) Identical-m:

$$\begin{aligned}F_{\text{out II}} &= \left(\frac{mz}{\overline{Y}_1}\right)^{3m}\frac{\Gamma(m)}{\Gamma(3m)}\\ &\times\left[\frac{(3m-1)!}{\left(m/\overline{Y}_1\right)^{3m}}-\exp\left(-\left(\frac{m}{\overline{Y}_1}\right)Y_0^k\right)\right.\\ &\left.\times\sum_{k=0}^{3m-1}\frac{(3m-1)!}{k!}\frac{Y_0^k}{\left(m/\overline{Y}_1\right)^{4m-k}}\right]\\ &+\left(\frac{mz}{\overline{Y}_2}\right)^{7m}\frac{\Gamma(m)}{\Gamma(7m)}\\ &\times\left[\frac{(7m-1)!}{\left(m/\overline{Y}_2\right)^{7m}}-\exp\left(-\left(\frac{m}{\overline{Y}_2}\right)Y_0^k\right)\right.\\ &\left.\times\sum_{k=0}^{7m-1}\frac{(7m-1)!}{k!}\frac{Y_0^k}{\left(m/\overline{Y}_2\right)^{8m-k}}\right]\\ &*\left[1-\left(\frac{mz}{\overline{Y}_1}\right)^{3m}\frac{\Gamma(m)}{\Gamma(3m)}\right.\\ &\times\left[\frac{(3m-1)!}{\left(m/\overline{Y}_1\right)^{3m}}-\exp\left(-\left(\frac{m}{\overline{Y}_1}\right)Y_0^k\right)\right.\\ &\left.\left.\times\sum_{k=0}^{3m-1}\frac{(3m-1)!}{k!}\frac{Y_0^k}{\left(m/\overline{Y}_1\right)^{4m-k}}\right]\right]\\ &+\left[1-\left(\frac{mz}{\overline{Y}_1}\right)^{3m}\frac{\Gamma(m)}{\Gamma(3m)}\right.\\ &\times\left[\frac{(3m-1)!}{\left(m/\overline{Y}_1\right)^{3m}}-\exp\left(-\left(\frac{m}{\overline{Y}_1}\right)Y_0^k\right)\right.\end{aligned}$$

$$\times \sum_{k=0}^{3m-1} \frac{(3m-1)!}{k!} \frac{Y_0^k}{\left(m/\overline{Y}_1\right)^{4m-k}} \Bigg] \Bigg]$$

$$* \Bigg[1 - \left(\frac{mz}{\overline{Y}_2}\right)^{7m} \frac{\Gamma(m)}{\Gamma(3m)}$$

$$\times \Bigg[\frac{(7m-1)!}{\left(m/\overline{Y}_2\right)^{7m}} - \exp\left(-\left(\frac{m}{\overline{Y}_2}\right) Y_0^k\right)$$

$$\times \sum_{k=0}^{7m-1} \frac{(7m-1)!}{k!} \frac{Y_0^k}{\left(m/\overline{Y}_2\right)^{8m-k}} \Bigg] \Bigg]$$

$$* \Bigg[\left(\frac{mz}{\overline{Y}_4}\right)^{7m} \frac{\Gamma(m)}{\Gamma(7m)}$$

$$\times \Bigg[\frac{(7m-1)!}{\left(m/\overline{Y}_4\right)^{7m}} - \exp\left(-\left(\frac{m}{\overline{Y}_4}\right) Y_0^k\right)$$

$$\times \sum_{k=0}^{7m-1} \frac{(7m-1)!}{k!} \frac{Y_0^k}{\left(m/\overline{Y}_4\right)^{8m-k}} \Bigg] \Bigg]. \tag{21}$$

(2) Nonidentical m:

$$F_{\text{out II}} = \sum_{i=1}^{4} \sum_{k=1}^{m_i} \frac{\overline{Y}_1^{m_i}}{\prod_{h=1}^{8} \overline{Y}_1^{m_h}} \prod_{j=1, j\neq i}^{4} \left(\frac{1}{\overline{Y}_j} - \frac{1}{\overline{Y}_i}\right)^{-m_j} F_{Yl}(Y_0)$$

$$+ \Bigg[1 - \sum_{i=1}^{4} \sum_{k=1}^{m_i} \frac{\overline{Y}_1^{m_i}}{\prod_{h=1}^{8} \overline{Y}_1^{m_h}}$$

$$\times \prod_{j=1, j\neq i}^{4} \left(\frac{1}{\overline{Y}_j} - \frac{1}{\overline{Y}_i}\right)^{-m_j} F_{Yl}(Y_0) \Bigg]$$

$$* \sum_{i=1}^{8} \sum_{k=1}^{m_i} \frac{\overline{Y}_2^{m_i}}{\prod_{h=1}^{8} \overline{Y}_2^{m_h}} \prod_{j=1, j\neq i}^{8} \left(\frac{1}{\overline{Y}_j} - \frac{1}{\overline{Y}_i}\right)^{-m_j} F_{Yl}(Y_0)$$

$$+ \Bigg[1 - \sum_{i=1}^{4} \sum_{k=1}^{m_i} \frac{\overline{Y}_1^{m_i}}{\prod_{h=1}^{8} \overline{Y}_1^{m_h}}$$

$$\times \prod_{j=1, j\neq i}^{4} \left(\frac{1}{\overline{Y}_j} - \frac{1}{\overline{Y}_i}\right)^{-m_j} F_{Yl}(Y_0) \Bigg]$$

$$* \Bigg[1 - \sum_{i=1}^{8} \sum_{k=1}^{m_i} \frac{\overline{Y}_2^{m_i}}{\prod_{h=1}^{8} \overline{Y}_2^{m_h}}$$

$$\times \prod_{j=1, j\neq i}^{8} \left(\frac{1}{\overline{Y}_j} - \frac{1}{\overline{Y}_i}\right)^{-m_j} F_{Yl}(Y_0) \Bigg]$$

$$* \sum_{i=1}^{8} \sum_{k=1}^{m_i} \frac{\overline{Y}_4^{m_i}}{\prod_{h=1}^{8} \overline{Y}_4^{m_h}} \prod_{j=1, j\neq i}^{8} \left(\frac{1}{\overline{Y}_j} - \frac{1}{\overline{Y}_i}\right)^{-m_j} F_{Yl}(Y_0). \tag{22}$$

3.3. Case III. In Figure 6, Y_1 are SNR of receiving signal at R1, Y_2, Y_3 are SNR of receiving signal at R2, Y_4, Y_5 are receiving signal SNR at R3, and Y_6, Y_7 and Y_8 are receiving signal SNR at D.

(1) Identical-m:

$$F_{\text{out III}} = \left(\frac{mz}{\overline{Y}_1}\right)^{3m} \frac{\Gamma(m)}{\Gamma(3m)}$$

$$\times \Bigg[\frac{(3m-1)!}{\left(m/\overline{z}_3\right)^{3m}} - \exp\left(-\left(\frac{m}{\overline{Y}_1}\right) Y_0^k\right)$$

$$\times \sum_{k=0}^{3m-1} \frac{(3m-1)!}{k!} \frac{Y_0^k}{\left(m/\overline{Y}_1\right)^{4m-k}} \Bigg]$$

$$+ \left(\frac{mz}{\overline{Y}_1}\right)^{7m} \frac{\Gamma(m)}{\Gamma(3m)}$$

$$\times \Bigg[\frac{(7m-1)!}{\left(m/\overline{z}_3\right)^{7m}} - \exp\left(-\left(\frac{m}{\overline{Y}_2}\right) {Y_0}^k\right)$$

$$\times \sum_{k=0}^{7m-1} \frac{(7m-1)!}{k!} \frac{Y_0^k}{\left(m/\overline{Y}_2\right)^{8m-k}} \Bigg]$$

$$* \Bigg[1 - \left(\frac{mz}{\overline{Y}_1}\right)^{3m} \frac{\Gamma(m)}{\Gamma(3m)}$$

$$\times \Bigg[\frac{(3m-1)!}{\left(m/\overline{z}_3\right)^{3m}} - \exp\left(-\left(\frac{m}{\overline{Y}_1}\right) Y_0^k\right)$$

$$\times \sum_{k=0}^{3m-1} \frac{(3m-1)!}{k!} \frac{Y_0^k}{\left(m/\overline{Y}_1\right)^{4m-k}} \Bigg] \Bigg]$$

$$+ \Bigg[1 - \left(\frac{mz}{\overline{Y}_1}\right)^{3m} \frac{\Gamma(m)}{\Gamma(3m)}$$

$$\times \Bigg[\frac{(3m-1)!}{\left(m/\overline{z}_3\right)^{3m}} - \exp\left(-\left(\frac{m}{\overline{Y}_1}\right) Y_0^k\right)$$

$$\times \sum_{k=0}^{3m-1} \frac{(3m-1)!}{k!} \frac{Y_0^k}{\left(m/\overline{Y}_1\right)^{4m-k}} \Bigg] \Bigg]$$

$$
\begin{aligned}
&* \left[1 - \left(\frac{mz}{\overline{Y}_1} \right)^{7m} \frac{\Gamma(m)}{\Gamma(3m)} \right. \\
&\quad \times \left[\frac{(7m-1)!}{(m/\overline{z}_3)^{7m}} - \exp\left(-\left(\frac{m}{\overline{Y}_2} \right) Y_0^k \right) \right. \\
&\quad \left. \left. \times \sum_{k=0}^{7m-1} \frac{(7m-1)!}{k!} \frac{Y_0^k}{(m/\overline{Y}_2)^{8m-k}} \right] \right] \\
&* \left(\frac{mz}{\overline{Y}_1} \right)^{7m} \frac{\Gamma(m)}{\Gamma(3m)} \\
&\times \left[\frac{(7m-1)!}{(m/\overline{z}_3)^{7m}} - \exp\left(-\left(\frac{m}{\overline{Y}_2} \right) Y_0^k \right) \right. \\
&\quad \left. \times \sum_{k=0}^{7m-1} \frac{(7m-1)!}{k!} \frac{Y_0^k}{(m/\overline{Y}_2)^{8m-k}} \right] \\
&+ \left[1 - \left(\frac{mz}{\overline{Y}_1} \right)^{3m} \frac{\Gamma(m)}{\Gamma(3m)} \right. \\
&\quad \times \left[\sum \frac{(3m-1)!}{(m/\overline{Y}_1)^{3m}} - \exp\left(-\left(\frac{m}{\overline{Y}_1} \right) Y_0^k \right) \right. \\
&\quad \left. \left. \times \sum_{k=0}^{3m-1} \frac{(3m-1)!}{k!} \frac{Y_0^k}{(m/\overline{Y}_1)^{4m-k}} \right] \right] \\
&* \left[1 - \left(\frac{mz}{\overline{Y}_2} \right)^{7m} \frac{\Gamma(m)}{\Gamma(3m)} \right. \\
&\quad \times \left[\frac{(7m-1)!}{(m/\overline{Y}_2)^{7m}} - \exp\left(-\left(\frac{m}{\overline{Y}_2} \right) Y_0^k \right) \right. \\
&\quad \left. \left. \times \sum_{k=0}^{7m-1} \frac{(7m-1)!}{k!} \frac{Y_0^k}{(m/\overline{Y}_2)^{8m-k}} \right] \right] \\
&* \left[1 - \left(\frac{mz}{\overline{Y}_4} \right)^{7m} \frac{\Gamma(m)}{\Gamma(3m)} \right. \\
&\quad \times \left[\frac{(7m-1)!}{(m/\overline{Y}_4)^{7m}} - \exp\left(-\left(\frac{m}{\overline{Y}_4} \right) Y_0^k \right) \right. \\
&\quad \left. \left. \times \sum_{k=0}^{7m-1} \frac{(7m-1)!}{k!} \frac{Y_0^k}{(m/\overline{Y}_4)^{8m-k}} \right] \right] \\
&* \left[1 - \left(\frac{mz}{\overline{Y}_4} \right)^{11m} \frac{\Gamma(m)}{\Gamma(11m)} \right. \\
&\quad \times \left[\frac{(11m-1)!}{(m/\overline{Y}_6)^{11m}} - \exp\left(-\left(\frac{m}{\overline{Y}_6} \right) Y_0^k \right) \right. \\
&\quad \left. \left. \times \sum_{k=0}^{11m-1} \frac{(11m-1)!}{k!} \frac{Y_0^k}{\left(\frac{m}{\overline{Y}_6} \right)^{12m-k}} \right] \right].
\end{aligned}
\tag{23}
$$

(2) Nonidentical m:

$$
\begin{aligned}
&F_{\text{out III}} \\
&= \sum_{i=1}^{4} \sum_{k=1}^{m_i} \frac{\overline{Y}_1^{m_i}}{\prod_{h=1}^{8} \overline{Y}_1^{m_h}} \prod_{j=1, j \neq i}^{4} \left(\frac{1}{\overline{Y}_j} - \frac{1}{\overline{Y}_i} \right)^{-m_j} F_{Yl}(Y_0) \\
&\quad + \left[1 - \sum_{i=1}^{4} \sum_{k=1}^{m_i} \frac{\overline{Y}_1^{m_i}}{\prod_{h=1}^{8} \overline{Y}_1^{m_h}} \prod_{j=1, j \neq i}^{4} \left(\frac{1}{\overline{Y}_j} - \frac{1}{\overline{Y}_i} \right)^{-m_j} F_{Yl}(Y_0) \right] \\
&\quad * \sum_{i=1}^{8} \sum_{k=1}^{m_i} \frac{\overline{Y}_2^{m_i}}{\prod_{h=1}^{8} \overline{Y}_2^{m_h}} \prod_{j=1, j \neq i}^{8} \left(\frac{1}{\overline{Y}_j} - \frac{1}{\overline{Y}_i} \right)^{-m_j} F_{Yl}(Y_0) \\
&\quad + \left[1 - \sum_{i=1}^{4} \sum_{k=1}^{m_i} \frac{\overline{Y}_1^{m_i}}{\prod_{h=1}^{8} \overline{Y}_1^{m_h}} \prod_{j=1, j \neq i}^{4} \left(\frac{1}{\overline{Y}_j} - \frac{1}{\overline{Y}_i} \right)^{-m_j} F_{Yl}(Y_0) \right] \\
&\quad * \left[1 - \sum_{i=1}^{8} \sum_{k=1}^{m_i} \frac{\overline{Y}_2^{m_i}}{\prod_{h=1}^{M} \overline{Y}_2^{m_h}} \prod_{j=1, j \neq i}^{8} \left(\frac{1}{\overline{Y}_j} - \frac{1}{\overline{Y}_i} \right)^{-m_j} F_{Yl}(Y_0) \right] \\
&\quad * \sum_{i=1}^{8} \sum_{k=1}^{m_i} \frac{\overline{Y}_4^{m_i}}{\prod_{h=1}^{8} \overline{Y}_4^{m_h}} \prod_{j=1, j \neq i}^{8} \left(\frac{1}{\overline{Y}_j} - \frac{1}{\overline{Y}_i} \right)^{-m_j} F_{Yl}(Y_0) \\
&\quad + \left[1 - \sum_{i=1}^{4} \sum_{k=1}^{m_i} \frac{\overline{Y}_1^{m_i}}{\prod_{h=1}^{8} \overline{Y}_1^{m_h}} \prod_{j=1, j \neq i}^{4} \left(\frac{1}{\overline{Y}_j} - \frac{1}{\overline{Y}_i} \right)^{-m_j} F_{Yl}(Y_0) \right] \\
&\quad * \left[1 - \sum_{i=1}^{8} \sum_{k=1}^{m_i} \frac{\overline{Y}_2^{m_i}}{\prod_{h=1}^{M} \overline{Y}_2^{m_h}} \prod_{j=1, j \neq i}^{8} \left(\frac{1}{\overline{Y}_j} - \frac{1}{\overline{Y}_i} \right)^{-m_j} F_{Yl}(Y_0) \right] \\
&\quad * \left[1 - \sum_{i=1}^{8} \sum_{k=1}^{m_i} \frac{\overline{Y}_4^{m_i}}{\prod_{h=1}^{8} \overline{Y}_4^{m_h}} \prod_{j=1, j \neq i}^{8} \left(\frac{1}{\overline{Y}_j} - \frac{1}{\overline{Y}_i} \right)^{-m_j} F_{Yl}(Y_0) \right] \\
&\quad * 1 - \sum_{i=1}^{12} \sum_{k=1}^{m_i} \frac{\overline{Y}_6^{m_i}}{\prod_{h=1}^{12} \overline{Y}_6^{m_h}} * \prod_{j=1, j \neq i}^{12} \left(\frac{1}{\overline{Y}_j} - \frac{1}{\overline{Y}_i} \right)^{-m_j} F_{Yl}(Y_0).
\end{aligned}
\tag{24}
$$

4. Numerical Analysis

In this section, we show numerical results of the analytical outage probability of train-to-train communication model in three cases. We plot the performance curves in terms of average signal-to-noise ratio (SNR) and also show computer simulation results for verification.

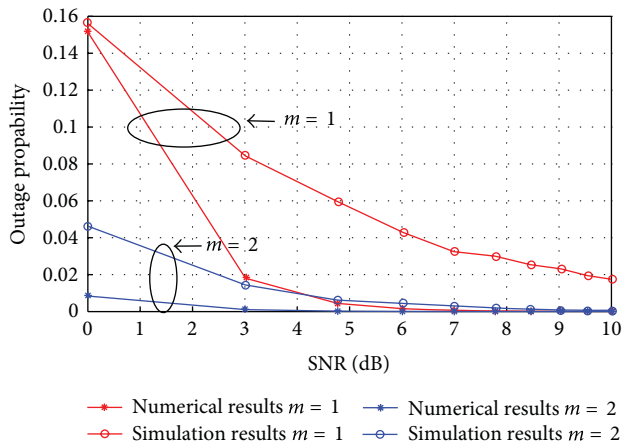

Figure 7: Outage probability of train-to-train communication in case I when $m = 1$ or $m = 2$.

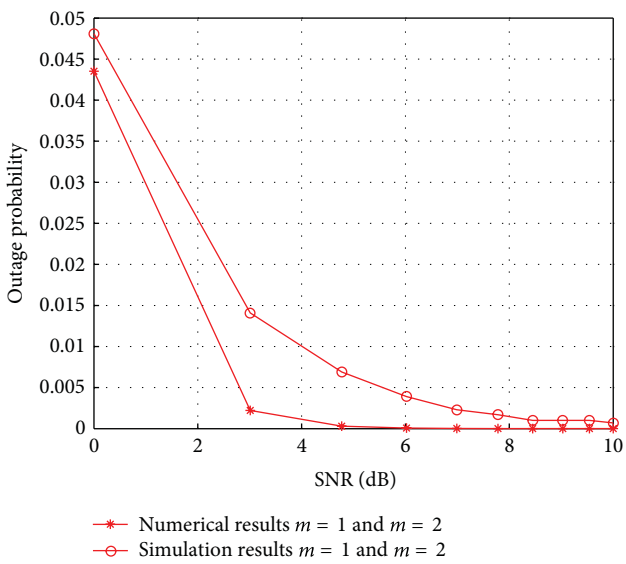

Figure 8: Outage probability of train-to-train communication in case I when $m = 3$.

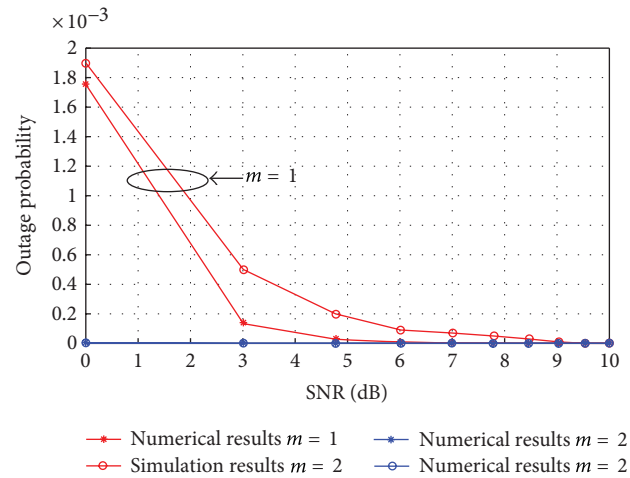

Figure 9: Outage probability of train-to-train communication in case II when $m = 1$ or $m = 2$.

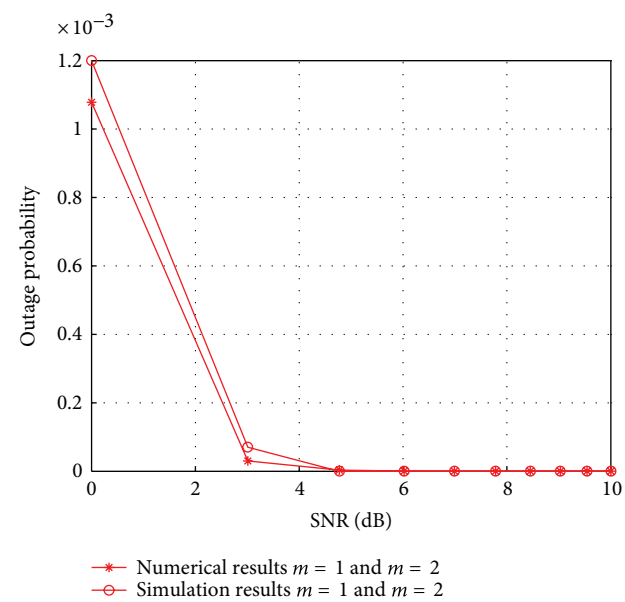

Figure 10: Outage probability of train-to-train communication in case II when $m = 3$.

According to the previous research, when the receiving SNR is 10 dB, the Bit Error rate (BER) is 10^{-6} which satisfies the communication requirements of high-speed railway set by UIC. Therefore, outage performances at SNR = 10 dB are crucial to the research of train-to-train communication model. If the wireless communication link in railway is disrupted, the railway safety is threatened severely. Figures 7, 9, and 11 show the numerical and simulation results of outage probability of train-to-train communication model versus SNR in case I, case II, and case III when $m = 1$ or $m = 2$. For $m = 1$ in Nakagami-m channel, the channel approximates Rayleigh channel, while for $m = 2$ the channel is Rice channel [14]. Because the condition of propagation channel is increasingly becoming better with the increment of parameter m, the outage performances of Rayleigh channel are not superior to those of Rice channel. As SNR is 10 dB, in Rayleigh channel, the outage probabilities of case I, case II, and case III are, 0.02, 0, and 0, respectively, while those of case I, case II, and case III are all 0 in Rice channel. AS for case I in Rayleigh channel, the outage probability is 0.02, which is bad for wireless communication. But the m parameter in high-speed railway is usually bigger than $m = 2$ in fact [14]. Figures 8, 10, and 12 show the numerical and simulation results of outage probability of train-to-train communication model versus SNR in case I, case II, and case III when $m = 1$ and $m = 2$. The outage probability is $7*10^{-4}$, 0, and 0 for three cases at SNR = 10 dB. Low outage probability contributes to the normal receipt of transmit signal and is rewarding to detection and decision of signal.

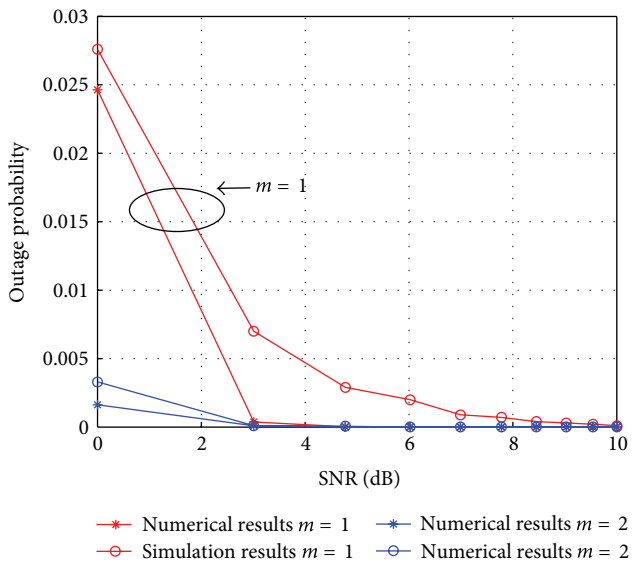

Figure 11: Outage probability of train-to-train communication in case III when $m = 1$ or $m = 2$.

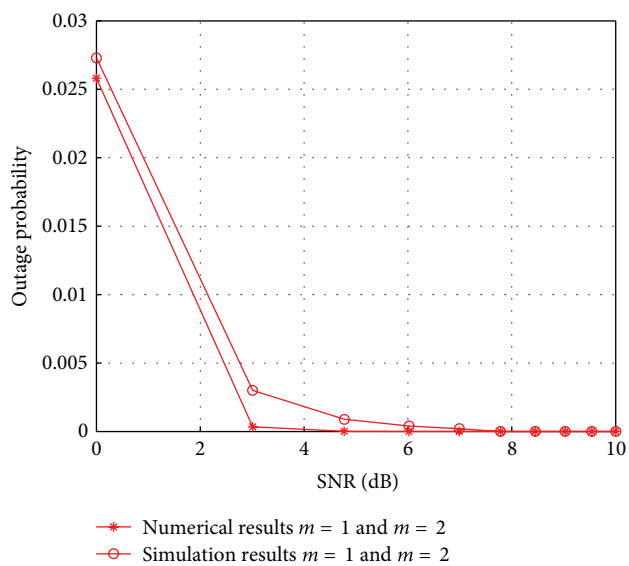

Figure 12: Outage probability of train-to-train communication in case III when $m = 1$ and $m = 2$.

5. Conclusion

This paper analyzes the end-to-end outage performance of high-speed-railway train-to-train communication model over independent identical and nonidentical Nakagami-m channels. The mechanism of such communication among trains can be divided into three cases based on occurrence of possible-occurrence relay trains. Numerical and simulation analysis shows that the outage probability of train-to-train communication model in three cases is approximately 0 over Nakagami-m ($m \geqslant 2$) channel in high-speed railway, which ensures the normal receipt of transmit signal.

Acknowledgments

This research was supported by the National Natural Science Foundation of China under Grant no. 61222105 the Program for New Century Excellent Talents in University under Grant NCET-09-0206, Fundamental Research Funds for the Central Universities under Grant nos. 2010JBZ008, 2012YJS017, 2012YJS001, and no. 2011YJS010, Key Project of State Key Lab under Grant no. RCS2011ZZ008, National Natural Science Foundation of China under Grant 60830001, Beijing Natural Science Foundation under Grant 4112048, and Program for Changjiang Scholars and Innovative Research Team in University under Grant no. IRT0949.

References

[1] J. M. Zhang and B. N. Han, "Analysis and calculation of the scheduled waiting time for the train route," in *Proceedings of the 4th International Conference on Intelligent Computation Technology and Automation (ICICTA '11)*, vol. 1, pp. 54–58, March 2011.

[2] T. Strang, M. M. Zu Hörste, and X. G. Gu, "A railway collision avoidance system exploiting ad-hoc inter-vehicle communication and GALILEO," in *Proceedings of the 13th World Congress and Exhibition on Intelligent Transportation Systems and Services*, pp. 51–56, London, UK, October 2006.

[3] C. R. García, A. Lehner, T. Strang, and M. Röckl, "Comparison of collision avoidance systems and applicability to rail transport," in *Proceedings of the 7th International Conference on Intelligent Transport Systems Telecommunications (ITST '07)*, pp. 1–6, 2007.

[4] C. R. García, A. Lehner, T. Strang, and K. Frank, "Channel model for train to train communication using the 400 MHz band," in *Proceedings of the IEEE Vehicular Technology Conference*, pp. 3082–3086, May 2008.

[5] C. R. García, A. Lehner, and T. Strang, "A broadcast vehicle-to-vehicle communication system in railway environments," in *Proceedings of the 1st Annual International Symposium on Vehicular Computing Systems*, pp. 70–76, 2008.

[6] A. Lehner, C. Rico-García, E. Wige, and T. Strang, "A multi-broadcast communication system for high dynamic vehicular ad-hoc networks," in *Proceedings of the International Conference on Ultra Modern Telecommunications and Workshops (ICUMT '09)*, pp. 1–6, October 2009.

[7] C. R. García, A. Lehner, T. Strang, O. Heirich et al., "Measurement and analysis of the direct train-to-train propagation channel in the 70 cm UHF-band," in *Proceedings of the 3rd International Workshop on Communication Technologies for Vehicles*, vol. 6596, pp. 45–57.

[8] P. Zhao, *The Operation and Reorganization of the High Speed Train*, China Railway, 2009.

[9] X. Cheng, C. X. Wang, D. I. Laurenson, S. Salous, and A. V. Vasilakos, "An adaptive geometry-based stochastic model for non-isotropic MIMO mobile-to-mobile channels," *IEEE Transactions on Wireless Communications*, vol. 8, no. 9, pp. 4824–4835, 2009.

[10] X. Cheng, C.-X. Wang, H. Wang, X. Gao et al., "Cooperative MIMO channel modeling and multi-link spatial correlation properties," *IEEE Journal on Selected Areas in Communications*, vol. 30, no. 2, pp. 388–396, 2012.

[11] Z. D. Zhong, B. Ai, and Q.Y. Liu, *Applications of Fundamental Theory of Railway Digital Mobile Communication System (GSM)*, Tsing Hua University Press, 2009.

[12] S. Gradshteyn and I. M. Ryzhik, *Table of Integrals, Series, and Products*, Academic Press, New York, NY, USA, 6th edition, 2000.

[13] G. K. Karagiannidis, N. C. Sagias, and T. A. Tsiftsis, "Closed-form statistics for the sum of squared Nakagami-m variates and its applications," *IEEE Transactions on Communications*, vol. 54, no. 8, pp. 1353–1359, 2006.

[14] R. S. He, Z. D. Zhong, B. Ai, and J. W. Ding, "An empirical path loss model and fading analysis for high-speed railway viaduct scenarios," *IEEE Antennas Wireless Propagation Letters*, vol. 10, pp. 808–812.

Hindawi Publishing Corporation
International Journal of Antennas and Propagation
Volume 2012, Article ID 475492, 9 pages
doi:10.1155/2012/475492

Research Article

A Novel Train-to-Train Communication Model Design Based on Multihop in High-Speed Railway

Pengyu Liu,[1] Bo Ai,[1] Zhangdui Zhong,[1] and Xiaojuan Zhou[2]

[1] *State Key Laboratory of Rail Traffic Control and Safety, Beijing Jiaotong University, Beijing 100044, China*
[2] *Department of Communication Engineering, University of Armed Police Force Engineering, Xian 710086, China*

Correspondence should be addressed to Bo Ai, aibo@ieee.org

Received 22 July 2012; Accepted 16 October 2012

Academic Editor: César Briso Rodríguez

Railway telematics applications are currently attracting attention and are under intense research. Reliable railway telematics applications increasingly tend to require a subsidiary means to help existent control system make train operation safer and more efficient. Since 2006, train-to-train communication has been studied to respond to such requirements. A key characteristic of train-to-train communication is that operation control to avoid possible accidents is conducted among trains without help of a base station. This paper proposes a novel train-to-train communication model in a physical layer based on multihop and cooperation, taking a high-speed railway propagation channel into account. The mechanism of this model lies in the idea that a source train uses trains on other tracks as relays to transmit signals to destination train on the same track. Based on occurrence of these potential relays, such mechanism can be divided into three cases. In each case, BER is applied to evaluate properties of the proposed communication model. Simulation results show that BER of the train-to-train communication model decreases to 10^{-6} when SNR is 10 dB and that the minimum receiving voltage of this model is -84 dBm, which is 8 dBm lower than the standards established by the International Union of Railways (UIC) in a high-speed railway scenario.

1. Introduction

Railways are a powerful transportation systems which exert significant influence in supporting development of economies. Safety concerns in railways are attracting an increasing amount of attention at present, because the railways have assumed an increased responsibility for safeguarding the personal and property security. Railway accidents generally lead to serious consequences—loss of lives and property. These phenomena directly motivate the researchers to concentrate more on various systems for railway safety. The mainstream technique of railway safety in China is the Chinese Train Control System Level 3 (CTCS-3) based on the Global System for Mobile Communication for Railways (GSM-R) which acts as a radio interface to link trains with control center to exchange safety messages; this system ensures that trains are monitored by a real-time device and that they operate at a certain safe distance from each other [1].

It cannot be denied that the CTCS-3 system has proved to be an accurate technique for positioning and also provides a rapid exchange of motion state and control messages. However, according to statistics provided by the *American Federal Railroad Administration* (FRA) in the United States, about 8221 accidents threaten the passengers' personal safety in the past four years [2]. This is because a train driver could only be informed about potential collisions by an operation center. If the operation center fails to transmit control messages in an emergency, an accident will inevitably occur. Therefore, it is imperative to develop a novel technique to assist existing system to make control of train operation safer and more accurate. This technique allows the train conductors to keep updated with accurate information of traffic conditions in their vicinity [3]. On the basis of intertrain multihop communication, the train-to-train communication aims at detecting a potential collision and then broadcast prewarning messages to other trains on the same and neighboring tracks. When a control center system detects potential accidents, the train-to-train communication acts in an assisting role to immediately propagate messages to other trains and provide potential solutions to the driver to avoid

danger. Furthermore, its application also reduces outlays on infrastructure maintenance for base stations [4].

2. Related Work

In recent years, research on train-to-train communication has been carried out by several organizations, including the German Aerospace Center (DLR). Reference [5] discusses communication link design such as maximum data rate, frequency selection, and channel model, while [6] describes an overview of the state of the art in collision avoidance related to transportation systems for maritime, aircraft, and road transportation, and the RCAS is introduced. Reference [7] proposes a channel model for direct train-to-train communication appropriate for the 400 MHz band, and [8] presents analyses and results of a comprehensive measurement campaign investigating the propagation channel in case of direct communication between railway vehicles.

Though the RCAS has undergone some progress in physical-layer design, it only supports train operation velocity of lower than 200 Km/h, which is not applicable to a high-speed railway. Generally, the velocity of a high-speed railway train is up to 360 Km/h. In this case, safety distance among trains is 10 Km [9], which will result in severe path loss and poor receiving signal quality if two trains on the same track perform direct communication. The BER of the receiving signal is about 0.5.

To solve this problem, in this paper, we propose a train-to-train communication model in the physical layer based on multihop. In order to make up a poor receiving signal resulting from path loss, the multihop mechanism in which the source train uses trains operating on other tracks as relays to transmit signals to a destination train on the same track is adopted. This mechanism can be divided into three cases based on occurrence of other relay trains. A presumption can be made that an arrival procedure of a train follows the Poisson distribution and the arrival procedure is a negative exponent [10]. In contrast to the physical-layer model research in other papers [5, 6], the proposed train-to-train communication model, introducing OFDM and MIMO techniques, realizes intertrain adhoc communication based on the Poisson process in the high-speed railway scenarios.

The rest of this paper is organized as follows. Section 3 gives a description of the proposed train-to-train communication model based on multihop, and Section 4 derives BER expressions of three cooperative conditions. In Section 5, the parameter selection of the train-to-train model is discussed. Section 6 shows the simulation results of this model, and this paper is concluded in Section 7.

3. Proposed Train-to-Train Communication Model

The train-to-train communication model is presented in Figure 1, where the S, $R1$, and D represent a source terminal, a fixed-occurring relay terminal, and a destination terminal, respectively. The $R1$ is the train that meets S on another rail track, and the $R2$ and $R3$, respectively, represent the first possible-occurring relay terminal and the third possible-occurring relay terminal. The average operating velocities of the $R1$ and $R2$ are 100 m/s, and those of D and $R3$ are -100 m/s. Rail 1, Rail 2, Rail 3, and Rail 4 represent four parallel rail tracks.

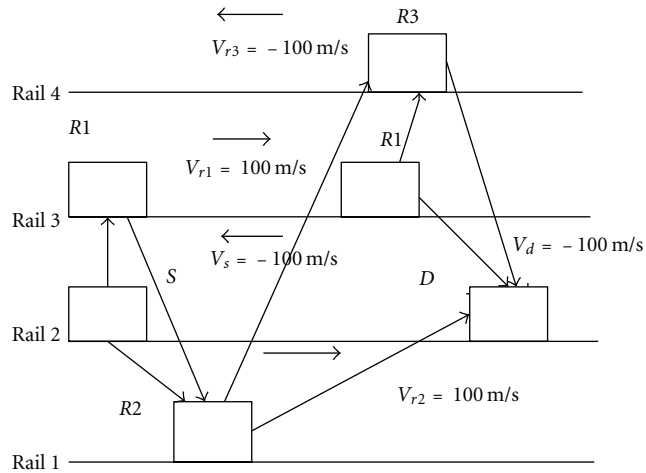

Figure 1: Communication mechanism of train-to-train model.

The communication mechanism of this model can be discussed under three cases based on the Poisson process. In the Poisson process, let sequence $\{X_n, n \geq 1\}$ denote the time interval between the $(n-1)$th and the nth event, called the sequence of interarrival times, and X_n follows an exponential distribution. If a certain event definitely occurs, X_n will be uniformly distributed in the time interval T [11]. The occurrence of potential relays follows the Poisson process. Due to the concept put forward in China that the train flow density of trains in a high-speed railway network tends to be the same as that of buses in road transportation [12], there is no doubt that a two-train meet among different tracks will always exist. These cases are described below.

3.1. Case I. The S transmits signals to the $R1$ on different rail tracks when they meet each other. At the same time, the S searches for the potential relay $R2$ on a neighboring rail track 1. If the $R2$ is not found, $R1$ will keep broadcasting messages within its communication coverage (6 Km) [5], and if it receives a response from D, their communication link will be held and the transmission between them is performed.

3.2. Case II. If the $R2$ is searched, the S and $R1$ simultaneously transmit the signals to the $R2$. The $R2$ also performs the search of the potential relay $R3$. If the $R3$ does not exist, it will operate for some seconds until the distance between $R2$ and D is within a communication range. Finally, the $R2$ and $R1$, acting as two relays of the source, will transmit the signals to the destination terminal.

3.3. Case III. If the $R3$ exists, it will receive the signals from the $R2$ and $R1$ and then combine them. Finally, the $R3$, $R2$, and $R1$, as three relays of the source, will forward the signals to the destination terminal.

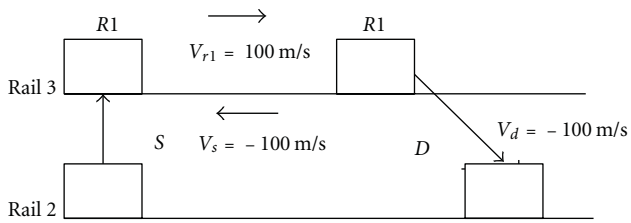

Figure 2: Communication model of Case I.

Under these cases, this paper respectively analyzes the reliability of the train-to-train communication model using the performance index BER.

4. Analysis of Train-to-Train Communication Model

4.1. Case I. Figure 2 describes the train-to-train communication model of Case I. The source S transmits the signals to the $R1$ as they meet each other. Total power is E, and the transmit signals are denoted as follows:

$$\begin{aligned}
\mathbf{X}_{S,R1,2k+1}(n) &= \Big(x_{S,R1,2k+1}(n);\\
&\quad n = \{N - N_{\mathrm{CP}} + 1, \ldots, N, 1, 2, \ldots, N\},\\
&\quad k = \left\{0, 2, \ldots, \frac{M-2}{2}\right\}\Big),\\
\mathbf{X}^*_{S,R1,2k+1}(n) &= \Big(x^*_{S,R1,2k+1}(n);\\
&\quad n = \{N - N_{\mathrm{CP}} + 1, \ldots, N, 1, 2, \ldots, N\},\\
&\quad k = \left\{0, 2, \ldots, \frac{M-2}{2}\right\}\Big),\\
\mathbf{X}_{S,R1,2k+2}(n) &= \Big(x_{S,R1,2k+2}(n);\\
&\quad n = \{N - N_{\mathrm{CP}} + 1, \ldots, N, 1, 2, \ldots, N\},\\
&\quad k = \left\{0, 2, \ldots, \frac{M-2}{2}\right\}\Big),\\
-\mathbf{X}^*_{S,R1,2k+2}(n) &= \Big(-x^*_{S,R1,2k+2}(n);\\
&\quad n = \{N - N_{\mathrm{CP}} + 1, \ldots, N, 1, 2, \ldots, N\},\\
&\quad k = \left\{0, 2, \ldots, \frac{M-2}{2}\right\}\Big).
\end{aligned} \tag{1}$$

The $\mathbf{X}_{S,R1,2k+1}(n)$, $\mathbf{X}_{S,R1,2k+2}(n)$, $\mathbf{X}^*_{S,R1,2k+1}(n)$, and $-\mathbf{X}^*_{S,R1,2k+2}(n)$ denote two different transmitting OFDM symbols and their conjugate forms. The $x_{S,R1,2k+1}(n)$, $x^*_{S,R1,2k+1}(n)$, $x_{S,R1,2k+2}(n)$, $x_{S,R1,2k+2}(n)$, and $-x^*_{S,R1,2k+2}(n)$ are the *Fast Fourier Transforms* (FFT) of the *Quadrature Phase Shift Keying* (QPSK) modulation symbol in each subcarrier of the OFDM symbol. In OFDM modulation, n represents the sequence number of the subcarrier. N and N_{CP}, are, respectively, the total number of subcarriers and the length of the cyclic prefix. M is the number of transmit OFDM symbols.

Considering Alamouti coding [13], $\mathbf{X}_{S,R1}$ denotes the transmit signals at the transmitter with two antennas (antenna 1 and antenna 2) and is expressed as below:

$$\mathbf{X}_{S,R1} = \begin{bmatrix} \mathbf{X}_{S,R1,2k+1}(n) & \mathbf{X}_{S,R1,2k+2}(n) \\ -\mathbf{X}^*_{S,R1,2k+2}(n) & \mathbf{X}^*_{S,R1,2k+1}(n) \end{bmatrix}. \tag{2}$$

Having taken multipaths and the Doppler effect into account, the impulse response of a channel can be written as

$$\begin{aligned}
\mathbf{H}_{1,S,R1,l} &= \big(\mathrm{a}_l \delta(n - n_l) \exp\big(2\pi T_s f_d (n - n_l)\big);\\
&\qquad n = \{N - N_{\mathrm{CP}} + 1, \ldots, N, 1, 2, \ldots, N\}\big),\\
\mathbf{H}_{2,S,R1,l} &= \big(\mathrm{a}_l \delta(n - n_l) \exp\big(2\pi T_s f_d (n - n_l)\big),\\
&\qquad n = \{N - N_{\mathrm{CP}} + 1, \ldots, N, 1, 2, \ldots, N\}\big)
\end{aligned} \tag{3}$$

$\mathbf{H}_{1,S,R1,l}$ and $\mathbf{H}_{2,S,R1,l}$ are channel impulse responses of a certain single path from the transmitter to the receiver with a 2×2 MIMO. l denotes the number of multipaths, f_d is the maximum Doppler frequency shift, n_l is the time delay of each path, and T_s is the sampling interval.

The $\mathbf{Y}_{1,S,R1,2k+1,l}$, $-\mathbf{Y}^*_{1,S,R1,2k+2,l}$, $\mathbf{Y}_{2,S,R1,2k+2,l}$, and $\mathbf{Y}^*_{1,S,R1,2k+1,l}$ are the receiving vectors at the receiver for two antennas, and they can be derived as follows:

$$\begin{aligned}
&\begin{bmatrix} \mathbf{Y}_{1,S,R1,2k+1,l} & \mathbf{Y}_{2,S,R1,2k+1,l} \\ -\mathbf{Y}^*_{1,S,R1,2k+2,l} & -\mathbf{Y}^*_{2,S,R1,2k+2,l} \end{bmatrix}\\
&= \sqrt{E/2} \begin{bmatrix} \mathbf{X}_{S,R1,2k+1} \odot \mathbf{H}_{1,S,R1,l} & \mathbf{X}_{S,R1,2k+1} \odot \mathbf{H}_{2,S,R1,l} \\ -\mathbf{X}^*_{S,R1,2k+2} \odot \mathbf{H}_{1,S,R1,l} & -\mathbf{X}^*_{S,R1,2k+2} \odot \mathbf{H}_{2,S,R1,l} \end{bmatrix}\\
&\quad + \begin{bmatrix} \mathbf{N}_{1,S,R1,2k+1,l} & \mathbf{N}_{2,S,R1,2k+1,l} \\ \mathbf{N}'_{1,S,R1,2k+2,l} & \mathbf{N}'_{2,S,R1,2k+2,l} \end{bmatrix},\\
&\begin{bmatrix} \mathbf{Y}_{1,S,R1,2k+2,l} & \mathbf{Y}_{2,S,R1,2k+2,l} \\ \mathbf{Y}^*_{1,S,R1,2k+1,l} & \mathbf{Y}^*_{2,S,R1,2k+1,l} \end{bmatrix}\\
&= \sqrt{E/2} \begin{bmatrix} \mathbf{X}_{S,R1,2k+2} \odot \mathbf{H}_{1,S,R1,l} & \mathbf{X}_{S,R1,2k+2} \odot \mathbf{H}_{2,S,R1,l} \\ \mathbf{X}^*_{S,R1,2k+1} \odot \mathbf{H}_{1,S,R1,l} & \mathbf{X}^*_{S,R1,2k+1} \odot \mathbf{H}_{2,S,R1,l} \end{bmatrix}\\
&\quad + \begin{bmatrix} \mathbf{N}_{1,S,R1,2k+2,l} & \mathbf{N}_{2,S,R1,2k+2,l} \\ \mathbf{N}'_{1,S,R1,2k+1,l} & \mathbf{N}'_{2,S,R1,2k+1,l} \end{bmatrix}.
\end{aligned} \tag{4}$$

$\mathbf{N}_{1,S,R1,2k+1,l}$, $\mathbf{N}_{2,S,R1,2k+1,l}$, $\mathbf{N}'_{1,S,R1,2k+2,l}$, $\mathbf{N}'_{2,S,R1,2k+2,l}$, $\mathbf{N}_{1,S,R1,2k+2,l}$, $\mathbf{N}_{2,S,R1,2k+2,l}$, $\mathbf{N}'_{1,S,R1,2k+1,l}$, and $\mathbf{N}'_{2,S,R1,2k+1,l}$ are the *Additive White Gaussian Noise* (AWGN) with a zero mean

$$\mathbf{Y}_{1,S,R1,2k+1} = \sum_{l=1}^{L} \mathbf{Y}_{1,S,R1,2k+1,l},$$

$$\mathbf{Y}_{2,S,R1,2k+1} = \sum_{l=1}^{L} \mathbf{Y}_{2,S,R1,2k+1,l},$$

$$\mathbf{Y}_{1,S,R1,2k+2} = \sum_{l=1}^{L} \mathbf{Y}_{1,S,R1,2k+2,l},$$

$$\mathbf{Y}_{1,S,R1,2k+2} = \sum_{l=1}^{L} \mathbf{Y}_{1,S,R1,2k+2,l},$$
$$\mathbf{Y}_{S,R1,2k+1} = \mathbf{Y}_{1,S,R1,2k+1} + \mathbf{Y}_{2,S,R1,2k+1},$$
$$\mathbf{Y}_{S,R1,2k+2} = \mathbf{Y}_{1,S,R1,2k+2} + \mathbf{Y}_{2,S,R1,2k+2}. \tag{5}$$

L is the total quantity of multipaths. By processing at the receiver, $\mathbf{Y}_{S,R1,2k+1}$ and $\mathbf{Y}_{S,R1,2k+2}$ are the final receiving vectors with signals of L paths added together.

Using the modified LS channel estimation, $\mathbf{H}'_{S,R1,2k+1}$ and $\mathbf{H}'_{S,R1,2k+2}$ are obtained to estimate the original source signals:

$$\mathbf{X}'_{S,R1,2k+1} = \mathbf{H}'^{-1}_{S,R1,2k+1} \odot \mathbf{Y}_{S,R1,2k+1},$$
$$\mathbf{X}'_{S,R1,2k+2} = \mathbf{H}'^{-1}_{S,R1,2k+2} \odot \mathbf{Y}_{S,R1,2k+2}. \tag{6}$$

$\mathbf{X}'_{S,R1,2k+1}$ and $\mathbf{X}'_{S,R1,2k+2}$ denote the estimation source signals, and the SNRs $\Upsilon_{R1,2k+1}$ and $\Upsilon_{R1,2k+2}$ at the relay can be written as

$$\Upsilon_{R1,2k+1} = \frac{E}{4N_0N}\left\|\mathbf{X}'_{S,R1,2k+1}\right\|^2,$$
$$\Upsilon_{R1,2k+2} = \frac{E}{4N_0N}\left\|\mathbf{X}'_{S,R1,2k+2}\right\|^2. \tag{7}$$

At the relay $R1$, the $\mathbf{X}'_{S,R1,2k+1}$ and $\mathbf{X}'_{S,R1,2k+2}$ are demodulated and then encoded again using QPSK and OFDM modulation to prepare them to be forwarded.

From the $R1$ to the destination, the transmitting signals $\mathbf{X}'_{S,R1,2k+1}$ and $\mathbf{X}'_{S,R1,2k+2}$ have experienced the same process as $\mathbf{X}_{S,R1,2k+1}$ and $\mathbf{X}_{S,R1,2k+2}$.

$\mathbf{X}'_{R1,D,2k+1}$ and $\mathbf{X}'_{R1,D,2k+2}$ are the estimation relay signals, and the SNRs $\Upsilon_{D,2k+1}$ and $\Upsilon_{D,2k+2}$ at the relay can be written as

$$\Upsilon_{D,2k+1} = \frac{E}{4N_0N}\left\|\mathbf{X}'_{R1,D,2k+1}\right\|^2,$$
$$\Upsilon_{D,2k+2} = \frac{E}{4N_0N}\left\|\mathbf{X}'_{R1,D,2k+2}\right\|^2. \tag{8}$$

P_e is the BER of the QPSK and can be expressed as below [13]:

$$P_e = Q\left(\sqrt{2\Upsilon}\right), \tag{9}$$

where Υ is the SNR.

The BER of the relay strategy *Decode and Forward* (DF) can be written as [14]

$$P_e = Q\left(\sqrt{2\Upsilon}\right) + Q\left(\sqrt{2\Upsilon}\right) - 2Q\left(\sqrt{2\Upsilon}\right)Q\left(\sqrt{2\Upsilon}\right). \tag{10}$$

$P_{e,2k+1}$ and $P_{e,2k+2}$ are the BER of the $(2k+1)$th and $(2k+2)$th OFDM symbols:

$$P_{e,2k+1} = Q\left(\sqrt{2\Upsilon_{R1,2k+1}}\right) + Q\left(\sqrt{2\Upsilon_{D,2k+1}}\right) - 2Q\left(\sqrt{2\Upsilon_{R1,2k+1}}\right)Q\left(\sqrt{2\Upsilon_{D,2k+1}}\right). \tag{11}$$

The channel encoding is applied to enforce the error detection and correction at the receiver, and considering adoption interleaving and a (7, 4) cyclic code, the destination's BERs of the$(2k+1)$th and $(2k+2)$th OFDM symbols can be

$$P_{e,\mathrm{I},2k+1} = \sum_{m=t+1}^{n} C_n^m \left(P_{e,2k+1}\right)^m \left(1 - P_{e,2k+1}\right)^{n-m},$$
$$P_{e,\mathrm{I},2k+2} = \sum_{m=t+1}^{n} C_n^m \left(P_{e,2k+2}\right)^m \left(1 - P_{e,2k+2}\right)^{n-m}. \tag{12}$$

$P_{e,\mathrm{I},2k+1}$ and $P_{e,\mathrm{I},2k+2}$ are the BERs of the $(2k+1)$th and $(2k+2)$th OFDM symbols at the destination terminal, t is the number of errors which can be corrected, and n is the total number of bit streams.

4.2. Case II. The distance between source and destination terminals is 10 Km, which is out of the set communication range (6 Km). It is therefore feasible to communicate with the destination terminal via $R2$ within the communication range on the neighboring track. Because the average velocity of the $R2$ is 100 m/s, the operation time interval in the communication range is 50 s, considering 1 km as the reserve margin.

Figure 3 gives a description of the train-to-train communication model of Case II. At time slot m, the source transmits the signals to $R1$, when they meet each other. The transmit signals are the same as those of Case I. At the same time, S searches $R2$ on the neighboring track. The occurrence of the $R2$ is on the basis of the Poisson process. Supposing the occurrence of $R2$ is event 1, denoted as $S1$, the coming of $S1$ follows exponential distribution within the time interval T of which the average strength λ is 180 s [9]. The coming probability P_{S1} of event $S1$ in the time interval T can be obtained as follows:

$$T = \frac{10{,}000\,\mathrm{m}}{(100\,\mathrm{m/s}) - (-100\,\mathrm{m/s})} = 50\,\mathrm{s},$$
$$P_{S1} = 1 - \exp\left(-\frac{t}{\lambda}\right)\Big|_{T=50\,\mathrm{s},\lambda=180\,\mathrm{s}} = 0.2425. \tag{13}$$

When the event $S1$ is determinately occurring, its distribution in the 50 s is uniform U (0, 50).

At time slot $m+1$, the source and $R1$ simultaneously transmit the signals to the $R2$, and the transmit signals $\mathbf{X}_{S,R2}(n)$ and $\mathbf{X}_{R1,R2}(n)$ from S and $R2$ are written as

$$\mathbf{X}_{S,R2}(n) = (x_{S,R1}(n);\ n = \{N - N_{\mathrm{CP}} + 1, \ldots, N, 1, 2, \ldots, N\}),$$
$$\mathbf{X}_{R1,R2}(n) = (x_{S,R1}(n);\ n = \{N - N_{\mathrm{CP}} + 1, \ldots, N, 1, 2, \ldots, N\}). \tag{14}$$

Like Case I, the transmitter adopts OFDM and Alamouti coding technique. The transmit signals are transmitted with multipath and Doppler effects and are processed by the relay $R2$ to acquire the estimation signals.

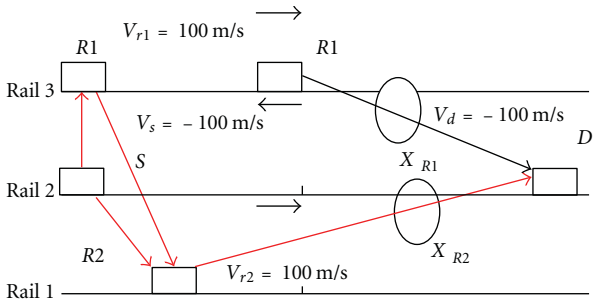

Figure 3: Communication model of Case II.

After decoding and reencoding the receiving signals, the $R2$ operates for some seconds until the distance between $R2$ and D is within the communication range.

$R2$ and $R1$, as two relays of the source, jointly transmit the estimation signals $\mathbf{X}'_{R1}$ and $\mathbf{X}'_{R2}$ to the destination terminal, on the assumption that the relays $R2$ and $R1$ coordinate perfectly. The estimation signals at the destination terminal are $\mathbf{X}''_{R1}$, $\mathbf{X}''_{R2}$ and the SNRs Υ_{R1} and Υ_{R2} at the destination terminal are as expressed below:

$$\Upsilon_{R1} = \frac{E}{4N_0N}\|\mathbf{X}''_{R1}\|^2,$$
$$\Upsilon_{R2} = \frac{E}{4N_0N}\|\mathbf{X}''_{R2}\|^2. \tag{15}$$

Case II is composed of two links which are a relay link (S-$R2$-D) and an equivalent direct link ($R1$-D). The BER of the receiving signal at the destination terminal can be written as

$$P_e = \left(1 - Q\left(\sqrt{\Upsilon_{R2}}\right)\right)Q\left(\sqrt{\Upsilon_{R1} + \Upsilon_{R2}}\right) + Q\left(\sqrt{\frac{(\Upsilon_{R1} - \Upsilon_{R2})^2}{\Upsilon_{R1} + \Upsilon_{R2}}}\right)Q\left(\sqrt{\Upsilon_{R2}}\right). \tag{16}$$

Using channel encoding including interleaving and the (7, 4) cyclic code, the $P_{e,\mathrm{II}}$ can be derived as

$$P_{e,\mathrm{II}} = \sum_{m=t+1}^{n} C_n^m (P_e)^m (1 - P_e)^{n-m}. \tag{17}$$

4.3. Case III. The occurrence of $R3$ is like $R2$, wherein the coming probability P_{S2} of event $S2$ in the time interval T of 50 s is

$$P_{S2} = 1 - \exp\left(-\frac{t}{\lambda}\right)\Big|_{T=50,\ \lambda=180} = 0.2425. \tag{18}$$

The communication model in Figure 4 can be considered to be composed of two basic models. One is marked with red lines, while the other is marked with blue lines. The principle of the red model is the same as that of the communication model in Figure 2 of which the SNR $\Upsilon_{R1,R2}$ at the destination terminal is written as

$$\Upsilon_{R1,R2} = \frac{E}{4N_0N}\left\|\mathbf{X}''_{R1,R2}\right\|^2. \tag{19}$$

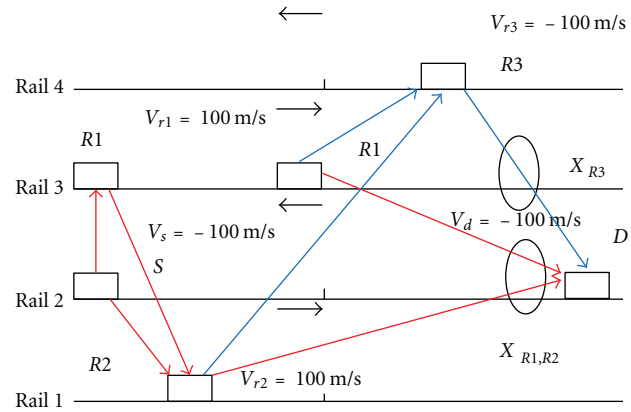

Figure 4: Communication model of Case III.

Then the red model can be considered equivalent to a direct link from the relay $R1$ to the destination D. The $\mathbf{X}''_{R3}$ is the estimation signals of the relay link ($R1$-$R3$-D) at the destination, and the SNR Υ_{R3} is

$$\Upsilon_{R3} = \frac{E}{4N_0N}\|\mathbf{X}''_{R3}\|^2. \tag{20}$$

Combining the relay link with the direct link, the BER of the communication model in Figure 4 is

$$P_e = \left(1 - Q\left(\sqrt{\Upsilon_{R3}}\right)\right)Q\left(\sqrt{\Upsilon_{R1,R2} + \Upsilon_{R3}}\right) + Q\left(\sqrt{\frac{(\Upsilon_{R1,R2} - \Upsilon_{R3})^2}{\Upsilon_{R1,R2} + \Upsilon_{R3}}}\right)Q\left(\sqrt{\Upsilon_{R3}}\right), \tag{21}$$

$$P_{e,\mathrm{III}} = \sum_{m=t+1}^{n} C_n^m (P_e)^m (1 - P_e)^{n-m}. \tag{22}$$

5. Numerical Analysis

5.1. Frequency Selection. The maximum propagation distance of the proposed train-to-train communication model is 6 Km. In order to avoid drastic signal attenuation of a long transmit distance, considering the Hata-Okumura suburban model [15], it is suitable to choose a frequency among the UHF band. The frequency determined at 300 MHz and the change of the path loss of the signal with distance in a suburban area is presented in Figure 5. As shown in Figure 5, the path loss of the signal in a suburban area at the distance of 6 Km is −142.23 dB.

5.2. Channel Model. The channel model used in this paper is the train-to-train suburban communication model in COST 207 [16, 17], which has six paths and whose maximum time delay is 5 μs. The speed of the high speed train is up to 100 m/s, so the Doppler frequency shift, in the range of [−200, 200] Hz, is added to each of six paths. The parameters of the suburban model in COST 207 are listed in Table 1.

5.3. Transmit Power. The minimum receiving level of the high-speed railway is −92 dBm [18], which is published

Table 1: Parameters of the suburban model in COST 207.

Number of path	Time delay (μs)	Path power
1	0	1
2	0.1	0.4
3	0.2	0.16
4	0.3	0.06
5	0.4	0.03
6	0.5	0.01

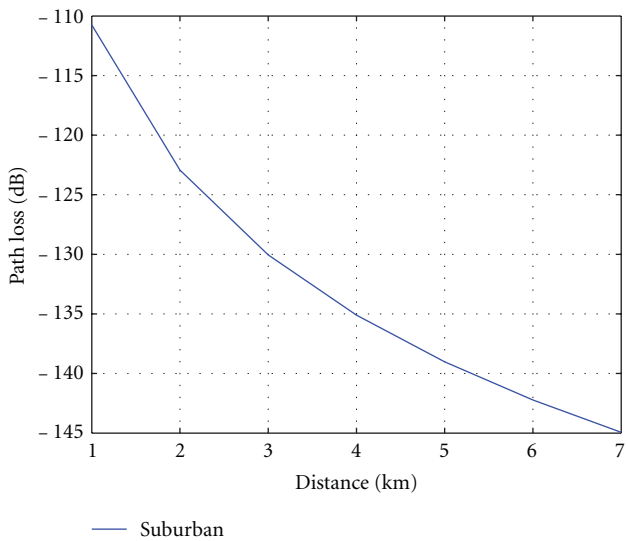

Figure 5: Change of the path loss of the signal with distance in suburban area.

by UIC. The required SNR for the best reception is 10 dB and the bandwidth of train-to-train communication is 1 MHz. For the longest communication distance, the path loss is −142.23 dB. Therefore the transmit power P can be calculated by

$$\begin{aligned} P &= 10\log_{10}(\mathrm{KTB}) + \mathrm{SNR} - L_{\text{Path Loss}} + \sigma 2 \\ &= 10\log_{10}\left(1.38 * 10^{-23}\frac{J}{K} * 290\,\mathrm{K} * 10^{6}\right) \\ &\quad + 10\,\mathrm{dB} + 142.23\,\mathrm{db} + 3\,\mathrm{dB} \\ &= 11.25\,\mathrm{dBW}\ (13.59\,\mathrm{W}). \end{aligned} \tag{23}$$

As is shown in (23), the lowest transmit power of train-to-train communication is 13.59 W.

5.4. Key Technique. The bit stream from the source is firstly mapped to the symbol with $\pi/4$-QPSK and then the OFDM modulation is performed. For the OFDM, there are 1024 subcarriers with 512 mainly applied to transmit useful messages. The length of the cyclic prefix is 128 and the interval of the pilot is set to 5. The bandwidth is 1 MHz.

6. Simulation Result

The train-to-train communication model performance is measured in terms of the BER by altering the SNR using the Monte Carlo simulation. The results indicate that the train-to-train communication model works better with BER = 10^{-6} at SNR = 10 dB which satisfies the requirements of the transmission of the train control and prewarning messages [19]. The simulation results of the proposed train-to-train communication model are listed below, and as a contrast, the BER of the two-train direct communication on the same track without multihop is also presented.

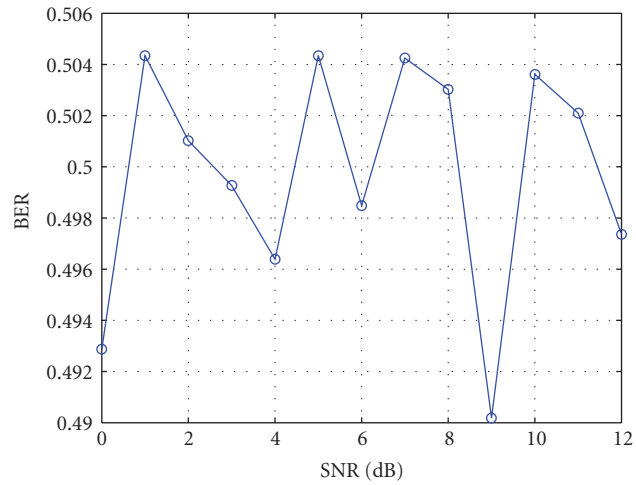

Figure 6: BER of two-train direct communication on the same track without multihop and cooperation.

In Figure 6, two trains on the same track communicate with each other directly without any help from other trains. In this situation, we can see the BER fluctuates around 0.5, which does not ensure messages are transmitted correctly and may easily result in a severe railway traffic accident. This simulation result shows that it is necessary to introduce some trains as relays to help source trains propagate messages to destination trains.

Figure 7 presents the BER performance of train-to-train communication model under Case I, Case II, and Case III with SNR from 0 dB to 12 dB. From Figure 7, Case II has better performance than Case I and Case III at a low SNR. When the SNR is above 4 dB, the performance of Case II is comparable to that of Case III, but is much better than Case III until SNR = 8 dB. It can be concluded that at a low SNR the possible relay $R1$ and $R2$ are able to ensure accurate transmission of the control and prewarning messages.

From the derivation above, the BERs $P_{e,\mathrm{II}}$, $P_{e,\mathrm{I}}$, and $P_{e,\mathrm{III}}$ of Case I, Case II, and Case III are written as

$$\begin{aligned} P_{e,\mathrm{I}} = \sum_{m=t+1}^{n} C_n^m &\left(Q\left(\sqrt{2\Upsilon_{R1}}\right) + Q\left(\sqrt{2\Upsilon_D}\right)\right. \\ &\left. -2Q\left(\sqrt{2\Upsilon_{R1}}\right)Q\left(\sqrt{2\Upsilon_D}\right)\right)^m \\ &\times\left(1 - Q\left(\sqrt{2\Upsilon_{R1}}\right) + Q\left(\sqrt{2\Upsilon_D}\right)\right. \\ &\left. -2Q\left(\sqrt{2\Upsilon_{R1}}\right)Q\left(\sqrt{2\Upsilon_D}\right)\right)^{n-m}, \end{aligned}$$

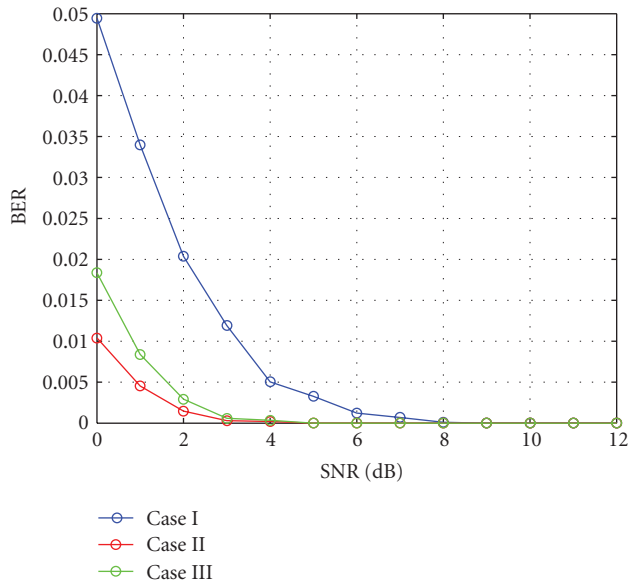

Figure 7: BER of Case I, Case II, and Case III of train-to-train communication model.

$$P_{e,\mathrm{II}} = \sum_{m=t+1}^{n} C_n^m \left(\left(1 - Q\left(\sqrt{\Upsilon_{R2}}\right)\right) Q\left(\sqrt{\Upsilon_{R1} + \Upsilon_{R2}}\right) + Q\left(\sqrt{\frac{(\Upsilon_{R1} - \Upsilon_{R2})^2}{\Upsilon_{R1} + \Upsilon_{R2}}}\right) Q\left(\sqrt{\Upsilon_{R2}}\right)\right)^m \times \left(1 - \left(1 - Q\left(\sqrt{\Upsilon_{R2}}\right)\right) Q\left(\sqrt{\Upsilon_{R1} + \Upsilon_{R2}}\right) + Q\left(\sqrt{\frac{(\Upsilon_{R1} - \Upsilon_{R2})^2}{\Upsilon_{R1} + \Upsilon_{R2}}}\right) Q\left(\sqrt{\Upsilon_{R2}}\right)\right)^{n-m},$$

$$P_{e,\mathrm{III}} = \sum_{m=t+1}^{n} C_n^m \left(\left(1 - Q\left(\sqrt{\Upsilon_{R3}}\right)\right) Q\left(\sqrt{\Upsilon_{R1,R2} + \Upsilon_{R3}}\right) + Q\left(\sqrt{\frac{(\Upsilon_{R1,R2} - \Upsilon_{R3})^2}{\Upsilon_{R1,R2} + \Upsilon_{R3}}}\right) Q\left(\sqrt{\Upsilon_{R3}}\right)\right)^m \times \left(1 - \left(1 - Q\left(\sqrt{\Upsilon_{R3}}\right)\right) Q\left(\sqrt{\Upsilon_{R1,R2} + \Upsilon_{R3}}\right) + Q\left(\sqrt{\frac{(\Upsilon_{R1,R2} - \Upsilon_{R3})^2}{\Upsilon_{R1,R2} + \Upsilon_{R3}}}\right) Q\left(\sqrt{\Upsilon_{R3}}\right)\right)^{n-m}. \tag{24}$$

Supposing SNR = 10 dB, the theoretical value of the BERs under Case I, Case II, and Case III all approach zero, which corresponds to the simulation result in Figure 6.

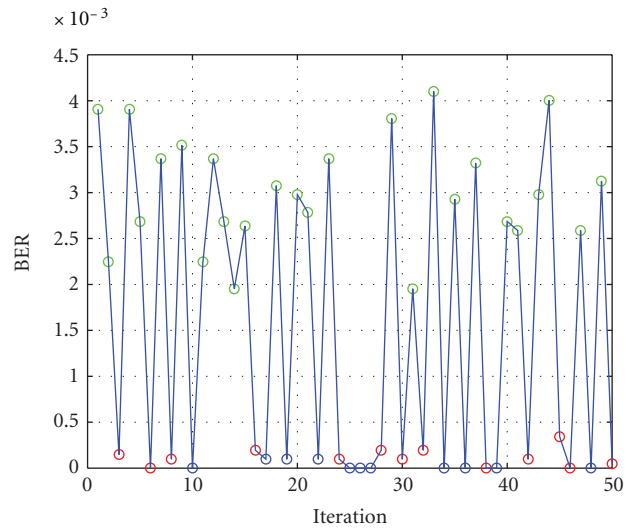

Figure 8: BER of train-to-train communication model SNR = 5 dB based on the Poisson process.

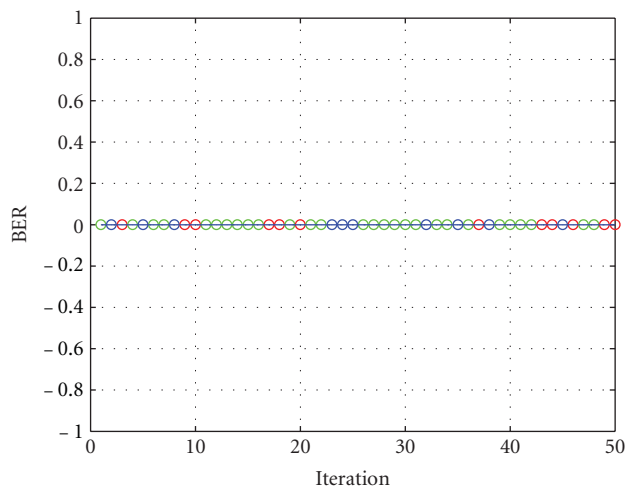

Figure 9: BER of train-to-train communication model at at SNR = 10 dB based on the Poisson process.

Figures 8 and 9 describe the BER performance of the train-to-train communication model based on the Poisson process when SNR = 5 dB and 10 dB. Using the Monte Carlo method, the simulation is repeated 50 times. At each time, the topology of possibly-occurring relays is different. In these figures, the blue dots represent Case I, while the red and green dots represent Case II and Case III, respectively. At SNR = 0 dB, the BERs of Case I, Case II, and Case III are all maintained at about 10^{-2}. At SNR = 5 dB, the BER of Case I declines to 10^{-3}, and particularly the BERs of Case II and Case III reach 10^{-4}. When SNR = 10 dB, the BER is basically maintained at 0 in 50 Monte Carlo simulations. It is proved that at SNR = 10 dB the reliability of the train-to-train communication model is sufficient to satisfy the needs of safety of the high-speed railway.

According to the analysis above, the train-to-train communication has some advantages over the GSM-R and RCAS

Table 2: Comparison of technique index of the GSM-R, RCAS, and train-to-train in physical layer.

Technique index	GSM-R	RCAS	Train-to-Train
Bandwidth (MHz/W)	10^{-2}	10	0.067
Minimum receiving SNR (dB/MHz/W)	3.32	2.5	0.66
Average BER (/MHz/W)	$2.5 * 10^{-6}$	10^{-4}	$7.4 * 10^{-8}$
Transmit power (W/MHz)	40	0.1	13.59
Coverage area (Km)	3	5	6
Minimum delay (s)	1	\	10
Frequency (MHz)	900	460	300

in the physical layer, such as minimum receiving SNR, average BER, and coverage area, which are listed in Table 2 [4–7, 18].

Admittedly, the minimum time delay of the train-to-train communication model is longer than that of the GSM-R. The minimum time delay of train-to-train communication model is 10 s. However, as a subsidiary role, the duty of the train-to-train communication model is to transmit the prewarning messages accurately when the existing train control system is malfunctioning. Once the front train is stopping on the rail track because of an accident, after 10 s' message transmit delay, the remaining distance S between neighboring trains on the same rail track can be calculated as

$$S = 10\,\text{Km} - \left(360\,\text{Km/h} * \frac{10\,\text{s}}{3600}\right) = 9\,\text{Km}. \tag{25}$$

The braking distance of a high-speed train is about 5 km at the speed of 300 km/h [20]. As seen from (25), the remaining 9 km is sufficient for the drivers to decide how to deal with the emergency. That is, the time delay of 10 s absolutely does not affect the following processes and reaction to the prewarning messages of the following trains on the same track.

7. Conclusion

This paper proposes a novel multihop train-to-train communication model using 300 MHz based on the Poisson process in the scenario of a high-speed railway, introducing OFDM and MIMO. The BER of the train-to-train model is decreased to 10^{-6} when SNR is 10 dB, and the minimum receiving level of this model is -84 dBm corresponding to the standards established by UIC in a high-speed railway scenario. In contrast to the GSM-R and RCAS, the train-to-train communication model has advantages in minimum receiving SNR, average BER, and coverage area in the physical layer, which ensures accurate transmission of the control and prewarning messages.

Acknowledgments

This research was supported by the Program for New Century Excellent Talents in University under Grant no. NCET-09-0206, Fundamental Research Funds for the Central Universities under Grant no. 2010JBZ008 and no. 2011YJS010, Key Project of State Key Lab under Grant no. RCS2011ZZ008, National Natural Science Foundation of China under Grant no. 60830001, Beijing Natural Science Foundation under Grant no. 4112048, and Program for Changjiang Scholars and Innovative Research Team in University under Grant no. IRT0949.

References

[1] P. Y. Liu, B. Ai, and Z. D. Zhong, "A message broadcast model for train-to-train communication network," *Information-An International Interdisciplinary Journal*. In press.

[2] "Accidents in Deciding Frequency by Cause," http://safetydata.fra.dot.gov/officeofsafety/publicsite/Query/inctally1.aspx.

[3] C. R. Garcia, A. Lehner, and T. Strang, "A broadcast vehicle-to-vehicle communication system in railway environments," in *Proceedings of the 1st Annual International Symposium on Vehicular Computing Systems*, 2008.

[4] T. Strang, M. M. zu Hörste, and X. G. Gu, "A railway collision avoidance system exploiting ad-hoc inter-vehicle communications and GALILEO," in *Proceedings of the 13th World Congress and Exhibition on Intelligent Transportation Systems and Services (ITS '06)*, London, UK, 2006, http://citeseerx.ist.psu.edu/viewdoc/summary?doi=10.1.1.140.4267.

[5] A. Lehner, C. Rico-García, E. Wige, and T. Strang, "A multi-broadcast communication system for high dynamic vehicular ad-hoc networks," in *Proceedings of the International Conference on Ultra Modern Telecommunications and Workshops (ICUMT '09)*, pp. 1–6, October 2009.

[6] C. R. García, A. Lehner, T. Strang, and M. Röckl, "Comparison of collision avoidance systems and applicability to rail transport," in *Proceedings of the 7th International Conference on Intelligent Transport Systems Telecommunications (ITST '07)*, pp. 1–6, June 2007.

[7] C. R. García, A. Lehner, T. Strang, and K. Frank, "Channel model for train to train communication using the 400 MHz band," in *Proceedings of the IEEE 67th Vehicular Technology Conference-Spring (VTC '08)*, pp. 3082–3086, May 2008.

[8] A. Lehner, C. Rico García, T. Strang, and O. Heirich, "Measurement and analysis of the direct train to train propagation channel in the 70 cm UHF-band," in *Proceedings of the 3rd International Workshop on Communication Technologies for Vehicles*, vol. 6569, pp. 45–57, 2011.

[9] P. Zhao, *The Operation and Reorganization of the High Speed Train*, China Railway Publishing House, 2009.

[10] J. M. Zhang and B. M. Han, "Analysis and calculation of the scheduled waiting time for the train route," in *Proceedings of the 4th International Conference on Intelligent Computation Technology and Automation (ICICTA '11)*, vol. 1, pp. 54–58, March 2011.

[11] S. M. Ross, *Stochastic Process*, John Wiley & Sons, New York, NY, USA, 1996.

[12] http://news.xinhuanet.com/fortune/2011-07/01/c_121609685.htm.

[13] K. J. Ray Liu, A. K. Sadek, W. F. Su, and A. Kwasinski, *Cooperative Communications and Networking*, Publishing House of Electronics Industry, 2010.
[14] J. G. Proakis, *Digital Communication*, McGraw–Hill, London, UK.
[15] H. B. Cheng and Y. D. Yao, "Power adaptation for multi-hop networks with end-to-end BER requirements," *IEEE Transactions on Vehicular Technology*, vol. 59, no. 7, pp. 3545–3554, 2010.
[16] M. Patzold, *Mobile Fading Channels*, John Wiley & Sons, New York, NY, USA, 2002.
[17] L. Xiong, X. Lu, Z. Zhong, B. Ai, and M. Zhu, "Simulation on the characteristics of the wireless channel for high-speed railway GSM-R system," *China Railway Science*, vol. 31, no. 5, pp. 84–89, 2010.
[18] GSM-R QoS Working Group, *O-2475 ERTMS/GSM-R Quality of Service Test Specification*, UIC, Paris, Farnce, 2006.
[19] Z. D. Zhong, B. Ai, and Q. Y. Liu, *Applications of Fundamental Theory of Railway Digital Mobile Communication System (GSM)*, TsingHua University Press, 2009.
[20] Z. M. Wu, J. Y. ZUO, and C. Tian, "Discussion on the design parameter of emergency brake distance of high-speed train," *Electric Locomotives & Mass Transit Vehicles*, vol. 32, no. 4, pp. 1–4, 2009.

Hindawi Publishing Corporation
International Journal of Antennas and Propagation
Volume 2012, Article ID 625374, 15 pages
doi:10.1155/2012/625374

Research Article

State Modelling of the Land Mobile Propagation Channel with Multiple Satellites

Daniel Arndt,[1] Alexander Ihlow,[1] Albert Heuberger,[2] and Ernst Eberlein[2]

[1] *Department of Electrical Engineering and Information Technology, Ilmenau University of Technology, 98693 Ilmenau, Germany*
[2] *Communications Department, Fraunhofer Institute for Integrated Circuits (IIS), 91058 Erlangen, Germany*

Correspondence should be addressed to Daniel Arndt, daniel.arndt@tu-ilmenau.de

Received 27 July 2012; Accepted 8 October 2012

Academic Editor: César Briso Rodríguez

We evaluate a new approach for multisatellite state modelling: the Master-Slave approach. By this concept slave satellites are modelled according to an existing master, whereas the correlation between multiple slaves is omitted. Master-Slave is therefore a generic name for a state modelling concept, for which different realisations are possible. As a possible realisation we present the Conditional Assembling Method. For modelling of only two satellites (one master and one slave), the Conditional Assembling Method enables an accurate resimulation of the correlation coefficient between the satellites and the probabilities of single and combined states. Based on this condition, the performance of Master-Slave for three, four, and five satellites is evaluated in terms of state probability modelling. Therefore, the correlation coefficients and the all bad-state probabilities with Master-Slave are compared with the measurements for different elevation angles and azimuth angle separations of the multisatellite system. Master-Slave has a high modelling error in case of small azimuth separation between the slave satellites (except that one slave has a small azimuth separation to the master). Furthermore, a master satellite with a high elevation provides a lower probability error compared to a master with low elevation.

1. Introduction

Satellites play an important role in today's commercial broadcasting systems. In cooperation with terrestrial repeaters they can ensure uninterrupted service of multimedia content (e.g., audio and video streaming) to stationary, portable, and mobile receivers. However, in case of mobile reception fading regularly disrupts the signal transmission due to shadowing or blocking objects between satellite and receiver. To mitigate these fading effects, diversity techniques such as angle diversity (multiple satellites) and time diversity (interleaving) are attractive. For link-level studies of the land mobile satellite (LMS) channel, statistical channel models are frequently used that are able to generate time series of the received fading signal [1–3].

Statistical LMS channel models describe several fading processes of the received signal: slow variations of the signal are caused by obstacles between the satellite and the receiver, which induce varying shadowing conditions of the direct signal component. Fast signal variations are caused by multipath effects due to static or moving scatterers in the vicinity of the mobile terminal. For short time periods these two components (*slow and fast variations*) are usually modelled by a stationary stochastic process, for example, as a Loo-distributed fading signal [1]. For longer time periods the received signal cannot be assumed as stationary. Therefore, statistical LMS channel models describe different receiving states to assess the large dynamic range of the received signal. The states (very slow variations) correspond to slowly varying environmental conditions (e.g., line of trees, buildings, zones with line-of-sight condition) in the transmission path. Figure 1 shows a state-of-the-art LMS narrowband model for single-satellite reception according to Prieto-Cerdeira et al. [4]. It describes two states: a "good" state (corresponding to line-of-sight/light shadowing) and a "bad" state (corresponding to heavy shadowing/blockage). Within the states this model assumes a stationary Loo-distributed fading signal. It includes a slow fading component (lognormal fading) corresponding to varying shadowing conditions of the direct signal and a

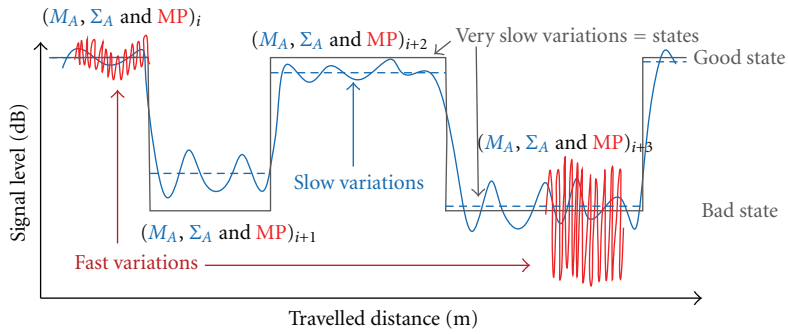

Figure 1: Signal components of a two-state LMS channel model.

fast fading component due to multipath effects. To enable a realistic modelling over the full dynamic range of the received signals, a random set of Loo parameters (M_A, Σ_A, and MP) is generated after each state transition.

Focus of recent activities is the extension of this model for dual-satellite and multisatellite reception. It is realised by introducing correlation between states and between statistical parameters for fast and slow variations. However, the dominating part of the overall signal correlation stems from the state correlation.

Focus of this paper is state sequence modelling for multisatellite systems, assuming two states per satellite: "good" state and "bad" state. For this purpose, a new method for state sequence generation is introduced: the Master-Slave approach. Within Master-Slave it is assumed that each slave satellite depends only on a master satellite, whereas the correlation between different slaves is not described.

The paper is organised as follows: Section 2 gives an overview on state modelling approaches for single- and dual-satellite reception. In Section 3 the concept Master-Slave and a first implementation are introduced. Afterwards, in Section 4 a validation of Master-Slave for multisatellite reception in terms of state probability modelling is presented. Finally in Section 5 the conclusions are drawn.

2. State Modelling for Single-Satellite and Dual-Satellite Reception

In this section available state modelling approaches for single- and dual-satellite reception are summarised.

2.1. Channel State Models for Single-Satellite Systems

2.1.1. First-Order Markov Model. A Markov model is a special random process for generating discrete samples corresponding to channel states s of a predefined sample length. For a first-order Markov model, each state depends only on the previous state. The conditional probabilities of state s_{n+1} given the state s_n are described by state transition probabilities p_{ij}. Therefore, the only parameter of the Markov chain is the state transition probability matrix (STPM) $\mathbf{P}_{\text{trans}} \in \mathbb{R}_{0+}^{N\times N}$ with N being the number of states. The main characteristic of a first-order Markov chain is that it enables an exact modelling of the state probability and the average state duration. The state duration probability density function (SDPDF) of the first-order Markov chain follows an exponential distribution, which is found as not realistic for the LMS channel [5, 6]. The first-order Markov model is used in early LMS models [2, 3].

2.1.2. Semi-Markov Model. To improve the state duration modelling for the LMS channel, semi-Markov chains were proposed in [5]. In contrast to the first-order Markov model, the state transitions do not occur at concrete time intervals. In fact, the time interval of the model staying in state i depends directly on its SDPDF. As with the first-order Markov model, the state transitions are described with the state transition probability p_{ij}, but with $i \neq j$. Assuming a single-satellite model of only two states, the state transition probability is $p_{ij} = 1$. The semi-Markov model allows some options to describe the SDPDF of each state, which defines the number of required parameters for the semi-Markov model. An overview is given in [7].

2.1.3. Dynamic Markov Model. A further method to improve the state duration modelling are dynamic Markov chains introduced in [6]. For dynamic Markov chains the state transition probability depends on the current state duration n with $p_{ij} = f(n)$. Therefore, the two-dimensional STPM is extended to a three-dimensional state transition probability tensor (STPT) $\mathcal{P}_{\text{trans}} \in \mathbb{R}_{0+}^{N\times N\times n_{\max}}$, where $n_{\max}$ corresponds to the maximum state length. The dynamic Markov model enables an exact reproduction of the state probabilities and also an exact remodelling of the measured SDPDF. As a disadvantage, a high number of parameters are required to describe the STPT. Model approximations to reduce the number of parameters are presented in [6].

2.2. Channel State Models for Dual-Satellite Systems

2.2.1. Straightforward Method: Extension to a Multistate Model. The first-order Markov model, semi-Markov model, and the dynamic Markov model can be easily adapted for dual- or multisatellite modelling. This can be achieved by combining the single-satellite states "good" and "bad" from two satellites into joint states: "good good," "good bad," "bad

good," and "bad bad". In case of the first-order Markov model, the 2×2 STPM becomes a 4×4 STPM. For the dynamic Markov model a $4 \times 4 \times n_{\max}$ STPT is required for the state series simulation. In case of the semi-Markov approach a 4×4 STPM and four separate state duration statistics are required for the dual-satellite modelling.

An obvious problem with this straightforward approach is the exponential growth of the number of parameters with the number of satellites. A multisatellite model has N^k combined states with N being the number of states per satellite and k being the number of satellites.

2.2.2. Lutz Model. In [8] a state model for two correlated satellites based on first-order Markov chains was developed. This algorithm is based on first-order Markov chains and generates a joint STPM (4×4 elements) from two independent single-satellite STPMs (each with 2×2 elements), only by the use of one correlation coefficient. Using the joint STPM, a joint sequence of four combined states can be generated. The high flexibility of this algorithm becomes clear, since it requires only single-satellite parameter sets that are easy to derive from measurements and are already available in the literature for different elevation angles and a high number of environments. Databases for correlation coefficients are available as well for different environments, elevation angles, and angular separations of the azimuth and elevation angles. In contrast to this Lutz model, the above mentioned straightforward methods need complete datasets for any combination of elevation angles, azimuth angle separations, and environments to achieve the same variability. The Lutz model accurately resimulates the state probabilities of each single satellite as well as of the combined states. A limitation is that there is no flexibility in describing the state duration distribution. Furthermore, the current approach in [8] is limited to the usage of two satellites with two states per satellite.

3. State Modelling for Multisatellite Reception: The Master-Slave Approach

In general, all state models mentioned in the previous section are extendable to multiple satellites by assuming a multistate model with combined states. However, the number of required parameters for these models grows exponentially with the number of satellites. In practise, already the description of a satellite system with two satellites is challenging [7]. To avoid excessive complexity of a state model parametrisation with more than two satellites, the Master-Slave approach was proposed in [9]. Within the Master-Slave approach it is assumed that each slave satellite depends only on a master satellite, whereas the correlation between the slaves is not described.

Figure 2 demonstrates the Master-Slave approach with four satellites. Within Master-Slave only three satellite links in terms of correlation coefficients are described therefore. A full description of a four-satellite system would require the description of six correlations. In case of k satellites the Master-Slave approach describes $k-1$ satellite links, whereas the full description requires $k \cdot (k-1)/2$ links. As a result, Master-Slave reduces the complexity of a k-satellite model by $2/k$.

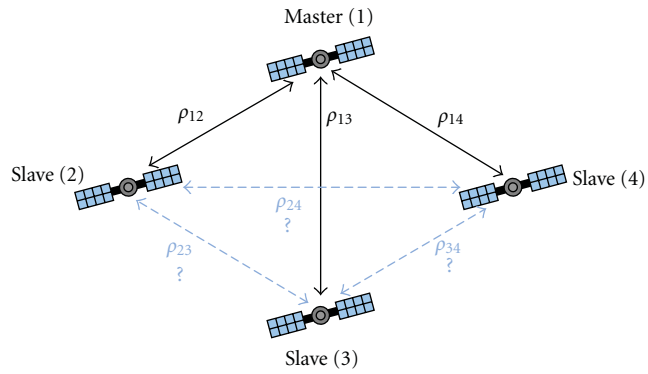

Figure 2: Master-Slave approach for multisatellite modelling. Several slave satellites are modelled according to the correlation to one master satellite, while neglecting the correlation between the slave satellites. The Master-Slave method has a reduced complexity compared to the conventional approach, where each individual correlation is described.

It is not surprising that the missing correlation branches between the slaves could be a reduction of relevant information in case of multisatellite modelling. Therefore, a performance analysis of Master-Slave for multisatellite modelling (with at least three satellites) is found in Section 4. A first realisation of Master-Slave is described in Section 3.1.

3.1. First Realisation of State Modelling with Master-Slave: Conditional Assembling Method. The Master-Slave approach in its simplest form can be reduced to a two-satellite modelling problem, that is, the modelling of the master and one slave. The challenge within Master-Slave is the generation of a slave state sequence based on an existing master state sequence by providing, for example, a certain state probability and a correlation coefficient between the satellites. For this purpose, the conditional state sequences of the slave in case of a constant master state have to be analysed.

According to this condition, various realisations of Master-Slave are possible. Thus, the term Master-Slave describes a concept—not a concrete implementation.

In the following we present one possible realisation of Master-Slave that we define as *Conditional Assembling Method* (cf. Figure 3). For parametrisation, the principle of the Conditional Assembling Method is first to concatenate all parts of the slave state sequence for which the master is in "good" state. Afterwards, this state sequence is parametrised following an arbitrary Markov model (e.g., first-order Markov, semi-Markov). Same procedure is done for the slave state sequence in case master is in "bad" state.

The simulation is done in reversed order. First, the master state sequence is modelled. Second, two conditional slave state sequences with respect to the master state are generated independently (i.e., the conditional slave sequence for master is "good," and the conditional slave sequence for master is "bad"). For master and conditional slave states an arbitrary

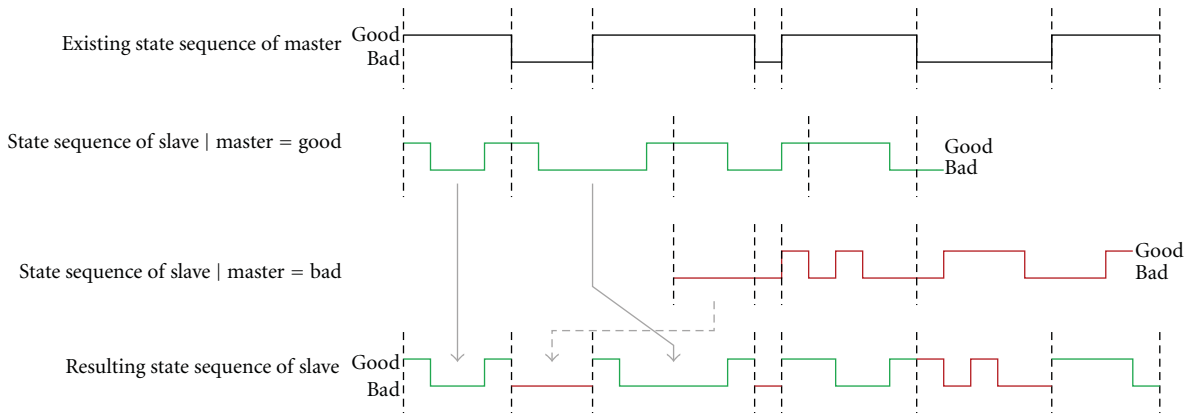

Figure 3: Realisation of Master-Slave with the *Conditional Assembling Method*: Given a master sequence, two independent conditional slave sequences are generated for the cases "master is good" and "master is bad." Different state models (1st-order Markov, semi-Markov, etc.) can be chosen individually therefore. Finally, the slave sequence is composed by piecewise assembling the two conditional sequences according to the master sequence. In this way the correlation coefficient between master and slave, the individual state probabilities, and the combined state probabilities can be accurately described.

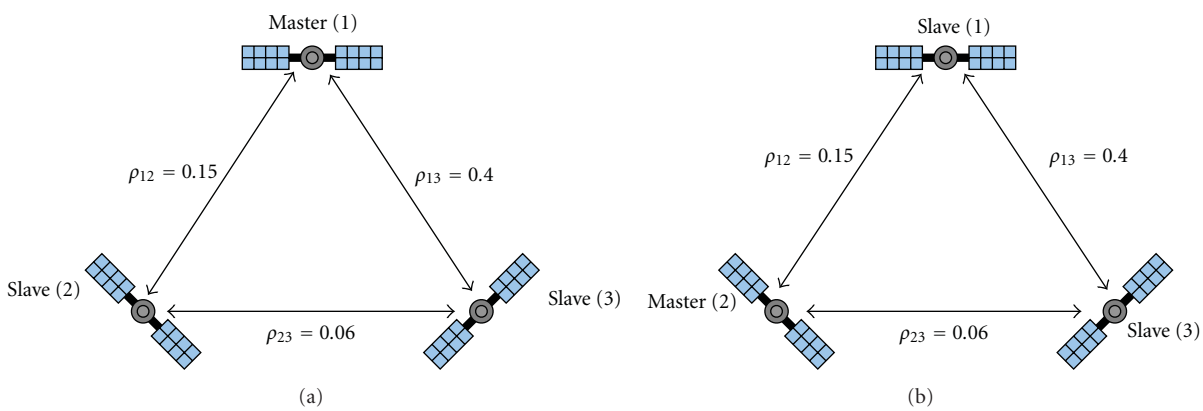

Figure 4: (a) Appropriate mapping of a three-satellite constellation for the Master-Slave approach (Mapping 1)—the correlation between the slaves is low. (b) Inappropriate mapping of the three-satellite constellation (Mapping 2)—the correlation between the slaves is high.

Markov model can be used. The final state sequence of the slave is composed of parts from both conditional sequences according to the current master state. To provide a sample-by-sample generation of the slave state sequence, the current conditional slave state generator is kept in "standby" mode when a state transition of the master is obtained.

In case that the chosen Markov model accurately describes the state probabilities of the master as well as the conditional state probabilities of the slave in case of a constant master state, then the state probabilities of the slave, the joint state probabilities, and the correlation coefficient between the satellites are perfectly remodelled. Furthermore, the state durations of the master sequence can be modelled with arbitrary accuracy (by, e.g., taking a complex model such as dynamic Markov).

However, the Conditional Assembling Method has some limitations in state duration modelling of the combined states ("good good," "good bad," etc.) and of the slave states (cf. Section 4.4).

3.2. Exemplary Evaluation of Master-Slave. To validate the Master-Slave concept for multisatellite reception, Figure 4 shows an exemplary constellation of three satellites including correlation coefficients as obtained during SDARS measurements from the project MiLADY [9, 10]. Since only the correlation between the master and slaves is described, the simulation results depend highly on the definition of the master satellite. For this purpose, in Figure 4 two mappings (Mapping 1 and Mapping 2) are defined by assuming different positions of master and slave satellites. Based on these two definitions, Figure 5 shows the resimulation results for the Master-Slave approach in terms of correlation coefficients, state probabilities, and mean state durations.

In case of Master-Slave the slave satellites are modelled independently. In theory, the correlation coefficient between two independent state sequences is zero. In fact, within Master-Slave the correlation coefficient between the slaves ρ_{slaves} depends on the individual correlation coefficients

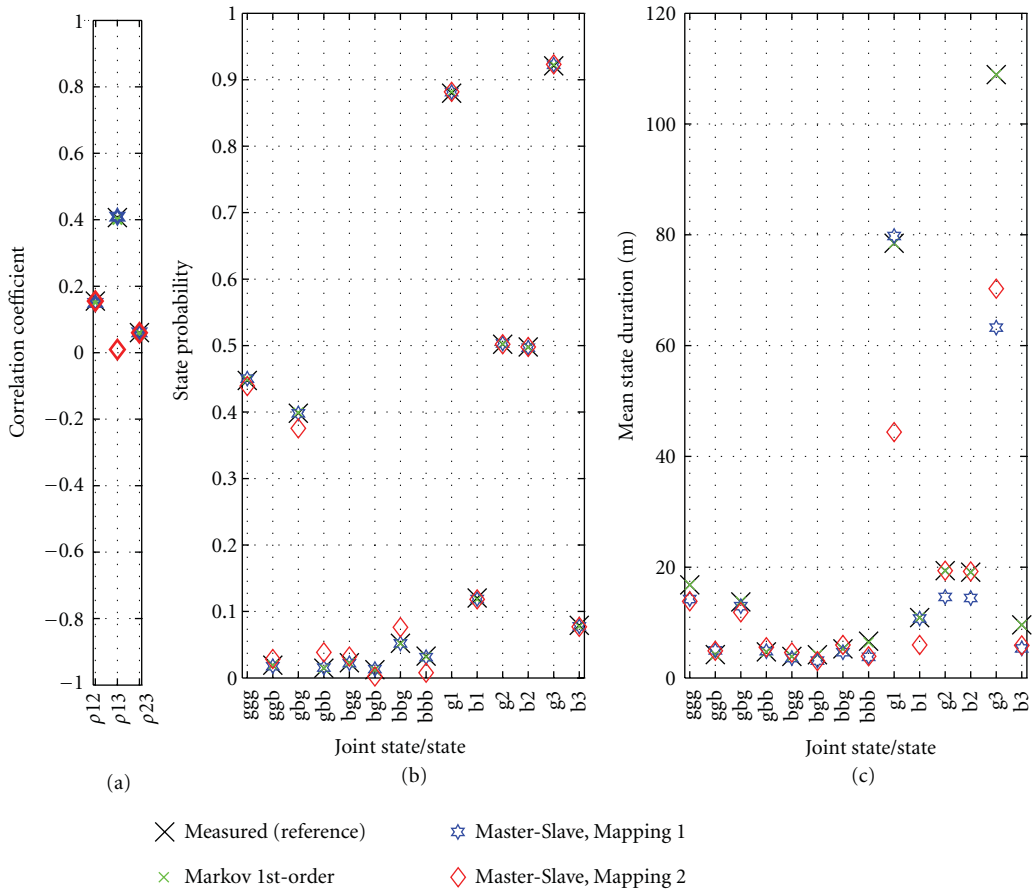

Figure 5: Correlation coefficient (a), state probability (b), and mean state duration (c) for the three-satellite constellation mappings (Mapping 1 and Mapping 2) from Figure 4. Data was taken from measurements of 5.4 km length in a suburban environment. Resimulation gives the following results: clearly, the resulting correlation coefficient between the slave satellites deviates for Mapping 2. The joint state probability is modelled accurately in case of Mapping 1, while Mapping 2 shows deviations. The mean state duration shows deviations in all cases (notation of states: g—"good," b—"bad," ggg—"good good good," etc.).

between master and the slaves (cf. (9) in the appendix). It always holds $|\rho_{\text{slaves, Master-Slave}}| \leq |\rho_{\text{slaves, measured}}|$.

For comparison, the results of a first-order Markov model (using a 8×8 STPM for 8 joint states) are presented. It is obtained that the first-order Markov model enables an accurate description of correlation coefficients between all satellites, of state probabilities, and of average state durations for single satellite states and combined states. The Master-Slave realisation with Conditional Assembling Method in this example is based on the first-order Markov model as well (i.e., both the master state sequence and the conditional state sequences of the slaves are modelled with first-order Markov chains). The result is that for Mapping 1 and Mapping 2 the state probabilities of the individual satellites, the correlation coefficients between master and slaves, and the mean state durations of the master (which has a different position in the examples) are modelled accurately.

Mapping 1 was defined such that the correlation between the slaves is low (with $\rho_{\text{slaves}} = 0.06$). The higher correlation coefficients between master and slaves ($\rho_{12} = 0.15$ and $\rho_{13} = 0.40$) provide some correlation of the slaves as well. In Mapping 1 ρ_{slaves} is remodelled accurately. As a consequence, also the joint state probabilities ("good good good", ...,"bad bad bad") are remodelled accurately.

In Mapping 2 the correlation between the slaves is high (with $\rho_{\text{slaves}} = 0.40$). Due to low correlation coefficients between the master and the slaves ($\rho_{12} = 0.15$ and $\rho_{23} = 0.06$), $\rho_{\text{slaves}} \approx 0$ and deviates strongly from the measurements. As a result, the joint state probabilities are not accurately remodelled. For the application of system planning it should be noted that in case of describing an insufficient correlation a higher diversity gain for the multisatellite constellation will be predicted.

Hence, Mapping 2 suggests a lower probability of the combined state "bad bad bad" than obtained from measurements. Such a modelling error should be avoided. A solution for Master-Slave is an appropriate definition of master and slave satellites. Therefore, in Section 4 the performance of Master-Slave for different positions of master and slaves is evaluated.

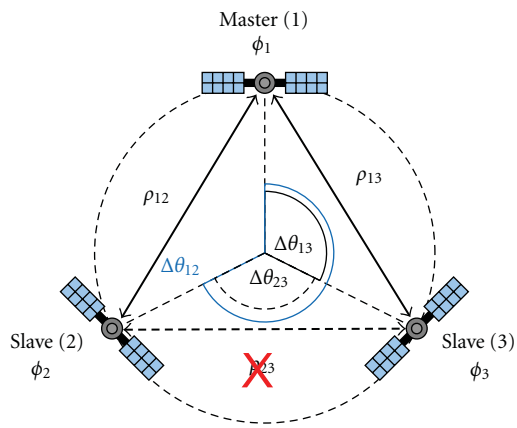

FIGURE 6: Three-satellite constellation for the Master-Slave analysis with elevation angles ϕ, azimuth angle separations $\Delta\theta$, and correlation coefficients ρ.

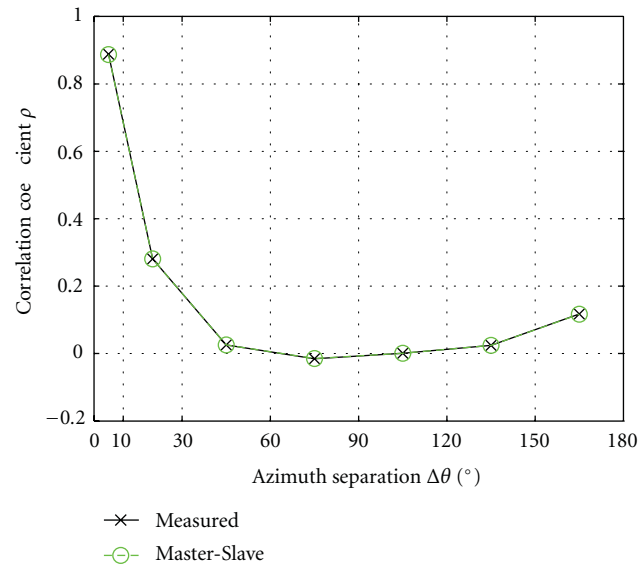

FIGURE 7: State correlation coefficient ρ between two satellites with dependency on the azimuth angle separation $\Delta\theta$ derived from measurements and recalculated with Master-Slave. The Master-Slave approach with Conditional Assembling Method presented in this paper resimulates accurately the correlation coefficients for the two-satellite constellation (master and slave). The elevation angles are $\phi_1 = \phi_2 = 15°$.

4. Validation of State Probability Modelling with Master-Slave

This section will focus on the modelling accuracy when using the Master-Slave approach incorporating three satellites. Quality criterion is the deviation of the joint "bad" state probability (ΔP_{bbb}), depending on the azimuth and elevation constellation. At the end of this section, we will derive constraints for appropriate satellite constellations and how to map them into the Master-Slave context.

4.1. Analysis of a Three-Satellite System. Basis of the analysis is a three-satellite constellation according to Figure 6. In the sequel, the master satellite is always referred to as index 1, while indices 2 and 3 refer to the slaves. The constellation (and the mapping) is described by the elevation angles ϕ_1, ϕ_2, and ϕ_3 and the azimuth angle separations $\Delta\theta_{12}$, $\Delta\theta_{13}$, and $\Delta\theta_{23}$. Following the Master-Slave approach, only the correlations between master and slave are described (ρ_{12} and ρ_{13}), while the correlation between the slaves (ρ_{23}) is neglected. In the following, the consequences of the neglected correlation ρ_{23} are investigated.

4.1.1. Influence of the Azimuth Angle Separation. Figure 7 shows the state-correlation coefficient ρ between two satellites with dependency on their azimuth angle separation $\Delta\theta$. The elevation angles of both satellites are $\phi_1 = \phi_2 = 15°$; the driving direction can be assumed as uniformly distributed between 0 and 360°. These data were derived from analysing dual-satellite constellations of GNSS measurements in urban environments during the project MiLADY and are presented in detail in [7]. It can be observed that low azimuth angle separations lead to a high correlation, while for $\Delta\theta = 45° \cdots 150°$ the satellites are almost uncorrelated. A slight increase of the correlation is obtained for the antipodal constellation ($\Delta\theta \approx 180°$). Due to the uniformly distributed driving direction the graph is symmetrical to $\Delta\theta = 0°$ and $\Delta\theta = 180°$.

Based on these results for the dual-satellite case we now analyse the consequences of neglecting the slave correlation ρ_{23} in the Master-Slave approach. Following the configuration according to Figure 6, we compare ρ_{23} after resimulation using the Master-Slave approach versus the measured results. Figure 8 shows both cases with dependency on each of the azimuth angle separations $\Delta\theta_{12}$, $\Delta\theta_{13}$, and $\Delta\theta_{23}$. The error is given by $\Delta\rho_{23} = |\rho_{23,\,\text{measured}} - \rho_{23,\,\text{Master-Slave}}|$. Clearly, this error is large when the two slaves come close to each other, that is, $\Delta\theta_{12} \approx \Delta\theta_{13}$—except when one slave is close to the master.

Besides correctly remodelling the state correlation, for designing mobile satellite communication systems a very important parameter is the probability of all satellites being in "bad" state, that is, P_{bbb}. It characterises the probability of service unavailability for the entire system and requires special attention, therefore. According to Figure 9, in the measured scenario $P_{\text{bbb}} \approx 0.8$ if all three satellites are colocated, and $P_{\text{bbb}} \approx 0.6$ if two of the three satellites are colocated. Considering the probability error $\Delta P_{\text{bbb}} = |P_{\text{bbb,\,measured}} - P_{\text{bbb,\,Master-Slave}}|$ (the dashed red line in Figure 9) as a quality measure of the modelling approach, we can extend the analysis to further parameters. Therefore, in the next section the elevation-angle dependency is investigated.

For the sake of completeness, we show the consequences when neglecting not only the correlation between the slaves, but neglecting a further correlation as well as neglecting all correlations in the three-satellite system: as can be observed from Figure 10, for azimuth angle separations of $\Delta\theta \leq \approx 30°$

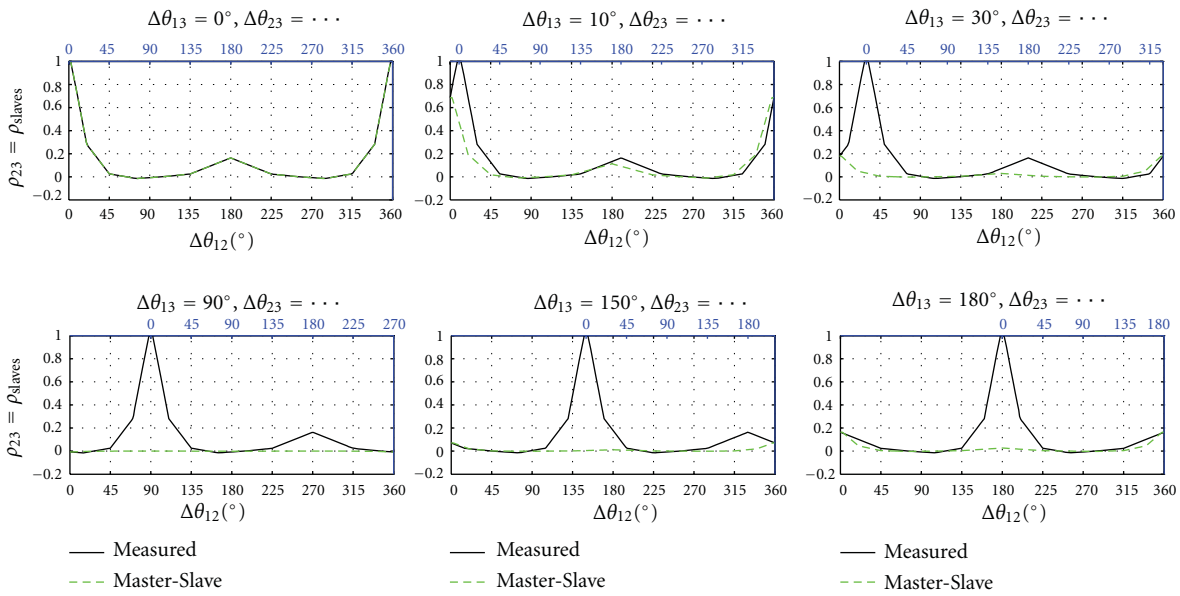

Figure 8: Correlation coefficients between the slaves (ρ_{23}) with dependency on the azimuth angle separations $\Delta\theta_{12}$, $\Delta\theta_{13}$, and $\Delta\theta_{23}$ from measurements and recalculated with Master-Slave. $\Delta\theta_{13}$ is kept constant in each subfigure. The elevation angles are $\phi_1 = \phi_2 = \phi_3 = 15°$.

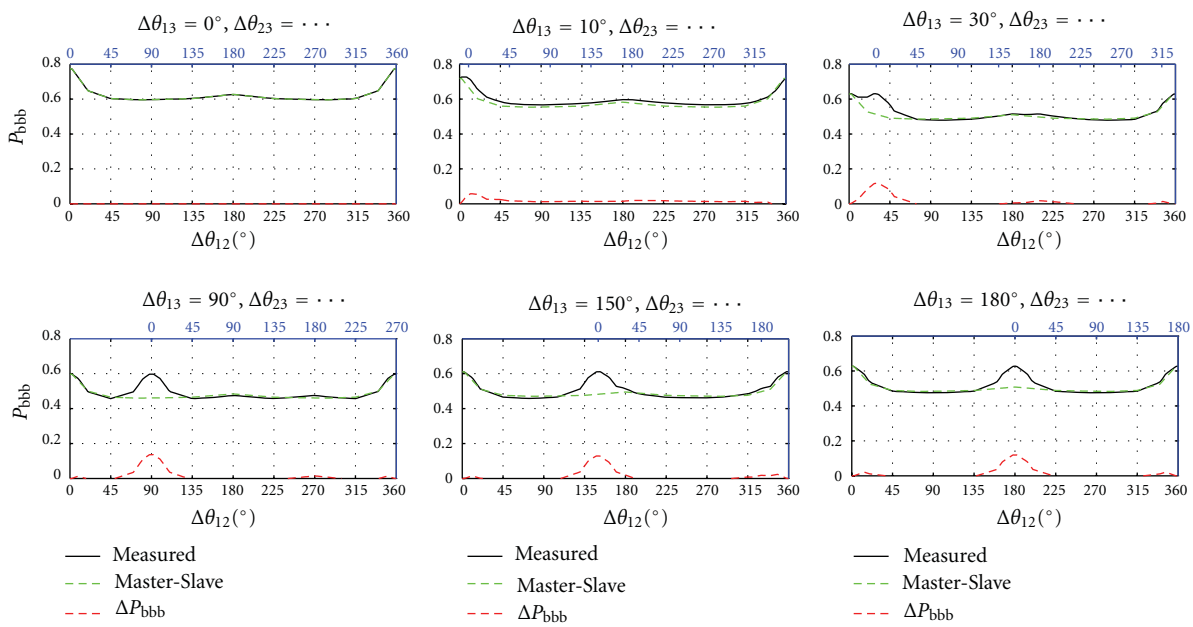

Figure 9: "bad bad bad" state probabilities (P_{bbb}) of three satellites for different azimuth angle separations $\Delta\theta$ from measurements and recalculated with Master-Slave. The elevation angles are $\phi_1 = \phi_2 = \phi_3 = 15°$, where the "bad" state probability of each individual satellite is $P_{\text{b}} = 0.77$.

the correlation cannot be neglected. Furthermore, the correlation should be considered for antipodal constellations, as can be seen for $\Delta P_{\text{bbb, dual-sat + 1 independent}}$.

4.1.2. Influence of the Elevation Angles. Based on the validation of Master-Slave with dependency on the azimuth angle separation, we now incorporate the elevation angles as further variables. The Figures 11 and 12 show the probability error ΔP_{bbb} with Master-Slave with dependency on the azimuth separations $\Delta\theta_{12}$ and $\Delta\theta_{13}$ for different combinations of elevation angles between master, slave satellite 2, and slave satellite 3. Figure 11 shows results with a constant master elevation $\phi_1 = 15°$, Figure 12 for $\phi_1 = 45°$, respectively. The figures include also the results from Figure 10 for the special case $\phi_1 = \phi_2 = \phi_3 = 15°$. Since the slave satellite 2, and slave satellite 3 can be exchanged, only the lower triangle is shown. From Figures 11 and 12 appropriate and inappropriate constellations (and

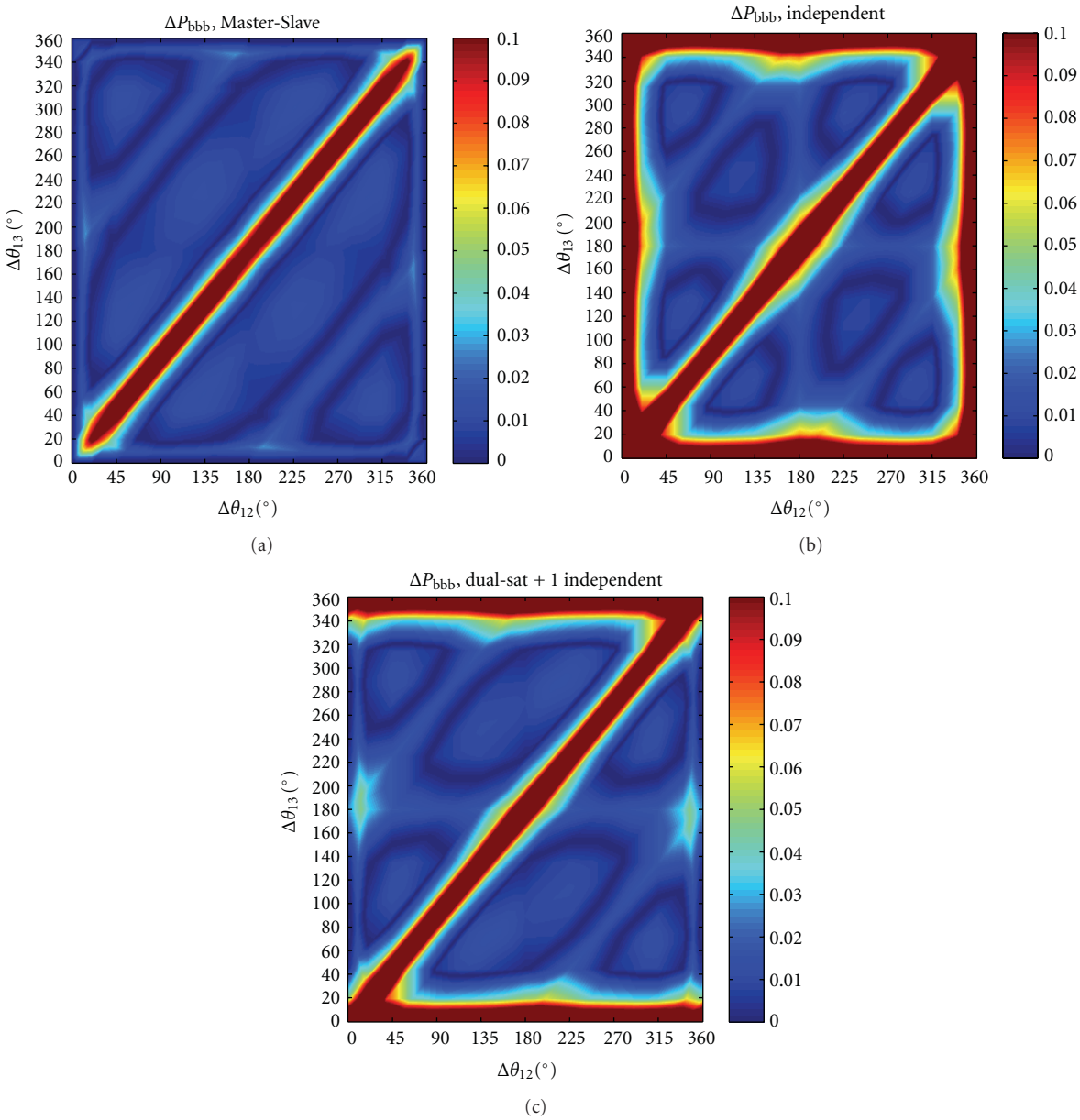

Figure 10: Performance comparison for three-satellite modelling between Master-Slave method (a), independent modelling (b), and a two-satellite model + one independent satellite (c). The figures show the difference between measured and resimulated "bad bad bad" state probability (ΔP_{bbb}) for different azimuth angle separations (θ_{12} and θ_{13}) of two slave satellites. The elevation angles are $\phi_1 = \phi_2 = \phi_3 = 15°$.

mappings) for the three-satellite Master-Slave approach can be determined. The following is obtained.

(i) Assuming constant elevation angles (represented by one subfigure), the error ΔP_{bbb} is maximal for a low azimuth separation between the slaves, while some azimuth separation to the master exists. This error can be avoided by redefinition of the system such that the low azimuth separation is between the master and one of the slaves.

(ii) If one of the slaves has a higher elevation than the master and the second slave (e.g., $\phi_1 > \phi_2$ and ϕ_3), then the error ΔP_{bbb} for low slave separations is reduced with respect to $\phi_1 = \phi_2 = \phi_3$. The reason is that the correlation coefficient and therefore the correlation error between slaves are lower due to the elevation angle separation.

(iii) The error ΔP_{bbb} with Master-Slave is high when both slaves have a higher elevation than the master.

(iv) Comparing Figures 11 and 12, it is obtained that a master with a high elevation has great benefits. For all positions of the slaves the error ΔP_{bbb} for elevation $\phi_1 = 45°$ is much lower than for $\phi_1 = 15°$.

(v) Comparing the constellations $\phi_1 = \phi_2 = \phi_3 = 15°$ and $\phi_1 = \phi_2 = \phi_3 = 45°$ it is seen that

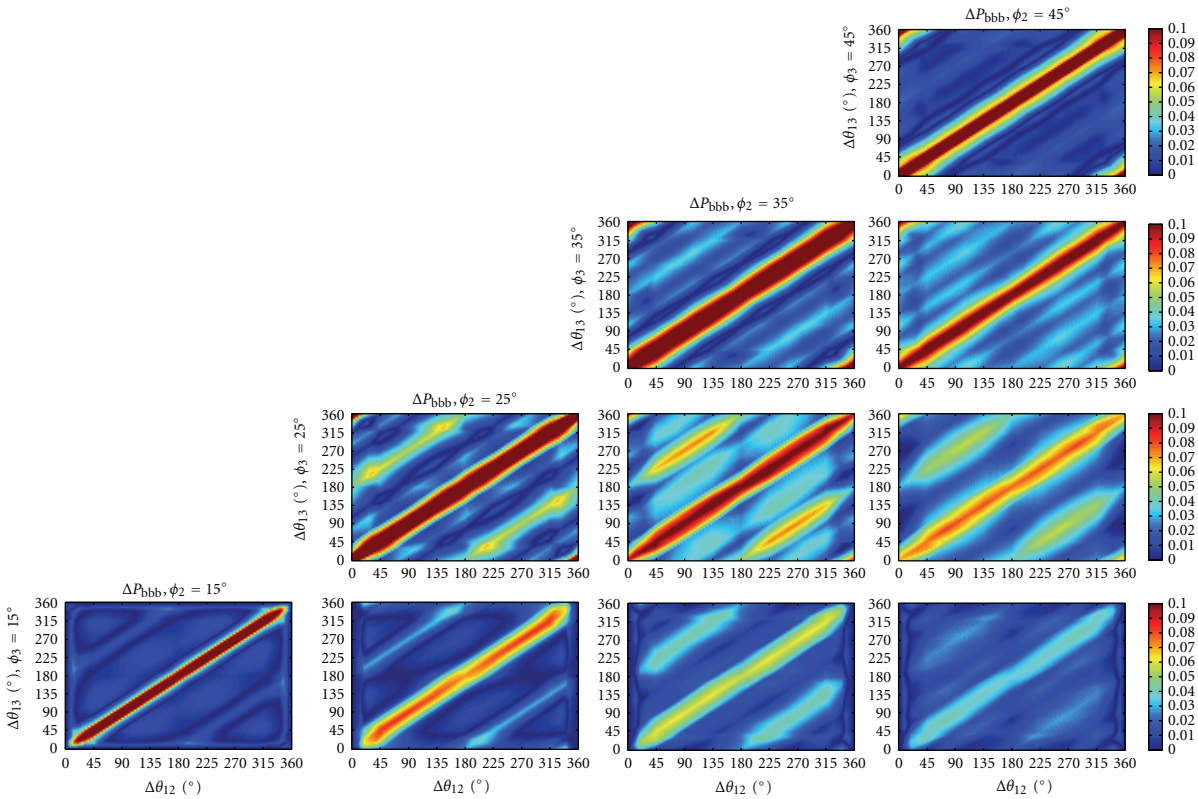

Figure 11: Difference between measured and resimulated "bad bad bad" state probability (ΔP_{bbb}) for different elevation angles (ϕ_2 and ϕ_3) and azimuth angle separations (θ_{12} and θ_{13}) of two slave satellites. The master elevation is constant at $\phi_1 = 15°$.

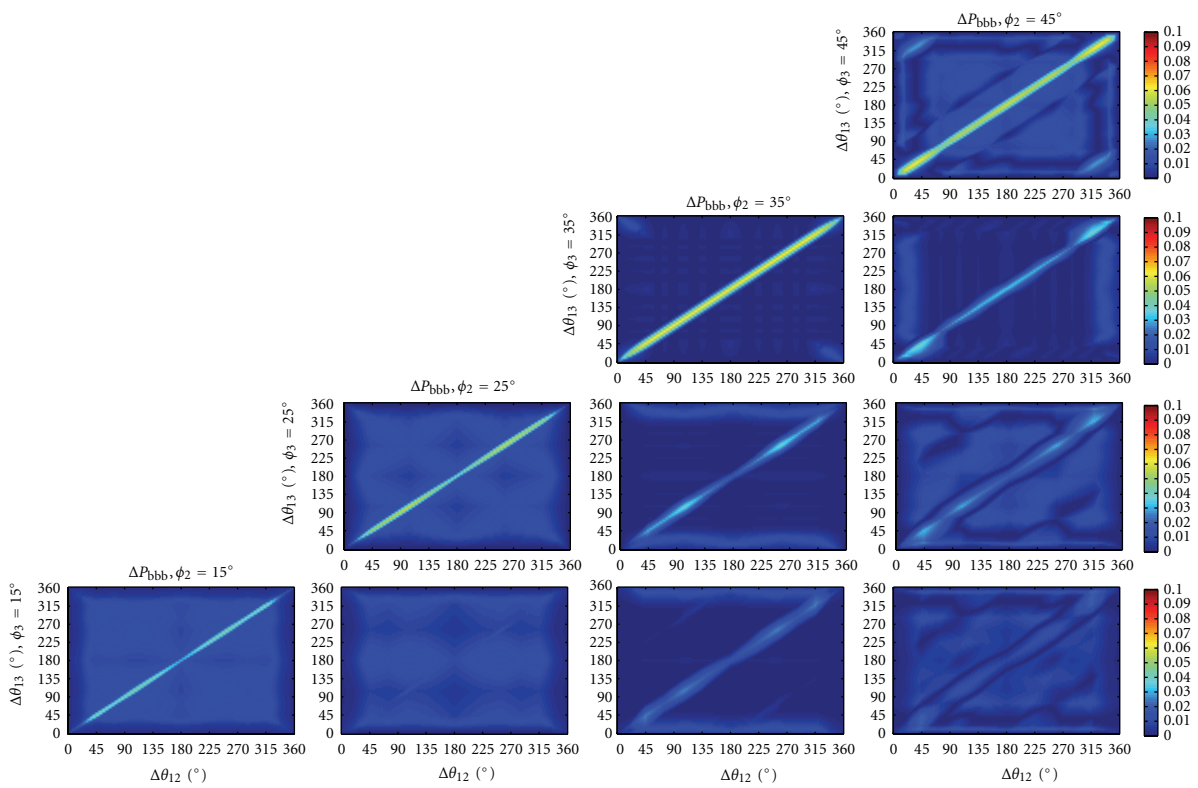

Figure 12: Difference between measured and resimulated "bad bad bad" state probability (ΔP_{bbb}) for different elevation angles (ϕ_2 and ϕ_3) and azimuth angle separations (θ_{12} and θ_{13}) of two slave satellites. The master elevation is constant at $\phi_1 = 45°$.

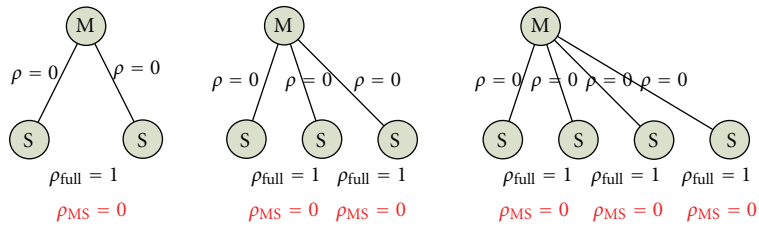

Figure 13: Worst cases for Master-Slave modelling: there is no correlation between master and slave satellites ($\rho = 0$), but full correlation between the slaves ($\rho_{\text{slaves}} = 1$).

the higher elevation angles provide a lower probability error ΔP_{bbb}. It should be noted that the correlation error $\Delta\rho$ in case of some elevation angles is similar. This result is therefore based on the satellite state probabilities, which depends on the current elevation angle. An analysis of the relation between single satellite state probabilities and the probability error with Master-Slave is found in Section 4.2.

(vi) A great performance difference is seen between the constellations $\phi_1 = 15°, \phi_2 = 45°$, and $\phi_3 = 45°$ and $\phi_1 = 45°, \phi_2 = 45°$, and $\phi_3 = 15°$. Although the satellites have the same position on the hemisphere, for the second mapping nearly no limitations of azimuth angle separations are obtained. An examination on the influence of different elevation angles of master and slave satellites is done in Section 4.2.

4.2. Estimation of Worst-Case Probability Error for Master-Slave with Three, Four, and Five Satellites. From the results in the previous section it is known that a high probability error occurs when master and slave satellites are weakly correlated, but the correlation between slaves is high. Worst case would be no correlation between master and slave and full correlation between slaves. Figure 13 shows worst cases for Master-Slave with three, four, and five satellites (please note that $\rho = 1$ between the satellites is not realistic, since different satellites must be exactly colocated therefore) Based on these worst-case constellations, an examination on the probability error $\Delta P_{\text{all bad}}$ (we define $P_{\text{all bad}}$ as the worst reception case of the multisatellite system. It includes P_{bb}, P_{bbb}, and P_{bbbb} for a system with two, three, and four satellites, respectively) for the Master-Slave approach with more than three satellites is possible.

The highest satellite diversity gain ($= P_{\text{b}} - P_{\text{all bad}}$) with a multisatellite system is provided if all satellites are uncorrelated ($\rho = 0$). In this case, the probability of the combined state is the product of the individual state probabilities: $P_{\text{all bad}} = P_{\text{b}}^k$ with k being the number of satellites. In contrast, a multisatellite system has no gain if all satellites are fully correlated ($\rho = 1$). Then it holds $P_{\text{all bad}} = P_{\text{b}}$.

Assuming the constellations in Figure 13 the Master-Slave model would provide uncorrelated slave satellites with $\rho = 0$. As a consequence, the Master-Slave model has k uncorrelated channels and for the combined state results $P_{\text{all bad}} = P_{\text{b}}^k$ (assuming same state probabilities of the individual satellites). In fact, the multisatellite systems in Figure 13 have only two uncorrelated channels. The probability error of Master-Slave is therefore $\Delta P_{\text{all bad}} = P_{\text{b}}^2 - P_{\text{b}}^k$.

Figure 14 shows the worst-case probability error $\Delta P_{\text{all bad}}$ with dependency on the "bad" state probability P_{b} of the individual satellites. It represents that the reception for all satellites have the same elevation. As a general tendency, a reduction of the probability P_{b} (e.g., due to an increased elevation) of the single satellites provides a reduction of $\Delta P_{\text{all bad}}$. This situation was obtained in Figures 11 and 12 between constellations $\phi_1 = \phi_2 = \phi_3 = 15°$ and $\phi_1 = \phi_2 = \phi_3 = 45°$.

Figure 15 evaluates the worst-case probability error $\Delta P_{\text{all bad}}$ for different elevation angles of the master and the slaves. It is seen that a high elevation angle of the master provides a lower error $\Delta P_{\text{all bad}}$.

4.3. Appropriate Constellations for Master-Slave Approach with Three, Four, and Five Satellites. This section concludes appropriate and inappropriate satellite positions for Master-Slave with three satellites and extends it for the multisatellite case.

Figure 16 (left) shows combinations of azimuth separations between master (1) and slave (2) $\Delta\theta_{12}$ and master (1) and slave (3) $\Delta\theta_{13}$ for which the modelling error ΔP_{bbb} exceeds a certain threshold. Assuming that $\Delta P_{\text{bbb}} \leq 0.05$ is an acceptable modelling result, appropriate and inappropriate regions (in terms of $\Delta\theta$) are found therefore for the Master-Slave approach with three satellites.

Concrete examples are given in Figure 16: by defining a certain position of satellite 2 (it has initially no constraints in terms of appropriate positions) the inappropriate azimuth separations for satellite 3 are detected. Figure 17 presents appropriate zones for satellite 3 for predefined positions of satellite 2 in a polar diagram. Given the example in Figure 16, the inappropriate positions of satellite 3 are $\Delta\theta_{13} = \Delta\theta_{12} \pm 20°$—except when satellite 2 is close to the master.

Outgoing from the three-satellite analysis, a quantitative estimation for inappropriate zones for systems with more than three satellites is possible. It is done by decomposing the multisatellite constellation into combinations of each one master and two slaves. For example, from a four-satellite system the combinations master-slave2-slave3, master-slave2-slave4, and master-slave3-slave4 are separately evaluated. The result is that inappropriate positions of each slave depend on the position of another slave. Based on this method,

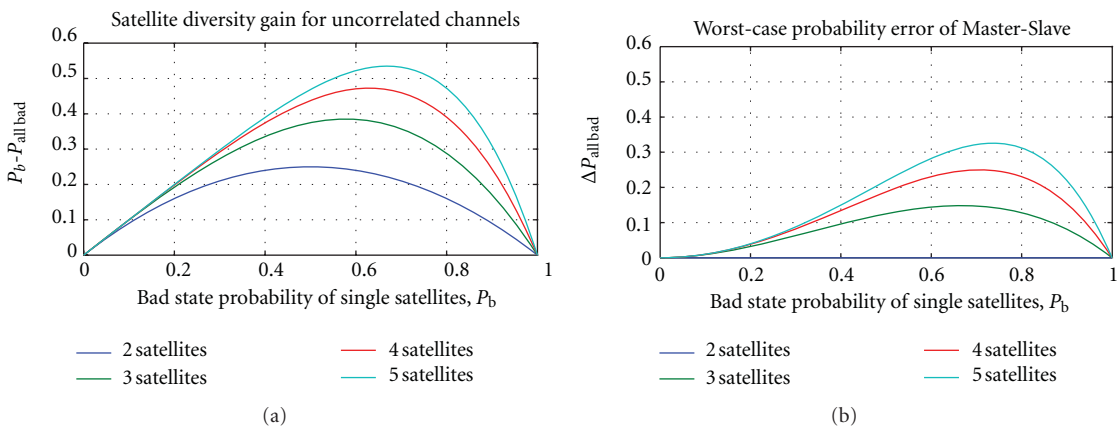

Figure 14: (a) Satellite diversity gain of uncorrelated satellites with dependency on the bad state probability of the individual satellites P_b, and the number of satellites k. It represents the improvement of a system with k uncorrelated channels to a system with one channel. (b) Worst-case probability error of the Master-Slave approach (constellations from Figure 13) with dependency on the bad state probability of the individual satellites, and the number of satellites (it is k uncorrelated channels minus 2 uncorrelated channels).

Figure 15: Worst-case probability error of the Master-Slave approach (constellations from Figure 13) with dependency on the bad state probability of the slave satellites, the number of satellites, and the master probability $P_{b,\text{Master}} = 0.2$ (a) and $P_{b,\text{Master}} = 0.8$ (b). A low bad state probability of the master ($\widehat{=}$ high elevation) is beneficial.

Figure 18 shows exemplary constellations of a four-satellite system with predefined positions of satellites 2 and 3. The result is possible positions of satellite 4, for which the Master-Slave approach provides reliable results. In one of the constellations (third from left) there is no option for satellite 4, since the constellation between S2 and S3 is already inappropriate.

Figure 19 shows constellations of a system with five satellites. Appropriate positions of satellite 5 are resulting from defined positions of satellites 2, 3, and 4.

It can be concluded that with a higher number of satellites the range of appropriate positions decreases.

Please remember that the "inappropriate zones" define only constellations where ΔP_{bbb} is below a certain threshold (0.05 was selected exemplarily). For a system with more than three satellites it means that $\Delta P_{\text{all bad}}$ may not be simulated correctly with Master-Slave. It makes no statement about the absolute error $\Delta P_{\text{all bad}}$. Constellations are even possible where $\Delta P_{\text{all bad}}$ can be neglected, although the Master-Slave constellation was found as inappropriate.

4.4. State Duration Modelling with Master-Slave. In Section 3.1 we presented the Conditional Assembling Method as a first realisation of the Master-Slave approach. It provides an accurate modelling of the state probabilities of the single satellites as well as of the combined satellites for *dual-satellite* reception. However, for the configuration of satellite broadcasting systems with long time interleaving, an accurate modelling of the fading signal over time is crucial.

Figure 20 shows therefore the state duration statistics of the "bad" state from satellite 1 and satellite 2 and of the combined "bad bad" state. The complementary state duration CDFs from measurements are compared with resimulation results of a Master-Slave model and with a dual-satellite semi-Markov model as presented in [7].

It is seen that the Conditional Assembling Method has some limitations for remodelling the duration statistic for the combined "bad bad" state and of the slave satellites' "bad" state. In contrast, the duration statistic of the master satellite can be exactly remodelled by using complex approaches like dynamic Markov chains.

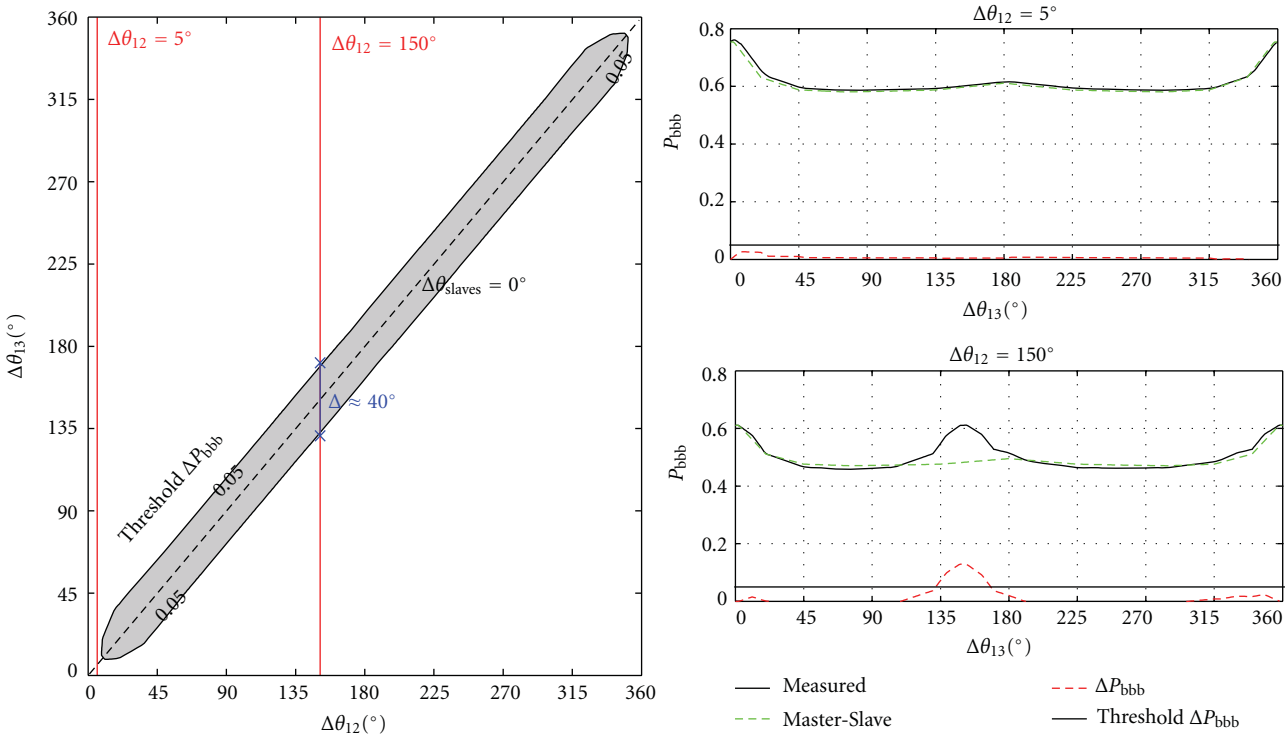

Figure 16: Left: Inappropriate Master-Slave constellations (grey field) with dependency on the azimuth angle separations between master and slaves ($\Delta\theta_{12}$ and $\Delta\theta_{13}$) for $\phi_1 = \phi_2 = \phi_3 = 15°$. They are assumed for $\Delta P_{\text{bbb}} > 0.05$ (cf. Figure 11). Right: Assuming satellite 2 has position $\Delta\theta_{12} = 5°$, then there is no constraint for the position of satellite 3 ($\Delta\theta_{13}$). Assuming satellite 2 has position $\Delta\theta_{12} = 150°$, then satellite 3 with $130° \leq \Delta\theta_{13} \leq 170°$ is inappropriate for Master-Slave.

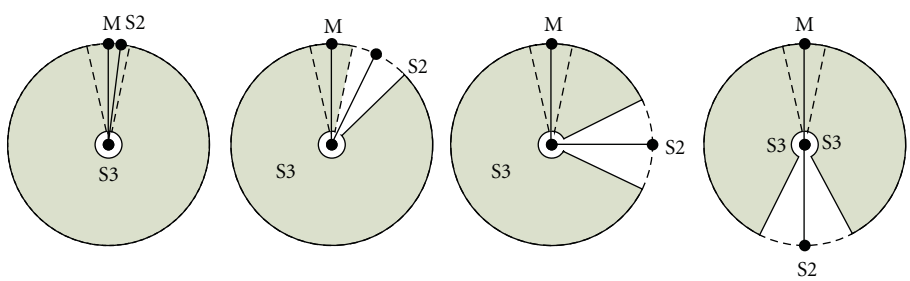

Figure 17: Appropriate constellations of three satellites for the usage of a Master-Slave approach (M—Master, S2, S3—Slaves, with $\phi_{\text{M}} = \phi_2 = \phi_3$). The coloured fields indicate appropriate positions of S3. The inappropriate positions for S3 are $\pm 20°$ around $\Delta\theta_{12}$.

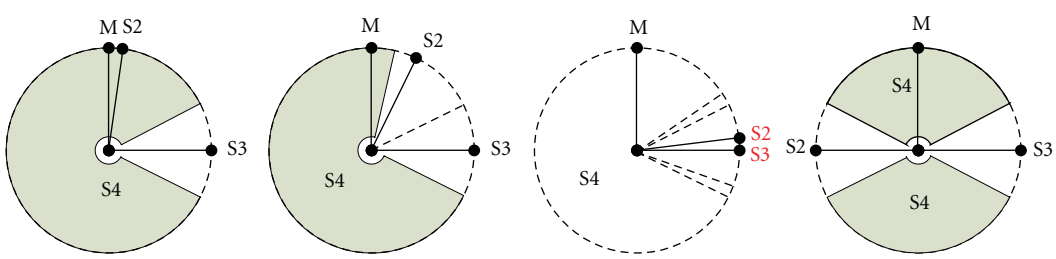

Figure 18: Appropriate constellations of four satellites for the usage of a Master-Slave approach (M—Master, S2,3,4—Slaves, with $\phi_{\text{Master}} = \phi_{\text{slaves}}$). The coloured fields indicate appropriate positions of S4. In the third case there is an inappropriate constellation for Master-Slave, since S2 and S3 are highly correlated.

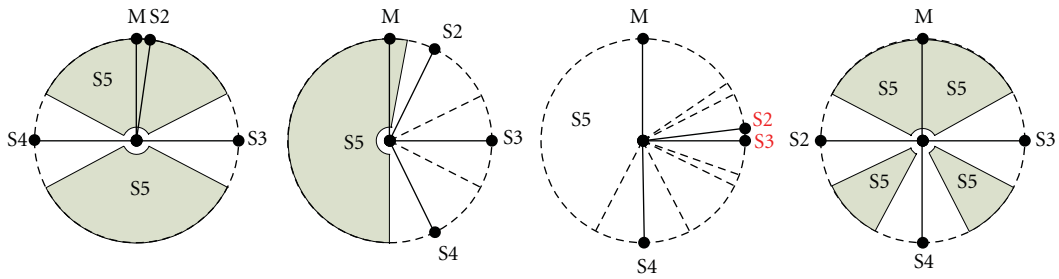

Figure 19: Appropriate constellations of five satellites for the usage of a Master-Slave approach. (M—Master, S2,3,4,5—Slaves, with $\phi_{\text{Master}} = \phi_{\text{slaves}}$). The coloured fields indicate appropriate positions of S5. In the third case there is an inappropriate constellation for Master-Slave, since S2 and S3 are highly correlated.

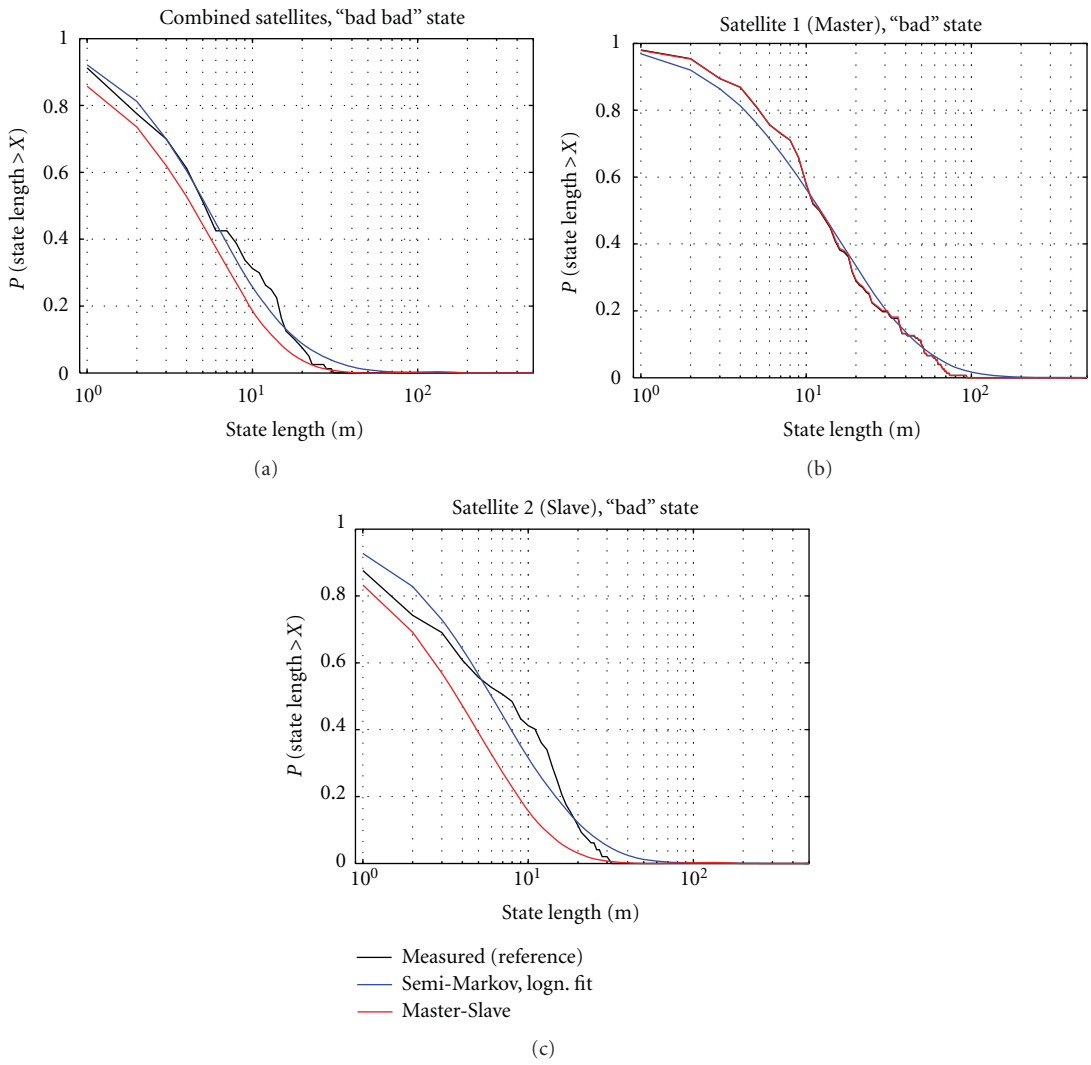

Figure 20: State duration statistics of the combined "bad bad" state (a) and single satellite "bad" states (b and c) derived from the measurements and resimulated with two modelling approaches. The 4-state semi-Markov approach resimulates accurately the state duration statistics. The Master-Slave approach with the "Conditional Assembling Method" resimulates accurately the state durations of the Master satellite but has limitations in duration modelling of the joint states and the slave states.

For comparison, the dual-satellite semi-Markov model with lognormal approximation of the state duration distribution resimulates more accurately the statistics of the slave satellite and of the combined system.

It can be concluded that for state modelling of a dual-satellite system the Master-Slave approach with "Conditional Assembling Method" would not be the first choice.

An extensive validation of different Master-Slave realisations with focus on accurate state duration modelling is therefore the topic of ongoing work.

5. Conclusions

In this paper we presented a new approach for multisatellite state modelling: the Master-Slave approach. The primary concept is that slave satellites are modelled according to an existing master state sequence, whereas the correlation between multiple slaves is omitted. Master-Slave is therefore a generic name for a modelling concept, for which different state models can be applied (such as first-order Markov, semi-Markov, and dynamic Markov models).

As a possible realisation of Master-Slave we described the "Conditional Assembling Method". It enables an *exact* resimulation of the correlation coefficient, the single satellite state probabilities, and the combined state probabilities between one master and one slave.

Based on this result, a detailed performance evaluation of Master-Slave for a three-satellite system is carried out in terms of state probability modelling. Therefore, measured correlation coefficients between the satellites are compared with recalculated correlation coefficients from Master-Slave with dependency on the elevation angles and the azimuth angle separations of the three-satellite system. Afterwards, the probability of the state "bad bad bad" (P_{bbb}) resulting from Master-Slave is compared with analytically estimated values from measurements. The difference for P_{bbb} from Master-Slave and from measurements is defined as probability error. It was obtained that Master-Slave has a high probability error in case of a low azimuth separation and therefore a high correlation between the slave satellites. An exception is when one of the slaves has a high correlation to the master. Furthermore, a master satellite with a high elevation provides a lower probability error compared to a master with low elevation. It can be concluded that a probability error with Master-Slave can be mitigated by appropriate definition of master and slave satellites.

Based on the analysis with three satellites, a performance analysis of Master-Slave is extended for systems with more than three satellites in terms of state probability modelling. Therefore, appropriate and inappropriate constellations of satellites were estimated, and the probability errors for worst-case constellations with Master-Slave were predicted.

In the last part of this paper we indicated that the Master-Slave implementation of this paper (Conditional Assembling Method) has some limitations according to state duration modelling. An evaluation of state duration modelling with Master-Slave is the topic of ongoing research activities. It depends amongst others on the applied state model, such as semi-Markov and dynamic Markov and requires new concepts for the realisation of Master-Slave. However, the elaboration on state probability modelling in this paper is universally valid for Master-Slave.

Appendix

State Probabilities and Correlation Coefficients for the Conditional Assembling Method

The equilibrium state probabilities of the master states and of the conditional slave states are given by

$$\begin{aligned} \mathbf{p}^{\text{Master}} &= \begin{bmatrix} P_{\text{g}}^{\text{M}} & P_{\text{b}}^{\text{M}} \end{bmatrix}^T, \\ \mathbf{p}^{\text{Slave|Master=good}} &= \begin{bmatrix} P_{\text{g|g}}^{\text{S}} & P_{\text{b|g}}^{\text{S}} \end{bmatrix}^T, \\ \mathbf{p}^{\text{Slave|Master=bad}} &= \begin{bmatrix} P_{\text{g|b}}^{\text{S}} & P_{\text{b|b}}^{\text{S}} \end{bmatrix}^T. \end{aligned} \tag{A.1}$$

$P_{i|j}^{\text{S}}$ defines the probability of the slave state i in case of the master state is j.

Calculation of Probabilities for Joint States and Slave States (One Master, One Slave). From the master probabilities and conditional slave probabilities the combined probability vector $\mathbf{p}^{\text{joint}}$ is calculated:

$$\mathbf{p}^{\text{joint}} = \begin{bmatrix} P_{\text{gg}} \\ P_{\text{gb}} \\ P_{\text{bg}} \\ P_{\text{bb}} \end{bmatrix} = \begin{bmatrix} P_{\text{g}}^{\text{M}} \cdot P_{\text{g|g}}^{\text{S}} \\ P_{\text{g}}^{\text{M}} \cdot P_{\text{b|g}}^{\text{S}} \\ P_{\text{b}}^{\text{M}} \cdot P_{\text{g|b}}^{\text{S}} \\ P_{\text{b}}^{\text{M}} \cdot P_{\text{b|b}}^{\text{S}} \end{bmatrix}. \tag{A.2}$$

Based on $\mathbf{p}^{\text{joint}}$ the state probabilities of the slave can be calculated finally:

$$\mathbf{p}^{\text{Slave}} = \begin{bmatrix} P_{\text{g}}^{\text{S}} \\ P_{\text{b}}^{\text{S}} \end{bmatrix} = \begin{bmatrix} P_{\text{gg}} + P_{\text{bg}} \\ P_{\text{gb}} + P_{\text{bb}} \end{bmatrix}. \tag{A.3}$$

Calculation of State Probabilities with One Master and Multiple Slaves. Analogously to the two-satellite case, the combined probability vector $\mathbf{p}^{\text{joint}}$ for multiple satellites (with k satellites) is calculated from the master probabilities and multiple conditional slave probabilities:

$$\mathbf{p}^{\text{joint}} = \begin{bmatrix} P_{\text{ggg..g}} \\ P_{\text{ggg..b}} \\ \cdots \\ P_{\text{gbg..b}} \\ P_{\text{gbb..g}} \\ \cdots \\ P_{\text{bbb..b}} \end{bmatrix} = \begin{bmatrix} P_{\text{g}}^{\text{M}} \cdot P_{\text{g|g}}^{\text{S}(2)} \cdot P_{\text{g|g}}^{\text{S}(3)} \cdot, \ldots, \cdot P_{\text{g|g}}^{\text{S}(k)} \\ P_{\text{g}}^{\text{M}} \cdot P_{\text{g|g}}^{\text{S}(2)} \cdot P_{\text{g|g}}^{\text{S}(3)} \cdot, \ldots, \cdot P_{\text{b|g}}^{\text{S}(k)} \\ \cdots \\ P_{\text{g}}^{\text{M}} \cdot P_{\text{b|g}}^{\text{S}(2)} \cdot P_{\text{g|g}}^{\text{S}(3)} \cdot, \ldots, \cdot P_{\text{b|g}}^{\text{S}(k)} \\ P_{\text{g}}^{\text{M}} \cdot P_{\text{b|g}}^{\text{S}(2)} \cdot P_{\text{b|g}}^{\text{S}(3)} \cdot, \ldots, \cdot P_{\text{g|g}}^{\text{S}(k)} \\ \cdots \\ P_{\text{b}}^{\text{M}} \cdot P_{\text{b|b}}^{\text{S}(2)} \cdot P_{\text{b|b}}^{\text{S}(3)} \cdot, \ldots, \cdot P_{\text{g|b}}^{\text{S}(k)} \end{bmatrix}. \tag{A.4}$$

Correlation Coefficient between Master and Slave. Since only two states per satellite are assumed, the phi coefficient ϕ [11]

is used to describe the correlation coefficient between two satellites:

$$\phi = \frac{n_{11} \cdot n_{22} - n_{12} \cdot n_{21}}{\sqrt{(n_{1X})(n_{2X})(n_{X1})(n_{X2})}}. \tag{A.5}$$

n_{ij} is the number of samples where sequence 1 has state i and sequence 2 has state j. For state modelling this formula can be adapted by using the joint state probabilities of two satellites:

$$\rho_{\text{states}} = \frac{P_{\text{gg}} \cdot P_{\text{bb}} - P_{\text{gb}} \cdot P_{\text{bg}}}{\sqrt{\left(P_{\text{gg}} + P_{\text{gb}}\right)\left(P_{\text{bb}} + P_{\text{bg}}\right)\left(P_{\text{gg}} + P_{\text{bg}}\right)\left(P_{\text{bb}} + P_{\text{gb}}\right)}}. \tag{A.6}$$

Correlation Coefficient between Two Slaves. The correlation coefficient between the slaves depends on the combined state probabilities P'_{ij} of the slaves:

$$\rho_{\text{states, Slaves}} = \frac{P'_{\text{gg}} \cdot P'_{\text{bb}} - P'_{\text{gb}} \cdot P'_{\text{bg}}}{\sqrt{\left(P'_{\text{gg}} + P'_{\text{gb}}\right)\left(P'_{\text{bb}} + P'_{\text{bg}}\right)\left(P'_{\text{gg}} + P'_{\text{bg}}\right)\left(P'_{\text{bb}} + P'_{\text{gb}}\right)}}. \tag{A.7}$$

The combined state probabilities P'_{ij} of the slaves can be calculated from the joint state probabilities of the whole system Master (1)-Slave (2)-Slave (3). According to (A.4) it holds:

$$\mathbf{p}^{\text{joint(Slave2, Slave3)}} = \begin{bmatrix} P'_{\text{gg}} \\ P'_{\text{gb}} \\ P'_{\text{bg}} \\ P'_{\text{bb}} \end{bmatrix} = \begin{bmatrix} P_{\text{ggg}} + P_{\text{bgg}} \\ P_{\text{ggb}} + P_{\text{bgb}} \\ P_{\text{gbg}} + P_{\text{bbg}} \\ P_{\text{gbb}} + P_{\text{bbb}} \end{bmatrix}$$

$$= \begin{bmatrix} P^{\text{M}}_{\text{g}} \cdot P^{\text{S(2)}}_{\text{g|g}} \cdot P^{\text{S(3)}}_{\text{g|g}} + P^{\text{M}}_{\text{b}} \cdot P^{\text{S(2)}}_{\text{g|b}} \cdot P^{\text{S(3)}}_{\text{g|b}} \\ P^{\text{M}}_{\text{g}} \cdot P^{\text{S(2)}}_{\text{g|g}} \cdot P^{\text{S(3)}}_{\text{b|g}} + P^{\text{M}}_{\text{b}} \cdot P^{\text{S(2)}}_{\text{g|b}} \cdot P^{\text{S(3)}}_{\text{b|b}} \\ P^{\text{M}}_{\text{g}} \cdot P^{\text{S(2)}}_{\text{b|g}} \cdot P^{\text{S(3)}}_{\text{g|g}} + P^{\text{M}}_{\text{b}} \cdot P^{\text{S(2)}}_{\text{b|b}} \cdot P^{\text{S(3)}}_{\text{g|b}} \\ P^{\text{M}}_{\text{g}} \cdot P^{\text{S(2)}}_{\text{b|g}} \cdot P^{\text{S(3)}}_{\text{b|g}} + P^{\text{M}}_{\text{b}} \cdot P^{\text{S(2)}}_{\text{b|b}} \cdot P^{\text{S(3)}}_{\text{b|b}} \end{bmatrix}. \tag{A.8}$$

By inserting (A.8) in (A.7) the correlation coefficient between the slaves $\rho_{\text{states, Slaves}}$ can be described as a function of the correlation coefficients between master and slave (2) and master and slave (3):

$$\rho_{\text{states, Slaves}} = \rho_{\text{states, Master, Slave2}} \cdot \rho_{\text{states, Master, Slave3}}. \tag{A.9}$$

Conflict of Interests

The authors declare that they have no conflict of interests.

Acknowledgments

The state analysis in this paper is based on measurement data from the project MiLADY [9]. This project was funded by the ARTES 5.1 Programme of the Telecommunications and Integrated Applications Directorate of the European Space Agency.

References

[1] C. Loo, "A statistical model for a land mobile satellite link," in *Proceedings of the International Conference on Communications (ICC '84)*, vol. 2 of *Links for the future: Science, systems and services for communications*, pp. 588–594, 1984.

[2] E. Lutz, D. Cygan, M. Dippold, F. Dolainsky, and W. Papke, "The land mobile satellite communication channel—recording, statistics, and channel model," *IEEE Transactions on Vehicular Technology*, vol. 40, no. 2, pp. 375–386, 1991.

[3] F. P. Fontán, M. Vázquez-Castro, C. E. Cabado, J. P. García, and E. Kubista, "Statistical modeling of the LMS channel," *IEEE Transactions on Vehicular Technology*, vol. 50, no. 6, pp. 1549–1567, 2001.

[4] R. Prieto-Cerdeira, F. Pérez-Fontán, P. Burzigotti, A. Bolea-Alama∼nac, and I. Sanchez-Lago :, "Versatile two-state land mobile satellite channel model with first application to DVB-SH analysis," *International Journal of Satellite Communications and Networking*, vol. 28, pp. 291–315, 2010.

[5] L. E. Bråten and T. Tjelta, "Semi-Markov multistate modeling of the land mobile propagation channel for geostationary satellites," *IEEE Transactions on Antennas and Propagation*, vol. 50, no. 12, pp. 1795–1802, 2002.

[6] M. Milojević, M. Haardt, E. Eberlein, and A. Heuberger, "Channel modeling for multiple satellite broadcasting systems," *IEEE Transactions on Broadcasting*, vol. 55, no. 4, pp. 705–718, 2009.

[7] D. Arndt, A. Ihlow, T. Heyn, A. Heuberger, R. Prieto-Cerdeira, and E. Eberlein, "State modelling of the land mobile propagation channel for dual-satellite systems," *EURASIP Journal on Wireless Communications and Networking*, vol. 2012, article 228, 2012.

[8] E. Lutz, "A Markov model for correlated land mobile satellite channels," *International Journal of Satellite Communications*, vol. 14, no. 4, pp. 333–339, 1996.

[9] E. Eberlein, A. Heuberger, and T. Heyn :, "Channel models for systems with angle diversity—the MiLADY project," in *Proceedings of the ESA Workshop on Radiowave Propagation Models, Tools and Data for Space Systems*, Noordwijk, the Netherlands, 2008.

[10] T. Heyn, E. Eberlein, D. Arndt et al., "Mobile satellite channel with angle diversity: the MiLADY project," in *Proceedings of the 4th European Conference on Antennas and Propagation (EuCAP '10)*, Barcelona, Spain, April 2010.

[11] H. Cramer, *Mathematical Methods of Statistics*, Princeton University Press, Princeton, NJ, USA, 1946.

Hindawi Publishing Corporation
International Journal of Antennas and Propagation
Volume 2012, Article ID 862945, 9 pages
doi:10.1155/2012/862945

Research Article

Fading Analysis for the High Speed Railway Viaduct and Terrain Cutting Scenarios

Jinghui Lu, Gang Zhu, and Bo Ai

State Key Laboratory of Rail Traffic Control and Safety, Beijing Jiaotong University, Beijing 100044, China

Correspondence should be addressed to Bo Ai, aibo@ieee.org

Received 27 July 2012; Accepted 12 November 2012

Academic Editor: César Briso Rodríguez

A good understanding of the fading characteristics in high speed railway environment is essential for the design of a high reliable railway wireless network. In this paper, measurements have been taken in both high speed viaduct and terrain cutting scenarios using track side base stations (BSs) of the railway wireless network in China. The measurement sites have been chosen with special care; thus the whole measured route can be characterized either by viaduct or terrain cutting. Kolmogorov-Smirnov (K-S) test has been first introduced in the statistical analysis to find out which is the most appropriate model for the small scale fading envelope. Though both Rice and Nakagami distributions provide a good fit to the first-order envelope data in both scenarios, only the Rice model generally fits the second-order statistics data accurately. For the viaduct scenario, higher Rice K factor can be observed. The change tendency of the K factor as a function of distance in the two scenarios is completely different. It can be concluded that the over bridges which span the railway tracks in terrain cutting scenario would affect the Rice K value severely.

1. Introduction

As an international standard for railway communication and applications, GSM-R (GSM for Railway) has been adopted by China as a wireless communication platform to transfer security data of train control. With the rapid development of high speed railways in China, GSM-R networks have been widely deployed along the railway lines. Since GSM-R aims to transmit security data and information for train control, failure or obstruction of the wireless network will inevitably affect the normal running of the railway system. To provide a safe and reliable network, the design of a railway wireless network is of vital importance. In the meanwhile, appropriate wireless network design and optimization rely heavily on accurate prediction of radio wave propagation.

The propagation environment of the high speed railways is a lot different from the common public wireless network. As indicated in [1], typically a railway track is full of terrain cuttings, tunnels, bridges, and so forth. Track side base stations (BSs) are often used to provide a seamless coverage. Besides, the BS antenna is always much higher than the surrounding environment to insure that there is a line-of-sight (LOS) component between the BS antenna and the train antenna. So far, channel analysis in these special railway environments has attracted more and more research interests. The measured path loss values in viaduct scenarios have been analyzed in [2–4], respectively, and the path loss exponents have been found between 2 and 4. A more general path loss model for viaduct scenarios has been proposed in [5], considering the influences of viaduct height and BS antenna relative height. The Rice K factor in the viaduct and terrain cutting scenarios along the high speed railway was first estimated by a moment-based estimator, which employed the second and the fourth moments of the signal envelope [6]. However, statistical analysis of two moment-based estimators shows that moment-based estimator using the first and second moments of the signal envelope can be a better estimator, as it has better asymptotic performance [7]. And Rice K factor as a function of distance has been studied in [8], which shows the K factor decreases linearly in the distance. However, the estimation interval of the Rice K factors was set to 100 m, which we believe is too large to reflect the fast variation of the K factors.

Besides, though Nakagami distribution has been widely accepted to be a very good fit to mobile radio channel characteristics [9, 10], it has never been studied for the

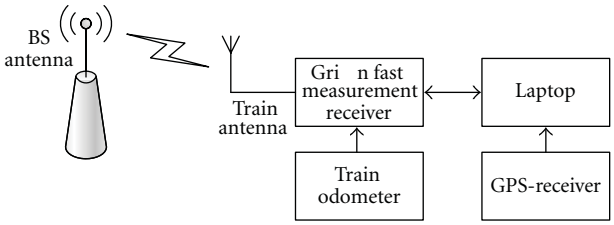

Figure 1: Measurement system.

small scale envelope characteristics in railway scenarios. The objective of this work is to fill this gap by investigating the suitability of Nakagami distribution for describing the small scale fading envelope. Moreover, second-order statistics of the received envelope, such as the level crossing rate (LCR) and average fade duration (AFD), have not been fully investigated. Although recent work compared the measured second-order statistics with the theoretical values of Rayleigh, Rice, and Nakagami models in viaduct scenario [11], no paper has reported the results of terrain cutting scenario. These statistics provide useful information for the statistic analysis of burst errors and the design of error-correcting codes.

This rest of the paper is organized as follows. A brief description of the measurement system and scenarios is given in Section 2. Theoretical models for the small scale fading channel are described in Section 3. Section 4 shows the measurement results of the two scenarios, including the envelope distribution and second-order statistics. Conclusions are drawn in Section 5.

2. Measurement Setup

The narrowband measurements were done along the Zhengzhou-Xi'an high-speed railway of China with a special test system, which can collect signal level data from GSM-R track side BSs. During the measurements, the train was moving at a high speed of about 277–300 km per hour. The measurement system in the train periodically recorded the signal power value every 10 centimeters. Two typical viaduct and terrain cutting scenarios have been selected for analysis. And the measurements have been done twice in two different days to eliminate the effect of the measurement error. The following sections describe the measurement system and the measurement scenarios in greater detail.

2.1. Measurement System. The measurement system shown in Figure 1 consists of a receive antenna mounted on the top of the train, a Willteck 8300 Griffin fast measurement receiver, a train odometer, a global positioning system (GPS) device, and a laptop to record the test data. The measurement receiver operated in the distance trigger mode. So the train odometer was able to send a trigger signal to the receiver at intervals of 10 centimeters. A software installed in the laptop can store the measured data. And geographic location data of the measured samples can be provided by the GPS device. Table 1 shows some measurement parameters of the two scenarios. The transmit antennas are both directional and cross-polarized. The receive antennas are omnidirectional.

Table 1: Measurement parameters.

Parameter	Viaduct	Terrain cutting
Transmit power	40 dBm	40 dBm
Transmit frequency	932.4 MHz	932.8 MHz
Transmit antenna height	23 m	33 m
Transmit antenna gain	17 dB	17 dB
Receive antenna height	3.5 m	3.5 m
Receive antenna gain	0 dB	0 dB
Average train speed	78.9 m/s	82.0 m/s

2.2. Measurement Scenarios. The two chosen scenarios are shown in Figure 2. The viaduct scenario depicted in Figure 2(a) seems a very good propagation environment, as there are few obstacles and scatters. A satellite image of the measured viaduct is also displayed in Figure 2(b), which shows the whole measurement route from BS ZX1706D to BS ZX1705D. During the measurements, BS ZX1706D was transmitting signal. However, the terrain cutting scenario displayed in Figure 2(c) seems more complex for radio wave propagation. Steep slopes on both sides of the railway tracks may block the radio wave or produce multiple reflections. The slopes covered with grass have a height of about 7-8 meters. The degree of inclination is about 70 degree. A satellite image of the measured terrain cutting is also displayed in Figure 2(d). Five over bridges which span the railway tracks can be observed in this figure. These bridges are built to facilitate traffic on the two sides of the terrain cutting. Later the effect of the over bridges on radio propagation will be illustrated. BS ZX1714D was transmitting signal during the test. The whole measurement area from BS ZX1714D to BS 1713D can be characterized by terrain cutting scenario. In both scenarios, the railway tracks are almost straight and the BS antennas are situated 17 and 37 m away from the railway tracks.

3. Theoretical Models

Various theoretical models have been presented to describe the small scale fading behavior of the mobile channel. In this section, both the envelope distribution and second-order statistics of the Rayleigh, Rice, and Nakagami fading models are discussed.

3.1. Envelope Distribution. The Rayleigh probability density function (PDF) is given by [12]

$$p(r) = \frac{r}{\sigma^2} \exp\left(-\frac{r^2}{2\sigma^2}\right) \quad (0 \le r \le \infty). \tag{1}$$

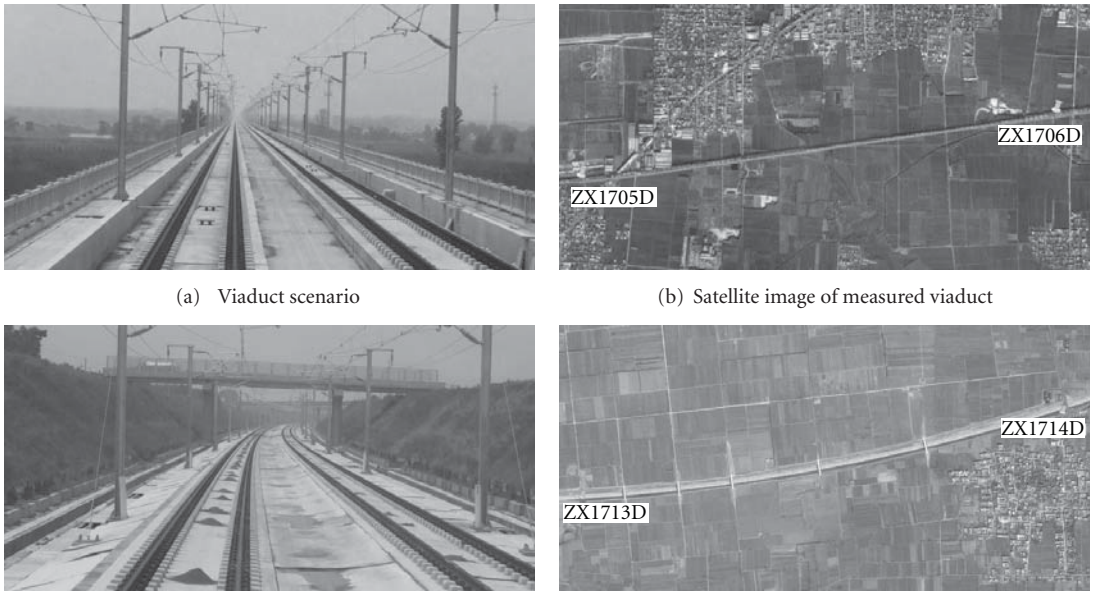

(a) Viaduct scenario (b) Satellite image of measured viaduct

(c) Terrain cutting scenario (d) Satellite image of measured terrain cutting

Figure 2: Measurement scenarios.

And the maximum likelihood estimate of the parameter σ is

$$\sigma_e = \sqrt{\frac{1}{2}E(r^2)}, \tag{2}$$

where $E(r^2)$ is the second moments of the measured samples.

The Rice PDF is expressed as

$$p(r) = \frac{r}{\sigma^2}\exp\left(-\frac{r^2+s^2}{2\sigma^2}\right)I_0\left(\frac{r\cdot s}{\sigma^2}\right) \quad (s \geq 0, r \geq 0), \tag{3}$$

where function I_0 is the modified Bessel function of the first kind and zero-order. The Rice distribution is often described in terms of a parameter K which is defined as the ratio between the direct or strong component power of the signal and the variance of the multipath. It is given by

$$K = \frac{s^2}{2\sigma^2}. \tag{4}$$

The parameter K is known as the Rice factor and completely specifies the Rice distribution. Different methods have been proposed for estimating the Rice K factor. Though the maximum likelihood estimator (MLE) can yield optimal results, it is relatively cumbersome and time consuming [13]. A simple K estimation method based on the moments of the receiver envelope has also been proposed. It has been validated by [7] that moment-based estimator using the first and second moments of the signal envelope has a better asymptotic performance, compared to the one using the second and fourth moments of the envelope. The estimator based on the first and second moments of the signal envelope is used in this paper, though it is a little complex.

The moments of the Rice distribution can be expressed as [7]

$$\begin{aligned}\mu_n &= E[R^n(t)] \\ &= (\sigma^2)^{n/2}\Gamma\left(\frac{n}{2}+1\right)\exp(-K)\,{}_1F_1\left(\frac{n}{2}+1;1;K\right),\end{aligned} \tag{5}$$

where ${}_1F_1(\cdot;\cdot;\cdot)$ is the confluent hypergeometric function, and $\Gamma(\cdot)$ is the gamma function. To derive K, define the following functions of K

$$f_{n,m}(K) = \frac{\mu_n^m}{\mu_m^n} \quad (n \neq m). \tag{6}$$

Since $f_{n,m}(K)$ depends only on K, K can be derived by inverting the corresponding $f_{n,m}(K)$. When $n = 1$ and $m = 2$, (6) can be calculated using (5) as

$$f_{1,2}(K) = \frac{\pi e^{-K}}{4(K+1)}\left[(K+1)I_0\left(\frac{K}{2}\right) + KI_1\left(\frac{K}{2}\right)\right]^2. \tag{7}$$

From (6), $f_{1,2}(K)$ can also be expressed as

$$f_{1,2}(K) = \frac{\mu_1^2}{\mu_2}, \tag{8}$$

where μ_1 and μ_2 can be calculated according to the moments of the measured samples, which can be given by

$$\hat{\mu}_k = \frac{1}{N}\sum_{l=0}^{N-1} R^k(lT_s), \tag{9}$$

where $R(lT_s)$ is the measured envelope value, T_s is the sampling period, and N is the number of available samples. The corresponding estimator $\hat{K}_{1,2}$ can be obtained by combining

(7) and (8). However, this involves the complex numerical procedure of inverting (7). A simple way to solve the problem is to implement a lookup table. To be specific, first create a lookup table by calculating all the $f_{1,2}$ values for a predefined range of K values according to (7). Then compare the $f_{1,2}$ results from (8) with the values stored in the lookup table. At last the K value which gives the least deviation of $f_{1,2}$ is chosen as the estimated K factor.

The Nakagami PDF of the envelope r is given by

$$p(r) = \frac{2m^m r^{2m-1}}{\Gamma(m)\Omega^m} \exp\left(-\frac{mr^2}{\Omega}\right), \tag{10}$$

where m is the Nakagami parameter defined as the ratio between Ω squared and the variance of the envelope squared

$$m = \frac{\Omega^2}{\mathrm{Var}(r^2)} \tag{11}$$

and Ω is the average power, given by

$$\Omega = E[r^2]. \tag{12}$$

The Gamma function is given by

$$\Gamma(m) = \int_0^\infty x^{m-1} \exp(-x)dx. \tag{13}$$

As is generally well accepted, the parameter Ω can be reasonably estimated by

$$\hat{\Omega} = N^{-1} \sum_{i=1}^{N} R_i^2, \tag{14}$$

where N is the number of available samples R_i of the envelope. On the contrary, the shape parameter m can be estimated using different methods. In [14], the performance of the inverse normalized variance, Tolparev-Polyakov, and the Lorenz estimators have been compared through Monte Carlo simulation. And the inverse normalized variance estimator has been proved to be superior to the other two estimators. Thus, it is adopted as the estimator in our paper, which is given by

$$\hat{m} = \frac{\mu_2^2}{\mu_4 - \mu_2^2}. \tag{15}$$

3.2. Second Order Statistics. The LCR of the signal envelope reveals information about how fast the received signal changes with time. It is defined as the average number of times the signal envelope crosses a certain threshold level in a positive-going direction per second. And the AFD is defined as the average time that the fading signal envelope remains below a certain threshold level [15]. Exact formulas for second-order statistics of the Rayleigh, Rice, and Nakagami fading models have been derived in the literature and their fit to the empirical data has also been investigated in various scenarios. It is widely accepted that the goodness of fit for second-order statistics do not appear to be dependent on the accuracy of fit for first-order statistics [16, 17]. As a result, it is essential to compare our measurement results to all of the three theoretical models, which are listed below.

For a fading signal, the LCR expressions for Rayleigh, Rice [18], and Nakagami [19] models are

$$\begin{aligned} N_{\text{Rayleigh}}(\rho) &= \sqrt{2\pi} f_d \rho \exp(-\rho^2) \\ N_{\text{Rice}}(\rho) &= \sqrt{2\pi(K+1)} f_d \rho \exp(-K-(K+1)\rho^2) \\ &\quad \times I_0\left(2\sqrt{K(K+1)}\rho\right) \\ N_{\text{Nakagami}}(\rho) &= \sqrt{2\pi} f_d \frac{m^{m-(1/2)}}{\Gamma(m)} \rho^{2m-1} \exp(-m\rho^2), \end{aligned} \tag{16}$$

where $\rho = R/\sqrt{E[R^2]}$ is the value of the specified level R, normalized to the local rms amplitude of the fading envelope, f_d is the maximum Doppler frequency, which can be calculated by

$$f_d = \frac{v}{\lambda}, \tag{17}$$

where v is the average speed of the mobile, and λ is the wavelength of the carrier signal. And K is the Rice factor, m is the Nakagami parameter. Their values can be estimated from the measured envelope samples.

The AFD formulas for Rayleigh, Rice, and Nakagami models can be expressed as

$$\begin{aligned} T_{\text{Rayleigh}}(\rho) &= \frac{\exp(\rho^2) - 1}{\sqrt{2\pi} f_d \rho} \\ T_{\text{Rice}}(\rho) &= \frac{\left[1 - Q\left(\sqrt{2K}, \sqrt{2(K+1)\rho^2}\right)\right]}{\sqrt{2\pi(K+1)} f_d \rho} \\ &\quad \times \frac{\exp(K + (K+1)\rho^2)}{I_0\left(2\sqrt{K(K+1)}\rho\right)} \\ T_{\text{Nakagami}}(\rho) &= \frac{\Gamma(m, m\rho^2)\exp(m\rho^2)}{\sqrt{2\pi} m^{2m-1} f_d \rho^{2m-1}}. \end{aligned} \tag{18}$$

4. Measurement Results

4.1. Data Processing. To determine the small scale fading statistics of the received signal envelope, the effects of the path loss and shadowing have to be removed first. In order to extract the fading envelope, the received signal is normalized to its local mean value. So, for the received sample $r(x_i)$, the local mean value is given by

$$r(x_i)_m = \frac{1}{W} \cdot \sum_{i-W/2}^{i+W/2} r(x_i), \tag{19}$$

where W represents the number of samples in a sliding window (or bin) for the computation. This local mean value is computed for each individual sample in a bin and the normalized samples are then used for distribution fitting. As suggested by [20], a bin size of 40λ is used for analysis, which corresponds to an average distance of approximately

Table 2: K-S testing results at 5% significance level.

	First run		Second run	
	Viaduct	Terrain cutting	Viaduct	Terrain cutting
Rayleigh	19.0%	48.8%	20.1%	52.5%
Rice	74.7%	85.2%	74.7%	93.8%
Nakagami	81.0%	89.5%	78.9%	92.6%

13 m. For the sampling rate used for these measurements, this distance translates to approximately 128 samples per bin.

For the first-order envelope, Kolmogorov-Smirnov (K-S) test is implemented to investigate the fitting performance of the predefined distributions for all the bins in both scenarios. It has been applied in [21–23] as a goodness-of-fit test method to verify the suitability of a hypothesized distribution and identify the distribution which best represents the experimental results.

The K-S statistic D_N, which measures the maximum deviation between the hypothesized distribution and the empirical distribution derived from the measured data, is given by [24]

$$D_N = \max|S_N(x) - F(x)|, \tag{20}$$

where $S_N(x)$ is the cumulative distribution function (CDF) of the empirical data, $F(x)$ is the CDF of the hypothesized distribution, and N is the number of samples. The value D_N is then compared with a critical value J, which is a function of significance level and the sample size N [25]. If $D_N < J$, then the hypothesized distribution is equal to the empirical distribution. In other words, the hypothesized distribution has passed the K-S test.

4.2. Distribution Fitting Results. Table 2 shows the K-S testing results. The numerical values represent the percentages of the bins which have passed the test. It is clear that both Rice and Nakagami distribution fit the measured data very well in the two scenarios, as they both have fitted more than 74% of the bins. The differences between the fitting results of the Rice and Nakagami distribution are fairly small. On the contrary, Rayleigh distribution has only fitted a minority of tested bins. Additionally, sample plots of the empirical CDF for a particular bin and theoretical model fits are given in Figures 3 and 4. The close resemblance between empirical distributions and the Rice and Nakagami distributions can be seen in these figures. At the same time, the Rayleigh distributions have a large deviation from the measurement data. And both the Rice and Nakagami distributions have passed the K-S tests for the bins shown here, while Rayleigh distributions have failed to pass the tests. Similar results can be observed in most of the bins. It has thus demonstrated the validity of the K-S test.

4.3. Rice K Characteristics. As the Rice model has a relatively strong physical significance, it has been selected to analyze the fading statistics in viaduct and terrain cutting scenarios. From the above test results, it can been seen that not all of the bins can be characterized as Rice distribution. Due to the randomness and complexity of the multipath signal components, signal envelope samples of some bins may show a complete different distribution. Thus, in order to obtain more accurate results, the estimated K values which haven't passed the K-S test are discarded in the statistical analysis. Table 3 presents some statistics of the estimated Rice factors

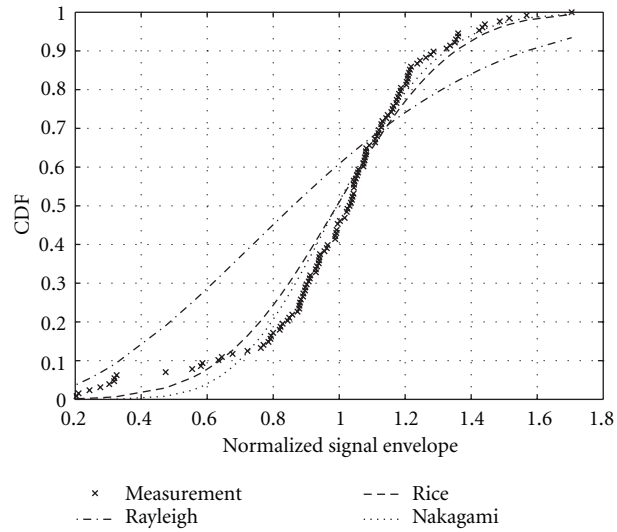

Figure 3: Sample empirical CDF of the small scale signal envelope and theoretical model fits for viaduct scenario. The Rice K factor is 5.56 and Nakagami parameter m is 4.37.

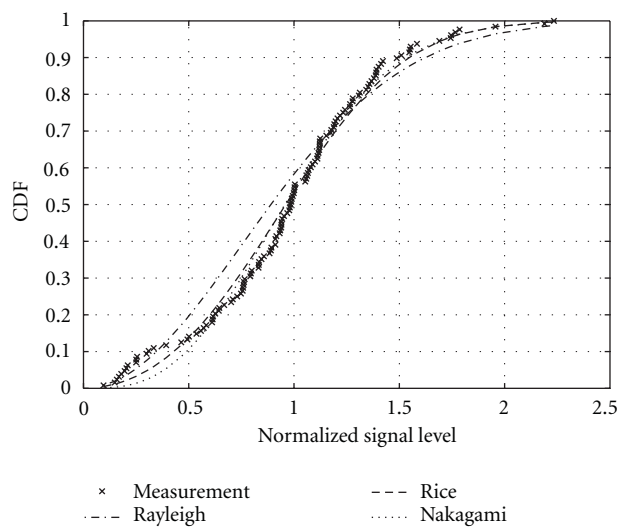

Figure 4: Sample empirical CDF of the small scale signal envelope and theoretical model fits for terrain cutting scenario. The Rice K factor is 1.43 and Nakagami parameter m is 1.59.

Table 3: Rice K statistics.

Scenarios	Rice K			
	Minimum	Maximum	Mean	Standard deviation
Viaduct	0	5.5600	2.3874	1.3314
Terrain cutting	0	4.9200	1.3390	1.1329

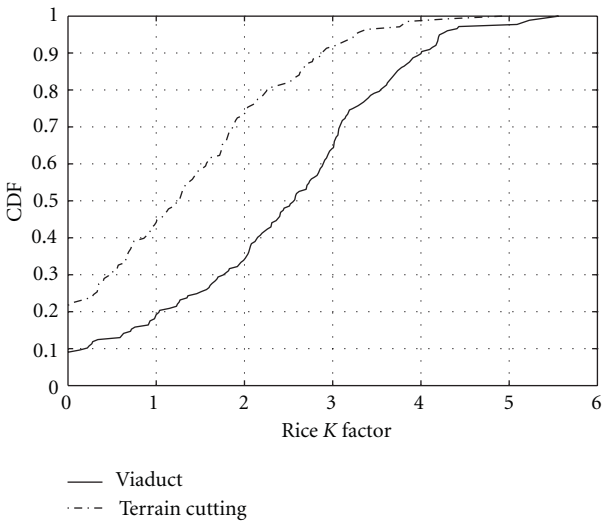

Figure 5: CDF of the K factors in both scenarios.

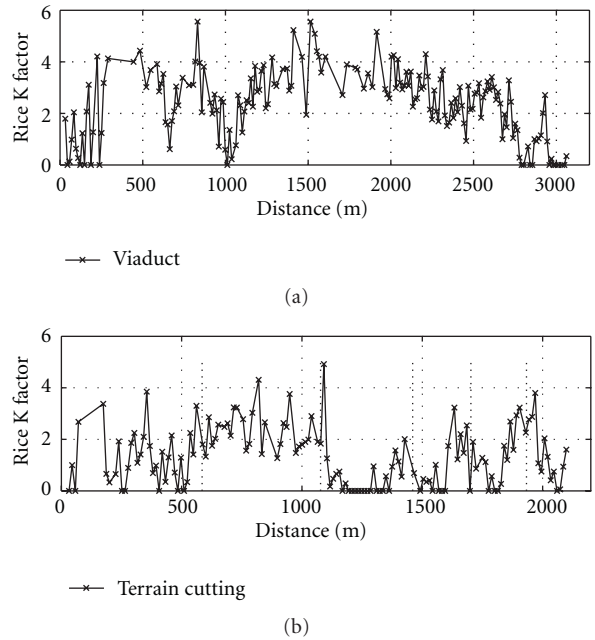

Figure 6: Rice K factor as a function of distance.

(as a linear power ratio) in both scenarios, including the minimum, maximum, mean, and standard deviation values. It is seen that viaduct scenario appears to be a less severe fading channel compared to terrain cutting scenario since the mean K value of the viaduct scenario is larger than that of the terrain cutting scenario. The standard deviation values of both scenarios are approximately the same.

The CDF of the obtained K factors in both scenarios is also shown in Figure 5. It can be seen that for any given probability value, the K value of the viaduct scenario is larger than that of the terrain cutting scenario, further confirming the relative severe propagation environment of the terrain cutting scenario. In most of the cases (about 90%), K value is within the interval 0–4 for viaduct scenario, while the value is 0–2.9 for terrain cutting scenario. In addition, approximately 22% of the K values in terrain cutting scenario are zero, which implies a kind of fading as severe as Rayleigh fading. However, the proportion of zero K values in viaduct scenario is only 9%.

Figure 6 shows the plot of the Rice K factors as a function of BS-train separation distance for both scenarios. In viaduct scenario, the Rice K value tends to increase in the first few hundred meters. This could be explained by the fact that directional antennas are used in the railway wireless networks. The effect of the directional antenna is also reflected in the received signal power, which is low near the BS and gradually increases with the distance. Then the K value shows a general decreasing trend. In terrain cutting scenario, the increasing trend of K value for the first few hundred meters is not obvious. The reason for this is that existence of slopes may weaken the LOS component. The rest part of the Rice K values does not have a regular change tendency as in the viaduct scenario. Instead, it fluctuates sharply. Locations of the five over bridges are also marked in the figure by five vertical dotted lines. It is observed that the Rice K value tends to drop rapidly after passing the over bridges and then rise again. This phenomenon is extremely obvious for the last four over bridges. Thus the K value appears to change periodically according to the existence of the bridge, while this is not observed in viaduct scenario.

4.4. Second-Order Statistics. All the obtained envelope data are first used to calculate the LCR and AFD values. After that, the measured envelope values are fitted to the theoretical distributions and then theoretical LCR and AFD values can be derived. For viaduct, the obtained Rice K factor is 2.32 and Nakagami parameter m is 1.99. For terrain cutting, the Rice K factor is 1.29 and Nakagami parameter m is 1.50. Both the empirical and theoretical LCR and AFD values are computed for threshold levels from -20 dB to 10 dB.

The empirical and theoretical LCR results in viaduct and terrain cutting scenario for the first measurement are shown in Figure 7. Fairly large LCR values per second can be observed in the figure. This is due to the fact that the train was moving at a very high speed. According to the theoretical formulas (16), the LCR per second increases linearly with the maximum Doppler frequency, which is a monotonic increasing function of the average speed of the mobile station. For viaduct scenario, a good agreement between the empirical LCR and Rice model can be seen for any threshold values, while a bad agreement between empirical data and the Rayleigh model can also be found. Although the Nakagami model does not give good fit for most of the threshold values, it gives excellent fit for the threshold values smaller than -15 dB. It is found that good match between the Nakagami and empirical CDFs does not guarantee a good match for the corresponding LCR curves. The same behavior is also obtained for the second measurement, confirming that close match for the first-order statistics may yield dissimilar second-order statistics [16]. For the terrain cutting scenario, as shown in Figure 7(b), the Rice model still gives better fit

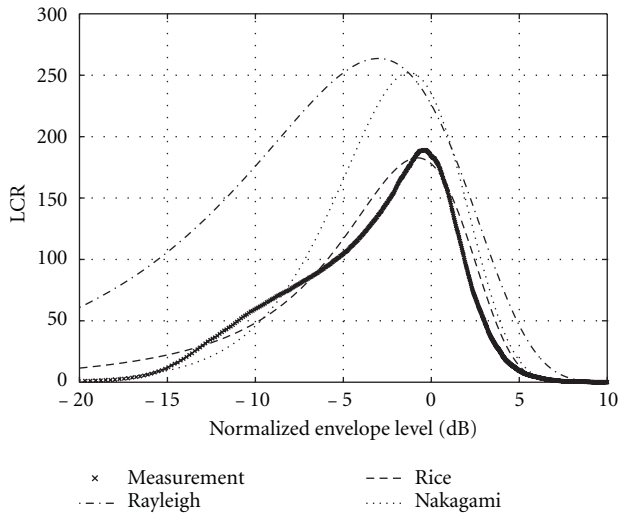

(a) Viaduct scenario

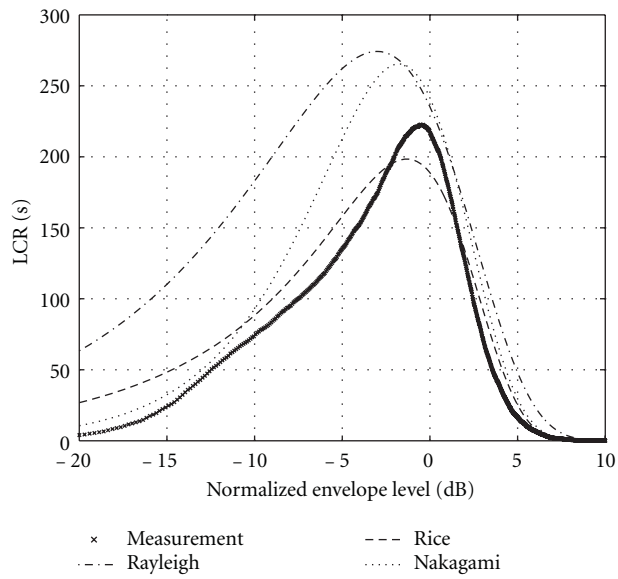

(b) Terrain cutting scenario

Figure 7: Empirical LCR results in both scenarios for the first measurement, together with the theoretical results of Rayleigh, Rice, and Nakagami fading models.

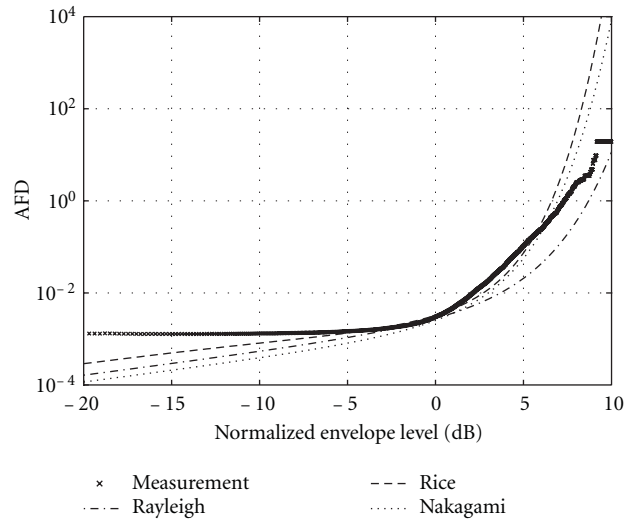

(a) Viaduct scenario

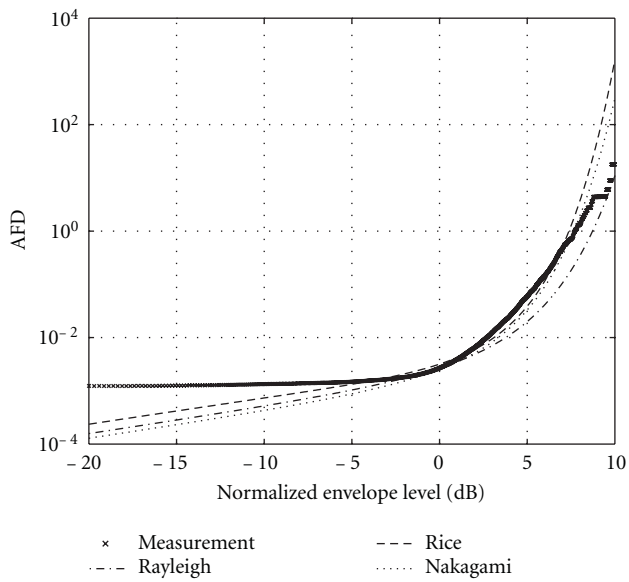

(b) Terrain cutting scenario

Figure 8: Empirical AFD results in both scenarios for the first measurement, together with the theoretical results of Rayleigh, Rice, and Nakagami fading models.

than the other two models. But the deviation between the empirical results and the Rice model is larger than that of the viaduct scenario, especially for the threshold value near 0 dB. The Rayleigh model still gives the worst fit, while the Nakagami model gives a relatively better fit. Still, a relative independence of the goodness of fit between the first-order and second-order statistics can be observed.

The empirical and theoretical AFD results in viaduct and terrain cutting scenario for the first measurement are shown in Figure 8. The AFD values are plotted on a logarithmic scale to highlight the slight difference (not visible on a linear scale) between the empirical and theoretical AFDs. For both scenarios, Rice model offers the best fit for most threshold values. However, it deviates larger for the lower and upper part of the curve. On the other hand, Nakagami model is more accurate for the threshold values larger than 0 dB. The theoretical Rayleigh values are always less than the measured AFD values.

5. Conclusion

This paper has presented empirical fading characteristic results in typical high speed railway viaduct and terrain cutting scenarios. Measurements were done by a special test system for GSM-R. The small scale fading envelope distribution has been fitted to theoretical Rayleigh, Rice, and Nakagami distributions. K-S test has been specially introduced as a goodness-of-fit test method to verify the suitability of a

hypothesized distribution and the results show that both Rice and Nakagami distribution can describe the empirical data very well. Statistical analysis of the Rice K factors indicates that in most cases the value is within the interval 0–4 for viaduct scenario, while the value is 0–2.9 for terrain cutting scenario. And about 22% of the Rice K values in terrain cutting scenario are zero, which reveals that radio wave experiences more severe fading in terrain cutting scenario than in viaduct scenario. Further study of the Rice K factor as a function of distance suggests that in viaduct scenario the K value tends to increase in the first few hundred meters due to the directional antenna. Then it shows a general decreasing trend for the rest part of the distance. On the contrary, the K value exhibits an irregular change tendency with distance in terrain cutting scenario. It is found that the K value appears to drop and rise periodically by the effect of the over bridges which span the railway tracks. Though both Rice and Nakagami distributions provide a good fit to the first-order envelope data in both scenarios, only the Rice model generally fits the second-order statistics data accurately. This result verifies that the goodness of fit between the first-order envelope statistics and second-order statistics is relatively independent. These results will certainly enable better comprehension of the propagation channel in typical high speed railway scenarios and thus have important implications for the system design of the network.

Acknowledgments

This work is supported in part by the Joint Funds of the Fundamental Research Funds for the Central Universities under Grant no. 2010JBZ008 and 2012YJS017, State Key Program of NSFC (Grant no. 60830001), the State Key Laboratory of Rail Traffic Control and Safety (Contract no. RCS2008ZZ006), (Contract no. RCS2008ZZ007), (Contract no. RCS2010 K008), Beijing Jiaotong University. At last but not least, the authors would like to thank the anonymous reviewers for their valuable comments and suggestions to improve the quality of this paper.

References

[1] C. Briso, C. Cortés, F. J. Arqués, and J. I. Alonso, "Requirements of GSM technology for the control of high speed trains," in *Proceedings of the 13th IEEE International Symposium on Personal, Indoor and Mobile Radio Communications (PIMRC '02)*, vol. 2, pp. 792–793, September 2002.

[2] H. Wei, Z. Zhong, K. Guan, and B. Ai, "Path loss models in viaduct and plain scenarios of the high-speed railway," in *Proceedings of the 5th International ICST Conference on Communications and Networking in China (ChinaCom '10)*, pp. 1–5, August 2010.

[3] R. He, Z. Zhong, B. Ai, L. Xiong, and H. Wei, "A novel path loss model for high-speed railway viaduct scenarios," in *Proceedings of the 7th International Conference on Wireless Communications, Networking and Mobile Computing (WiCOM '11)*, pp. 1–4, September 2011.

[4] J. Lu, G. Zhu, and B. Ai, "Radio propagation measurements and modeling in railway viaduct area," in *Proceedings of the 6th International Conference on Wireless Communications, Networking and Mobile Computing (WiCOM '10)*, pp. 1–5, September 2010.

[5] R. He, Z. Zhong, B. Ai, and J. Ding, "An empirical path loss model and fading analysis for high-speed railway viaduct scenarios," *IEEE Antennas and Wireless Propagation Letters*, vol. 10, Article ID 5981374, pp. 808–812, 2011.

[6] L. Gao, Z. Zhong, B. Ai, and L. Xiong, "Estimation of the Ricean K factor in the high speed railway scenarios," in *Proceedings of the 5th International ICST Conference on Communications and Networking in China (CHINACOM '10)*, pp. 1–5, August 2010.

[7] C. Tepedelenlioğlu, A. Abdi, and G. B. Giannakis, "The Ricean K factor: estimation and performance analysis," *IEEE Transactions on Wireless Communications*, vol. 2, no. 4, pp. 799–810, 2003.

[8] R. He, Z. Zhong, B. Ai, and J. Ding, "Propagation measurements and analysis for high-speed railway cutting scenario," *Electronics Letters*, vol. 47, no. 21, pp. 1167–1168, 2011.

[9] M. Nakagami, "The m-distribution-a general formula of intensity distributionof rapid fading," in *Statistical Method of Radio Propagation*, 1960.

[10] H. Suzuki, "A statistical model for urban radio propogation," *IEEE Transactions on Communications*, vol. 25, no. 7, pp. 673–680, 1977.

[11] L. Gao, Z. Zhong, B. Ai, L. Xiong, and H. Zhang, "Analysis and emulation of the small-scale fading characteristics in the high-speed rail scenarios," in *Proceedings of the 6th International ICST Conference on Communications and Networking in China (CHINACOM '11)*, pp. 1181–1185, August 2011.

[12] T. S. Rappaport, *Wireless Communications: Principles and Practice*, Prentice Hall, New York, NY, USA, 2nd edition, 2002, http://www.worldcat.org/isbn/0130422320.

[13] L. J. Greenstein, D. G. Michelson, and V. Erceg, "Moment-method estimation of the Ricean K-factor," *IEEE Communications Letters*, vol. 3, no. 6, pp. 175–176, 1999.

[14] A. Abdi and M. Kaveh, "Performance comparison of three different estimators for the nakagami m parameter using Monte Carlo simulation," *IEEE Communications Letters*, vol. 4, no. 4, pp. 119–121, 2000.

[15] B. Talha and M. Patzold, "Level-crossing rate and average durationof fades of the envelope of mobile-to-mobile fading channelsin cooperative networks under line-of-sight conditions," in *Proceedings of the IEEE GlobalTelecommunications Conference (GLOBECOM '08)*, pp. 1–6, December 2008.

[16] A. Abdi, K. Wills, H. A. Barger, M. S. Alouini, and M. Kaveh, "Comparison of the level crossing rate and average fade duration of Rayleigh, Rice, and Nakagami fading models with mobile channel data," in *Proceedings of the 52nd Vehicular Technology Conference (VTC '00)*, pp. 1850–1857, September 2000.

[17] M. D. Yacoub, M. V. Barbin, M. S. de Castro, and J. E. B. Vargas, "Level crossing rate of Nakagami-m fading signal: field trials and validation," *Electronics Letters*, vol. 36, no. 4, pp. 355–357, 2000.

[18] G. Stüber, *Principles of Mobile Communication*, Kluwer Academic, New York, NY, USA, 1996.

[19] M. D. Yacoub, M. D. Yacoub, J. E. V. Bautista, and L. Guerra de Rezende Guedes, "On higher order statistics of the Nakagami-m distribution," *IEEE Transactions on Vehicular Technology*, vol. 48, no. 3, pp. 790–794, 1999.

[20] W. C. Y. Lee, "Estimate of local average power of a mobile radio signal," *IEEE Transactions on Vehicular Technology*, vol. 34, no. 1, pp. 22–27, 1985.

[21] V. Nikolopoulos, M. Fiacco, S. Stavrou, and S. R. Saunders, "Narrowband fading analysis of indoor distributed antenna systems," *IEEE Antennas and Wireless Propagation Letters*, vol. 2, pp. 89–92, 2003.

[22] D. Kim, M. A. Ingram, and W. W. Smith, "Measurements of small-scale fading and path loss for long range RF tags," *IEEE Transactions on Antennas and Propagation*, vol. 51, no. 8, pp. 1740–1749, 2003.

[23] M. Boutin, A. Benzakour, C. L. Despins, and S. Affes, "Radio wave characterization and modeling in underground mine tunnels," *IEEE Transactions on Antennas and Propagation*, vol. 56, no. 2, pp. 540–549, 2008.

[24] P. K. Tang, Y. H. Chew, L. C. Ong, M. K. Haldar, and L. Bin, "Small-scale transmission statistics of UWB signals for body area communications," in *Proceedings of the IEEE 64th Vehicular Technology Conference (VTC '06)*, pp. 1–5, September 2006.

[25] B. C. Liu, K. H. Lin, and J. Y. Chen, "Ricean K-factor estimation in cellular communications using kolmogorov-smirnov statistic," in *Proceedings of the Asia-Pacific Conference on Communications (APCC '06)*, pp. 1–5, September 2006.

Hindawi Publishing Corporation
International Journal of Antennas and Propagation
Volume 2012, Article ID 507094, 6 pages
doi:10.1155/2012/507094

Application Article

Impact of Ship Motions on Maritime Radio Links

William Hubert,[1] Yvon-Marie Le Roux,[2] Michel Ney,[3] and Anne Flamand[1]

[1] *Communications Department, DCNS, France*
[2] *Electronic Department and Labsticc, Telecom Bretagne, France*
[3] *Microwaves Department and Labsticc, Telecom Bretagne, France*

Correspondence should be addressed to William Hubert, william.hubert@telecom-bretagne.eu

Received 27 July 2012; Revised 22 October 2012; Accepted 7 November 2012

Academic Editor: Thomas Kürner

The improvement of maritime radio links often requires an increase of emitted power or receiver sensitivity. Another way is to replace the poor antenna gains of traditional surface ship whips by novel antenna structures with directive properties. However, ship motions, especially when launches are involved, may affect the radio link quality. Therefore, a tool for modelling the impact of ship motions on such antenna structures was developed. It helps the specification of antenna radiating parameters and improves the radio link performance evaluation. This tool includes a deterministic two-ray model for radio-wave propagation over the sea surface. The geometrical 3D engine for ship motions has the advantage to be compatible with any propagation model and antenna structure.

1. Introduction

This paper presents the development of a deterministic transmission channel model for the improvement of a high data rate (>10 Mbits·s^{-1}) radio-link in the S-band (2 to 4 GHz). This link is supposed to reach the largest possible range between small surface ships. First, the link budget at the approach of the radio horizon by means of the ITU P.526 model [1] was computed. It shows that establishing such a link between ships requires a huge increase in emitted power if poor antenna gains (about 2 dBi) are used. Hence, the purpose of the transmission model is to help the specification of novel antenna structures with gains above 10 dBi. To reproduce the real situation as accurately as possible, especially when ship motions are relevant, a 3D geometrical model was developed. The computational engine can accommodate any antenna and propagation model. However, a simple two-ray model and dipole antennas are used in this paper for illustrative example.

After a description of the propagation model, a section is then devoted to the presentation of the geometrical context for the integration of ship motions. The next section is dedicated to the computation of the maximum antenna angular deviation for given sea-wave data. Then, the integration of antenna radiating parameters is explained. Finally, an expression of the received power is derived using channel matrix formalism, followed by a presentation of simulated results.

2. Propagation Model

The propagation is described by a two-ray model that includes a direct path between the transmitter (A) and the receiver (B) and a path coherently reflected (in P) by the sea surface (Figure 1). This model has recently been confirmed in [2] by measurements. It is applied here on a spherical earth of effective radius R_e which corresponds to a mean atmospheric refractive index. The coherently reflected path is obtained according to the Snell-Descartes law and its amplitude is primarily determined by the Fresnel reflection coefficients:

$$\rho_{\parallel} = \frac{\sin\varphi - (1/\eta)\sqrt{\eta - \cos^2\varphi}}{\sin\varphi + (1/\eta)\sqrt{\eta - \cos^2\varphi}} \tag{1}$$

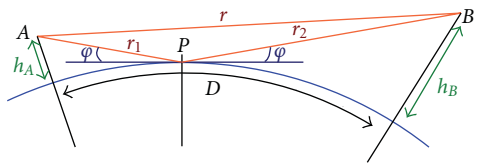

Figure 1: 2D geometry of the two-ray model.

for the vertical (or electric field parallel to the incidence plane) polarization,

$$\rho_{\perp} = \frac{\sin\varphi - \sqrt{\eta - \cos^2\varphi}}{\sin\varphi + \sqrt{\eta - \cos^2\varphi}} \tag{2}$$

for the horizontal (or orthogonal to the incidence plane) polarization.

In the above expressions, η stands for the relative complex permittivity of the sea water surface. It can be defined by the Debye formula applied by Stogryn in [3].

The reflected energy is also affected by a divergence factor which produces a larger aperture of the beam after reflection. Its expression is given by Beckmann and Spizzichino in [4] and depends on geometric parameters previously defined in Figure 1:

$$\mathrm{FD} = \left[1 + \frac{2r_1r_2}{R_e(r_1+r_2)\sin\varphi}\right]^{-1/2}\left[1 + \frac{2r_1r_2}{R_e(r_1+r_2)}\right]^{-1/2}. \tag{3}$$

The model validity is primarily bounded by the variations of FD. This factor must not be used after a limiting distance which corresponds to the transition between the two-ray model and the ITU P.526 model. An attempt of integrating the latter does not give enough satisfaction with regard to the transition range. Moreover, the program objective is to assist the antenna specification. So, the design of the link is done at long range by means of the ITU model. Comparison between these different models is shown in Figure 2, obtained at 2.4 GHz, with an effective isotropic radiated power (EIRP) of 1 Watt, with both antennas at 6 meters above the sea surface.

Expected results are obtained in Figure 2 since good vertical and poor horizontal spatial diversities are observed. Besides, it appears worthless to take benefits from the polarization diversity observed at short ranges because of the unfavorable two-ray recombination in horizontal polarization.

Finally, a second factor is applied to the specularly reflected energy in presence of sea waves. If a normal distribution hypothesis of sea surface elevations is made, the reduction factor ρ_r depends on their standard deviation σ. According to Miller et al. [5], the reduction factor is given by the following expression:

$$\rho_r = \exp\left[-2(2\pi g)^2\right] \cdot I_0\left[2(2\pi g)^2\right], \tag{4}$$

in which

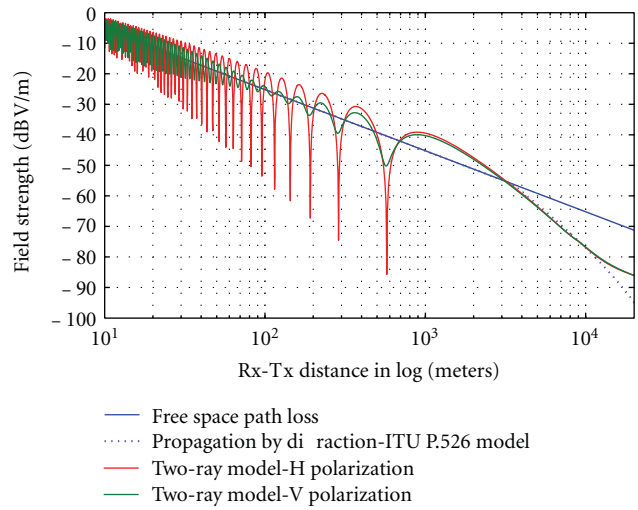

Figure 2: Field strength (dB V/m) versus distance (log scale).

(i) $g = (\sigma \sin\varphi)/\lambda$ is the Rayleigh criterion,

(ii) $I_0[\cdot]$ is the modified Bessel function of the first kind and order zero, and

(iii) λ is the EM wavelength in meters.

Figure 3 is obtained with the same parameters as before but for a sea state 3 on Douglas sea scale ($\sigma = 0.5$ meters). A slight swell is sufficient to significantly reduce the coherently reflected energy. The result is a partial vanishing of fading figures. The energy which is no longer coherently reflected leads to a diffuse scattering. However, diffusion is not yet integrated in this deterministic model. Further improvements could be made by introducing that diffuse component in the propagation model. A good starting point would be the analysis proposed in [6] by Karasawa and Shiokawa.

3. Integration of Ship Motions

The previously defined 2D geometry has to evolve to three dimensions to integrate ship motions. A global coordinate system $(O, \vec{X}, \vec{Y}, \vec{Z})$, in which O is the Earth center, is shown in Figure 4. Angle α is defined according to the Intership distance D (Figure 1) and β stands for their relative orientation.

All coordinates will be further expressed in this global system by means of translation vectors and rotation matrices. Then, a local coordinate system attached to each ship center of mass is defined wherein ship motions are described (Figure 5).

Regarding the ship motions, one shall define below the dedicated terms related to the local coordinate system:

(i) *heave* is a translation along $\vec{z}$ axis (vertical motion),

(ii) *roll* is a rotation about $\vec{x}$ axis,

(iii) *pitch* is a rotation about $\vec{y}$ axis.

The above motions can be simply described by sinus functions. Therefore, they are characterized here by their

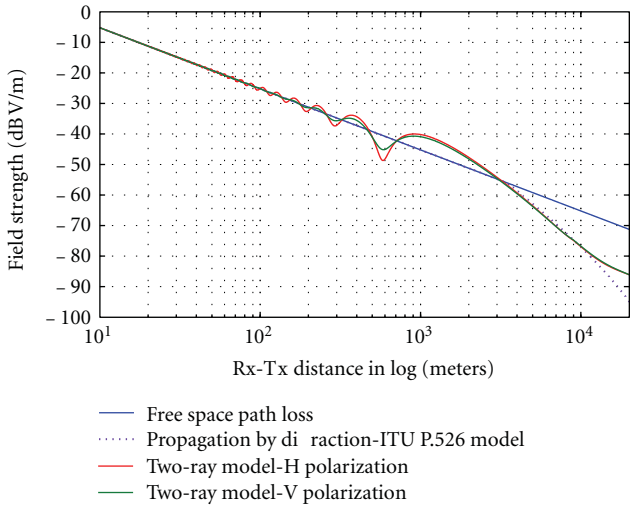

Figure 3: Field strength (dB V/m) versus distance (log scale), sea state 3 on Douglas scale.

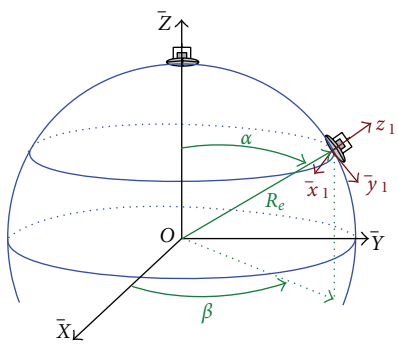

Figure 4: Global coordinate system for ship positions.

amplitude and period only. Further improvements could be made by introducing recorded data of real ship motions. Antenna locations are also described in this system by their onboard coordinates with a proper orientation. Finally, a coordinate system attached to the antenna center (A) is introduced according to antenna measurements or simulations (Figure 6).

By expressing all geometric objects in the global coordinate system, antenna position and velocity, rays arrival, and departure angles can be determined at any time.

4. Maximum Angular Deviation

Without real ship motion records, approximate geometrical relations can be derived for antenna maximum angular deviation from vertical direction. Knowing the maximum crest-to-trough wave height $H_{\max}$ and the wavelength λ_s, one can evaluate the maximum antenna angular deviation:

$$\theta_{\max} = \arcsin\left(\frac{\pi H_{\max}}{\sqrt{\lambda_s^2 + \pi^2 H_{\max}^2}}\right). \tag{5}$$

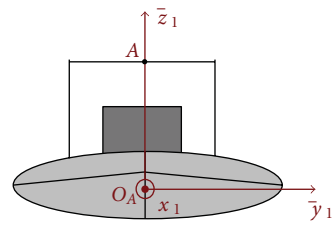

Figure 5: Local coordinate system for the ship in A, front view of the ship.

Several simulations have shown that this angular deviation represents the maximum deviation from the position at rest for distances above 100 meters. For linearly polarized antennas, it also leads to a maximum polarization loss factor (PLF) given by

$$\mathrm{PLF}_{\mathrm{dB}} = 20\log_{10}(\cos 2\theta_{\max}). \tag{6}$$

Using the fundamental mode of the Pierson-Moskowitz spectrum for fully developed regular wind waves [7], a complete data set is defined for the studied case. It includes the period T_s and the standard deviation of sea-wave elevations σ:

$$\begin{aligned} H_{\max} &\simeq 5.7\,\mathrm{m}, \qquad T_s \simeq 9.2\,\mathrm{s}, \\ \lambda_s &\simeq 131.4\,\mathrm{m}, \qquad \sigma \simeq 1\,\mathrm{m}. \end{aligned} \tag{7}$$

What is introduced in (5) leads to

$$\theta_{\max} = 7.6^\circ. \tag{8}$$

Note that the result on $\theta_{\max}$ remains approximately constant for any $H_{\max}$. This is due to the fully developed regular wind wave assumption. However, if both $H_{\max}$ and λ_s are determined by any means (models or measurements), (5) still holds for small ships.

5. Antenna Integration

A radiation vector function $\mathbf{F}$ is introduced to account for polarisation state and antenna gain along any direction. As in [8], $\mathbf{F}$ depends on the realized gain (which integrates impedance mismatch) for a given set of departure (emitting antenna) or arrival (receiving antenna) angles:

$$\mathbf{F} = \sqrt{G(\chi,\psi)}\,\mathbf{U} = \sqrt{G(\chi,\psi)}\begin{pmatrix} U_\chi(\chi,\psi) \\ U_\psi(\chi,\psi) \end{pmatrix}. \tag{9}$$

In the above expression, χ and ψ stand for the elevation angle and the azimuth angle, respectively. $\mathbf{U}$ is a normalized vector which corresponds to the complex ratio (amplitude and phase) emitted (or received) along $\vec{u}_\chi$ and $\vec{u}_\psi$ components (see Figure 6).

A database was created for the simulations. It consists of multiple tables of data extracted from electromagnetic (EM) simulators, in our case HFSS. These tables represent

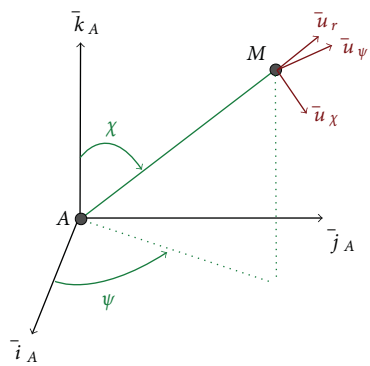

Figure 6: Antenna coordinate system with unit vectors for field components.

realised gain and antenna field components as expressed in (9). Finally, for wide band communications, the radiation vector function database $\mathbf{F}$ would have to be generated for several frequencies.

6. Expression of the Received Power

First of all, a channel matrix is built by using the unit vectors (see Figure 6) expressed in the same coordinate frame. It expresses intrinsically the PLF. Then, the spherical-divergence and phase terms are applied to obtain the direct-path channel matrix:

$$\mathbf{C}_{\mathrm{DP}} = \frac{1}{r}\begin{pmatrix} \vec{u}_\chi^A \cdot \vec{u}_\chi^B & \vec{u}_\psi^A \cdot \vec{u}_\chi^B \\ \vec{u}_\chi^A \cdot \vec{u}_\psi^B & \vec{u}_\psi^A \cdot \vec{u}_\psi^B \end{pmatrix} e^{-j2\pi r/\lambda}. \tag{10}$$

Radiation vector functions for the transmitting antenna $\mathbf{F}^A(\chi,\psi)$ and for the receiving antenna $\mathbf{F}^B(\chi,\psi)$ are then applied to both sides of this matrix to obtain a transmission scalar s_{DP}. Thus, with (9) and (10),

$$s_{\mathrm{DP}} = \frac{1}{r}\sqrt{G^A}\sqrt{G^B}\begin{pmatrix} U_\chi^B & U_\psi^B \end{pmatrix} \times \begin{pmatrix} \vec{u}_\chi^A \cdot \vec{u}_\chi^B & \vec{u}_\psi^A \cdot \vec{u}_\chi^B \\ \vec{u}_\chi^A \cdot \vec{u}_\psi^B & \vec{u}_\psi^A \cdot \vec{u}_\psi^B \end{pmatrix} \begin{pmatrix} U_\chi^A \\ U_\psi^A \end{pmatrix} e^{-j2\pi r/\lambda}. \tag{11}$$

For the coherently reflected path, unit vectors $\vec{u}_{\chi,\psi}^{A,B}$ have to be decomposed into a parallel $\vec{u}_\parallel$ and an orthogonal $\vec{u}_\perp$ components to the sea surface as shown in Figure 7.

Then, one can define the reflection dyadic $\overline{\overline{\mathbf{R}}}$:

$$\overline{\overline{\mathbf{R}}} = \mathrm{FD} \cdot \rho_r \cdot \begin{pmatrix} \rho_\parallel & 0 \\ 0 & \rho_\perp \end{pmatrix} \tag{12}$$

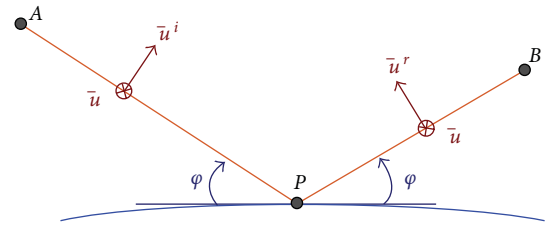

Figure 7: Unit vector definition for reflection.

in which $\rho_\parallel$, $\rho_\perp$, FD, and ρ_r are defined in (1), (2), (3), and (4), respectively. Thus, the propagation channel matrix for the reflected path becomes

$$\mathbf{C}_{\mathrm{RP}} = \frac{1}{r_1+r_2}\begin{pmatrix} \vec{u}_\chi^B \cdot \vec{u}_\parallel^r & \vec{u}_\chi^B \cdot \vec{u}_\perp \\ \vec{u}_\psi^B \cdot \vec{u}_\parallel^r & \vec{u}_\psi^B \cdot \vec{u}_\perp \end{pmatrix} \times \overline{\overline{\mathbf{R}}} \begin{pmatrix} \vec{e}_\chi^A \cdot \vec{u}_\parallel^i & \vec{u}_\psi^A \cdot \vec{u}_\parallel^i \\ \vec{e}_\chi^A \cdot \vec{u}_\perp & \vec{u}_\psi^A \cdot \vec{u}_\perp \end{pmatrix} e^{-j2\pi(r_1+r_2)/\lambda}. \tag{13}$$

The same approach used to obtain (11) is applied to derive the second scalar for the coherently reflected path:

$$s_{\mathrm{RP}} = \frac{1}{r_1+r_2}\sqrt{G^A}\sqrt{G^B}\begin{pmatrix} U_\chi^B & U_\psi^B \end{pmatrix} \begin{pmatrix} \vec{u}_\chi^B \cdot \vec{u}_\parallel^r & \vec{u}_\chi^B \cdot \vec{u}_\perp \\ \vec{u}_\psi^B \cdot \vec{u}_\parallel^r & \vec{u}_\psi^B \cdot \vec{u}_\perp \end{pmatrix} \times \overline{\overline{\mathbf{R}}} \begin{pmatrix} \vec{u}_\chi^A \cdot \vec{u}_\parallel^i & \vec{u}_\psi^A \cdot \vec{u}_\parallel^i \\ \vec{u}_\chi^A \cdot \vec{u}_\perp & \vec{u}_\psi^A \cdot \vec{u}_\perp \end{pmatrix} \begin{pmatrix} U_\chi^A \\ U_\psi^A \end{pmatrix} e^{-j2\pi(r_1+r_2)/\lambda}. \tag{14}$$

Note that the unit vectors $\vec{u}_{\chi,\psi}^{A,B}$ and radiation vector functions in (11) and (14) are not the same because antenna polarization and gain are subject to change with the propagation direction. Finally, using classical formulas, one can evaluate the received power P_r as a function of the supplied power at antenna terminals P_f:

$$P_r = \left(\frac{\lambda}{4\pi}\right)^2 P_f \left|s_{\mathrm{DP}} + s_{\mathrm{RP}}\right|^2 \tag{15}$$

in which s_{DP} and s_{RP} are given by (11) and (14), respectively. In the above expressions, time (related to ship motions) and frequency (for electromagnetic wave propagation) are involved.

7. Simulated Results

A simulation with a transmitter which undergoes the previously defined motions (sea state 5 on Douglas scale) and a receiver ashore (motionless) is proposed. Both antennas are at six meters above the sea surface with a distance of 700 meters between them. As shown in Figure 2, this range naturally leads to a ray recombination equal to the free-space path loss. Both antennas are dipoles with maximum gain of 2.1 dBi. Variations of the received power versus time are shown in Figure 8. Different simulations have

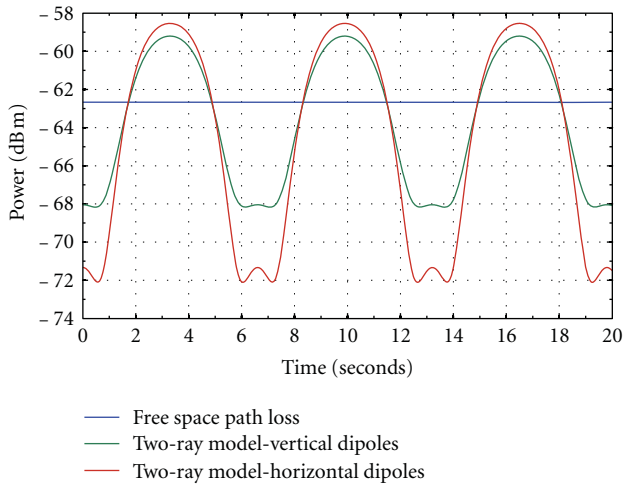

Figure 8: Received power versus time, sea-state 5, ship motions in the incidence plane.

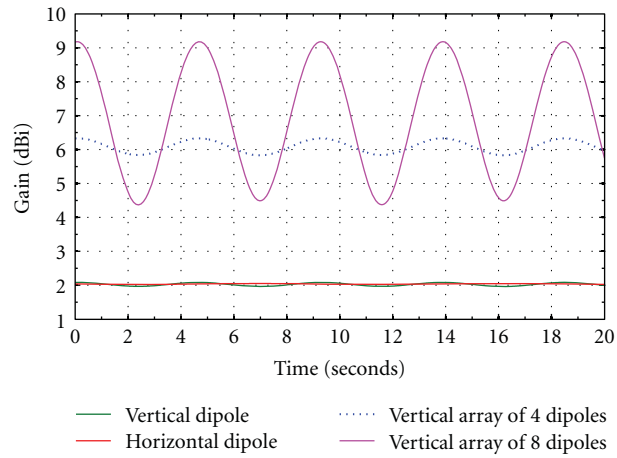

Figure 9: Gains at transmission on the direct path with dipole and arrays of dipoles.

shown that those variations are mainly due to the two-ray recombination which changes with movements. On the other hand, significant losses are observed if antennas with relatively high directivity are used. To illustrate this, Figure 9 shows the gain at transmission for the direct path and for antenna arrays which have higher directivity. Note that similar results are obtained for the reflected path. The maximum gain of the linear vertical array of 8 dipoles is greater than 9 dBi, but its half-power beam aperture angle is less than $2\theta_{\max}$. As a result, instantaneous effective gain fluctuates to values below the ones obtained by linear vertical array of 4 dipoles. This confirms that the -3 dB elevation aperture angle has to be at least in the order of $2\theta_{\max}$ (given by (5)) to preclude large gain reductions. Note that ship motions in the azimuth plane have negligible impact on the gain variation.

Finally, several simulations show that ship motions lead to a polarization loss factor less (PLF) than 3 dB. This indicates that using circular polarization does not bring any advantage because of the deep fadings produced by horizontal polarization (see Figure 2).

8. Conclusion

The description of a maritime radio link channel simulator was presented. It includes a two-ray propagation model, antenna parameters, and three-dimensional (3D) ship motion model. Each component of the simulator is independent as the ship motion calculation engine can be used with any propagation model or antennas. The objective of the simulator is to provide a reliable tool for antenna specification and channel performance evaluation. First results show that classical behaviour of the two-ray model remains the main contribution to the channel characteristics if the condition on the maximum deviation angle $\theta_{\max}$ is fulfilled. Antenna -3 dB elevation beam aperture has to be chosen according to ship motions, given a radio-link-operational sea state. In addition, the use of vertically polarized antenna seems to be the most advantageous option. The maximum deviation angle expression is provided and, for small-ship motions, both the polarisation loss factor and the decrease in antenna gain can be predicted. For larger ships, the only parameter that has to be known is the maximum angular deviation between roll and pitch.

Conflict of Interests

The authors declare that there is no conflict of interests with ANSYS, editor of HFSS.

Acknowledgments

This work has been done with the support of DCNS and Telecom Bretagne, Mines-Telecom Institute.

References

[1] ITU Rec. P. 526-12, "Propagation by diffraction," ITU, Geneva, Switzerland, 2012.

[2] Y. M. Le Roux, J. Ménard, C. Toquin, J. P. Jolivet, and F. Nicolas, "Experimental measurements of propagation characteristics for maritime radio links," in *Proceedings of the 9th International Conference on Intelligent Transport Systems Telecommunications (ITST '09)*, pp. 364–369, October 2009.

[3] A Stogryn, "Equations for calculating the dielectric constant of saline water," *IEEE Transactions on Microwave Theory and Techniques*, vol. 19, no. 8, pp. 733–736, 1971.

[4] P. Beckmann and A. Spizzichino, *The Scattering of Electromagnetic Waves From Rough Surfaces*, Artech House, 1963.

[5] A. R. Miller, R. M. Brown, and E. Vegh, "New derivation for the rough-surface reflection coefficient and for the distribution of sea-wave elevations," *IEE Proceedings H*, vol. 131, no. 2, pp. 114–116, 1984.

[6] Y. Karasawa and T. Shiokawa, "Simple prediction method for L-band multipath fading in rough sea conditions," *IEEE Transactions on Communications*, vol. 36, no. 10, pp. 1098–1104, 1988.

[7] L. Gardenal, B. Philibert, and R. M. Turner, "Study of the interaction of electromagnetic waves on a sea surface: improvement of the algorithm of low-altitude tracking of radar targets," in *Proceedings of the Canadian Conference on Electrical and Computer Engineering*, vol. 2, pp. 693–696, 1994.

[8] B. Uguen, L. M. Aubert, and F. T. Talom, "A comprehensive MIMO-UWB channel model framework for ray tracing approaches," in *Proceedings of the IEEE International Conference on Ultra-Wideband (ICUWB '06)*, pp. 231–236, September 2006.

Hindawi Publishing Corporation
International Journal of Antennas and Propagation
Volume 2012, Article ID 183145, 11 pages
doi:10.1155/2012/183145

Research Article

Propagation Mechanism Modeling in the Near-Region of Arbitrary Cross-Sectional Tunnels

Ke Guan,[1] Zhangdui Zhong,[1] Bo Ai,[1] Ruisi He,[1] Yuanxuan Li,[1] and César Briso Rodríguez[2]

[1] *State Key Laboratory of Rail Traffic Control and Safety, Beijing Jiaotong University, Beijing 100044, China*
[2] *Escuela Universitaria de Ingeniería Técnica de Telecomunicación, Universidad Politècnica de Madrid, 28031 Madrid, Spain*

Correspondence should be addressed to Ke Guan, myecone@hotmail.com

Received 24 April 2012; Accepted 24 September 2012

Academic Editor: Thomas Kürner

Along with the increase of the use of working frequencies in advanced radio communication systems, the near-region inside tunnels lengthens considerably and even occupies the whole propagation cell or the entire length of some short tunnels. This paper analytically models the propagation mechanisms and their dividing point in the near-region of arbitrary cross-sectional tunnels for the first time. To begin with, the propagation losses owing to the free space mechanism and the multimode waveguide mechanism are modeled, respectively. Then, by conjunctively employing the propagation theory and the three-dimensional solid geometry, the paper presents a general model for the dividing point between two propagation mechanisms. It is worthy to mention that this model can be applied in arbitrary cross-sectional tunnels. Furthermore, the general dividing point model is specified in rectangular, circular, and arched tunnels, respectively. Five groups of measurements are used to justify the model in different tunnels at different frequencies. Finally, in order to facilitate the use of the model, simplified analytical solutions for the dividing point in five specific application situations are derived. The results in this paper could help deepen the insight into the propagation mechanisms in tunnels.

1. Introduction

Effective prediction models of propagation properties in tunnels are highly requested in the design and planning phases of advanced radio systems. In order to describe the propagation characteristics inside tunnels, most models presented in the last four decades indicate that there is a "critical distance" [1, 2], normally called the break point [1–3]. Before the break point is the near-region, where the high-order modes are significant; guided propagation has not been well established, and, therefore, the signal suffers larger loss. After the break point is the far-region, where the high order modes have been greatly attenuated; guided propagation has been stabilized and undergoes a smaller loss [2, 4–6].

The distance from the transmitter to the break point is expressed by [1]

$$Z_{NR} = \mathrm{Max}\left(\frac{W^2}{\lambda}, \frac{H^2}{\lambda}\right), \tag{1}$$

where Z_{NR}, W, H, and λ denote the length of near-region, the width and the height of rectangular tunnel, as well as the signal wavelength in metres. This formula can be applied in arched and circular tunnel cases as the EM field distribution and attenuation of the modes in arched and circular tunnels are almost the same as the rectangular tunnel [7]. Please note that Z_{NR} is inversely proportional to the wavelength.

By making a review on the development of wireless communication systems, we can find that the near-region inside tunnels lengthens greatly resulting from the increase of working frequencies. In the public communication field, the representative systems can be listed as GSM (Global System for Mobile Communications), 3G (3rd Generation), Wi-Fi (Wireless Fidelity), and WiMAX (World Interoperability for Microwave Access). Their frequencies are 900/1800 MHz, 2 GHz, 2.4/5 GHz, 3.8 GHz, 5.7 GHz, and 5.8 GHz, respectively. By assuming the maximum of the width and the height of the equivalent rectangular tunnel to be 15 m, which is very common for the double-track subway tunnel

or railway tunnel, (1) calculates the length of the near-region in each system as 675/1350 m, 1500 m, 1800/3750 m, 2850 m, 4275 m, and 4350 m, respectively. In the dedicated communication area, the list could be TETRA (Terrestrial Trunked Radio) [8], GSM-R (Global System for Mobile Communications for Railway) [9], CBTC (Communication-Based Train Control System) [10], and DSRC (Dedicated Short-range Communications) [11]. Their frequencies are 400 MHz, 900 MHz, 2.4 GHz, and 5.8/5.9 GHz, respectively. The corresponding near-regions can be 300 m, 675 m, 1800 m, and 4350/4425 m, respectively. This great change reveals the fact that the near-region may occupy most of the propagation cell at high frequencies. Especially in some short tunnels or high reliable systems that require a moderate overlapping of the transmitters, the whole propagation cell could even only be in the near-region. However, there is no unanimous consensus, yet there is on the propagation in the near-region. Some researchers are inclined to interpret the propagation before the break point with the single ray (free space) theory [6, 12, 13], whereas others contend that it should be described by the multimode waveguide model [1, 2, 14]. In fact, a big deal of evidence proves that the free space mechanism should be established firstly and the multi-mode propagation mechanism comes later. Thus, in order to clearly reveal the propagation mechanism situation in the near-region, it is essential to model the accurate location of the dividing point between the two mechanisms. This paper presents a novel general analytical model that can be employed in arbitrary cross-sectional tunnels.

2. Modeling for the Propagation Mechanisms and Their Dividing Point

2.1. Geometrical Modeling for Rectangular, Circular, and Arched Tunnels. Generally speaking, rectangular, circular, and arched tunnels cover almost all the realistic application situations. An extensive comparison of theoretical and experimental results allowed us to show that the copolar field variation in an arched tunnel can be predicted with sufficient accuracy by using modal theory and assuming a rectangular tunnel [15]. Meanwhile, the EM field distribution and attenuation of the modes in circular waveguide are almost the same as the rectangle waveguide [16]. Hence, in the analysis of the propagation loss in the multi-mode waveguide segment, the tunnel's cross section is treated as an equivalent rectangle with a width of w and a height of h. A Cartesian coordinate system is set with its origin located at the center of the rectangle tunnel.

In the case of an arched tunnel, the size of the equivalent rectangular waveguide that is used in the model can be computed by taking the main horizontal dimension h close to the tunnel's floor size and computing the vertical dimension w using the "rule of thumb", that is,

$$h = \sqrt{4R^2 - w^2}, \tag{2}$$

where R is the radius of the arched-ceiling/wall's circle. This idealized geometry is common in modern road and railway tunnels [17]. In the case of a circular tunnel, $w = h = 2R$, where R is the radius of the radius of the cross-sectional circle.

2.2. Propagation Loss in Different Propagation Mechanisms

2.2.1. Propagation Loss in the Free Space Propagation Segment. In the adjacent region of the transmitter antenna, the angles of incidence from the ray to the wall (vertical, horizontal, and circular) are high resulting in high attenuation of reflected rays, whereas the path difference between direct and reflected rays may also cause additional attenuation; thus, only the direct ray significantly contributes to the strength of the received signal. The channel loss in this segment follows the free space loss attenuation [18]

$$PL(dB) = -10\log_{10}\left[\frac{\lambda^2}{(4\pi)^2|z_r - z_t|^2}\right], \tag{3}$$

where $|z_r - z_t|$ is the distance between the transmitter and receiver in meters and λ is the signal wavelength.

2.2.2. Propagation Loss in the Multimode Waveguide Segment. According to the modal theory, an equivalent rectangular tunnel can be regarded as an oversized imperfect hollow rectangular waveguide. Since the UHF is much higher than the cutoff frequency of the fundamental modes which is very low, a wide range of E_{mn} multiple modes propagate when the free space segment ends [12].

By employing the modal theory, the general expression of the attenuation constant with horizontally and vertically polarized E_{mn} modes inside various tunnels [19], such as circular tunnel, rectangular tunnel, arched tunnel, oval tunnel, and so forth can be given by

$$\begin{aligned}\alpha(m,n)^h &= \varphi\lambda^2\left(\frac{m^2\varepsilon_r}{w^3\sqrt{\varepsilon_r - 1}} + \frac{n^2}{h^3\sqrt{\varepsilon_r - 1}}\right)\frac{dB}{m},\\ \alpha(m,n)^v &= \varphi\lambda^2\left(\frac{m^2}{w^3\sqrt{\varepsilon_r - 1}} + \frac{n^2\varepsilon_r}{h^3\sqrt{\varepsilon_r - 1}}\right)\frac{dB}{m},\end{aligned} \tag{4}$$

where w and h denote the maximum of the width and the height, respectively; φ is a coefficient, its value varies by the different shape of the tunnel [20]: rectangular tunnel, $\varphi = 4.343$; circular tunnel, $\varphi = 5.09$; arched tunnel, $\varphi = 5.13$. ε_v and ε_h are relative permittivity for vertical and horizontal walls, with the typical values for concrete: $\varepsilon_v = \varepsilon_h = 5$ [1].

Besides the geometry of the tunnel, the roughness of walls of the tunnel influences the propagation loss as well. Hence, the attenuation owing to the roughness introduced by [2] is involved in the model. Finally, the propagation loss in the multi-mode waveguide segment can be obtained by considering both the polarizations and the roughness of walls;

$$\begin{aligned}L_{mn}^{v/h}(dB) = {}& 10\log_{10}\left[\sum_{i=1}^{m}\sum_{j=1}^{n}\times\sqrt{10^{2\alpha(i,j)^h|z_r - z_t|} + 10^{2\alpha(i,j)^v|z_r - z_t|}}\right]\\ &+ 8.686\pi^2\gamma^2\lambda\left(\frac{1}{w^4} + \frac{1}{h^4}\right)|z_r - z_t|,\end{aligned} \tag{5}$$

where γ is the root-mean-square roughness.

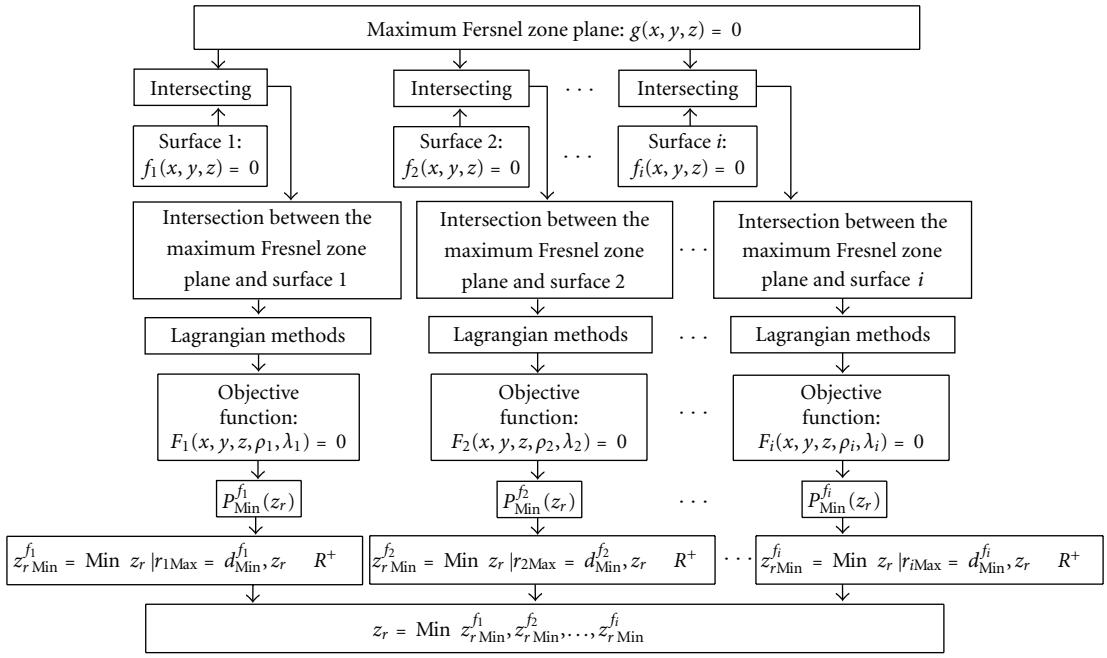

Figure 1: Flow chart of modeling for the diving point in arbitrary cross-sectional tunnels.

2.3. Modeling for Dividing Point between Different Propagation Mechanisms in Arbitrary Cross-Sectional Tunnels. In order to clarify the propagation mechanism situation, it is necessary to model accurately the location of the dividing point between the free space propagation segment and the multi-mode waveguide segment.

On the basis of the analysis of the propagation procedure inside tunnels, it can be known that the point where the first Fresnel zone is tangent to the walls of the tunnel is the dividing point between the two mechanisms. However, the localization of it is not an easy work. Since the interaction between the first Fresnel zone and the walls depends on a large number of factors, such as the locations of the transmitter and receiver, the dimensions of the tunnel, the working frequency, the computational time would be intolerable if all the elements were considered when we track the interaction and its change law. Thus, it is desirable to find a simple parameter representing the interaction.

According to the geometry, it is easy to determine the distance between the tangent line/curve (of the maximum Fresnel zone plate and the walls) and the middle point (of the line of sight between transmitter and receiver). If this distance is larger than the radius of the maximum first Fresnel zone plate, the first Fresnel zone can be treated as almost clear. We have to admit that in this case some parts inside the first Fresnel zone could still be blocked. But since the first Fresnel zone is a flat ellipsoid, such kind of slight obstruction does not result in many effective reflected rays or obvious diffractive loss. Hence, the free space propagation model can still work. When this distance is smaller than the radius, which means even the widest part of the first Fresnel zone is blocked, more severe obstruction occurs in the other parts. Thus, the relative relation between this distance and the radius can be employed to reflect the interaction between the first Fresnel zone and the walls to some extent. Furthermore, the location of the dividing point can be deduced when the distance and the radius are equal.

Figure 1 illustrates the flow chart of the concrete modeling process. The first step is to geometrically model the arbitrary cross-sectional tunnel and all the relative components. Figure 2 depicts the three-dimensional geometry schematic diagram of an arbitrary cross-sectional tunnel, transmitter, receiver, line of sight, and the maximum first Fresnel zone.

According to the three-dimensional solid geometry, the arbitrary cross-sectional tunnel consists of a set of plane surfaces and curved surfaces whose coordinates x, y, and z satisfy the following equation

$$f_i(x, y, z) = 0, \quad i = 1, 2, \ldots, n. \tag{6}$$

The coordinates of transmitter, receiver, and the middle point on the line of sight between transmitter and receiver are $P_t(x_t, y_t, z_t)$, $P_r(x_r, y_r, z_r)$, and $P_0(x_0, y_0, z_0)$; their relationships are expressed by

$$x_0 = \frac{x_r + x_t}{2}, \quad y_0 = \frac{y_r + y_t}{2}, \quad z_0 = \frac{z_r + z_t}{2}. \tag{7}$$

Then, the maximum Fresnel zone plane can be expressed by a plane in general type

$$\begin{aligned}(x_r - x_t)\left(x - \frac{x_r + x_t}{2}\right) + (y_r - y_t)\left(y - \frac{y_r + y_t}{2}\right) \\ + (z_r - z_t)\left(z - \frac{z_r + z_t}{2}\right) = 0.\end{aligned} \tag{8}$$

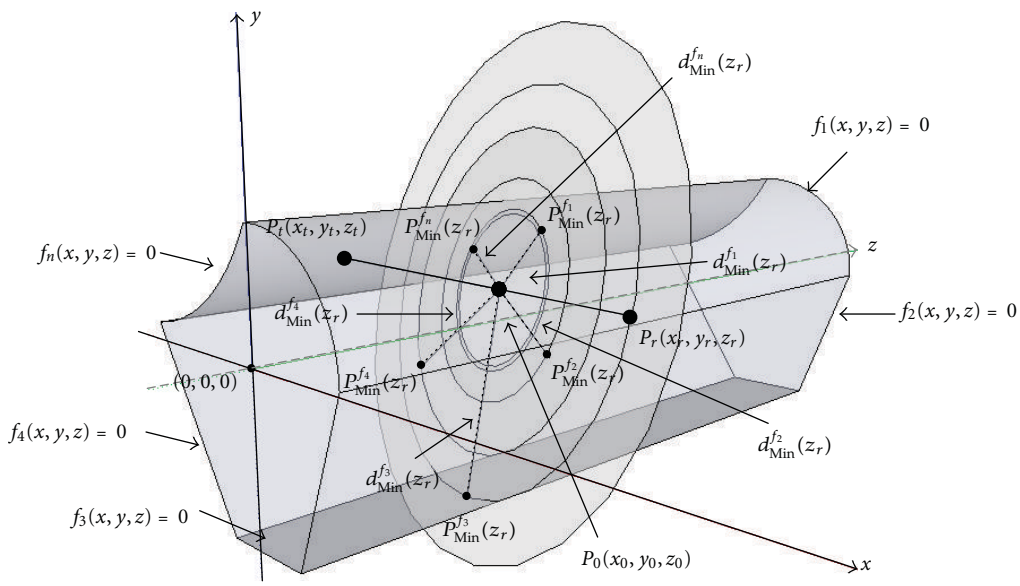

Figure 2: Detailed schematic diagram of the propagation inside arbitrary cross-sectional tunnels with the first Fresnel zone clearance.

Thus, the intersection between the maximum Fresnel zone plane and the surface f_i of the tunnel is a curve or a line which can be written by

$$\begin{aligned}(x_r - x_t)\left(x - \frac{x_r + x_t}{2}\right) + (y_r - y_t)\left(y - \frac{y_r + y_t}{2}\right)\\ + (z_r - z_t)\left(z - \frac{z_r + z_t}{2}\right) = 0,\\ f_i(x, y, z) = 0, \quad i = 1, 2, \ldots, n.\end{aligned} \tag{9}$$

Define the first equation as a function $g(x, y, z)$ by

$$\begin{aligned}g(x, y, z) = (x_r - x_t)\left(x - \frac{x_r + x_t}{2}\right)\\ + (y_r - y_t)\left(y - \frac{y_r + y_t}{2}\right)\\ + (z_r - z_t)\left(z - \frac{z_r + z_t}{2}\right).\end{aligned} \tag{10}$$

Define the second equation as a function $f_i(x, y, z)$.

In order to find the minimal distance between the intersection (line/curve) and the middle point $P_0(x_0, y_0, z_0)$ on the line of sight, the Lagrange multiplier method seeking extremum is employed. Construct a function as follows:

$$\begin{aligned}F_i(x, y, z, \rho_i, \lambda_i) = \left(x - \frac{x_r + x_t}{2}\right)^2 + \left(y - \frac{y_r + y_t}{2}\right)^2\\ + \left(z - \frac{z_r + z_t}{2}\right)^2 + \rho_i \cdot g(x, y, z)\\ + \lambda_i \cdot f_i(x, y, z),\end{aligned} \tag{11}$$

where ξ, and μ are the Lagrange multipliers. By seeking partial derivative of x, y, and z, respectively, (11) can be transformed to

$$\begin{aligned}\frac{\partial F_i}{\partial x} &= 2\left(x - \frac{x_r + x_t}{2}\right) + \rho_i \cdot (x_r - x_t) + \lambda_i \cdot \frac{\partial f_i}{\partial x} = 0,\\ \frac{\partial F_i}{\partial y} &= 2\left(y - \frac{y_r + y_t}{2}\right) + \rho_i \cdot (y_r - y_t) + \lambda_i \cdot \frac{\partial f_i}{\partial y} = 0,\\ \frac{\partial F_i}{\partial z} &= 2\left(z - \frac{z_r + z_t}{2}\right) + \rho_i \cdot (z_r - z_t) + \lambda_i \cdot \frac{\partial f_i}{\partial z} = 0,\\ \frac{\partial F_i}{\partial \rho_i} &= (x_r - x_t)\left(x - \frac{x_r + x_t}{2}\right) + (y_r - y_t)\left(y - \frac{y_r + y_t}{2}\right)\\ &\quad + (z_r - z_t)\left(z - \frac{z_r + z_t}{2}\right) = 0,\\ \frac{\partial F_i}{\partial \lambda_i} &= f_i = 0.\end{aligned} \tag{12}$$

By seeking the simultaneous solution of (12), the coordinate of intersection point with the minimal distance to $P_0(x_0, y_0, z_0)$ can be obtained: $p^{f_i}_{\text{Min}}(x^{f_i}(z_r), y^{f_i}(z_r), z^{f_i}(z_r))$. Therefore, the minimal distance between P_0 and the intersection (line/curve) between the maximum Fresnel zone plane and the surface f_i of the tunnel can be expressed as

$$\begin{aligned}d^{f_i}_{\text{Min}}(z_r) = \Bigg[\left(x^{f_i}(z_r) - \frac{x_r + x_t}{2}\right)^2\\ + \left(y^{f_i}(z_r) - \frac{y_r + y_t}{2}\right)^2\\ + \left(z^{f_i}(z_r) - \frac{z_r + z_t}{2}\right)^2\Bigg]^{1/2}.\end{aligned} \tag{13}$$

On the basis of the propagation theory, the radius of the first Fresnel zone is determined by

$$r_1 = \sqrt{\frac{\lambda d_1 d_2}{d_1 + d_2}}, \tag{14}$$

where d_1 denotes the distance between the transmitter and the interaction between the line of sight and the first Fresnel zone, and d_2 denotes the distance between the receiver and the interaction. When the interaction is the middle point P_0, $d_1 = d_{P_tP_0} = d_2 = d_{P_0P_r} = (1/2)d_{P_tP_r}$. At this point, the radius gets the maximum value of the first Fresnel zone

$$r_{1\,\mathrm{Max}}(z_r) = \frac{1}{2}\sqrt{\lambda d_{P_tP_r}}. \tag{15}$$

The propagation theory indicates that the free space loss channel model can be applied if the first Fresnel zone is free of any obstacles. Therefore, if only the wall $f_i(x, y, z)$ of the tunnel could be touched by the maximum first Fresnel zone, the dividing point between two propagation mechanisms locates at $z_{r\,\mathrm{Min}}^{f_i}$ which is the minimal positive real root of the

$$r_{1\,\mathrm{Max}}(z_r) = d_{\mathrm{Min}}^{f_i}(z_r). \tag{16}$$

Hence, $z_{r\,\mathrm{Min}}^{f_i}$ can be expressed by

$$z_{r\,\mathrm{Min}}^{f_i} = \mathrm{Min}\left\{z_r \mid r_{i\,\mathrm{Max}} = d_{\mathrm{Min}}^{f_i}, z_r \in R^+\right\}, \tag{17}$$

which means the maximum first Fresnel zone first touches the surface $f_i(x, y, z)$ of tunnels.

However, in fact, there are totally n walls of the arbitrary cross-sectional tunnels that could be tangent to the maximum first Fresnel zone. Therefore, the dividing point locates at z_r when the maximum first Fresnel zone first touches any one of the walls. Thus, the dividing point locates at

$$z_r = \mathrm{Min}\left\{z_{r\,\mathrm{Min}}^{f_i}, i = 1, 2, \ldots, n\right\}, \tag{18}$$

which means the maximum first Fresnel zone first touches any one of the surfaces of tunnels.

3. Dividing Point Model Validation in Rectangular, Circular, and Arched Tunnels

Theoretically, the general model can be employed in arbitrary cross-sectional tunnels by substituting various parameters. Here, we give the specific model and corresponding validation in the main types of tunnels in reality (rectangular, circular, and arched tunnels), respectively.

3.1. Dividing Point Model in Rectangular Tunnel. Figure 3 demonstrates the propagation inside a rectangular tunnel with the first Fresnel zone clearance. In a rectangular tunnel, two vertical walls and two horizontal planes can possibly obstruct the first Fresnel zone; thus, by substituting following functions:

(i) Left vertical wall: $f_{\text{Pla-}L} : x = -b$;

(ii) Right vertical wall: $f_{\text{Pla-}R} : x = b$;

(iii) ceiling: $f_{\text{Pla-}C} : y = a$;

(iv) Floor: $f_{\text{Pla-}F} : y = -c$;

to (6), $d_{\mathrm{Min}}^{\text{Pla-}L}(z_r)$, $d_{\mathrm{Min}}^{\text{Pla-}R}(z_r)$, $d_{\mathrm{Min}}^{\text{Pla-}C}(z_r)$, and $d_{\mathrm{Min}}^{\text{Pla-}F}(z_r)$ corresponding to the minimal distance from P_0 to the intersection line on the left vertical wall, right vertical wall, ceiling, and floor can be obtained. By using (16), the dividing point location of $z_{r\,\mathrm{Min}}^{\text{Pla-}L}$, $z_{r\,\mathrm{Min}}^{\text{Pla-}R}$, $z_{r\,\mathrm{Min}}^{\text{Pla-}C}$, and $z_{r\,\mathrm{Min}}^{\text{Pla-}F}$, corresponding to the touching of the maximum first Fresnel zone and the left wall, right wall, ceiling, and floor of rectangular tunnels, respectively, can be derived as

$$\begin{aligned}
z_{r\,\mathrm{Min}}^{\text{Pla-}L} &= \mathrm{Min}\left\{z_r \mid r_{1\,\mathrm{Max}}(z_r) = d_{\mathrm{Min}}^{\text{Pla-}L}, z_r \in R^+\right\},\\
z_{r\,\mathrm{Min}}^{\text{Pla-}R} &= \mathrm{Min}\left\{z_r \mid r_{1\,\mathrm{Max}}(z_r) = d_{\mathrm{Min}}^{\text{Pla-}R}, z_r \in R^+\right\},\\
z_{r\,\mathrm{Min}}^{\text{Pla-}C} &= \mathrm{Min}\left\{z_r \mid r_{1\,\mathrm{Max}}(z_r) = d_{\mathrm{Min}}^{\text{Pla-}C}, z_r \in R^+\right\},\\
z_{r\,\mathrm{Min}}^{\text{Pla-}F} &= \mathrm{Min}\left\{z_r \mid r_{1\,\mathrm{Max}}(z_r) = d_{\mathrm{Min}}^{\text{Pla-}F}, z_r \in R^+\right\}.
\end{aligned} \tag{19}$$

Then, the dividing point between two propagation mechanisms inside a rectangular tunnel locates at z_r:

$$z_r = \mathrm{Min}\left(z_{r\,\mathrm{Min}}^{\text{Pla-}R}, z_{r\,\mathrm{Min}}^{\text{Pla-}R}, z_{r\,\mathrm{Min}}^{\text{Pla-}C}, z_{r\,\mathrm{Min}}^{\text{Pla-}F}\right). \tag{20}$$

In order to validate the performance of the model in rectangular tunnels, a set of measurements is taken in one of the longest tunnels of the new 450 km high-speed train line from Madrid to Lleida in Spain [1]: $\lambda = 0.33$, $a = 3.15$, $b = 5.35$, $c = 3.15$, $x_t = -5.15$, $y_t = 0.85$, $z_t = 0$, $x_r = -2.35$, and $y_r = -0.15$. By seeking the minimal positive real root of the simultaneous solution of (12), the results are the coordinates of the intersection points in each surface with the minimal distance to $P_0(x_0, y_0, z_0)$ in the rectangular tunnel: $p_{\mathrm{Min}}^{\text{Pla-}L}(-5.35, 0.35, 15.58)$, $p_{\mathrm{Min}}^{\text{Pla-}R}(5.35, 0.35, 497.33)$, $p_{\mathrm{Min}}^{\text{Pla-}C}(-3.75, 3.15, 47.1)$, and $p_{\mathrm{Min}}^{\text{Pla-}F}(-3.75, -3.15, 73.54)$. By solving (16) and (17), $z_{r\,\mathrm{Min}}^{\text{Pla-}L} = 30.86$, $z_{r\,\mathrm{Min}}^{\text{Pla-}R} = 994.72$, $z_{r\,\mathrm{Min}}^{\text{Pla-}C} = 94.14$, and $z_{r\,\mathrm{Min}}^{\text{Pla-}F} = 147.12$. Hence, according to (18), the dividing point locates at $z_r = 30.86$ in this case. Comparison results are shown in Table 1.

Table 1: Comparisons of the dividing point between the model, and the measurements inside rectangular circular, and arched tunnels.

Tunnel	Frequency (GHz)	Measured result	Theoretical prediction
Railway tunnel in Spain [1]	0.9	30–35 m	30.86 m
Vehicle tunnel in France [21]	0.45	35–40 m	37.88 m
Vehicle tunnel in France [21]	0.9	70–75 m	75.76 m
Pedestrian tunnel in Europe [12]	0.4	15 m	13.65 m
Road tunnel Austria-Slovenia [12]	0.4	15 m	15.41 m

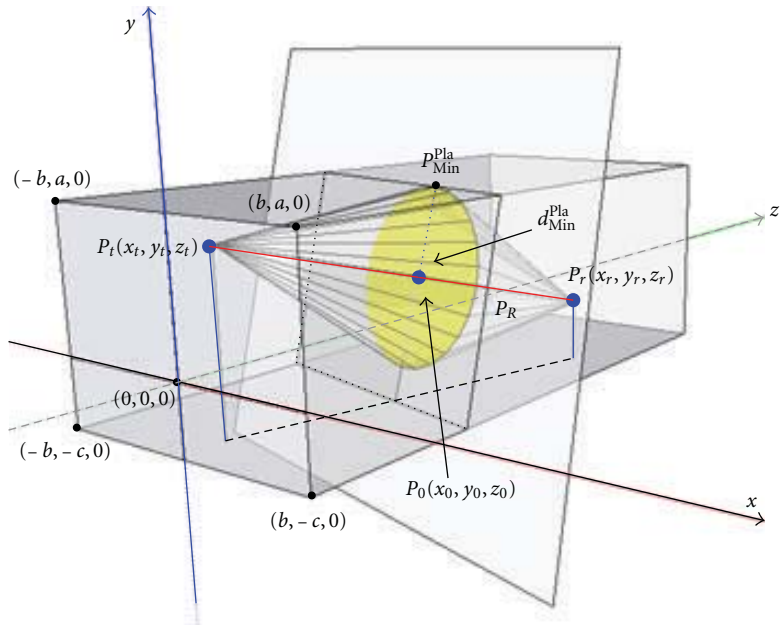

Figure 3: Detailed schematic diagram of the propagation inside rectangular tunnels with the first Fresnel zone clearance.

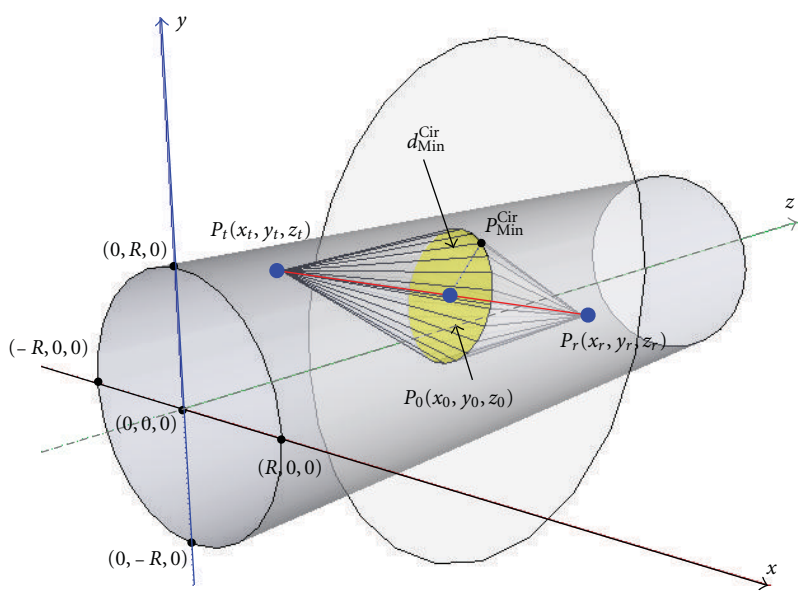

Figure 4: Detailed schematic diagram of the propagation inside circular tunnels with the first Fresnel zone clearance.

3.2. Dividing Point Model in Circular Tunnel. Figure 4 illustrates the propagation inside circular tunnel with the first Fresnel zone clearance. In circular tunnel, the circular walls can possibly obstruct the first Fresnel zone; thus, by substituting the following function:

(i) Circular wall: $f_{\text{Cir}} : x^2 + y^2 = R^2$ to (6), $d_{\text{Min}}^{\text{Cir}}(z_r)$ corresponding to the minimal distance from P_0 to the intersection curve on the circular wall can be obtained. By using (16), the dividing point location of $z_{r\,\text{Min}}^{\text{Cir}}$ corresponding to the touching of the maximum first Fresnel zone and the circular wall of tunnels can be obtained as

$$z_{r\,\text{Min}}^{\text{Cir}} = \text{Min}\left\{z_r \mid r_{1\,\text{Max}}(z_r) = d_{\text{Min}}^{\text{Pla-}L}, z_r \in R^+\right\}. \quad (21)$$

Then, the dividing point between mechanisms inside a circular tunnel locates at z_r:

$$z_r = \text{Min}\left(z_{r\,\text{Min}}^{\text{Cir}}\right) = z_{r\,\text{Min}}^{\text{Cir}}. \quad (22)$$

In order to validate the performance of the model in circular tunnels, two groups of experiments in a 3.5 km-long straight tunnel in the Massif Central of south-central France reported in [21] have been employed. Relevant parameters in these measurements are cited as follows:

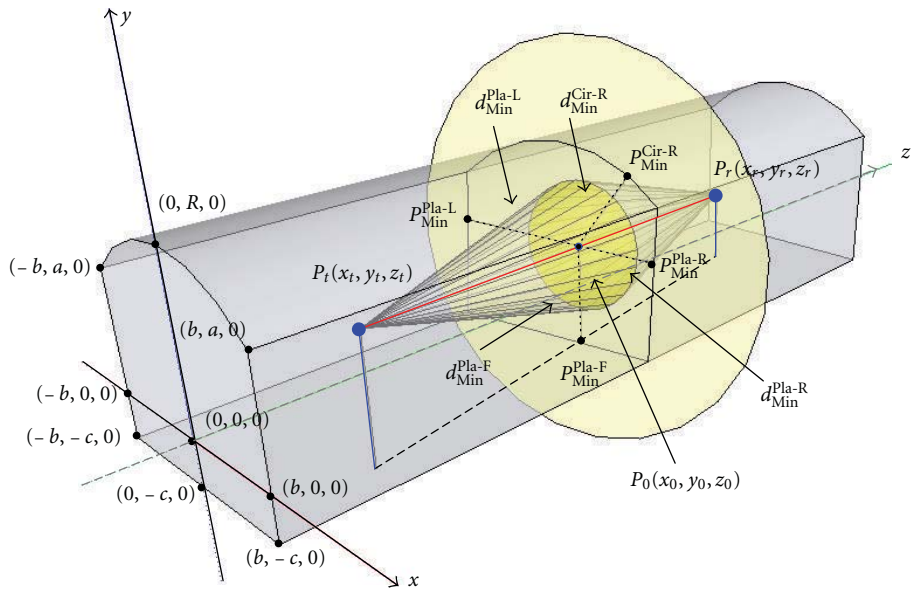

Figure 5: Detailed schematic diagram of the propagation inside the arched tunnel "Type I" with the first Fresnel zone clearance.

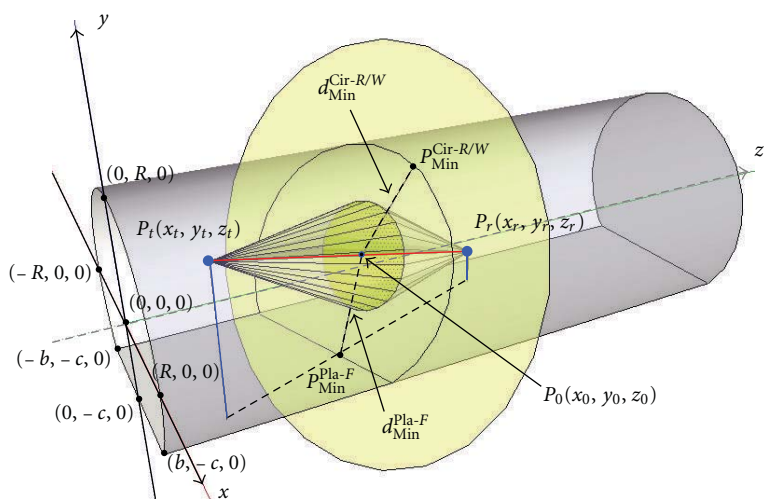

Figure 6: Detailed schematic diagram of the propagation inside the arched tunnel "Type II" with the first Fresnel zone clearance.

(i) first group of measurements [21]: $\lambda = 0.66$, $R = 4.3$, $x_t = 1.8$, $y_t = 0$, $z_t = 0$, $x_r = 1.8$, $y_r = 0$.

(ii) second group of measurements [21]: $\lambda = 0.33$, $R = 4.3$, $x_t = 1.8$, $y_t = 0$, $z_t = 0$, $x_r = 1.8$, $y_r = 0$.

In the case of the first group, by seeking the simultaneous solution of (12), the minimal positive real root is the coordinate of intersection point with the minimal distance to $P_0(x_0, y_0, z_0)$ in the measured tunnel: $p_{\text{Min}}^{\text{Cir}}(4.3, 0, 18.94)$. By solving (16) and (17), $z_{r\,\text{Min}}^{\text{Cir}} = 37.88$. Hence, according to (18), the dividing point locates at $z_r = 37.88$. In term of the second group, $p_{\text{Min}}^{\text{Cir}}(4.3, 0, 37.88)$, $z_{r\,\text{Min}}^{\text{Cir}} = 75.76$. All the comparison results are shown in Table 1.

3.3. Dividing Point Model in Arched Tunnel. There are mainly two kinds of arched tunnels. "Type I" consists of three plane walls and an arched roof; "Type II" includes arched walls and roof, but a plane floor, more like a semicircle. Figures 5 and 6 demonstrate the cross-sectional geometry for both types of arched tunnels. It is noteworthy that both the arched tunnel "Type I" and "Type II" can be seen as a combination of a circular tunnel and a rectangular tunnel, but in different configurations. Hence, the dividing point can be modeled in a circular tunnel and a rectangular tunnel independently and then determined by their specific combinations.

Figure 5 shows the propagation inside the arched tunnel "Type I" with the first Fresnel zone clearance. In "Type I", two vertical walls and the floor in the rectangular tunnel as well as the arched roof in the circular tunnel can possibly obstruct the first Fresnel zone; thus, by substituting the functions of the roof, walls, and floor to (6):

(i) left vertical wall: $x = -b$;

(ii) right vertical wall: $x = b$;

(iii) floor: $y = -c$;

(iv) arched roof: $x^2 + y^2 = R^2$, $|x| \le b$, $a \le y \le R$;

$d_{\text{Min}}^{\text{Cir-}R}(z_r)$, $d_{\text{Min}}^{\text{Pla-}R}(z_r)$, $d_{\text{Min}}^{\text{Pla-}L}(z_r)$, and $d_{\text{Min}}^{\text{Pla-}F}(z_r)$ corresponding to the minimal distance from P_0 to the intersection (line/curve) on the arched roof, the right/left wall and the floor can be obtained. By employing (17), the dividing point location of $z_{r\text{Min}}^{\text{Cir-}R}$, $z_{r\text{Min}}^{\text{Pla-}R}$, $z_{r\text{Min}}^{\text{Pla-}L}$, and $z_{r\text{Min}}^{\text{Pla-}F}$ corresponding to the touching of the maximum first Fresnel zone and every wall of arched tunnels can be deduced as

$$\begin{aligned} z_{r\text{Min}}^{\text{Cir-}R} &= \text{Min}\left\{z_r \mid r_{1\,\text{Max}}(z_r) = d_{\text{Min}}^{\text{Cir-}R}, z_r \in R^+\right\}, \\ z_{r\text{Min}}^{\text{Pla-}R} &= \text{Min}\left\{z_r \mid r_{1\,\text{Max}}(z_r) = d_{\text{Min}}^{\text{Pla-}R}, z_r \in R^+\right\}, \\ z_{r\text{Min}}^{\text{Pla-}L} &= \text{Min}\left\{z_r \mid r_{1\,\text{Max}}(z_r) = d_{\text{Min}}^{\text{Pla-}L}, z_r \in R^+\right\}, \\ z_{r\text{Min}}^{\text{Pla-}F} &= \text{Min}\left\{z_r \mid r_{1\,\text{Max}}(z_r) = d_{\text{Min}}^{\text{Pla-}F}, z_r \in R^+\right\}. \end{aligned} \tag{23}$$

Thus, the dividing point inside the arched tunnel "Type I" locates at z_r:

$$z_r = \text{Min}\left(z_{r\text{Min}}^{\text{Cir-}R}, z_{r\text{Min}}^{\text{Pla-}R}, z_{r\text{Min}}^{\text{Pla-}L}, z_{r\text{Min}}^{\text{Pla-}F}\right). \tag{24}$$

Figure 6 illustrates the propagation inside the arched tunnel "Type II" with the first Fresnel zone clearance. In "Type II", only the floor in the rectangular tunnel and the arched roof/wall in the circular tunnel can possibly obstruct the first Fresnel zone; therefore, by substituting the functions of the arched roof and the floor to (6):

(i) floor: $y = -c$;

(ii) arched roof: $x^2 + y^2 = R^2, -c \le y \le R$;

$d_{\text{Min}}^{\text{Cir-}R/W}(z_r)$ and $d_{\text{Min}}^{\text{Pla-}F}(z_r)$ corresponding to the minimal distance from P_0 to the intersection (line/curve) on the arched roof/wall and the floor can be obtained. Then, the dividing point location of $z_{r\text{Min}}^{\text{Cir-}R/W}$ and $z_{r\text{Min}}^{\text{Pla-}F}$ corresponding to the touching of the maximum first Fresnel zone and every wall can be derived as

$$\begin{aligned} z_{r\text{Min}}^{\text{Cir-}R/W} &= \text{Min}\left\{z_r \mid r_{1\,\text{Max}}(z_r) = d_{\text{Min}}^{\text{Cir-}R}, z_r \in R^+\right\}, \\ z_{r\text{Min}}^{\text{Pla-}F} &= \text{Min}\left\{z_r \mid r_{1\,\text{Max}}(z_r) = d_{\text{Min}}^{\text{Pla-}F}, z_r \in R^+\right\}. \end{aligned} \tag{25}$$

The dividing point inside the arched tunnel "Type II" locates at z_r:

$$z_r = \text{Min}\left(z_{r\text{Min}}^{\text{Cir-}R/W}, z_{r\text{Min}}^{\text{Pla-}F}\right). \tag{26}$$

Two groups of measurement campaigns have been used for validating the model in arched tunnels.

(i) The first group of received signal strength measurements are performed in a railway tunnel typical to Europe at 400 MHz. The tunnel is 520 m long and originally engineered for a railway, but the line was closed, and it is now used by pedestrians and cyclists [12]: $\lambda = 0.75$, $R = 2.35$, $x_t = 0$, $y_t = 0$, $z_t = 0$, $x_r = 0$, $y_r = 0$, $A = 0$, and $c = 1.5$. By joint solving (12), the coordinate of intersection point with the minimal distance to $P_0(x_0, y_0, z_0)$ in the arched tunnel can be derived: $p_{\text{Min}}^{\text{Cir-}R/W}(0, 2.35, 13.48)$, $p_{\text{Min}}^{\text{Pla-}F}(0, -1.5, 6.85)$. By solving (16) and (17), $z_{r\text{Min}}^{\text{Cir-}R/W} = 27$, $z_{r\text{Min}}^{\text{Pla-}F} = 13.65$. Hence, the dividing point locates at $z_r = 13.65$.

(ii) The second set of measurements are carried out in a dual carriageway road tunnel linking Austria and Slovenia at 400 MHz. The tunnel was closed in one direction at the time, while the second lane operated normally [12]: $\lambda = 0.75$, $R = 5.28$, $x_t = 3.2$, $y_t = -0.8$, $z_t = 0$, $x_r = 3.2$, $y_r = -0.8$, $c = 2.5$. By seeking the simultaneous solution of (12), the coordinate of intersection point with the minimal distance to $P_0(x_0, y_0, z_0)$ can be obtained: $p_{\text{Min}}^{\text{Cir-}R/W}(5.12, -1.28, 10.47)$, $p_{\text{Min}}^{\text{Pla-}F}(3.2, -2.5, 7.71)$. so, $z_{r\text{Min}}^{\text{Cir-}R/W} = 20.94$, $z_{r\text{Min}}^{\text{Pla-}F} = 15.41$. Equation (18) indicates the dividing point locating at $z_r = 15.41$, which means the Maximum first Fresnel zone first touches the roof of the arched tunnel.

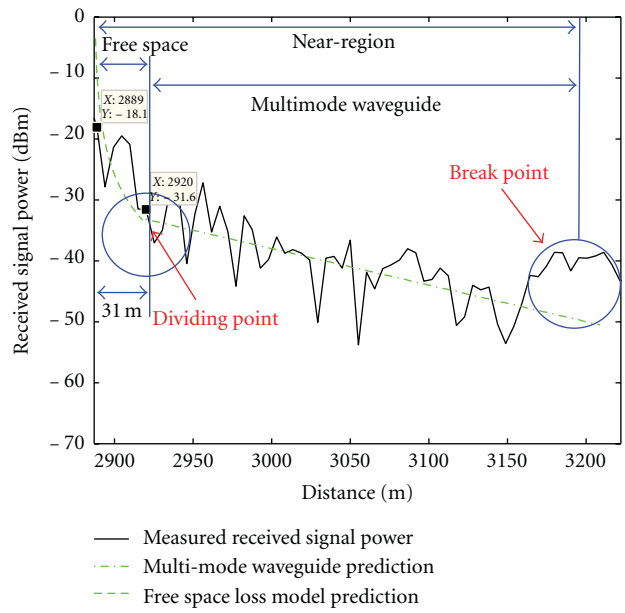

Figure 7: Comparisons between measurement and theory on the propagation mechanisms and their dividing point in the near-region inside an arched tunnel.

3.4. Validation Results. Table 1 illustrates the global comparisons of the dividing point between the results of model and the measurements inside rectangular, circular, and arched tunnels. The location of the dividing point is extracted from the measurements in the following way: the free space propagation model was compared with the measured received signal power; then, the point, in front of which the fitting is good and behind which is bad, was found. As shown in Table 1, the results indicate that the model for the dividing

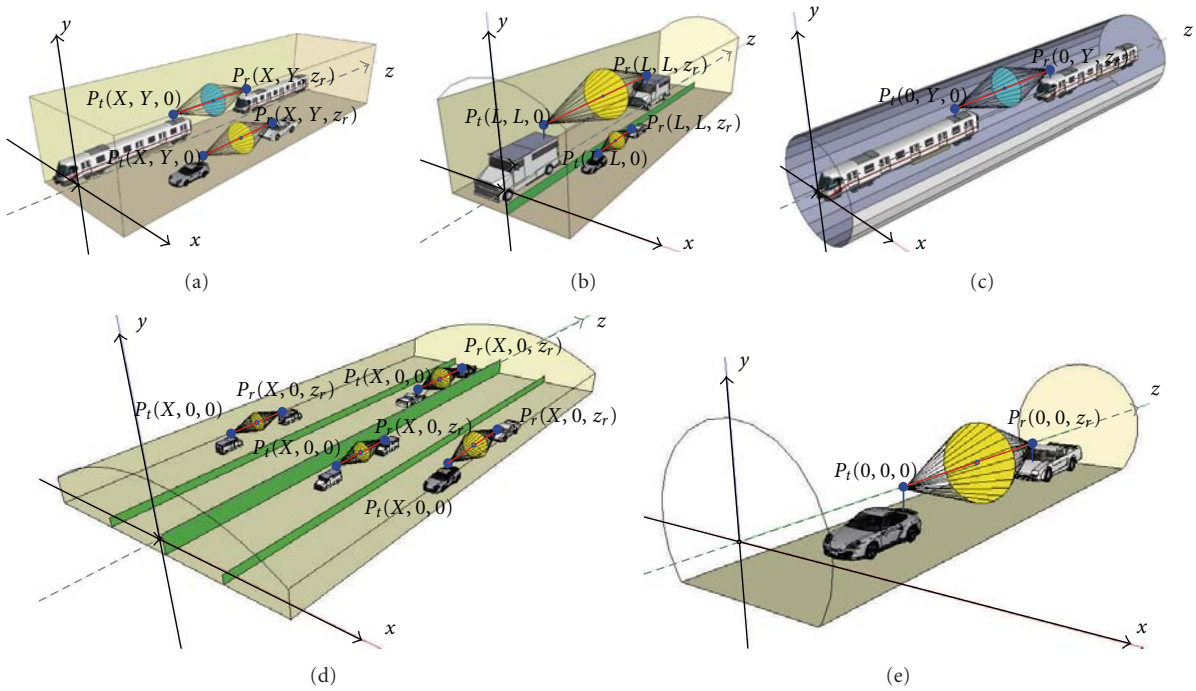

Figure 8: (a) specific situation one; (b) specific situation two; (c) specific situation three; (d) specific situation Four; (e) specific situation five.

point has a good performance in different types of tunnels at various frequencies.

To clearly depict the effect of the entire propagation model in the near-region of arbitrary cross-sectional tunnels, the measurement carried out in a railway tunnel in Spain at 900 MHz [1] has been employed. As shown in Figure 7, the dividing point separates two propagation segments. The propagation in the segment before the dividing point follows the free space mechanism, and corresponding free space loss model has a good agreement with the measured received signal power. The segment after the dividing point is dominated by the multi-mode waveguide mechanism, and the multimode waveguide loss model shows a good performance as well. The accurate location of the dividing point clearly distinguishes between two propagation mechanisms in the near-region. Therefore, the previous different and seemingly conflicting views [1, 2, 6, 12–14] have been unified by this general model.

All the validation results and comparisons offered above implies that the model for the propagation mechanisms and their dividing point in the near-region are valid and easy to be used in arbitrary cross-sectional tunnels.

4. Dividing Point Model Simplification and Discussion

In some real applications, the locations of transmitters and receivers, as well as the motion trajectories of mobile stations follow certain rules. In this section, the simplified formulas of the diving point model in rectangular, circular, and arched tunnels are deduced corresponding to five application situations.

Figure 8(a) illustrates specific situation one: in some systems, such as Dedicated Short-Range Communications (DSRC) [11], the communication is going on between different vehicles (car or carriage). In this case, the transmitter and the receiver always have similar heights and similar tracks: $x_t = x_r = X$, $y_t = y_r = Y$. Figure 8(b) depicts specific situation two, which can be met in DSRC, particularly in the dual carriageway road tunnel where the antennas of transmitter and receiver on vehicle have similar horizontal and vertical distance from the center of the cross-section: $x_t = x_r = y_t = y_r = L$. Figure 8(c) shows specific situation three: unlike specific situation two, this situation usually occurs in the one-way narrow tunnel, for both car and train. That means all the communication units move along the central track with similar high antennas: $x_t = x_r = 0$, $y_t = y_r = Y$. Figure 8(d) demonstrates specific situation four: like specific situation three, this situation requirements can be met in multi-way wide tunnel, for both cars and trains. In this case, all the communication units move along the same track and the antennas' heights approximately equal the center of the cross-section: $x_t = x_r = X$, $y_t = y_r = 0$; Figure 8(e) shows specific situation five: in some long tunnels, especially with the operating frequency of several GHz, the near-region is very long. In this case, by using the modal theory, the transmitter and the receiver can be approximated to be located at the center of the tunnel's cross-section: $x_t = x_r = 0$, $y_t = y_r = 0$.

Table 2: Simplification of the dividing point model in certain specific situations.

Situation	Condition	Tunnel	Type	Dividing point z_r
One	$(x_t = x_r = X,$	Rectangular	—	$\mathrm{Min}\left(\frac{4(a-Y)^2}{\lambda}, \frac{4(b \pm X)^2}{\lambda}, \frac{4(c+Y)^2}{\lambda}\right)$
	$y_t = y_r = Y)$	Circular	—	$\frac{4\left(R-\sqrt{X^2+Y^2}\right)^2}{\lambda}$
		Arched	Type I	$\mathrm{Min}\left(\frac{4\left(R-\sqrt{X^2+Y^2}\right)^2}{\lambda}, \frac{4(b \pm X)^2}{\lambda}, \frac{4(c+Y)^2}{\lambda}\right)$
		Arched	Type II	$\mathrm{Min}\left(\frac{4\left(R-\sqrt{X^2+Y^2}\right)^2}{\lambda}, \frac{4(c+Y)^2}{\lambda}\right)$
Two	$(x_t = x_r = L,$	Rectangular	—	$\mathrm{Min}\left(\frac{4(a-L)^2}{\lambda}, \frac{4(b \pm L)^2}{\lambda}, \frac{4(c+L)^2}{\lambda}\right)$
	$y_t = y_r = L)$	Circular	—	$\frac{4(R-\sqrt{2}L)^2}{\lambda}$
		Arched	Type I	$\mathrm{Min}\left(\frac{4(R-\sqrt{2}L)^2}{\lambda}, \frac{4(b \pm L)^2}{\lambda}, \frac{4(c+L)^2}{\lambda}\right)$
		Arched	Type II	$\mathrm{Min}\left(\frac{4(R-\sqrt{2}L)^2}{\lambda}, \frac{4(c+L)^2}{\lambda}\right)$
Three	$(x_t = x_r = 0,$	Rectangular	—	$\mathrm{Min}\left(\frac{4(a-Y)^2}{\lambda}, \frac{4b^2}{\lambda}, \frac{4(c+Y)^2}{\lambda}\right)$
	$y_t = y_r = Y)$	Circular	—	$\frac{4(R-Y)^2}{\lambda}$
		Arched	Type I	$\mathrm{Min}\left(\frac{4(R-Y)^2}{\lambda}, \frac{4b^2}{\lambda}, \frac{4(c+Y)^2}{\lambda}\right)$
		Arched	Type II	$\mathrm{Min}\left(\frac{4(R-Y)^2}{\lambda}, \frac{4(c+Y)^2}{\lambda}\right)$
Four	$(x_t = x_r = X,$	Rectangular	—	$\mathrm{Min}\left(\frac{4a^2}{\lambda}, \frac{4(b \pm X)^2}{\lambda}, \frac{4c^2}{\lambda}\right)$
	$y_t = y_r = 0)$	Circular	—	$\frac{4(R-X)^2}{\lambda}$
		Arched	Type I	$\mathrm{Min}\left(\frac{4(R-X)^2}{\lambda}, \frac{4(b \pm X)^2}{\lambda}, \frac{4c^2}{\lambda}\right)$
		Arched	Type II	$\mathrm{Min}\left(\frac{4(R-X)^2}{\lambda}, \frac{4c^2}{\lambda}\right)$
Five	$(x_t = x_r = 0,$	Rectangular	—	$\mathrm{Min}\left(\frac{4a^2}{\lambda}, \frac{4b^2}{\lambda}, \frac{4c^2}{\lambda}\right)$
	$y_t = y_r = 0)$	Circular	—	$\frac{4R^2}{\lambda}$
		Arched	Type I	$\mathrm{Min}\left(\frac{4R^2}{\lambda}, \frac{4b^2}{\lambda}, \frac{4c^2}{\lambda}\right)$
		Arched	Type II	$\mathrm{Min}\left(\frac{4R^2}{\lambda}, \frac{4c^2}{\lambda}\right)$

As shown in Table 2, the location of the dividing point in each case can be expressed by simple formulas corresponding to rectangular, circular, and arched tunnels (both "Type I" and "Type II").

All the simplified formulas provide an easy way to determine the location of the areas corresponding to different propagation mechanisms in the near-region, under the realistic application scenarios. Summarizing the general character of the simplified formulas, we have found that the minimal absolute distance between antennas and any of the tunnel surfaces is the dominant factor in the calculation of these cases. This conclusion can be very useful for the system designer to control different mechanism-based propagation areas in the near-region within tunnels. For instance, using this model, new communication based train control system designers can expand or suppress certain propagation mechanisms according their design requirements.

5. Conclusion

This paper clarifies the propagation mechanism situation in the near-region of tunnels. The main contribution of this paper is to present a general analytical approach and model for the dividing point between different propagation mechanisms in arbitrary cross-sectional tunnels for the first time. With the accurate localization of the dividing point, the existing seemingly conflicting views on the propagation in the near-region have been unified. From both the theoretical and measured results in five typical pedestrian, road, and railway tunnels, the dividing point locates from 13.65 to 75.76 m when the frequency ranges from 400 MHz to 900 MHz. This location could be further when the frequency is higher or when the transmitter/receiver is further away from the walls of tunnels.

In order to facilitate the implementation of the proposed model, the specific model in the main types of tunnels (rectangular, circular, and arched tunnels) is deduced. Particularly, in terms of five realistic application situations, the simplified models are given. It has been found that in these cases the minimal absolute distance between the antennas and any of the tunnel surfaces dominates the localization of the dividing point. This conclusion can effectively help system designers to control different mechanism-based propagation areas. The analysis, approach, and model in this paper can be essential and heuristic to a deeper understanding of the propagation mechanism inside tunnel, and can be applied in the realistic radio system design. Future work is to extend the presented model from the straight tunnel to the curved tunnel by considering the influence of the curve.

Acknowledgments

The authors express their thanks to the supports from the NNSF of China under Grants 60830001 and 61222105, Program for New Century Excellent Talents in University under Grant NCET-09-0206, Beijing NSF 4112048, Fundamental Research Funds for the Central Universities 2010JBZ008, State Key Laboratory of Rail Traffic Control and Safety (RCS2011ZZ008, RCS2010 K008, and RCS2011 K008), and TECRAIL Project of the Polytechnic University of Madrid IPT-2011-1034-370000.

References

[1] C. Briso-Rodríguez, J. M. Cruz, and J. I. Alonso, "Measurements and modeling of distributed antenna systems in railway tunnels," *IEEE Transactions on Vehicular Technology*, vol. 56, no. 5, pp. 2870–2879, 2007.

[2] Y. P. Zhang and Y. Hwang, "Enhancement of rectangular tunnel waveguide model," in *Proceedings of the Asia-Pacific Microwave Conference (APMC '97)*, pp. 197–200, December 1997.

[3] Y. P. Zhang and Y. Hwang, "Characterization of UHF radio propagation channels in tunnel environments for microcellular and personal communications," *IEEE Transactions on Vehicular Technology*, vol. 47, no. 1, pp. 283–296, 1998.

[4] J. Alonso, B. Izquierdo, and J. Romeu, "Break point analysis and modelling in subway tunnels," in *Proceedings of the 3rd European Conference on Antennas and Propagation (EuCAP '09)*, pp. 3254–3258, March 2009.

[5] K. Guan, Z. Zhong, B. Ai, and C. Briso-Rodríguez, "Research of propagation characteristics of break point; Near zone and far zone under operational subway condition," in *Proceedings of the 6th International Wireless Communications and Mobile Computing Conference (IWCMC '10)*, pp. 114–118, July 2010.

[6] Y. P. Zhang, "Novel model for propagation loss prediction in tunnels," *IEEE Transactions on Vehicular Technology*, vol. 52, no. 5, pp. 1308–1314, 2003.

[7] J. M. Molina-Garcia-Pardo, M. Lienard, A. Nasr, and P. Degauque, "On the possibility of interpreting field variations and polarization in arched tunnels using a model for propagation in rectangular or circular tunnels," *IEEE Transactions on Antennas and Propagation*, vol. 56, no. 4, pp. 1206–1211, 2008.

[8] ETSI ETR 300-3 ed.1 (2000-02), "Terrestrial Trunked Radio (TETRA), Voice plus Data (V+D), Designers' guide, Part 3: Direct Mode Operation (DMO)," 2000.

[9] http://www.uic.asso.fr.

[10] "IEEE standard for Communications-Based Train Control (CBTC) performance and functional requirements," 1999.

[11] Notice of Proposed Rulemaking and Order FCC 03-324, Federal Communications Commission, 2003.

[12] A. Hrovat, G. Kandus, and T. Javornik, "Four-slope channel model for path loss prediction in tunnels at 400 MHz," *IET Microwaves, Antennas and Propagation*, vol. 4, no. 5, pp. 571–582, 2010.

[13] Y. P. Zhang, G. X. Zheng, and J. H. Sheng, "Radio propagation at 900 MHz in underground coal mines," *IEEE Transactions on Antennas and Propagation*, vol. 49, no. 5, pp. 757–762, 2001.

[14] T. Klemenschits and E. Bonek, "Radio coverage of road tunnels at 900 and 1800 MHz by discrete antennas," in *Proceedings of the 5th IEEE International Symposium on PIMRC*, vol. 2, pp. 411–415, 1994.

[15] J. M. Molina-Garcia-Pardo, M. Lienard, A. Nasr, and P. Degauque, "On the possibility of interpreting field variations and polarization in arched tunnels using a model for propagation in rectangular or circular tunnels," *IEEE Transactions on Antennas and Propagation*, vol. 56, no. 4, pp. 1206–1211, 2008.

[16] M. Lienard and P. Degauque, "Natural wave propagation in mine environments," *IEEE Transactions on Antennas and Propagation*, vol. 48, no. 9, pp. 1326–1339, 2000.

[17] P. Mariage, M. Lienard, and P. Degauque, "Theoretical and experimental approach of the propagation of high frequency waves in road tunnels," *IEEE Transactions on Antennas and Propagation*, vol. 42, no. 1, pp. 75–81, 1994.

[18] S. Saunders, *Antennas and Propagation for Wireless Communication Systems*, John Wiley and Sons, Chichester, England, 2005.

[19] Z. changsen and M. Yan, "Effects of cross section of mine tunnel on the propagation characteristics of UHF radio wave Antennas," in *Proceedings of the 7th International Symposium on Propag. and EM Theory (ISAPE '06)*, pp. 1–5, 2006.

[20] C. S. Zhang and L. F. Guo, "Research on propagation characteristics of electromagnetic wave in tunnels with arbitrary cross sections," in *Proceedings of the 2nd International Conference on Future Computer and Communication (ICFCC '10)*, pp. V22–V25, May 2010.

[21] D. G. Dudley, M. Liénard, S. F. Mahmoud, and P. Degauque, "Wireless propagation in tunnels," *IEEE Antennas and Propagation Magazine*, vol. 49, no. 2, pp. 11–26, 2007.

Hindawi Publishing Corporation
International Journal of Antennas and Propagation
Volume 2012, Article ID 150267, 10 pages
doi:10.1155/2012/150267

Research Article

Statistical Modeling of Ultrawideband Body-Centric Wireless Channels Considering Room Volume

Miyuki Hirose, Hironobu Yamamoto, and Takehiko Kobayashi

Wireless Systems Laboratory, Tokyo Denki University, 5 Senju-Asahi-Cho, Adachi-Ku, Tokyo 120-8551, Japan

Correspondence should be addressed to Miyuki Hirose, miyuki@grace.c.dendai.ac.jp

Received 31 July 2012; Accepted 12 October 2012

Academic Editor: César Briso Rodríguez

This paper presents the results of a statistical modeling of onbody ultrawideband (UWB) radio channels for wireless body area network (WBAN) applications. Measurements were conducted in five different rooms. A measured delay profile can be divided into two domains; in the first domain ($0 < t \leq 4$ ns) there is either a direct (for line of sight) or diffracted (for nonline of sight) wave which is dependent on the propagation distance along the perimeter of the body, but essentially unrelated to room volume, and the second domain ($t > 4$ ns) has multipath components that are dominant and dependent on room volume. The first domain was modeled with a conventional power decay law model, and the second domain with a modified Saleh-Valenzuela model considering the room volume. Realizations of the impulse responses are presented based on the composite model and compared with the measured average power delay profiles.

1. Introduction

Wireless onbody area communication technologies are significant for both medical and nonmedical applications. Ultrawideband (UWB) technologies have been considered for use in wireless body area networks (WBANs) because of their possible low power consumption and antimultipath capabilities. Numerous studies have been carried out on UWB propagation characterization and the modeling of indoor UWB communication channels. A number of measurements relating to WBAN have been carried out to characterize and model on- and offbody UWB propagation in either a radio anechoic chamber or a specific room type [1–4]. The conventional UWB propagation loss model in these studies, however, did not consider the impact of surrounding environments. Since multipaths (in particular, the reflected waves from floors, walls, and ceilings) depend strongly on room volume, it is necessary to evaluate the variation of propagation characteristics in various environments. To address this problem, we measured UWB (3.1–10.6 GHz) radio propagation around the human body in a radio anechoic chamber and four different rooms and proposed a new UWB propagation loss model depending on the room volume [5]. In this study, time-domain statistical channel model will be the presented based on the same measurement campaign as [5].

As for statistical modeling of the channel impulse response, Fort et al. [3] separated the WBAN propagation channels into two parts: (1) diffraction around the body and (2) reflections off of nearby scatterers then back at the body, and modeled the second part using a modified Saleh-Valenzuela (SV) model [6]. The applicable area of the modified SV model in [6], however, was limited to wireless personal area networks not including human bodies. Roblin [7] scrutinized the separability of channels for various scenarios in three different rooms, concluded that UWB channels can be separated in the case of a relatively larger room, but it has not established a channel model. We also divided the channel responses into two parts which were then modeled by power decay law and a modified SV model depending on the room volume.

2. Measurement Setup

The measurement campaigns were conducted in five parallelepiped rooms as shown in Figure 1. The dimensions of Room A (a radio anechoic chamber) were measured

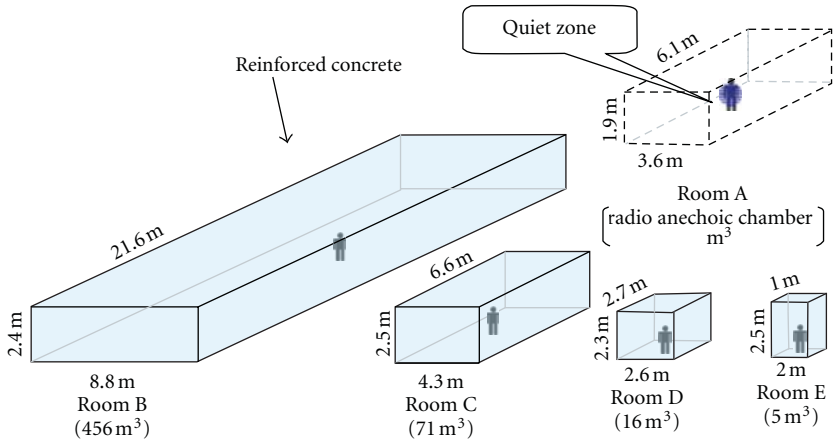

Figure 1: The outline of five rooms used for experiments.

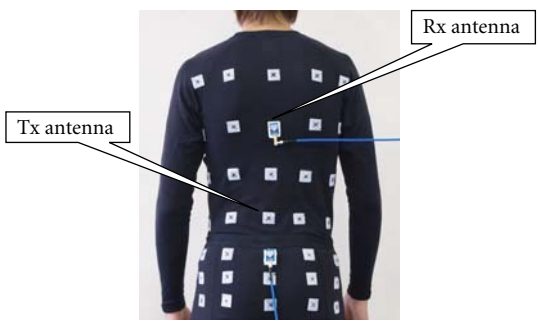

Figure 2: Placement of transmitting and receiving antennas on the body. Rectangular patches on the clothes are fabric hook-and-loop fasteners to fix the antennas.

between the apexes of the radio absorbers paneled on all surfaces. The radio anechoic chamber can be considered as a room extending to an infinite volume (i.e., free space) in terms of radio propagation. Rooms B to E were made of reinforced concrete, and their floors, walls, and ceilings were mostly covered with, respectively, linoleum, wallpaper, and plasterboard, all of which were lossy dielectrics. The measurements were carried out using a human subject (adult male, 1.72 m tall and 56 kg). The subject stood upright with the feet shoulder width apart in either a quiet zone of the radio anechoic chamber or the center of Rooms B to E. The UWB (3.1–10.6 GHz) propagation losses were measured with a vector network analyzer (VNA) between onbody meander line antennas [8]. The voltage standing wave ratio of the antennas was less than 2.5 between 3.1 and 10.6 GHz, and the omnidirectionality in the horizontal plane was within 3 dB in a free space. The transmitting antenna was fixed on the center back waist of the subject and placed at a height of 1.0 m from the floor, as shown in Figure 2. The receiving antenna was placed at approximately 100 mm intervals on the torso. Both antennas were vertically polarized and separated 10 mm from the subject body. When the receiving antenna was placed on the back of the subject's body, the path was roughly line of sight (LOS), and when on the front, it was non-LOS (NLOS). In total 69 receiving points around the torso were employed. The transmitting and receiving antennas were fed via coaxial cables, perpendicular to each other in configuration without crossing to reduce undesired cable coupling [9]. The calibration was conducted between the feeding points with a coaxial through adaptor. The frequency-domain transfer function (size = 1,024 = 751 measured within the 7.5-GHz bandwidth + 273 zero padding) was inversely Fourier transformed into a delay profile with the use of a rectangular window. Major specifications of the measurements are listed in Table 1.

Table 1: Specifications of the propagation measurements [5].

Bandwidth	3.1–10.6 GHz
Frequency sweeping points by VNA	751 points, 10-MHz interval
Calibration	Internal function of the VNA
Antennas	Meanderline UWB antennas [8]

3. Measurement Results and Modeling

Examples of the delay profiles when the receiving antenna was placed on the center chest (NLOS) and the back side (LOS) of the subject are presented in Figure 3. An increase in total received power was observed when the room volume was decreased (see Appendix A). This was attributed to the more affluent multipaths from the nearby floor, walls, and ceiling in Rooms B to E. The dominant propagation path in Room A (the radio anechoic chamber) was either a direct or a diffracted (around the body) wave, and thus the total reception power is lower than that in the other rooms. With decreasing room volume, mean free path lengths decreased, the power component contained in the multipaths increased, and consequently the total received power increased.

3.1. Division of Propagation Channels. A delay profile can be treated by dividing it into two domains, in the same way as [3, 7]: the first (approximately arriving time $0 < t \leq 4$ ns)

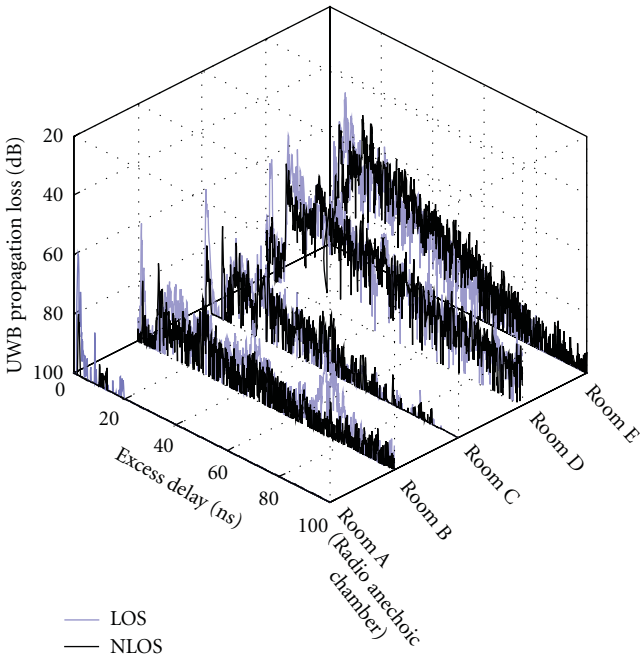

Figure 3: Example of the delay profiles measured in Rooms A to E [5].

and second ($t > 4$ ns) domains, as schematically shown in Figure 4. The first domain represents the contribution of the human alone, consisting of either direct (for LOS) or diffracted (for NLOS) wave measured in free space or radio anechoic chambers. And the second domain represents the contribution of the surrounding environments, consisting of remaining multipath components, which depend on room volume. Justification for dividing the profiles at $t = 4$ ns is given in Appendix B.

3.2. Statistical Analysis of the First Domain. The channel response in the first domain ($0 < t \leq 4$ ns) can be represented by

$$h_1(t) = h_{10} \cdot \left(\frac{d}{d_0}\right)^n \cdot \delta(t - t_0), \tag{1}$$

where h_{10} is the propagation gain at the reference distance d_0 ($= 0.1$ m), d is the propagation distance along the perimeter of the body, n is the propagation loss exponent, t_0 is the arrival time of the first wave, and $\delta(\cdot)$ is the Dirac delta function. The arrival time t_0 is proportional to d. Equation (1) represents a special case (when the room volume $V = \infty$) of the previously proposed UWB propagation loss model depending on room volume [5] (see Appendix C). The values of h_{10} and n in (1) were found to be 4.3×10^{-4} and 3.8 for LOS and 3.2×10^{-5} and 5.1 for NLOS, respectively, from the data of $\mathrm{PL_{dB}}$ shown in Figure 5. The statistics of the $h_1(t)$ followed lognormal distribution with a standard deviation of 4.4 dB ($\pm$0.5 dB) and 3.4 dB ($\pm$0.5 dB), for LOS and NLOS, respectively, where the values in the parentheses indicate 95% confidence intervals.

Table 2: Parameters of the first arriving multipath component.

	NLOS	LOS
ν	-2.8	-3.0
β_0	59.1	52.4

3.3. Statistical Analysis of the Second Domain. The second domain ($t > 4$ ns) can be represented by a modified SV model [6] based on a cluster concept of rays:

$$h_2(t) = \sum_{l=0}^{\infty} \sum_{k=0}^{\infty} \beta_{k,l} \delta(t - T_l - \tau_{k,l}), \tag{2}$$

where $\{\beta_{k,l}\}$ are the multipath gain coefficients, $\{T_l\}$ is the delay of the lth cluster, and $\{\tau_{k,l}\}$ is the delay of the kth multipath component relative to the lth cluster arrival time (T_l). Delay profiles measured in Rooms B, C, D, and E indicated that rays arrived in clusters, as shown in Figure 6, where the abscissas of the graphs are drawn in antilogarithm. While Fort et al. stated cluster interval times fit to the Weibull distribution [3], in all our cases, the arrival time intervals of the clusters were found to follow an exponential distribution by using Kolmogorov-Smirnov (K-S) test with a 95% confidence interval. This means that cluster arrivals are modeled as a Poisson arrival process with a fixed rate of Λ [1/ns]. Within each cluster, subsequent rays also arrived according to a Poisson process with another fixed rate of λ [1/ns]. The distribution of the cluster and ray arrival times are given by

$$\begin{aligned} p(T_l \mid T_{l-1}) &= \Lambda \exp[-\Lambda(T_l - T_{l-1})], \quad l > 0, \\ p(\tau_{k,l} \mid \tau_{(k-1),l}) &= \lambda \exp[-\lambda(\tau_{k,l} - \tau_{(k-1),l})], \quad k > 0, \end{aligned} \tag{3}$$

where Λ and λ are cluster arrival rate and ray arrival rate within each cluster, respectively. The IEEE 802.15.4a channel model [6] used a lognormal distribution rather than a Rayleigh distribution adopted in the original S-V model [10] for the multipath gain coefficients $\beta_{k,l}$. We also adopted a lognormal distribution for $\beta_{k,l}$ because of a better fitting to the measured data. The average power of both the clusters and the rays within the clusters are assumed to decay exponentially, such that the average power of the multipath component at a given delay $T_l + \tau_{k,l}$ is given by

$$\left\langle \beta_{k,l}^2 \right\rangle = \left\langle \beta_{0,0}^2 \right\rangle \exp\left(-\frac{T_l}{\Gamma}\right) \exp\left(-\frac{\tau_{k,l}}{\gamma}\right), \tag{4}$$

where $\langle \beta_{0,0}^2 \rangle$ is the expected value of the power of the first arriving multipath component, Γ is the delay exponent of the clusters, and γ is the decay exponent of the rays within a cluster. The first arriving multipath detected in measured delay profiles is lower with decreased room volume, as shown in Figure 7. The first multipath component, $\langle \beta_{0,0}^2 \rangle$, can be represented by

$$\left\langle \beta_{0,0}^2 \right\rangle = \beta_0 \cdot \left(\sqrt[3]{V}\right)^{\nu}. \tag{5}$$

The values of β_0 and ν are listed in Table 2.

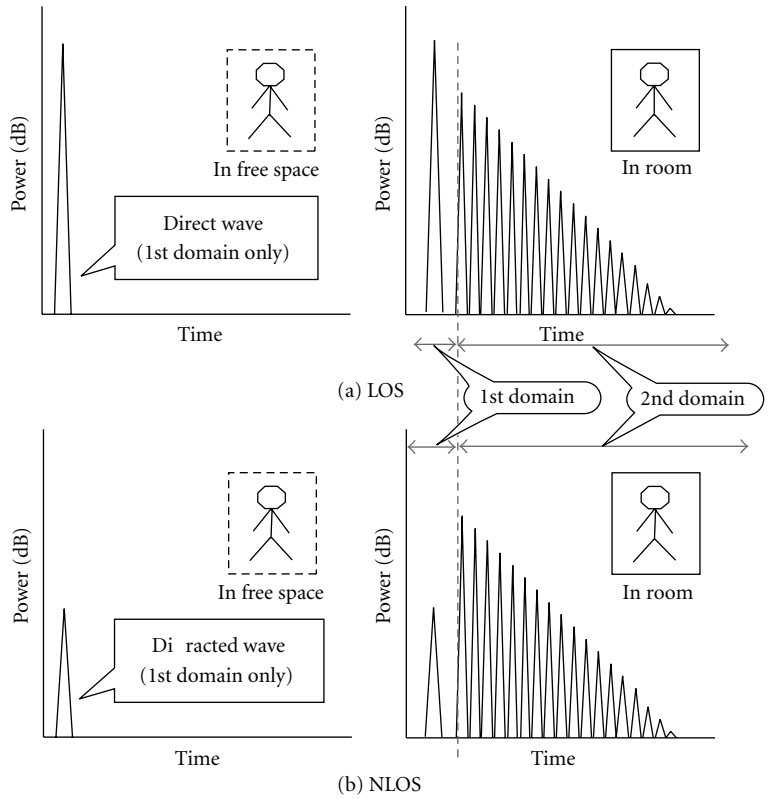

Figure 4: Conceptual diagram of the division of the delay profiles: (a) LOS and (b) NLOS. The first domain represents the delay profiles measured in free space or radio anechoic chambers and contains a direct or diffracted wave along the body. The second domain consists of the remaining multipath components.

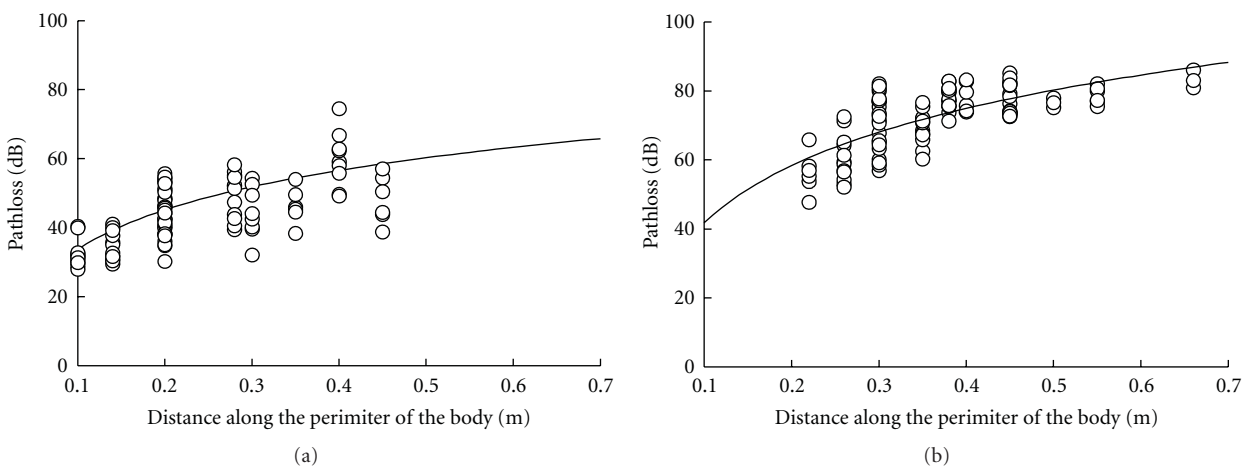

Figure 5: Ultrawideband pathloss onbody antennas measured in a radio anechoic chamber: (a) LOS and (b) NLOS.

The values of Λ, λ, Γ, and γ were derived from the delay profile data measured in Rooms B, C, D, and E. Figures 8 and 9 present those values against $V^{1/3}$ along with regression lines. Note that $V^{1/3}$ represents the mean free path length of the rays traveling within a room having a finite (or infinite) volume V. The cluster arrival time rate Λ[1/ns] is approximately 0.08, while the ray arrival time rate λ [1/ns] is 0.4 for both LOS and NLOS. While the arrival rates Λ and λ exhibited no apparent dependence on $V^{1/3}$ or LOS/NLOS scenarios as shown in Figure 8, the power decay factors Γ and γ slightly increased with $V^{1/3}$, as shown in Figure 9. The propagation distances (and therefore propagation losses) of rays increase with the room volume, and therefore the decay factors increase. The slope was steeper for the NLOS than for the LOS cases. The dependence of the cluster power-decay factor and

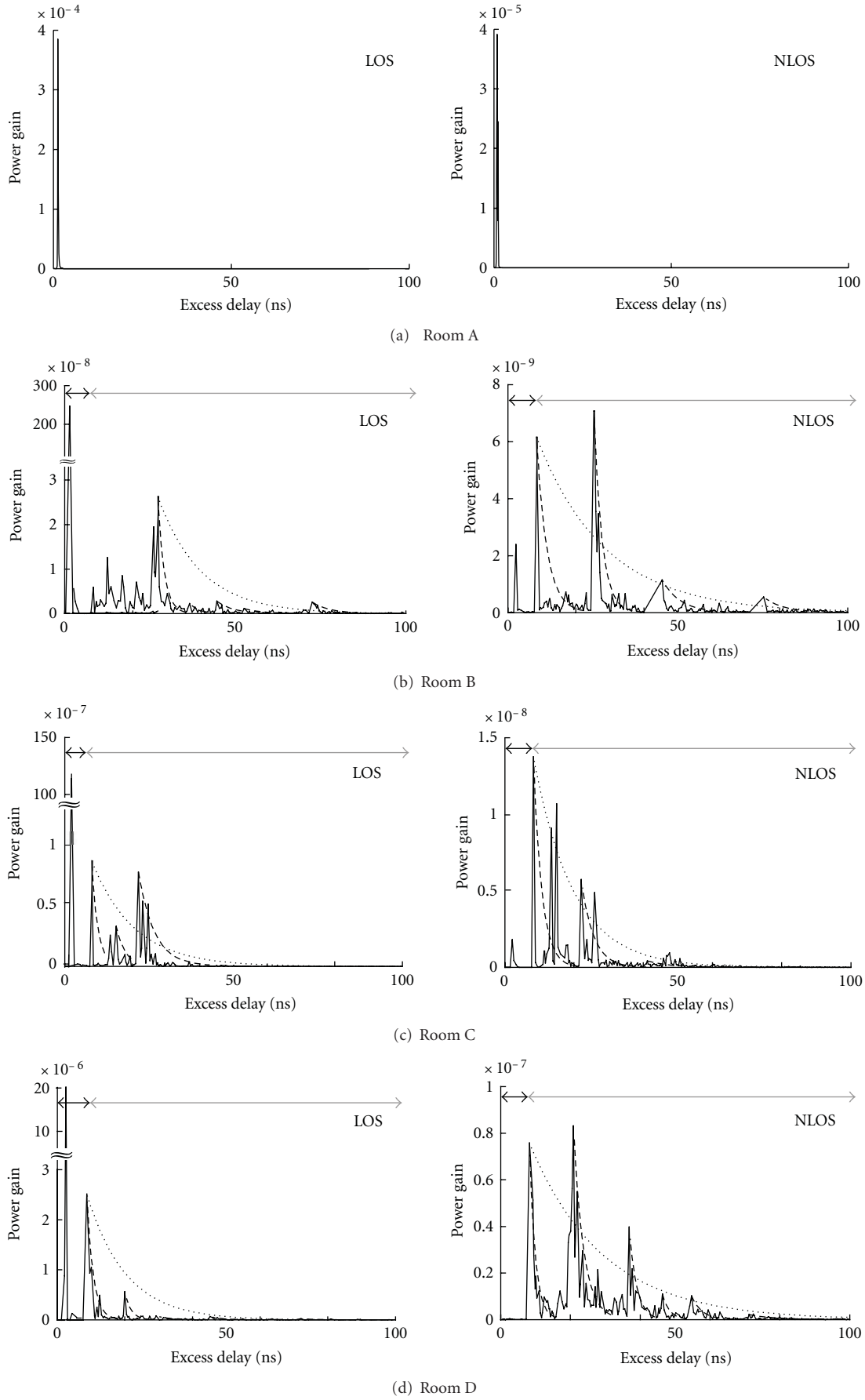

Figure 6: Continued.

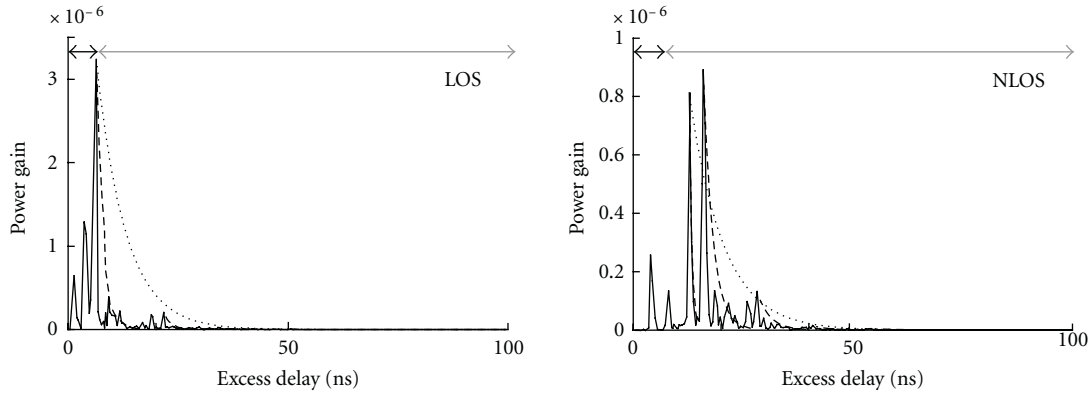

(e) Room E

Figure 6: Examples of the delay profiles measured in Rooms A to E. Profiles for LOS were measured at the center of the back and those for NLOS at the center of the chest. The dashed lines represent exponential power decay of the rays and the clusters. The black and grey arrows indicate the first and the second domains.

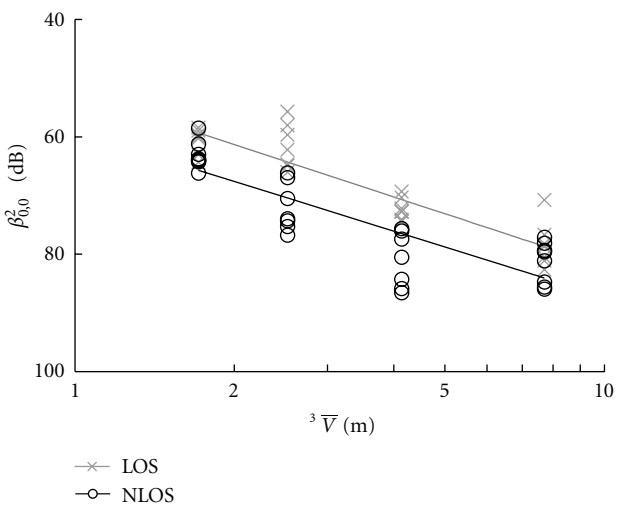

Figure 7: UWB propagation loss of the first ray within the first cluster against $V^{1/3}$.

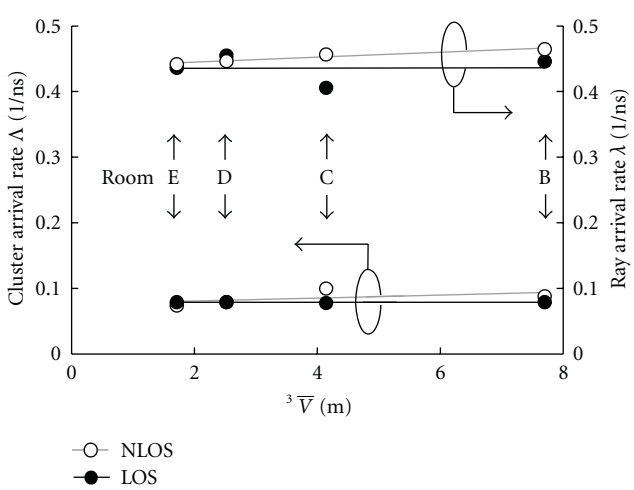

Figure 8: Arrival rates of clusters and rays within clusters.

Table 3: The parameter of decay factor functions for the cluster and the ray within the cluster.

		NLOS	LOS
Cluster	Γ' [ns/m]	1.25	0.70
	Γ_0 [ns]	10.0	7.1
Ray	γ' [ns/m]	0.28	0.11
	γ_0 [ns]	2.4	3.0

the ray power-decay factor on $V^{1/3}$, depicted in Figure 9, is formulated by

$$\Gamma = \Gamma_0 + \Gamma' \cdot \sqrt[3]{V},$$
$$\gamma = \gamma_0 + \gamma' \cdot \sqrt[3]{V}, \tag{6}$$

where Γ_0 and γ_0 are values of Γ and γ when imaginarily $V = 0$, Γ' and γ' are the slope of the cluster and the ray within the cluster against $V^{1/3}$, respectively. The values of Γ_0, γ_0, Γ', and γ' are listed in Table 3. Although the effect of shadowing has not been considered in this paper, it can be included in (2) after the same method as adopted in [6].

4. Realization of Onbody UWB Channels Based on the Composite Model

A composite statistical UWB channel model between onbody antennas is formulated by summing the models described in Section 3. A realization is calculated upon providing input data—whether the path is either LOS or NLOS—d (the distance between the antennas along the perimeter of the body), and the room volume, as shown in Figure 10. Once a number of realizations of the channel responses are calculated randomly, they are then served to estimate transmission performances (e.g., average bit error rates) and/or system capacity of communication systems, detection and false alarm rates of radar systems, and so forth, by simulation.

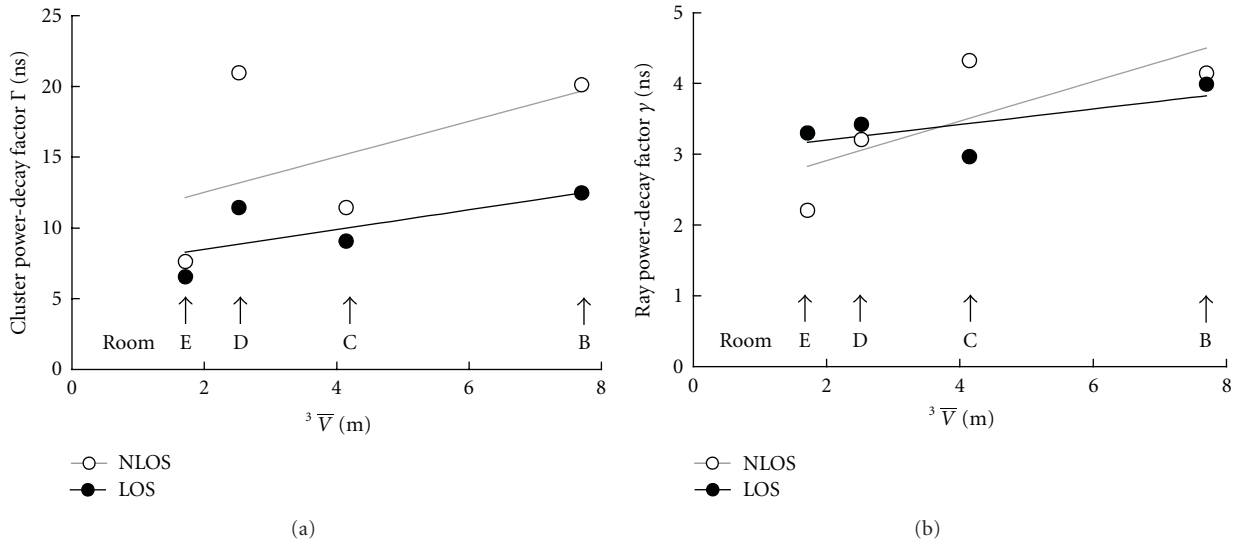

Figure 9: Power decay factors against $V^{1/3}$ for (a) the clusters and (b) the rays. The solid lines are the linear fitting.

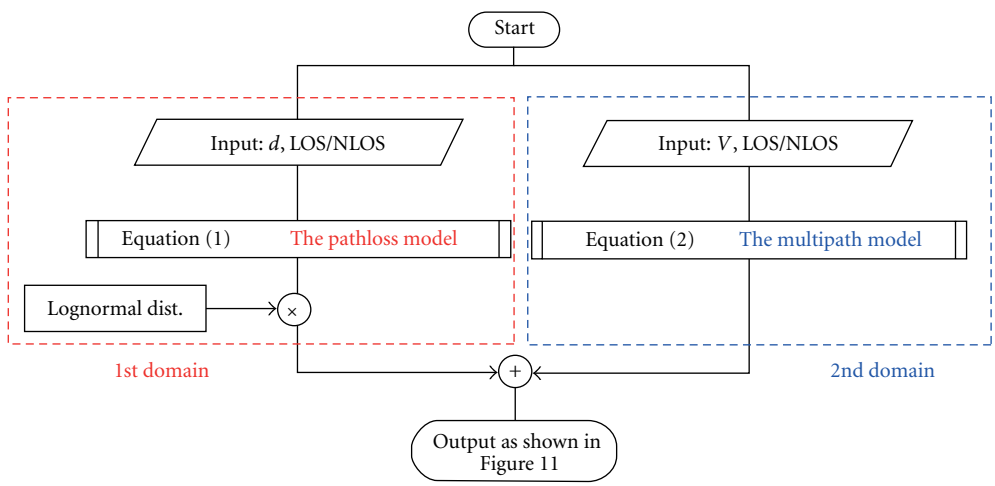

Figure 10: The flow chart of our model realization process.

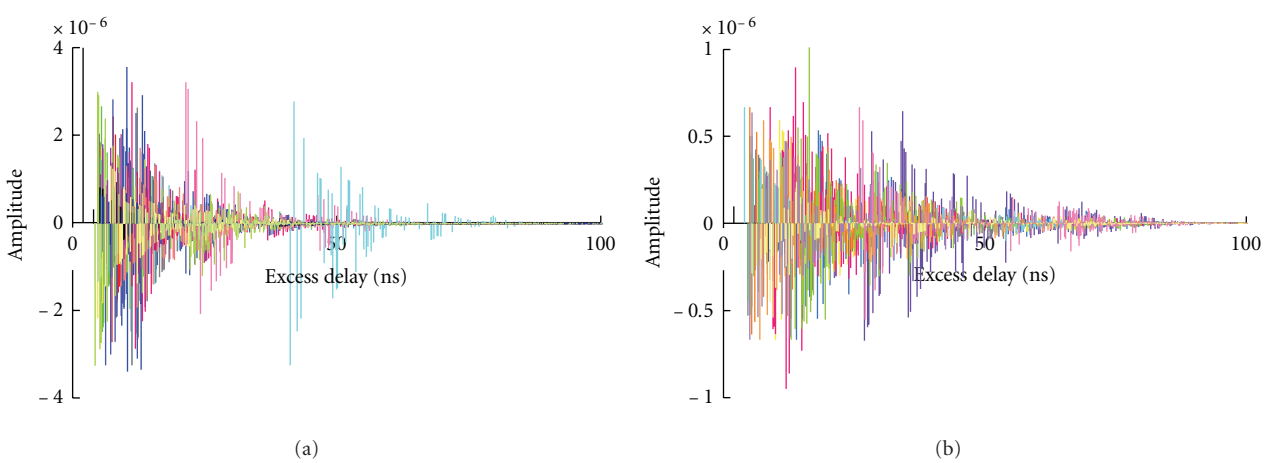

Figure 11: Examples of 20 channel response realizations for Room E ($V = 5\,\mathrm{m}^3$): (a) LOS and (b) NLOS.

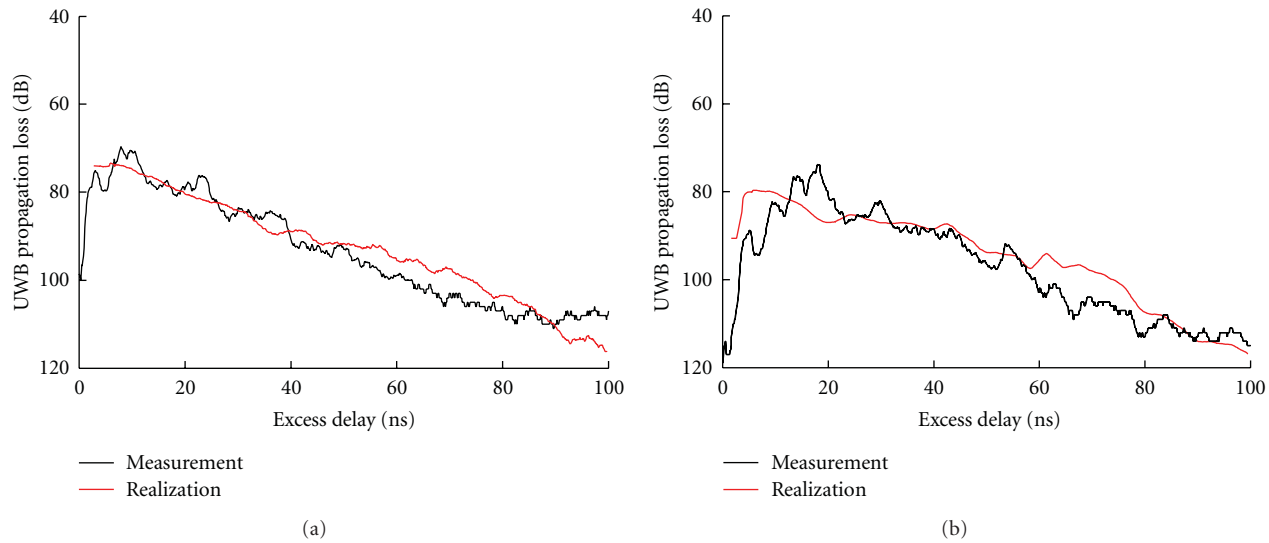

Figure 12: Comparison of the APDPs between 20 realizations and measured delay profiles of Room E ($V = 5\,\mathrm{m}^3$): (a) LOS and (b) NLOS.

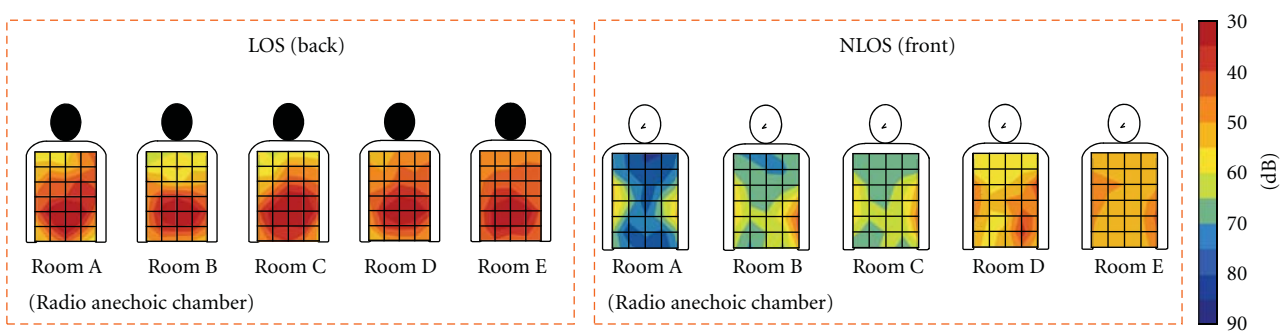

Figure 13: Spatial distribution of UWB propagation losses in the five rooms. The transmitting antenna was placed at point denoted by "*".

Examples of the channel response realizations for LOS and NLOS, assuming $d = 200\,\mathrm{mm}$ for LOS and $450\,\mathrm{mm}$ for NLOS and $V = 5\,\mathrm{m}^3$, are presented in Figure 11, where 20 realizations are overwritten. Average power delay profiles (APDPs) for LOS and NLOS were derived from these realizations and compared with the measured data. Moving average was conducted over a 3 ns period for calculating the APDPs. The APDPs derived from the calculated realizations and from the measured delay profiles reasonably agree, as shown in Figure 12. The validity of the proposed composite model was therefore confirmed.

5. Conclusions

In this study, a series of propagation measurements campaign were carried out between onbody antennas in five different rooms. A measured delay profile can be divided into two domains. In the first domain ($0 < t \leq 4\,\mathrm{ns}$), there is either a direct (for LOS) or diffracted (for NLOS) wave which depends on propagation distance along the perimeter of the body but essentially unrelated to room volume. This domain was modeled with a power decay law against the distance, and its amplitude followed a lognormal distribution. In the second domain ($t > 4\,\mathrm{ns}$), multipath components are dominant and dependent on room volume. Observations of the second domain indicate that rays generally arrive in clusters. Arrivals of clusters and rays within each cluster were found to be modeled by Poisson processes. As a result, the second domain was modeled by a modified Saleh-Valenzuela model with the use of lognormal distribution rather than Rayleigh distribution for multipath gain coefficients. Finally, the composite model to calculate the UWB onbody channel realizations was obtained by combining the two domains and validated with the use of the measured delay profiles.

Appendices

A. UWB Propagation Loss

Examples of spatial distributions of UWB propagation losses, measured in the same five rooms as those described in Section 2, are shown in Figure 13. The UWB propagation losses were calculated by integrating the power of the losses

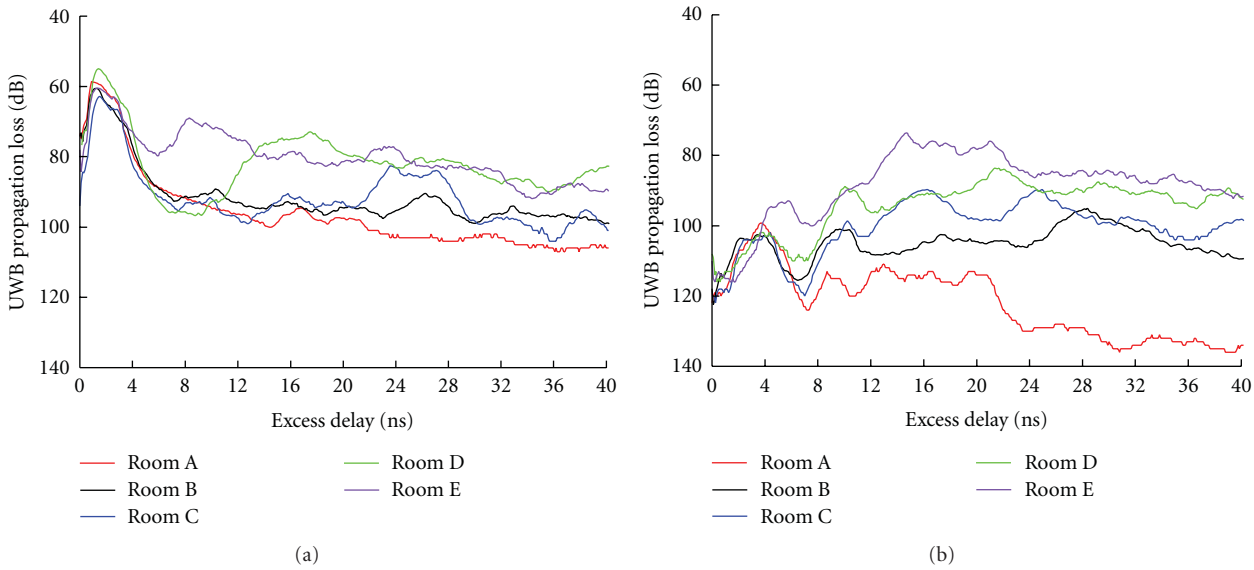

Figure 14: Measured average power delay profiles (averaged over 3 ns): (a) LOS and (b) NLOS.

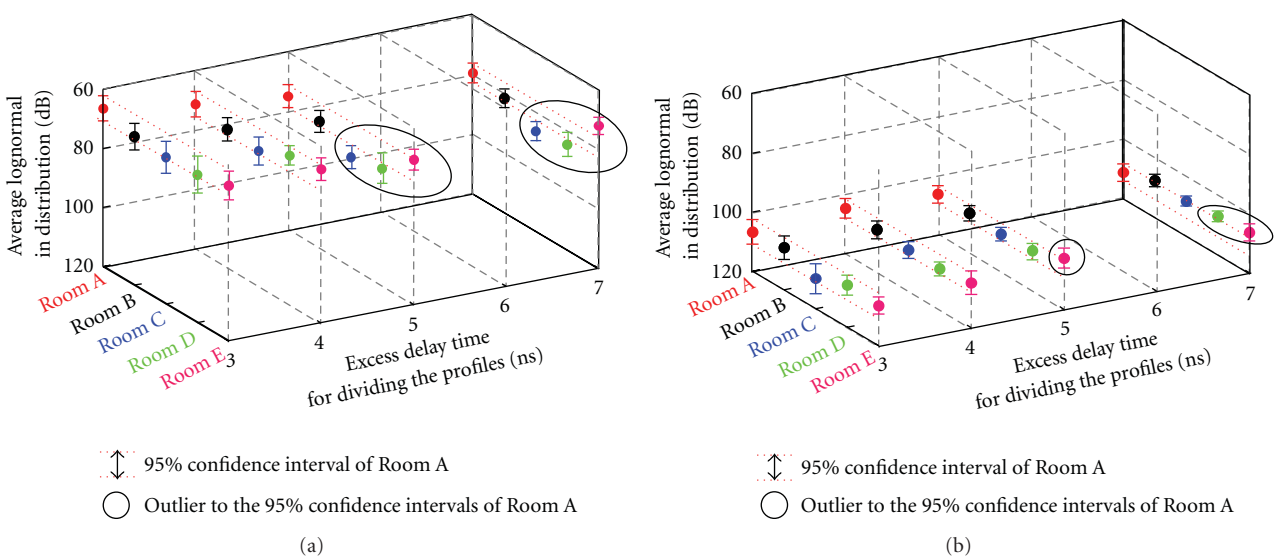

Figure 15: Averages in lognormal distribution fit to the propagation loss for Rooms A to E: (a) LOS and (b) NLOS. The dashed lines are the 95% confidence intervals of Room A (a radio anechoic chamber). The averages encircled by ovals are outliers to the 95% intervals of Room A.

between the feeding points of the antennas over occupied bandwidth:

$$\mathrm{PL_{dB}} = 10\log\left(\frac{1}{f_H - f_L}\int_{f_L}^{f_H} 10^{\mathrm{PL_{dB}}(f)/10}\,df\right), \qquad \text{(A.1)}$$

where $\mathrm{PL_{dB}}(f)$ is the propagation loss in dB measured at frequency f, and f_L and f_H are the lowest and highest frequencies. The propagation losses increased with decreasing the room volume, as shown in Figure 13.

B. Validity of 4 ns for Dividing the Delay Profiles

Figure 14 depicts average power delay profiles (averaged over 3 ns) for LOS and NLOS measured in Rooms A to E.

Curves are almost equal for a period between 0 and approximately 4 ns: the effect of the surrounding environment was insignificant up to 4 ns. Beyond the 4 ns, the propagation loss decreased (the curves move upward) with decreasing room volume. Furthermore, the amplitude distribution was examined to confirm the validity of $t = 4$ ns for dividing the delay profiles. The amplitudes within

the measured delay profiles were found to follow lognormal distribution up to an excess delay of 10 ns. The averages in the lognormal distribution up to 3, 4, 5, and 7 ns were estimated for LOS and NLOS, as shown in Figure 15, where the 95% confidence intervals derived of Room A data are plotted by dashed lines. While all the averages up to 4 ns for Rooms B to E fell within the 95% intervals, some (Rooms C, D, and E for LOS and Rooms D and E for NLOS) were outside the intervals, as shown in Figure 15. This fact also ratified the validity of $t = 4$ ns for dividing the profiles.

C. Proposed UWB Propagation Loss Model

Based on a series of propagation measurements conducted in a frequency bandwidth from 3.1 to 10.6 GHz, the authors proposed a UWB propagation loss model [5]:

$$\mathrm{PL_{dB}} = \mathrm{PL_{0dB}} + 10\left(n_\infty + \frac{n'}{\sqrt[3]{V}}\right)\log\left(\frac{d}{d_0}\right)[\mathrm{dB}], \qquad \text{(C.1)}$$

where $\mathrm{PL_{0dB}}$ is the propagation loss at the reference distance d_0 ($= 0.1$ m), n_∞ is the propagation loss exponent when the room volume $V = \infty$, and n' is the slope of n against $V^{-1/3}$. The values of $\mathrm{PL_{0dB}}$, n_∞, and n' for LOS and NLOS are given in [5].

Acknowledgments

This study was in part supported by the Japan Society for the Promotion of Science and the Academy of Finland with the Japan-Finland Bilateral Core Program. The authors would like to thank the program participants of the Tokyo Institute of Technology, Japan and Aalto University, Finland, for valuable discussions.

References

[1] T. Zasowski, F. Althaus, M. Stager, A. Wittneben, and G. Troster, "UWB for noninvasive wireless body area networks: channel measurements and results," in *Proceedings of the IEEE Conference on Ultrawideband Systems Technology (UWBST '03)*, pp. 285–289, November 2003.

[2] P. S. Hall and Y. Hao, Eds., *Antennas and Propagation for Body-Centric Wireless Communications*, Artech House, Boston, Mass, USA, 2006.

[3] A. Fort, J. Ryckaert, C. Desset, P. De Doncker, P. Wambacq, and L. Van Biesen, "Ultra-wideband channel model for communication around the human body," *IEEE Journal on Selected Areas in Communications*, vol. 24, no. 4, pp. 927–933, 2006.

[4] A. Sani, A. Alomainy, G. Palikaras et al., "Experimental characterization of UWB on-body radio channel in indoor environment considering different antennas," *IEEE Transactions on Antennas and Propagation*, vol. 58, no. 1, pp. 238–241, 2010.

[5] H. Yamamoto, M. Koiwai, and T. Kobayashi, "Measurements and modeling of ultra-wideband propagation losses around the human body dependent on room volume," *IEICE Transactions on Fundamentals of Electronics, Communications and Computer Sciences*, vol. E93, no. 12, pp. 2624–2633, 2010.

[6] A. F. Molisch, K. Balakrishnan, D. Cassioli et al., "IEEE 802. 15. 4a channel model—final report. Submitted to IEEE 802. 15 WPAN low rate alternative PHY task group 4a (TG4a)," Tech. Rep., IEEE 802. 15, 2004.

[7] C. Roblin, "On the separability of on-body and off-body clusters in the modeling of UWB WBAN channels for various indoor scenarios," in *Proceedings of the 5th European Conference on Antennas and Propagation (EUCAP '11)*, pp. 3148–3152, April 2011.

[8] Skycross, "3.1-10 GHz ultra-wideband antenna," http://www.Skycross.com/Products/PDFs/SMT-3TO10M-A.pdf.

[9] H. Yamamoto and T. Kobayashi, "Effects of feeding cable configurations on propagation measurements between small ultra wideband antennas for WBAN applications," in *Proceedings of the International Workshop on Future Wellness and Medical ICT Systems (FEELIT '08)*, September 2008.

[10] A. A. M. Saleh and R. A. Valenzuela, "A statistical model for indoor multipath propagation," *IEEE Journal on Selected Areas in Communications*, vol. 5, no. 2, pp. 128–137, 1987.

Hindawi Publishing Corporation
International Journal of Antennas and Propagation
Volume 2012, Article ID 701985, 10 pages
doi:10.1155/2012/701985

Research Article

Performance Evaluation of Closed-Loop Spatial Multiplexing Codebook Based on Indoor MIMO Channel Measurement

Junjun Gao, Jianhua Zhang, Yanwei Xiong, Yanliang Sun, and Xiaofeng Tao

Key Laboratory of Universal Wireless Communications of Ministry of Education, Beijing University of Posts and Telecommunications, Mailbox 92, Beijing 100876, China

Correspondence should be addressed to Junjun Gao, gaojunjun@bupt.edu.cn

Received 23 July 2012; Revised 24 October 2012; Accepted 24 October 2012

Academic Editor: Ai Bo

Closed-loop MIMO technique standardized in LTE can support different layer transmissions through precoding operation to match the channel multiplexing capability. However, the performance of the limited size codebook still needs to be evaluated in real channel environment for further insights. Based on the wideband MIMO channel measurement in a typical indoor scenario, capacity loss (CL) of the limited size codebook relative to perfect precoding is studied first in two extreme channel conditions. The results show that current codebook design for single layer transmission is nearly capacity lossless, and the CL will increase with the number of transmitted layers. Furthermore, the capacity improvement of better codebook selection criterions is very limited compared to CL. Then we define the maximum capacity boost achieved by frequency domain layer adaption (FDLA) and investigate its sensitivity to SNR and channel condition. To survey the effect of frequency domain channel variation on MIMO-OFDM system, we define a function to measure the fluctuation levels of the key channel metrics within a subband and reveal the inherent relationship between them. Finally, a capacity floor resulted as the feedback interval increases in frequency domain.

1. Introduction

The rapid data traffic growth in indoor environment raises a great challenge to modern communications to meet the peak data rate requirement. Thanks to the spatial parallel transmission, MIMO multiplexing technique can achieve promising spectrum efficiency and attracts large interests recently [1–4]. In general, better performance can be achieved if the channel state information (CSI) is available at the transmitter [5]. Fortunately, the indoor MIMO channel is usually slow time-varying due to the low mobility of the mobile terminals and scatters, which provides the favorable condition for applying closed-loop MIMO scheme to feed the CSI back. However, it is unrealistic to transmit the full CSI back to the transmitter due to the feedback channel limitation. Standardized in LTE, the transmitter and receiver share a common precoding matrix table (codebook), also only rank indicator (RI) and precoding matrix index (PMI) are sent back to indicate the number of transmitted layers and corresponding precoding matrix [6].

Codebook-based MIMO precoding systems have attracted great research interests recently. Channel capacity with quantized precoding matrix is studied in independent and identically distributed channels [7], where the precoding matrix is selected from a random codebook. Overloaded vector precoding [8] is proposed for single-user MIMO channels, where the number of data streams is larger than the minimum number of the transmit and receive antennas. The codebook-based precoding and equalization are jointly designed to improve the performance [9]. Codebook-based lattice-reduction-aided precoding is studied for coded MIMO systems to reduce the amount of feedback [10]. However, the limited size codebook usually results in capacity loss (CL) as a result of the interlayer interference [10, 11]. From the perspective of codebook selection, minimum CL is equivalent to maximize the capacity, yet no literature has studied it to reduce the complexity. Some recent indoor channel measurement results focus on different points, such as eigenvalue distribution [12], multilink separation [13], and dense multipath characteristics [14]. Performance evaluation is

important for practical MIMO deployment, such as HSDPA [15] and E-UTRA [16]. However, the precoding performance has not been evaluated in real indoor channel environment.

Increasing the system bandwidth (e.g., up to 100 MHz) is another effective method to satisfy the high data rate requirement. Consequently, the channel frequency-selective characteristic expands the available adaption dimension in MIMO-OFDM systems. Frequency domain layer adaption (FDLA) in subband level [6] can enhance the average spectral efficiency and achieve a tradeoff between the performance and amount of feedback bits. However, the performance of FDLA is greatly influenced by the channel variation within a subband. We would like to know the maximum performance potential of FDLA in real frequency-selective channels, and its relationship to the channel condition and SNR. The frequency domain variation of the eigenvalues is theoretically studied in adaptive MIMO beamforming systems [17]. The effect of frequency domain variation on the MIMO precoding performance has not been investigated in real indoor channels.

Channel measurement is the most straightforward and reliable method to acquire the real channel characteristics [18]. Based on the wideband MIMO channel measurement in a typical indoor scenario at 6 GHz, we propose a metric to distinguish various MIMO channel conditions. Two extreme cases of our campaign are selected for performance evaluation, which yield poor and fine multiplexing capabilities, respectively. In this paper, we focus on the following key problems.

(i) How is the CL related to channel condition, receiver type, and the number of transmitted layers?

(ii) Does the CL provide some insight into the codebook selection? Compared to the CL caused by the limited feedback, how much capacity improvement can be achieved by the use of better codebook selection criterion?

(iii) What is the maximum capacity boost of FDLA? How is it related to the channel condition and SNR?

(iv) How to measure the fluctuation levels of the key channel metrics within a subband? Is there any inherent relationship between them?

The major contributions of this paper are organized as follows. The exact CL expression and its upper bound are derived for single-layer and full-rank transmissions. We first utilize the concept of CL to obtain low-complexity codebook selection criterion, which can reduce the interlayer or interuser interference for single-user or multiuser MIMO. A robust channel condition metric is defined based on the measured channel data analysis. The maximum performance potential of FDLA in real frequency-selective channels is studied, and its relationship to the channel condition and SNR is also investigated. We define a function to measure the key channel metric fluctuation level within a subband and investigate the effect of frequency domain variation on MIMO-OFDM systems. Based on the proposed methods, the precoding performance is systematically evaluated in real indoor channel environment.

The remainder of this paper is organized as follows. Section 2 introduces the system model and proposes the framework of performance evaluation. Section 3 describes the measurement equipment and environment. Section 4 presents the key simulation results. In Section 5, a summary of this paper is given.

Notation. The (i, j)th element of the matrix $\mathbf{A}$ is $\{\mathbf{A}\}_{i,j}$. The superscript T and $\dagger$ represent the transpose and Hermitian transpose, respectively. The symbol $\mathrm{tr}(\cdot)$ denotes the matrix trace, and $\|\cdot\|_F^2$ is the square of the matrix Frobenius norm. The notation $\mathcal{E}(\cdot)$ is the expectation operation.

2. System Model and Evaluation

2.1. MIMO Precoding System Model. Considering a narrowband MIMO system with N_t transmit and N_r receive antennas, the channel matrix is denoted as $\mathbf{H} \in \mathcal{C}^{N_r \times N_t}$. Assuming $N_t \leq N_r$, the received signal can be represented as

$$\mathbf{y} = \mathbf{H}\mathbf{x} + \mathbf{n}, \tag{1}$$

where $\mathbf{y} \in \mathcal{C}^{N_r \times 1}$ is the received vector, $\mathbf{x} \in \mathcal{C}^{N_t \times 1}$ is the transmitted vector, and $\mathbf{n} \in \mathcal{C}^{N_r \times 1}$ is the additive noise vector with independent and identical distributed random elements satisfying $\mathcal{CN}(0, \sigma^2)$.

For fully exploiting the space dimension flexibility of the multiple antenna system, precoding operation is performed to achieve different layers transmission. Supposing the number of transmitted layers is L, the precoding process is expressed as $\mathbf{x} = \mathbf{P}\mathbf{s}$, where $\mathbf{P} \in \mathcal{C}^{N_t \times L}$ is the unitary precoding matrix satisfying $\mathbf{P}^\dagger\mathbf{P} = \mathbf{I}_L$. The effective $L \times 1$ transmit symbol vector is $\mathbf{s} = [s_1, \ldots, s_L]^T$, and the received signal can be rewritten as [5]

$$\mathbf{y} = \mathbf{H}\mathbf{P}\mathbf{s} + \mathbf{n}. \tag{2}$$

Assuming that the total transmit power P_T is uniformly distributed to L layers, $P_T = \mathcal{E}(\mathbf{s}^\dagger\mathbf{s}) = L\mathcal{E}(|s_i|^2)$, so the received SNR is $\gamma_0 = P_T/\sigma^2$.

Linear receiver can be used to recover the symbol of each layer with low complexity, and we consider zero-forcing (ZF) and minimum mean square error (MMSE) receivers in this paper. The output of the linear receiver can be represented as $\hat{\mathbf{y}} = \mathbf{\Psi}\mathbf{y}$, and the corresponding linear combiner $\mathbf{\Psi}$ and the SINR of the lth layer are, respectively, [11, 19]

$$\begin{aligned}
\mathbf{\Psi}_{\mathrm{ZF}} &= \left(\mathbf{P}^\dagger\mathbf{H}^\dagger\mathbf{H}\mathbf{P}\right)^{-1}(\mathbf{H}\mathbf{P})^\dagger, \\
\mathrm{SINR}_l &= \frac{\gamma_0}{L}\frac{1}{\left\{(\mathbf{P}^\dagger\mathbf{H}^\dagger\mathbf{H}\mathbf{P})^{-1}\right\}_{l,l}}, \\
\mathbf{\Psi}_{\mathrm{MMSE}} &= \left(\frac{L}{\gamma_0}\mathbf{I} + \mathbf{P}^\dagger\mathbf{H}^\dagger\mathbf{H}\mathbf{P}\right)^{-1}(\mathbf{H}\mathbf{P})^\dagger, \\
\mathrm{SINR}_l &= \frac{1}{\left\{\left(\mathbf{I} + \frac{\gamma_0}{L}\mathbf{P}^\dagger\mathbf{H}^\dagger\mathbf{H}\mathbf{P}\right)^{-1}\right\}_{l,l}} - 1.
\end{aligned} \tag{3}$$

The total capacity of L layers transmission with ZF and MMSE receivers can be represented as [11]

$$C_L = \sum_{l=1}^{L} \log_2(1 + \mathrm{SINR}_l). \tag{4}$$

The singular value decomposition (SVD) of $\mathbf{H}^\dagger\mathbf{H}$ is $\mathbf{H}^\dagger\mathbf{H} = \mathbf{V}\mathbf{\Lambda}\mathbf{V}^\dagger$, where the matrix $\mathbf{V}$ is unitary. The ordered diagonal elements of $\mathbf{\Lambda}$ are $\lambda_{\max} = \lambda_1 \geq \cdots \geq \lambda_{N_t} = \lambda_{\min} \geq 0$, and λ_l is the lth eigenvalue of $\mathbf{H}^\dagger\mathbf{H}$. For L layers transmission, the perfect precoding matrix $\mathbf{P} = \mathbf{V}_L$ is the first L columns of $\mathbf{V}$, $\mathbf{V}_L = [\mathbf{v}_1, \ldots, \mathbf{v}_L]$, where $\mathbf{v}_k$ denotes the kth column of $\mathbf{V}$.

Under perfect precoding assumption, parallel and independent layers are constructed as a result of the interlayer interference elimination. Hence, ZF and MMSE receivers are the same for any given SNR, then (4) becomes

$$C_L|_{\mathbf{P}=\mathbf{V}_L} = \sum_{l=1}^{L} \log_2\left(1 + \frac{\gamma_0}{L}\lambda_l\right). \tag{5}$$

Theorem 1. *In the high SNR region, the single layer transmission will outperform the full-rank transmission, $C_1 \geq C_{N_t}$, if the channel matrix $\mathbf{H}$ satisfies the following inequality:*

$$\|\mathbf{H}\|_F^2 - \lambda_{\max} \leq \frac{1}{\gamma_0} N_t(N_t - 1)\left(N_t^{1/(N_t-1)} - 1\right). \tag{6}$$

Proof. In the high SNR region, from (4), we have

$$\begin{aligned} C_{N_t} &\approx \log_2\left(\frac{\gamma_0}{N_t}\lambda_1\right) + \sum_{l=2}^{N_t} \log_2\left(1 + \frac{\gamma_0}{N_t}\lambda_l\right) \\ &\leq (N_t - 1)\log_2\left(1 + \frac{\gamma_0}{N_t(N_t-1)}\sum_{l=2}^{N_t}\lambda_l\right) \\ &\quad + \log_2\left(\frac{\gamma_0}{N_t}\lambda_1\right). \end{aligned} \tag{7}$$

The proof can be easily completed using the property of the matrix trace and Frobenius norm. □

For the special case of 2×2 MIMO configuration, (6) is simplified to

$$\lambda_{\min} \leq \frac{2}{\gamma_0}. \tag{8}$$

It indicates that the Demmel condition number K_D should satisfy the following term:

$$K_D = \frac{\|\mathbf{H}\|_F^2}{\lambda_{\min}} \geq \frac{\gamma_0\|\mathbf{H}\|_F^2}{2} \tag{9}$$

and the channel matrix will be more ill-conditioned as the SNR increases.

2.2. Codebook Capacity Loss. In practice, it is impossible for the transmitter to obtain the perfect precoding matrix due to the limitation of the feedback channel capacity. The RI and PMI are sent back to the transmitter which shares the same precoding codebook table with the receiver. The actual precoding matrix $\mathbf{P} \in \mathbf{W}_L$ is a quantized release of $\mathbf{V}_L$, where $\mathbf{W}_L$ is the limited size codebook designed for L layers transmission. Therefore, performance degradation is caused, and the CL is defined as follows [11]:

$$C_{\mathrm{loss}} = C_L|_{\mathbf{P}=\mathbf{V}_L} - C_L|_{\mathbf{P}\in\mathbf{W}_L}. \tag{10}$$

The CL is affected by the receiver types and codebook design. In the high SNR region, ZF and MMSE receivers yield the same performance [20], and the influence of the limited size codebook on CL is dominated. Thereby, we focus on the theoretical derivation of CL in high SNR case. Let $\mathbf{S} = \mathbf{P}^\dagger\mathbf{H}^\dagger\mathbf{H}\mathbf{P}$; its (i, j)th element can be easily written as

$$\{\mathbf{S}\}_{i,j} = \mathbf{p}_i^\dagger\left(\sum_{k=1}^{N_t}\lambda_k\mathbf{v}_k\mathbf{v}_k^\dagger\right)\mathbf{p}_j, \tag{11}$$

where $\mathbf{p}_i$ and $\mathbf{p}_j$ represent the ith and jth columns of the precoding matrix $\mathbf{P}$.

In the following, we consider two special cases to derive succinct expressions of CL in the high SNR region.

(1) $L = 1$: in this case, there is only one complex element in $\mathbf{S}$, and the SINR can be easily derived from (3):

$$\mathrm{SINR}_1 = \gamma_0\sum_{k=1}^{N_t}\lambda_k\left|\mathbf{p}_1^\dagger\mathbf{v}_k\right|^2. \tag{12}$$

Substituting (4) and (12) into (10), we get the CL expression and an upper bound of single layer transmission:

$$\begin{aligned} C_{\mathrm{loss}}|_{L=1} &= -\log_2\sum_{k=1}^{N_t}\frac{\lambda_k}{\lambda_1}\left|\mathbf{p}_1^\dagger\mathbf{v}_k\right|^2 \\ &\leq -\log_2\left|\mathbf{p}_1^\dagger\mathbf{v}_1\right|^2. \end{aligned} \tag{13}$$

(2) $L = N_t$: in this case, the matrix $\mathbf{P}$ is full rank, and satisfying $\mathbf{P}\mathbf{P}^\dagger = \mathbf{P}^\dagger\mathbf{P} = \mathbf{I}_{N_t}$. According to the definition of inverse matrix, we have $\mathbf{S}^{-1} = \mathbf{P}^\dagger\mathbf{V}\mathbf{\Lambda}^{-1}\mathbf{V}^\dagger\mathbf{P}$. With the aid of (11), the SINR of the lth layer can be represented as

$$\mathrm{SINR}_l = \frac{\gamma_0/N_t}{\sum_{k=1}^{N_t}\frac{1}{\lambda_k}\left|\mathbf{p}_l^\dagger\mathbf{v}_k\right|^2}. \tag{14}$$

Similar to the case of $L = 1$, invoking the property of concave function, we have

$$\begin{aligned} C_{\mathrm{loss}}|_{L=N_t} &= \sum_{l=1}^{N_t}\log_2\sum_{k=1}^{N_t}\frac{\lambda_l}{\lambda_k}\left|\mathbf{p}_l^\dagger\mathbf{v}_k\right|^2 \\ &\leq N_t\log_2\frac{1}{N_t}\sum_{l=1}^{N_t}\sum_{k=1}^{N_t}\frac{\lambda_l}{\lambda_k}\left|\mathbf{p}_l^\dagger\mathbf{v}_k\right|^2. \end{aligned} \tag{15}$$

For open-loop spatial multiplexing (OLSM) transmission [21], no CSI is available at the transmitter. It is equivalent that the precoding matrix is unit, $\mathbf{P} = \mathbf{I}_{N_t}$. Substituting into (15), we get the CL upper bound of OLSM transmission:

$$C_{\text{loss, OL}} \leq N_t \log_2 \frac{1}{N_t} \sum_{l=1}^{N_t} \sum_{k=1}^{N_t} \frac{\lambda_l}{\lambda_k} \left| \{\mathbf{V}\}_{l,k} \right|^2. \tag{16}$$

2.3. Codebook Selection. Though a general form of CL is difficult to obtain, we still expect to utilize its compact expressions in two considered special cases to simplify the codebook selection from the perspective of CL minimization. In this paper, the following selection criterions are compared.

2.3.1. Maximum Capacity (MC). The precoding matrix $\mathbf{P}$ is selected from the codebook set $\mathbf{W}_L$ to maximize the capacity. The capacity of each codebook is calculated according to (3)-(4). It can achieve the optimum performance at the price of high calculation complexity due to the matrix inversion.

2.3.2. Minimum Subspace Angle (MSA). An often used selection criterion is to minimize the Chordal distance [22] with much lower complexity than MC, expressed as

$$\min_{\mathbf{P} \in \mathbf{W}_L} \left\{ L - \sum_{l=1}^{L} \left| \mathbf{p}_l^{\dagger} \mathbf{v}_l \right|^2 \right\}. \tag{17}$$

2.3.3. Simplified MC. MC criterion is equivalent to minimizing CL in nature and can be simplified with the help of the compact CL expressions. From (13) and (15), a codebook selection criterion is directly obtained to minimize CL and organized as

$$\begin{aligned} &\max_{\mathbf{P} \in \mathbf{W}_L} \left\{ \sum_{k=1}^{N_t} \frac{\lambda_k}{\lambda_1} \left| \mathbf{p}_1^{\dagger} \mathbf{v}_k \right|^2 \right\}, \quad L = 1, \\ &\min_{\mathbf{P} \in \mathbf{W}_L} \left\{ \sum_{l=1}^{N_t} \sum_{k=1}^{N_t} \frac{\lambda_l}{\lambda_k} \left| \mathbf{p}_l^{\dagger} \mathbf{v}_k \right|^2 \right\}, \quad L = N_t. \end{aligned} \tag{18}$$

2.4. MIMO-OFDM System Evaluation. The channel matrix of the kth subcarrier is denoted as $\mathbf{H}^k$, $k = 1, 2, \ldots, K$, where K is the total number of subcarriers. The corresponding capacity $C^k(L^k, \mathbf{P}^k)$ with L^k layers and precoding matrix $\mathbf{P}^k$ can be calculated according to Section 2.1. The average spectral efficiency over the whole band is calculated as [20]

$$C = \frac{1}{K} \sum_{k=1}^{K} C^k \left(L^k, \mathbf{P}^k \right). \tag{19}$$

When the number of transmitted layers is fixed for all subcarriers and the precoding matrix of each subcarrier is optimally chosen from the corresponding codebook set, the capacity with L layers transmission can be represented as

$$C_L = \frac{1}{K} \sum_{k=1}^{K} \max_{\mathbf{P}^k} C^k \left(L, \mathbf{P}^k \right). \tag{20}$$

Due to the effect of frequency-selective fading, fixed layers transmission over the whole band is not the best strategy. The performance can be improved by layer adaption in frequency domain. Also the performance of FDLA will be upper bounded by the case that L^k is optimized in subcarrier level:

$$C_{\text{upper}} = \frac{1}{K} \sum_{k=1}^{K} \max_{L^k} \left\{ \max_{\mathbf{P}^k} C^k \left(L^k, \mathbf{P}^k \right) \right\}. \tag{21}$$

We define the maximum capacity boost of FDLA, $G_{\max}$, as the capacity difference between the capacity upper bound of FDLA and the capacity with optimum fixed layer transmission:

$$G_{\max} = C_{\text{upper}} - \max_{L} C_L \geq 0. \tag{22}$$

The capacity improvement of FDLA depends on the channel fluctuation level in frequency domain. We first propose an effective metric to express the channel multiplexing capability then measure its fluctuation level. Generally, K_D can be utilized to indicate the invertibility and full-rank multiplexing capability of the channel matrix [23]. However, it is not robust due to the dominated effect of the minimum channel eigenvalue; hence, its dynamic range in actual frequency-selective channel is very large (up to 40 dB or more) even if the channel yields favorable multiplexing capability across the whole band. More importantly, for MIMO systems with precoding at the transmitter, K_D cannot comprehensively express the channel multilayer multiplexing capability. Here we define a new channel multiplexing capability metric $\mathcal{M}$ as follows:

$$\mathcal{M} = \frac{\|\mathbf{H}\|_F^2}{\|\mathbf{H}\|_F^2 - \lambda_{\max}}, \tag{23}$$

where the numerator equals to the sum of the channel eigenvalues. The relationship between $\mathcal{M}$ and the channel condition number is

$$\mathcal{M} \leq \frac{K_D}{N_t - 1} \leq \frac{N_t}{N_t - 1} \frac{\lambda_{\max}}{\lambda_{\min}}. \tag{24}$$

Substituting (23) into (6), an equivalent expression is derived:

$$\mathcal{M} \geq \frac{\gamma_0 \|\mathbf{H}\|_F^2}{N_t (N_t - 1) \left(N_t^{1/(N_t - 1)} - 1 \right)}. \tag{25}$$

In the following, we define function $F(\zeta)$ to measure the channel fluctuation level within a subband:

$$F(\zeta) = \frac{\zeta \sum_{i=1}^{\zeta} x_i^2}{\left(\sum_{i=1}^{\zeta} x_i \right)^2} - 1, \tag{26}$$

where ζ is the number of the subcarriers within the subband, and x_i is the channel metric of the ith subcarrier belonging to the considered subband. x_i can be one element of the channel metric set $\{\|\mathbf{H}\|_F^2, \lambda_{\max}, \mathcal{M}\}$, where $\|\mathbf{H}\|_F^2$ is related to the received SNR and the performance of space time block codes [24, 25], and $\lambda_{\max}$ is the crucial parameter of MIMO beamforming scheme [26]. As $\zeta \to +\infty$, $F(\zeta)$ is actually the ratio between the variance and squared mean value of a random variable.

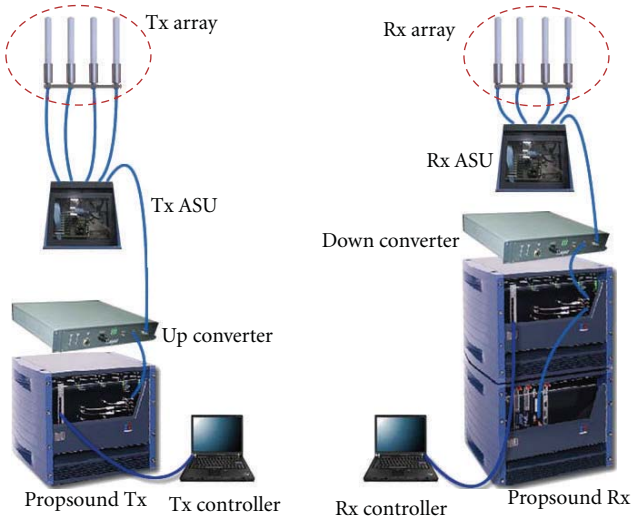

Figure 1: The setup of the MIMO channel measurement system.

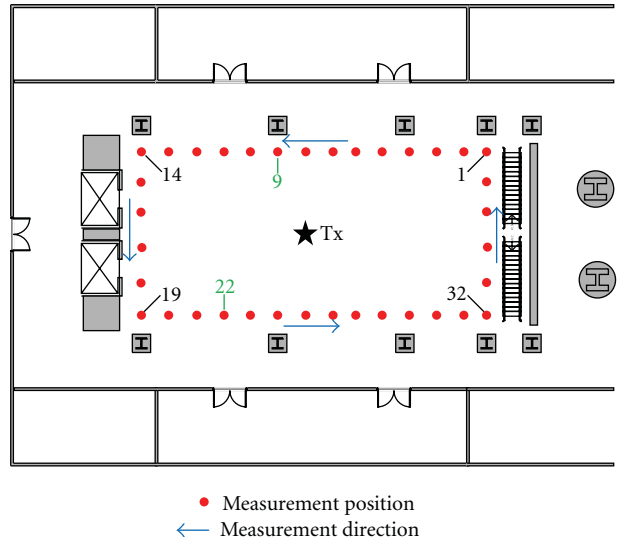

Figure 2: Indoor channel measurement layout and measurement position arrangement.

3. Measurement Description

3.1. Measurement Equipment. Measurement was performed in a teaching building of Beijing University of Posts and Telecommunications utilizing the Elektrobit PropSound Channel Sounder [27] system illustrated in Figure 1. External RF conversion modules are deployed at both transmit and receive sides to support the operating frequency 6 GHz. Uniform linear array (ULA) with four dipoles has been equipped at both sides, which can be replaced by omnidirectional array (ODA) to extract spatial angle parameters of multipaths. One complete set of MIMO channel realization called cycle is captured in a time-division multiplexing (TDM) method. The measurement of each antenna pairs is accomplished with the help of the high-speed antenna switching unit (ASU) to transfer the antennas in sequence. Before the measurement, a back-to-back test is required to obtain the system response for calibration purpose, where the transmitter and receiver are connected directly by cable using a 50 dB attenuator to prevent power overload at the receiver.

3.2. Measurement Environment. The measurement was conducted in a typical indoor hall of Beijing University of Posts and Telecommunications. The layout and measurement position arrangement are shown in Figure 2. The red dots represent the measurement positions, also the measurement position index and moving direction (blue arrow lines) are marked out. The height of the transmit antenna array is 3 m and marked by black pentacle. The transmit array remained stationary in the center of the hall during the experiment. The channel is sampled in a fixed-position method. The receiver moved to the next measurement position once more than 700 sets of channel realizations are collected. Total number of measurement positions is 36, and the line-of-sight (LOS) propagation component is always existent. The xth measurement position is denoted as Pos.x. The separation between two adjacent measurement positions is 1.6 m (32 wavelengths). Reflect and scatter components are created by surrounding concrete wall, square columns (1.2 m × 1.2 m), evaluators, stairs, and people. Total number of channel realizations is over 10^5. The detailed measurement configuration is listed in Table 1.

Table 1: Measurement configuration.

Items	Settings
Center frequency (GHz)	6
Bandwidth (MHz)	100
PN code length (chips)	255
Type of antenna array	ULA
Type of polarization	Vertical
Number of transmit antenna	4
Number of receive antenna	4
Element space of Tx (λ)	1
Element space of Rx (λ)	0.5
Height of Tx antenna (m)	3
Height of Rx antenna (m)	1.8

Although we have evaluated the MIMO channels of all measurement positions, it is convenient to pick out some typical measurement positions to address the key problems. We use the proposed metric $\mathcal{M}$ to distinguish different channel conditions. Hence, Pos.9 and Pos.22 with high and low $\mathcal{M}$ are selected and marked by green color in Figure 2, whose $\mathcal{M}$ are the upper and lower bounds of our measurement campaign, respectively. We use Case I and Case II to represent Pos.9 and Pos.22, respectively, and the cumulative probability curves of $\mathcal{M}$ are plotted in Figure 3.

4. Simulation Results

Based on the indoor MIMO channel measurement and data after processing, we present the simulation results in this section. We select the closed-loop spatial multiplexing

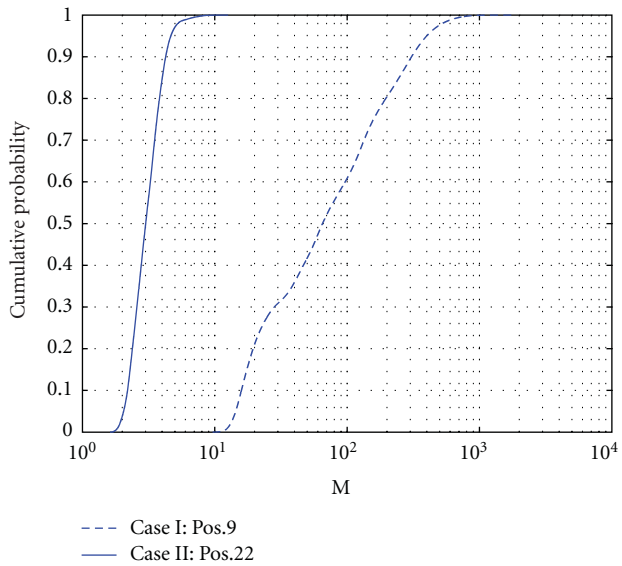

Figure 3: Cumulative probability of $\mathcal{M}$ in two considered cases.

(CLSM) codebook [6] standardized in LTE for evaluation, though the theoretical derivation in Section 2 is not limited by the codebook type. Each realization of the MIMO channel is transformed into the frequency domain by FFT, and the bandwidth of each subcarrier is 50 KHz. No power control strategy is adopted, and we consider single-user MIMO here. The symbols L1, L2, L3, and L4 represent the fixed layers transmission with one, two, three, and four layers, respectively.

4.1. Capacity with Perfect Precoding. Though unrealistic in practice, we wish to study the capacity with perfect precoding to provide the performance limit under different channel conditions. The upper bounds represent the maximum capacity of FDLA mentioned in (21). It can be found from Figure 4 that when the SNR is lower than 2 dB in Case I, $G_{\max} = C_{\text{upper}} - C_1 \rightarrow 0$, which indicates that single layer transmission is nearly optimal for all subcarrier and no benefit is obtained by FDLA. Similar phenomenon is observed in Case II when the SNR is higher than 23 dB. Moreover, the maximum capacity boost of FDLA is very limited and lower than 0.8 bit/s/Hz for all considered SNR under different channel conditions. The crossing point between the capacity curves of different layers transmission is greatly influenced by channel condition as indicated in (25), and the crossing point between L1 and L4 is about 13 dB and 0 dB in Case I and Case II, respectively.

4.2. Capacity with CLSM Codebook. The use of limited size codebook will bring interlayer interference and lead to performance degradation. We first compare the performance of different layers transmission with ZF and MMSE receivers and then evaluate the CL due to the limited feedback. From Figure 5, L1 transmissions with ZF and MMSE receivers yield the same performance over the whole SNR range, which can be easily proved through the SINR expressions (3). For multi-layer transmission, the performance of ZF and MMSE receivers will converge when the SNR is large enough. In Case I with high $\mathcal{M}$, the performance of MMSE receiver greatly outperforms ZF receiver in low and median SNR regions when $L \geq 2$. It indicates that the effect of noise is leading compared to the interlayer interference and suppressed by MMSE receiver which is equivalent to a matched filter in the low SNR region. In Case II with low $\mathcal{M}$, ZF and MMSE receivers yield identical performance within the considered SNR scope when $L < 4$, which reveals that the influence of the interlayer interference is dominant. The performance difference between two type receivers of L4 transmission in case II is led by the layer with the worst SINR. In conclusion, the performance of ZF and MMSE receivers will converge quickly within practical SNR range when $L < 4$, but the full-rank L4 transmission yields a much slower convergence speed. An interesting finding is that the FDLA upper bounds of ZF and MMSE receivers are approximately identical for any given SNR. Furthermore, the maximum capacity boost $G_{\max}$ of FDLA is especially significant in case of high $\mathcal{M}$.

Since the performance of MMSE receiver greatly exceeds ZF receiver in low SNR range, we expect to study the CL of different layers transmission with MMSE receiver. Figure 6 shows that L1 transmission suffers very slight capacity loss over the whole SNR scope, which indicates that current codebook design for L1 transmission is nearly capacity lossless. The main reason is that there is no interlayer interference, and the limited size codebook only causes a little beamforming direction bias which leads to a slight SNR gain decrease. As the number of transmitted layers increasing, the CL becomes more significant and especially severe for L4 transmission. It reveals that the limited size codebook set cannot simultaneously offer accurate beamforming vectors for multi-layer transmission to eliminate the interlayer interference and the situation gets worse when the transmitted layers increase. Moreover, the CL in high $\mathcal{M}$ case is larger than that of low $\mathcal{M}$ case, which can be roughly explained by the CL expression of full-rank transmission derived in (15). The percentage CLs of L1, L2, L3, and L4 transmissions relative to perfect precoding at 25 dB is respectively 5.5%, 21%, 30%, and 39% in Case I, corresponding to 3.8%, 6.7%, 8.2%, and 19.5% in Case II. Due to the CL difference, the crossing points between different layers transmissions are greatly changed compared to the perfect precoding case. For instance, the crossing points between L1 and L4 transmissions are, respectively, 27 dB and 2 dB in Case I and Case II.

4.3. Codebook Selection. Performance comparisons between the considered codebook selection criterions are given in Figure 7. For L1 transmission, MSA criterion is equivalent to the minimization of the CL upper bound derived in (13), and the MC and simplified MC criterions are essentially the same. All three selection criterions yield identical performance. Benefitting from taking the interlayer interference into account, the MC and simplified MC criterions outperform the MSA criterion for L4 transmission. Because the simplified MC criterion for L4 transmission is based on the CL upper bound in (15), performance decrease relative to MC

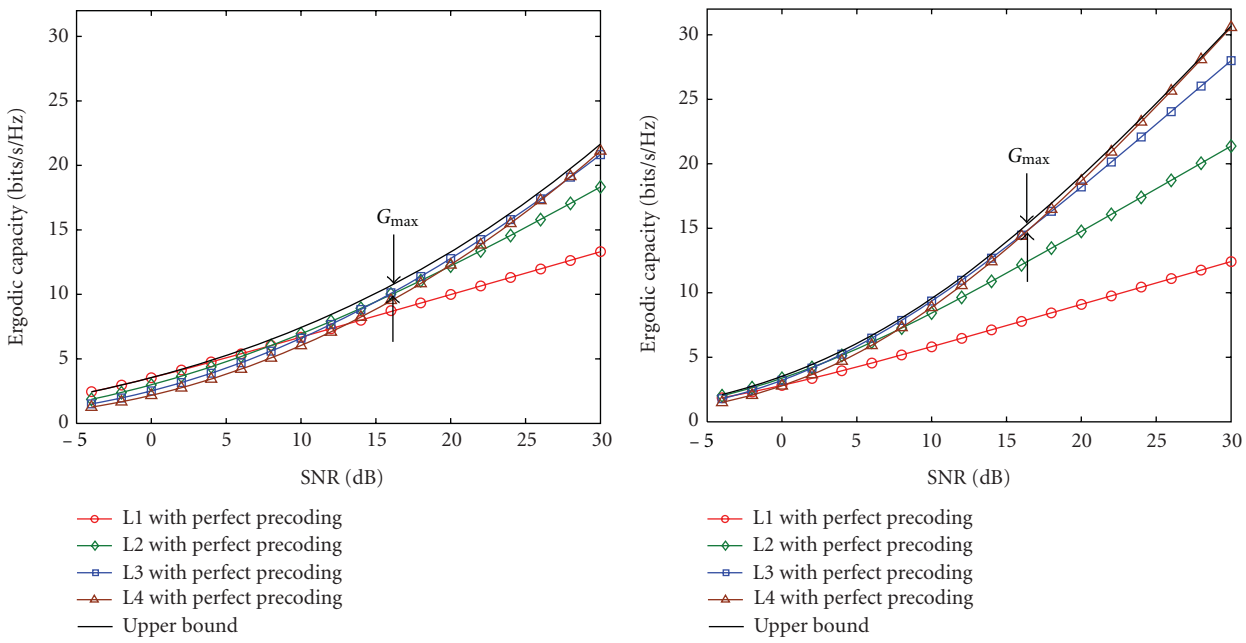

(a) Case I: high $\mathcal{M}$ (b) Case II: low $\mathcal{M}$

Figure 4: Capacity of different layer transmissions with perfect precoding.

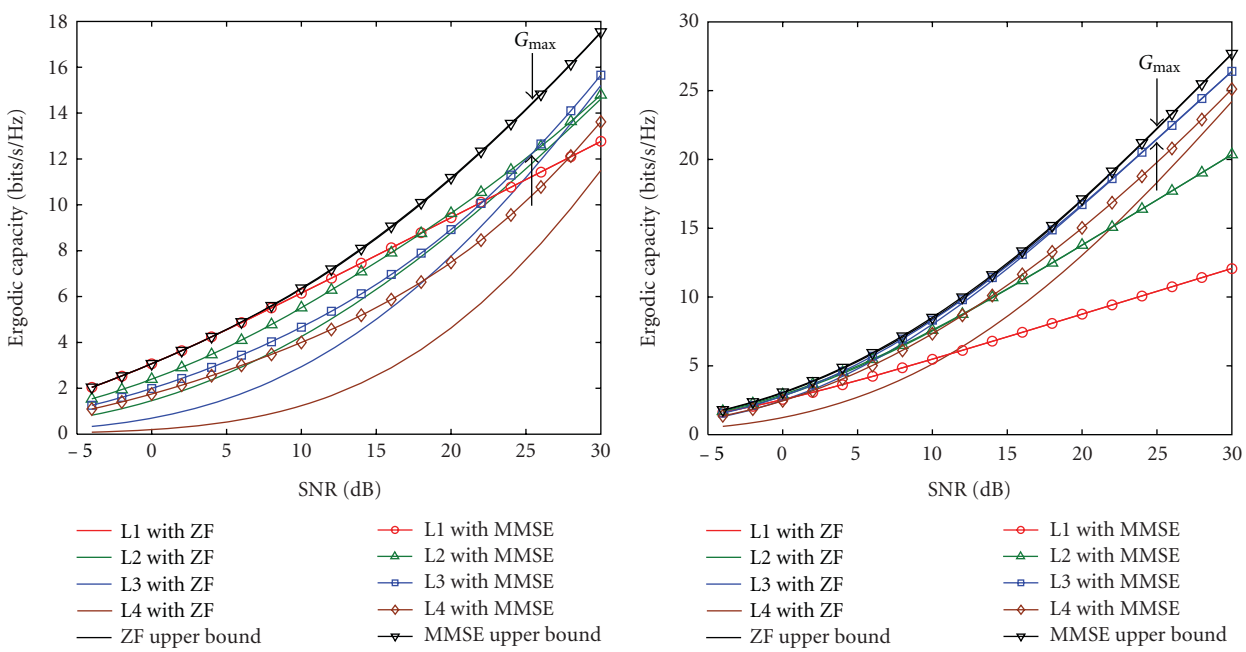

(a) Case I: high $\mathcal{M}$ (b) Case II: low $\mathcal{M}$

Figure 5: Capacity of different layer transmissions with ZF and MMSE receivers using CLSM codebook.

criterion is resulted. However, compared to the CL marked in Figure 6, the performance improvement by the use of better codebook selection criterions is very limited. To approve that, capacity comparison between CLSM and OLSM with L4 transmission is also plotted in Figure 8. In Case I, the capacity improvement of CLSM compared to OLSM is 1.72 bit/s/Hz at 30 dB; yet the CL due to the limited size CLSM codebook reaches 7.5 bit/s/Hz. Though considering single user here, it must be mentioned that the simplified MC criterion for full-rank transmission can also be used in multiuser MIMO to reduce the interference.

4.4. Effects of Channel Variation. In our measurement campaign, the transmitter and receiver are stationary during the

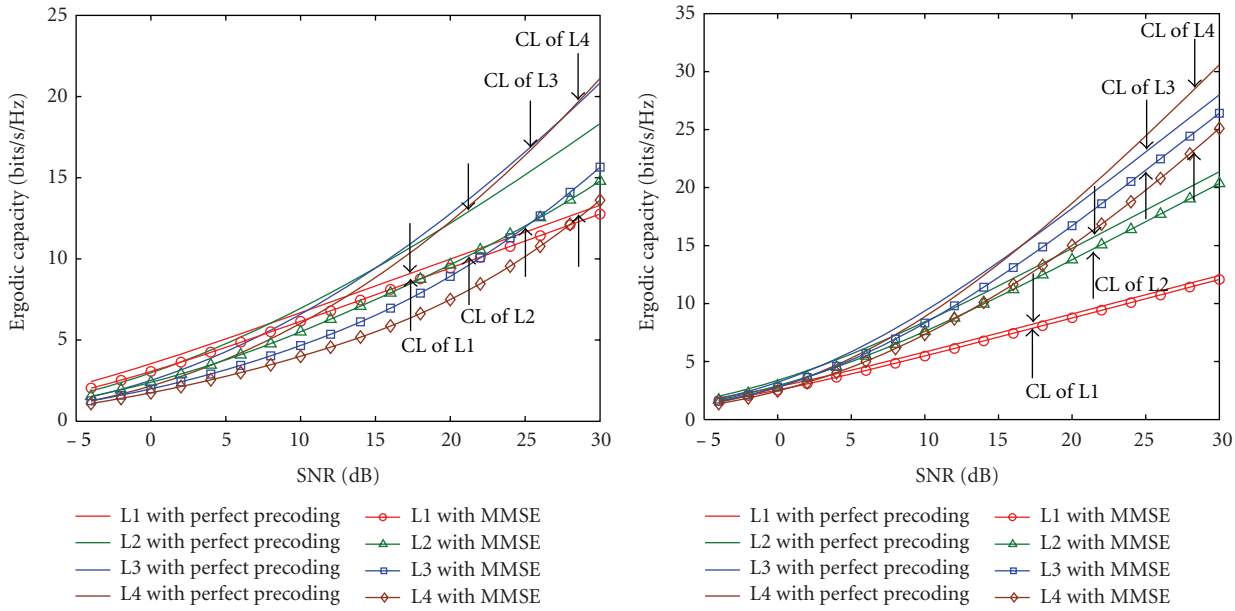

(a) Case I: high $\mathcal{M}$ (b) Case II: low $\mathcal{M}$

Figure 6: CL comparison between different layer transmissions with MMSE receiver using CLSM codebook.

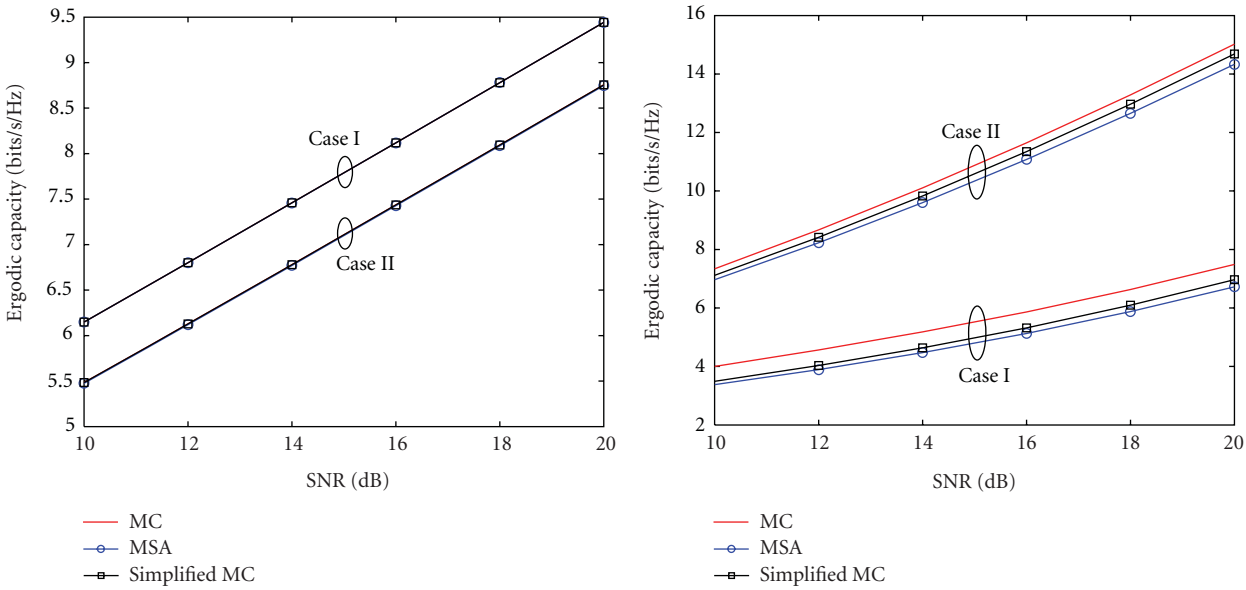

(a) L1 transmission (b) L4 transmission

Figure 7: Performance comparison between different codebook selection criterions for L1 and L4 transmissions with MMSE receiver.

channel sampling process, so we only consider the effect of frequency domain channel variation on the performance of MIMO-OFDM system here. The rich reflect and scatter objects in indoor environment result in channel frequency selective feature, thus expanding the available adaption dimension in frequency domain. The performance of FDLA is closely related to the channel fluctuation level within a subband. Using the function $F(\zeta)$ defined in (26), we first evaluate the key channel metrics $\{\|\mathbf{H}\|_F^2, \lambda_{\max}, \mathcal{M}\}$ fluctuation level within a subband. Then the influence of the frequency domain feedback interval on the performance of FDLA is investigated, which is helpful to achieve the tradeoff between the performance degradation and amount of feedback bits.

From Figure 9, the fluctuation level variations of $\|\mathbf{H}\|_F^2$ and $\lambda_{\max}$ are highly coherent, and an intuitive explanation is that the maximum eigenvalue dominates the power sum of all the layers. The fluctuation level of $\mathcal{M}$ seems to be related

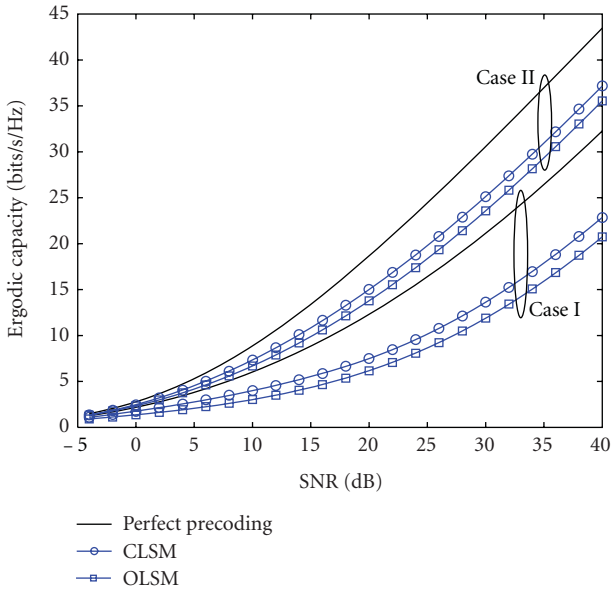

Figure 8: Capacity comparison between CLSM and OLSM for L4 transmission with MMSE receiver.

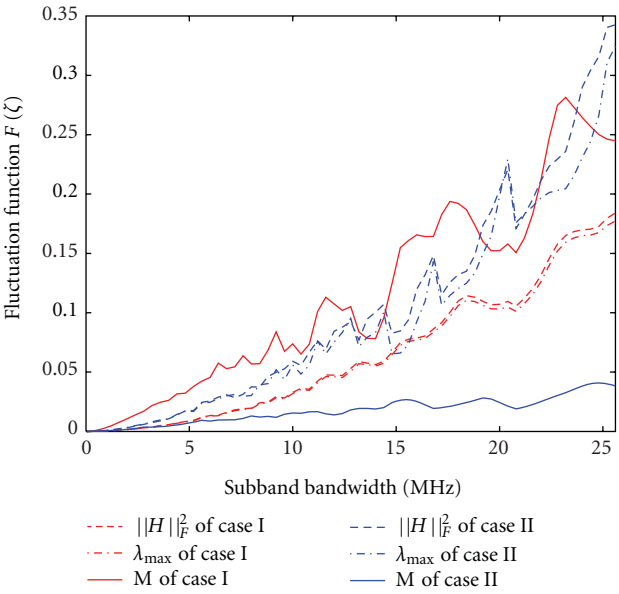

Figure 9: The fluctuation level variations of the key channel metrics.

to the value of $\mathcal{M}$ itself. In Case I with high $\mathcal{M}$, the fluctuation of $\mathcal{M}$ is severer than $\|\mathbf{H}\|_F^2$ and $\lambda_{\max}$. In contrast, the $\mathcal{M}$ varies much smoother within a subband in Case II.

In Figure 10, the percentage capacity is plotted, which is normalized by the FDLA upper bound C_{upper} in (21). A capacity floor is resulted as the transmitted layers feedback interval increasing, also the descend speed and value of the floor are related to the fluctuation level of the multiplexing capability metric $\mathcal{M}$. The higher the fluctuation level of M, the lower the value of the capacity floor. The maximum

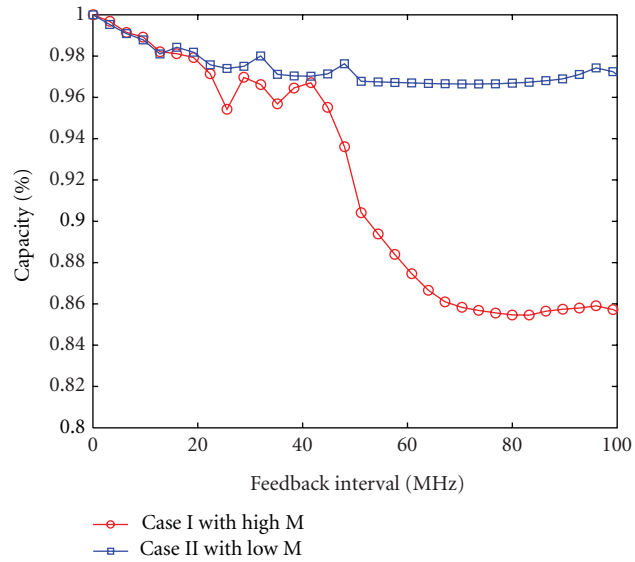

Figure 10: Percentage capacity variation as the transmitted layers feedback interval in frequency domain.

capacity degradation is about 3% and 14%, respectively, in two considered cases.

5. Conclusion

Based on the wideband MIMO channel measurement in a typical indoor scenario, this paper has evaluated the performance of LTE/LTE-A CLSM codebook and the effect of channel variation on MIMO-OFDM system. Under the perfect precoding assumption, very slight capacity gain is obtained by FDLA. However, considering the limited size codebook, the maximum capacity boost of FDLA is highly related to the SNR and channel conditions. It is interesting to find that the FDLA upper bounds of ZF and MMSE receivers are identical under different channel conditions. The results show that current codebook design for L1 transmission is nearly capacity lossless, and the CL increases with the number of transmitted layers. Generally, the CL in high $\mathcal{M}$ case is more significant than that in low $\mathcal{M}$ case. Furthermore, compared to the CL caused by the limited size codebook, the capacity improvement of better codebook selection criterions is very limited. It reveals that the fluctuation levels of $\|\mathbf{H}\|_F^2$ and $\lambda_{\max}$ within a subband are interrelated, and the fluctuation level of $\mathcal{M}$ is determined by the value of $\mathcal{M}$ itself. Finally, a capacity floor is resulted as the layer number feedback interval increasing, and the descending speed and value of the floor are greatly influenced by the fluctuation level of $\mathcal{M}$.

Acknowledgments

The research is supported in part by China Important National Science and Technology Specific Projects under Grant no. 2012ZX03001043-009 and by Telecommunications Science Technical Institute (Datang Telecommunication Technology and Industry Group).

References

[1] M. El-Hajjar and L. Hanzo, "Multifunctional mimo systems: a combined diversity and multiplexing design perspective," *IEEE Wireless Communications*, vol. 17, no. 2, pp. 73–79, 2010.

[2] C. S. Park, Y. P. E. Wang, G. Jöngren, and D. Hammarwall, "Evolution of uplink MIMO for LTE-advanced," *IEEE Communications Magazine*, vol. 49, no. 2, pp. 112–121, 2011.

[3] L. Liu, R. Chen, S. Geirhofer, K. Sayana, Z. Shi, and Y. Zhou, "Downlink MIMO in LTE-advanced: SU-MIMO versus MU-MIMO," *IEEE Communications Magazine*, vol. 50, no. 2, pp. 140–147, 2012.

[4] F. Boccardi, B. Clerckx, A. Ghosh et al., "Multiple-antenna techniques in LTE-advanced," *IEEE Communications Magazine*, vol. 50, no. 3, pp. 114–121, 2012.

[5] D. J. Love, R. W. Heath, V. K. N. Lau, D. Gesbert, B. D. Rao, and M. Andrews, "An overview of limited feedback in wireless communication systems," *IEEE Journal on Selected Areas in Communications*, vol. 26, no. 8, pp. 1341–1365, 2008.

[6] 3GPP TS 36.211, "Evolved universal terrestrial radio access (EUTRA), physical channels and modulation," vol. V10.4.0, 2012.

[7] W. Santipach and M. L. Honig, "Capacity of a multiple-antenna fading channel with a quantized precoding matrix," *IEEE Transactions on Information Theory*, vol. 55, no. 3, pp. 1218–1234, 2009.

[8] R. de Miguel, V. Gardašević, R. R. Müller, and F. F. Knudsen, "On overloaded vector precoding for single-user MIMO channels," *IEEE Transactions on Wireless Communications*, vol. 9, no. 2, pp. 745–753, 2010.

[9] P. Xiao, R. Tafazolli, K. Moessner, and A. Gluhak, "Codebook based single-user MIMO system design with widely linear processing," *IEEE Transactions on Communications*, vol. 60, no. 9, pp. 2408–2414, 2012.

[10] H. J. Yang, J. Chun, Y. Choi, S. Kim, and A. Paulraj, "Codebook-based lattice-reduction-aided precoding for limited-feedback coded MIMO systems," *IEEE Transactions on Communications*, vol. 60, no. 2, pp. 510–524, 2012.

[11] M. Zhang, M. Shafi, P. J. Smith, and P. A. Dmochowski, "Precoding performance with codebook feedback in a MIMO-OFDM system," in *Proceedings of the IEEE International Conference on Communications (ICC '11)*, pp. 1–6, June 2011.

[12] W. Kim, H. Lee, M. Kim, and H. Chung, "Distribution of eigenvalues for 2x2 MIMO channel capacity based on indoor measurements," *IEEE Transactions on Wireless Communications*, vol. 11, no. 4, pp. 1255–1259, 2012.

[13] C. Oestges and N. Czink, "Empirical investigation of multi-link separation for indoor MIMO channels," in *Proceedings of the IEEE International Symposium on Personal, Indoor and Mobile Radio Communications (PIMRC '11)*, pp. 945–949, September 2011.

[14] J. Poutanen, J. Salmi, K. Haneda, V. M. Kolmonen, and P. Vainikainen, "Angular and shadowing characteristics of dense multipath components in indoor radio channels," *IEEE Transactions on Antennas and Propagation*, vol. 59, no. 1, pp. 245–253, 2011.

[15] C. Mehlführer, S. Caban, and M. Rupp, "Measurement-based performance evaluation of MIMO HSDPA," *IEEE Transactions on Vehicular Technology*, vol. 59, no. 9, pp. 4354–4367, 2010.

[16] Y. Ofuji, H. Takahashi, S. Fukumoto, S. Abeta, and T. Nakamura, "Field experimental results of E-UTRA downlink with precoding and non-precoding MIMO," in *Proceedings of the IEEE 69th Vehicular Technology Conference*, pp. 1–5, April 2009.

[17] K. P. Kongara, P. J. Smith, and L. M. Garth, "Frequency domain variation of eigenvalues in adaptive MIMO OFDM systems," *IEEE Transactions on Wireless Communications*, vol. 10, no. 11, pp. 3656–3665, 2011.

[18] D. Dong, J. Zhang, Y. Zhang, and X. Nie, "Large scale characteristics and capacity evaluation of outdoor relay channels at 2.35 GHz," in *Proceedings of the IEEE 70th Vehicular Technology Conference Fall (VTC' 09)*, September 2009.

[19] R. W. Heath Jr., S. Sandhu, and A. Paulraj, "Antenna selection for spatial multiplexing systems with linear receivers," *IEEE Communications Letters*, vol. 5, no. 4, pp. 142–144, 2001.

[20] D. Tse and P. Viswanath, *Fundamentals of Wireless Communication*, Cambridge University Press, New York, NY, USA, 2005.

[21] A. Forenza, M. R. McKay, A. Pandharipande, R. W. Heath, and I. B. Collings, "Adaptive MIMO transmission for exploiting the capacity of spatially correlated channels," *IEEE Transactions on Vehicular Technology*, vol. 56, no. 2, pp. 619–630, 2007.

[22] N. Ravindran and N. Jindal, "Limited feedback-based block diagonalization for the MIMO broadcast channel," *IEEE Journal on Selected Areas in Communications*, vol. 26, no. 8, pp. 1473–1482, 2008.

[23] R. W. Heath and A. J. Paulraj, "Switching between diversity and multiplexing in MIMO systems," *IEEE Transactions on Communications*, vol. 53, no. 6, pp. 962–968, 2005.

[24] J. Huang and S. Signell, "Adaptive MIMO systems in 2×2 uncorrelated Rayleigh fading channel," in *Proceedings of the IEEE Wireless Communications and Networking Conference (WCNC '07)*, pp. 1114–1118, March 2007.

[25] J. Huang and S. Signell, "On spectral efficiency of low-complexity adaptive MIMO systems in Rayleigh fading channel," *IEEE Transactions on Wireless Communications*, vol. 8, no. 9, pp. 4369–4374, 2009.

[26] K. P. Kongara, P. H. Kuo, P. J. Smith, L. M. Garth, and A. Clark, "Performance analysis of adaptive MIMO OFDM beamforming systems," in *Proceedings of the IEEE International Conference on Communications (ICC '08)*, pp. 4359–4365, May 2008.

[27] Elektrobit, "Propsoundmultidimensional channel sounder," http://www.elektrobit.com/.

Hindawi Publishing Corporation
International Journal of Antennas and Propagation
Volume 2012, Article ID 423759, 7 pages
doi:10.1155/2012/423759

Application Article

Construction and Capacity Analysis of High-Rank LoS MIMO Channels in High Speed Railway Scenarios

Jingya Yang, Bo Ai, and Zhangdui Zhong

State Key Laboratory of Rail Traffic Control and Safety, Beijing Jiaotong University, Beijing 100044, China

Correspondence should be addressed to Bo Ai, aibo@ieee.org

Received 22 July 2012; Revised 22 October 2012; Accepted 22 October 2012

Academic Editor: Thomas Kürner

The validity of the maximum capacity criterion applied to realize high-rank line-of-sight (LoS) multiple-input multiple-output (MIMO) channels is investigated for high speed railway scenarios. Performance is evaluated by ergodic capacity. Numerical results demonstrate that by simply adjusting antenna spacing according to the maximum capacity criterion, significant capacity gains are achievable. We find relatively low sensitivity of the system to displacements from the optimal point and angle in relatively short range. Thus, we present two proposals to reconfigure antenna arrays so as to maximize LoS MIMO capacity in the high speed railway scenarios.

1. Introduction

MIMO presents an attractive solution for meeting the requirements of next generation wireless communication system for the high speed railway. Since a high speed data rate is required for efficient voice and data transmission services in the future railways, and the bandwidth resources for the railway are limited, the capacity cannot be improved through increasing bandwidth. So MIMO is considered as an effective technique in long-term evolution for railway (LTE-R) to ensure the efficiency and reliability for data transmissions [1].

The development of MIMO systems over the past decade is based on the assumption of i.i.d Rayleigh fading [2]. Although the assumption simplifies the analysis of MIMO systems, its validity is often violated due to either an specular wavefront or a strong direct component existing; then, the entries of the channel matrix can be more effectively modeled by the Ricean distribution. Conceptually, LoS propagation is viewed to limit MIMO advantages because the channel matrix is normally rank deficient [3, 4]. But some recent investigations have questioned this belief and proposed design methodologies in order to achieve subchannel orthogonally. The orthogonality of subchannels is a key condition for capacity maximization [5–9] and most methodologies are realized by placing the antenna elements sufficiently far apart.

The common characteristics of the above mentioned works are facts about the MIMO performance in a relatively short distance between transmitters and receivers, and meanwhile the low mobility of vehicles in scenarios. Thus, the performance of MIMO optimization design in high speed railways needs to be reassessed under a realistic high speed railway environment. In most scenarios of the high speed railway, the base stations are located less than 30 m away from the tracks, and most of the BS antenna heights are more than 30 meters, hence there are always a strong line-of-sight (LoS) path between the transmitters and the receivers. Moreover, the channels exhibit a sparse multipath structure due to the lack of sufficient scatters in the railway environment [10]. The channel consists of a direct LoS path and sparse multipath, which is known as LoS MIMO channel. The analysis of small-scale fading characteristics in viaduct scenarios is derived from measurements taken along the "Beijing-Tianjin" high-speed railway of China, refer to [11], which indicates that Ricean K-factor increases when the train gets closer to the base station; meanwhile, the number of resolvable paths and RMS spread for delay firstly increase and then decrease.

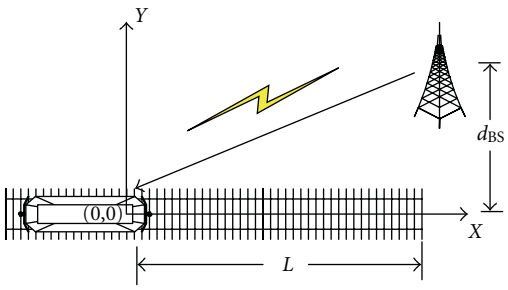

Figure 1: The simulation scenario.

In light of these facts, D2a scenario of WINNER II channel model is adopted, which is a realistic high speed railway transmission multipath propagation channel. The primary goal of the present paper is to verify the maximum capacity criterion in the high speed railway and then propose the methodologies for reconfigurable antenna arrays on maximizing the ergodic capacity of MIMO communication links through coverage area of the base station in viaduct scenarios.

The remainder of this paper is organized as follows. Section 2 discusses the simulation scenario and the WINNER II Channel Model. Section 3 develops the maximum capacity criterion. Section 4 concentrates on comparison and analysis of the simulation result and proposes two optimum proposals for reconfiguration antenna array in viaduct scenarios. Finally, Section 5 concludes this paper and summarizes the key findings.

2. High Speed Railway Channel Model

2.1. Scenario Description. According to the environment characteristics of high speed railways, D2a scenario is selected. D2a represents radio propagation in environments where MS is moving, possibly at very high speed, in a rural area. The link between the fixed network and the moving network (train) is typically an LoS type.

Figure 1 shows the setting for simulation in high speed railway scenarios. BS is located 14 m off the track and the height of this transmitter antenna array is 32 m above the ground. The receiver antenna array is installed on the top of the engine and its height is 3 m above the ground. The velocity of the train is set to 360 km/h towards the BS, and the track is parallel to the X-axis. The center frequency and bandwidth are 2.6 GHz and 100 MHz, respectively. In Figure 1, the geometry parameters are set to $L = 1000$ m, $d_{BS} = 14$ m, thus BS is located at the centre (500, 14).

2.2. WINNER II Channel Model. In WINNER II D2a channel model, each channel realization is generated by summing contributions of eight clusters; each cluster is composed of twenty subpaths, which are associated with different delay, power, angle-of-arrival (AOA), and angle-of-departure (AOD) [12]. As illustrated in Figure 2, consider a single link of a MIMO system with an S elements ULA for BS and a U elements ULA for MS.

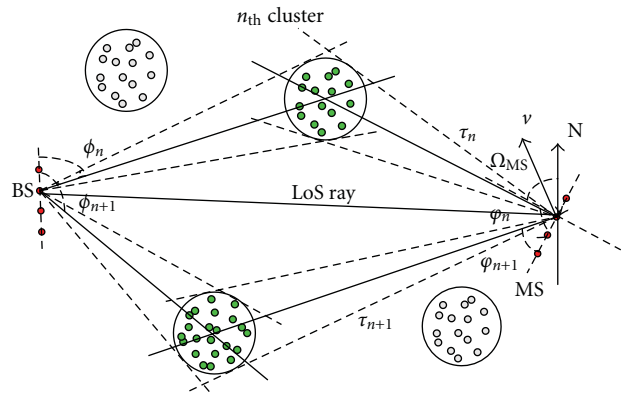

Figure 2: Single link in WINNER II channel model.

(1) *Generate the Delays τ.* Delays are drawn randomly from the delay distribution defined in [12]. With exponential delay distribution, calculate

$$\tau_n' = -r_\tau \sigma_\tau \ln(X_n), \tag{1}$$

where r_τ is the delay distribution proportionality factor (3.8 ns in D2a scenario), and σ_τ is delay spread defined as 40 ns. $X_n \sim \mathrm{Uni}(0,1)$ and cluster index $n = 1, \ldots, 8$.

Normalize the delays by subtracting with minimum delay and sort the normalized delays to descending order as follows:

$$\tau_n = \mathrm{sort}(\tau_n' - \min(\tau_n')). \tag{2}$$

In the case of LoS condition, additional scaling of delays is required to compensate the effect of LoS peak addition to the delay spread as follows:

$$\tau_n^{\mathrm{LoS}} = \tau_n / D, \tag{3}$$

where $D = 0.7705 - 0.0433K + 0.0002K^2 + 0.000017K^3$; K [dB] is the Ricean K-factor.

(2) *Generate the Cluster Powers P.* With exponential delay distribution the cluster powers are determined by

$$P_n' = \exp\left(-\tau_n \frac{r_\tau - 1}{r_\tau \sigma_\tau}\right) \cdot 10^{-Z_n/10}, \tag{4}$$

where $Z_n \sim N(0, \zeta)$ is the per cluster shadowing term in [dB]. Average the power so that sum power of all clusters is equal to one as

$$P_n = \frac{P_n'}{\sum_{n=1}^{N} P_n'}. \tag{5}$$

Assign the power of each ray within a cluster as P_n/M, where $M = 20$ is the number of rays per cluster.

For the two strongest clusters, say $n = 1$ and 2, rays are spread in delay to three subclusters (per cluster), and twenty rays of a cluster are mapped to sub-clusters as presented in Table 1.

Table 1: Subcluster information for intracluster delay spread clusters.

Sub-cluster	Mapping to rays	Power	Delay offset
1	1, 2, 3, 4, 5, 6, 7, 8, 19, 20	10/20	0 ns
2	9, 10, 11, 12, 17, 18	6/20	5 ns
3	13, 14, 15, 16	4/20	10 ns

Table 2: Ray offset angles within a cluster, given for 1°rms angle spread.

Ray number m	Basis vector of offset angles α_m
1, 2	0.0447
3, 4	0.1413
5, 6	0.2492
7, 8	0.3715
9, 10	0.5129
11, 12	0.6797
13, 14	0.8844
15, 16	1.1481
17, 18	1.5195
19, 20	2.1551

(3) *Generate the Azimuth Arrival Angles φ and Azimuth Departure Angles ϕ.* The AOA for the nth cluster is

$$\varphi_n = (X_n\varphi'_n + Y_n) - (X_n\varphi'_1 + Y_1) + \varphi_{\text{LOS}}, \tag{6}$$

where

$$\varphi'_n = \frac{2\sigma_{\text{AOA}}\sqrt{-\ln(P_n/\max(P_N))}}{C_{\text{LOS}}},$$

$$\sigma_{\text{AOA}} = \sigma_{\varphi/1.4},$$

$$C_{\text{LOS}} = C \times (1.1035 - 0.028K - 0.002K^2 + 0.00001K^3). \tag{7}$$

In the above equation σ_{AOA} is the standard deviation of arrival angles (factor 1.4 is the ratio of Gaussian std and corresponding RMS spread). φ_{LOS} is the LoS direction and component $Y_n \sim N(0, \sigma_{\text{AOA}}/5)$. Add the offset angles from Table 2 to cluster angles as

$$\varphi_{n,m} = \varphi_n + c_{\text{AOA}}\alpha_m, \tag{8}$$

where $\varphi_{n,m}$ is the AOA for each ray m of each cluster n; c_{AOA} is the cluster-wise rms azimuth spread of AOA ($c_{\text{AOA}} = 3°$ in D2a scenarios). The corresponding offset angle α_m is taken from Table 2. For departure angle ϕ_n, the procedure is analogous.

(4) *Draw the Random Initial Phase.* $\{\Phi^{VV}_{n,m}, \Phi^{VH}_{n,m}, \Phi^{HV}_{n,m}, \Phi^{HH}_{n,m}\}$ are the random initial phases for each ray m of each cluster n and for four different polarization combinations (vv, vh, hv, hh). Distribution for the initial phases is uniform, $\text{Uni}(-\pi, \pi)$. In the LoS case, draw also random initial phases $\{\Phi^{VV}_{\text{LoS}}, \Phi^{HH}_{\text{LoS}}\}$ for both VV and HH polarisations.

(5) *Generate the Cross-Polarisation Power Ratios (XPR) $\kappa_{n,m}$ for Each Ray m of Each Cluster n.* XPR is log-normal distributed. Draw XPR values as

$$\kappa_{n,m} = 10^{X/10}, \tag{9}$$

where $X \sim N(\sigma, \mu)$ is Gaussian distributed with σ and μ from [12] for XPR.

(6) *Generate the Channel Coefficients for Each Cluster n and Each Receiver and Transmitter Element Pair u, s.* For the clusters in D2a, say $n = 1, 2, \ldots, 8$, and uniform linear arrays (ULA), the channel coefficients are given by

$$H_{u,s,n}(t) = \sqrt{\frac{1}{K_R+1}}H'_{u,s,n}(t) + \delta(n-1)\sqrt{\frac{K_R}{K_R+1}}H_0(t), \tag{10}$$

where $\delta(\cdot)$ is the Dirac's delta function and K_R is the Ricean K-factor converted to linear scale. $H_0(t)$ is the channel coefficient corresponding to the single LoS ray. $H'_{u,s,n}(t)$ is the non-LoS channel coefficient component. $H_0(t)$ and $H'_{u,s,n}(t)$ are given by

$$\begin{aligned}
H_0(t) = {} & \begin{bmatrix} F_{tx,s,V}(\phi_{\text{LoS}}) \\ F_{tx,s,H}(\phi_{\text{LoS}}) \end{bmatrix}^T \\
& \cdot \begin{bmatrix} \exp\left(j\Phi^{VV}_{\text{LoS}}\right) & 0 \\ 0 & \exp\left(j\Phi^{HH}_{\text{LoS}}\right) \end{bmatrix} \begin{bmatrix} F_{rx,u,V}(\varphi_{\text{LoS}}) \\ F_{rx,u,H}(\varphi_{\text{LoS}}) \end{bmatrix} \\
& \cdot \exp(jd_s 2\pi\lambda_0^{-1}\sin(\phi_{\text{LoS}})) \\
& \cdot \exp(jd_u 2\pi\lambda_0^{-1}\sin(\varphi_{\text{LoS}})) \cdot \exp(j2\pi\nu_{\text{LoS}}t), \\
H'_{u,s,n}(t) = {} & \sqrt{P_n}\sum_{m=1}^{M} \begin{bmatrix} F_{tx,s,V}(\phi_{n,m}) \\ F_{tx,s,H}(\phi_{n,m}) \end{bmatrix}^T \\
& \cdot \begin{bmatrix} \exp\left(j\Phi^{VV}_{n,m}\right) & \sqrt{\kappa_{n,m}}\exp\left(j\Phi^{VH}_{n,m}\right) \\ \sqrt{\kappa_{n,m}}\exp\left(j\Phi^{HV}_{n,m}\right) & \exp\left(j\Phi^{HH}_{n,m}\right) \end{bmatrix} \\
& \cdot \begin{bmatrix} F_{rx,u,V}(\varphi_{n,m}) \\ F_{rx,u,H}(\varphi_{n,m}) \end{bmatrix} \cdot \exp(jd_s 2\pi\lambda_0^{-1}\sin(\phi_{n,m})) \\
& \cdot \exp(jd_u 2\pi\lambda_0^{-1}\sin(\varphi_{n,m})) \cdot \exp(j2\pi\nu_{n,m}t),
\end{aligned} \tag{11}$$

where $F_{rx,u,V}$ and $F_{rx,u,H}$ are the receiving antenna element u field patterns for vertical and horizontal polarizations, respectively, similarly F_{tx} is the transmitting antenna patterns. d_s and d_u are antenna spacing (m) between transmitter elements and receiver elements, respectively, and λ_0 is the wavelength on carrier frequency. ν_{LoS} and $\nu_{n,m}$ are the Doppler frequency shifts for the LoS ray and each ray m of each cluster n, respectively. The Doppler frequency

component is calculated from AOA, MS speed v, and direction of travel θ_v as follows:

$$\nu_{\text{LoS}} = \frac{\|v\| \cos(\varphi_{\text{LoS}} - \theta_v)}{\lambda_0}, \qquad \nu_{n,m} = \frac{\|v\| \cos(\varphi_{n,m} - \theta_v)}{\lambda_0}. \tag{12}$$

The CIR for each receiver and transmitter element pair u, s is given by

$$H_{(u,s)}(t) = \sum_{n=1}^{N_c} H_{u,s,n}(t - \tau_n). \tag{13}$$

2.3. Path Loss Model. Path loss model for the WINNER II D2a scenario has been developed based on results of measurements carried out within WINNER, and it is formed as

$$\text{PL} = 21.5 \log_{10}(D) + 44.2 + 20 \log_{10}\left(\frac{f_c}{5.0}\right), \tag{14}$$

where D is the distance between the transmitter and the receiver in (m), f_c is the system frequency in (GHz). Path loss factor PL is given as a parameter, which is multiplied to channel matrices.

3. Maximum LoS MIMO Capacity Criterion

Using the simplified maximum capacity criterion in LoS MIMO systems, the problem of reduced capacity in a LoS scenario can be overcome [8]. The validity of the new capacity criterion implementation was investigated by WINNER II channel model in the next section.

3.1. MIMO Channel Capacity. To assess the performance of the stochastic channel in the presence of scatter, the notion of ergodic capacity must be employed. Note that the transmit power is equal to P_T/S (at all transmit elements) as UPA (uniform power allocation) is used. The ergodic capacity of a MIMO system to be given by [13]

$$C = E\left\{\log_2\left(\det\left(I_U + \frac{\rho}{S} HH^H\right)\right)\right\}, \tag{15}$$

where ρ corresponds to the average received signal-to-noise ratio (SNR) at the input of the receiver, and $[\cdot]^H$ denotes the conjugate transpose. Extremely, the capacity in (15) is maximized for $HH^H = SI_U$, and this response corresponds to a channel with perfectly orthogonal MIMO subchannels.

3.2. Maximum $U \times S$ Capacity Criterion. It has been demonstrated that the capacity in LoS MIMO channel (ignoring any scatter components at this stage) is maximized, when the following criterion is fulfilled [8]:

$$d_s d_u = \lambda\left(\frac{1}{S} + p\right)\frac{D}{\sin\omega \sin\theta}, \quad \forall p \in \mathbb{Z}, \tag{16}$$

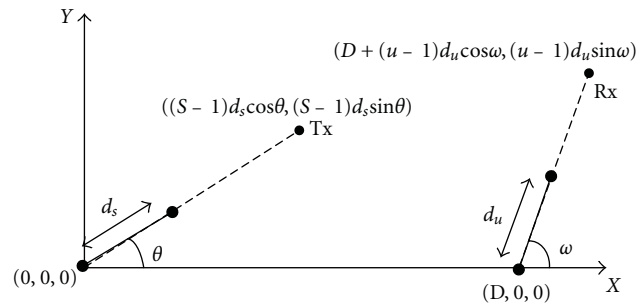

Figure 3: Positioning of the elements in a $U \times S$ MIMO system.

where D is the Tx-Rx distance, and [8] defines the distance between the first element of each array to equal D. The 3D geometric configuration is shown in Figure 3. θ and ω are the orientations of the arrays for Tx and Rx, respectively. Thus, by knowing the carrier frequency and the Tx-Rx distance, the optimal spacing can be easily calculated from the maximum LoS MIMO capacity criterion. In other words, this criterion for perfectly orthogonal MIMO subchannels architectures defines a number of MIMO architectures with antenna arrays fixed at optimal points.

4. Simulation Results

The high speed railway scenarios have its distinctive characteristics, such as a relatively long distance between transmitters and receivers, the high speed of 350 km/h or above, and a number of scatters. But the maximum capacity criterion only considers the LoS component of the channel response. The characteristics of railway scenarios must be accounted for evaluating the criterion. Thus, in this section, we evaluate the criterion (16) in practical high speed railway scenarios described in Figure 1.

We explore a 2×2 MIMO system operating at 2.6 GHz. And the orientations of the antenna arrays for Tx and Rx are perpendicular to the track as $\theta = 90^\circ$ and $\omega = 90^\circ$, respectively. Then, the maximum capacity criterion is simplified as $d_s d_u = \lambda D/2$, $p = 0$. Assuming interelement spacing d_s for reconfigurable antenna arrays equal to 1 m, the d_u can be calculated. In the high speed railway scenarios, the separated distance D between BS and MS is usually in order of hundreds of meters and is much larger than d_{BS}, therefore the approximation as $D = \sqrt{l^2 + d_{\text{BS}}^2} \approx l$ is used for simplification, where l is the separated distance between the projection of the BS and the projection of the train on X-axis. In Figure 4, we have optimal interelement spacings $d_s = 1$ m, and $d_u = 28.85$ m for the point $x = 0$ ($l = 500$ m). The K-factor is set to 9 dB. The ergodic capacity is plotted as a function of SNR for different interelement spacings. The simulated curves are generated according to (15).

It can be easily seen that the ULA with optimal antenna spacings shows superiority to other geometries over the entire SNR range. When the SNR reaches 20 dB, the capacity of optimal case is about 5 bps/Hz higher than that of ULA with 10λ interelement spacings. In addition, the ULA with 10λ interelement spacings shows superiority to the one with

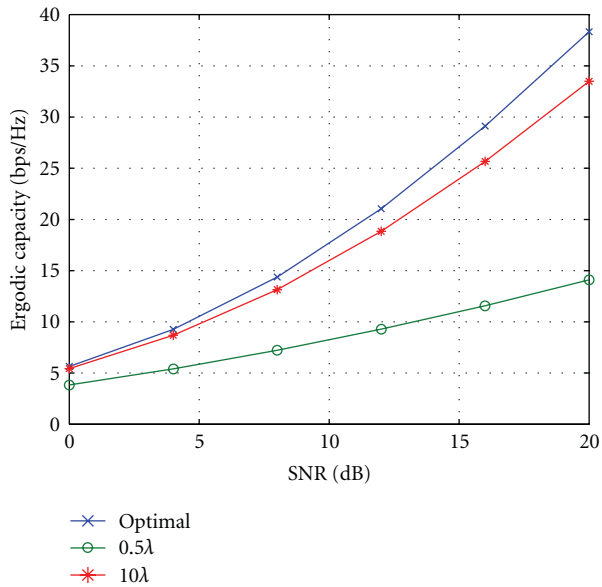

Figure 4: Ergodic capacity as a function of SNR for different antenna spacings (K-factor = 9 dB, l = 275 m).

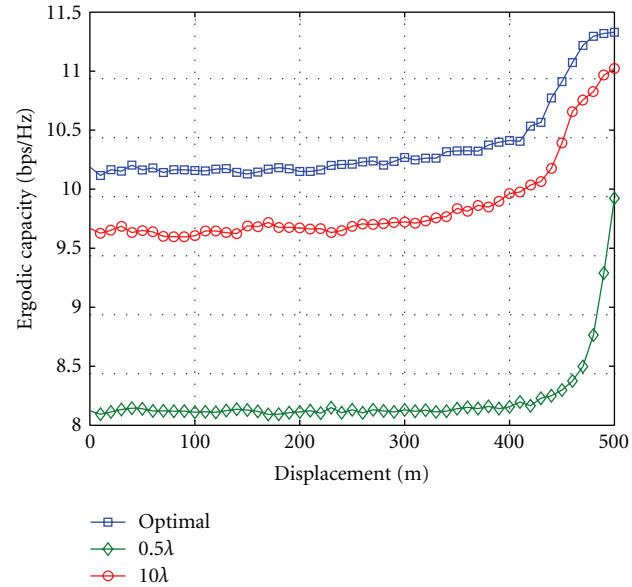

Figure 5: Ergodic capacity as a function of the displacement from the optimum point.

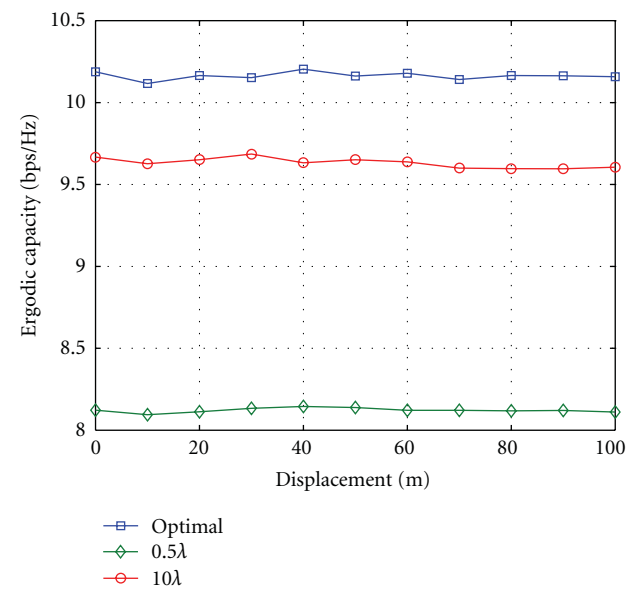

Figure 6: Ergodic capacity as a function of the displacement from the optimum point.

0.5λ interelement spacings. The reason is that placing the antenna elements far apart results in high resolution and low correlation of channel matrix and then it gives the high capacity.

4.1. Displacement. The criterion for high-rank LoS MIMO channels defines a number of MIMO architectures for systems with ULAs fixed at optimal locations. However, in high speed railway situations, there is a need for high capacity over an area, rather than to a fixed point. To examine the sensitivity of the performance of maximum capacity architectures in high speed railways, the capacity is now evaluated as a function of the displacement from the optimal point. The simulation is explored in the location range from 0 to 500 m, which is the whole trajectory, that is from the midpoint between two BSTs up to the point closest to another BST. And it is equivalent to a 500 m displacement range refering to the optimal point $x = 0$. The optimal interelement spacings are $d_s = 1$ m and $d_u = 28.85$ m. The received power gradually changes.

The variation of capacity with different displacements is shown in Figure 5. From this figure, the performance of optimal case shows superiority to other geometries over the entire trajectory. Above a displacement of 350 m or so, the curve of capacity is escalating faster and faster. The reason is the increased received power and the decreased degree of scattering. When the displacement reaches 500 m, the capacity of optimal case is about 1.5 bps/Hz higher than that of ULA with 0.5λ interelement spacings. In addition, the ULA with 10λ interelement spacings shows superiority to the one with 0.5λ interelement spacings. The reason is the high resolution and the low correlation of channel matrix.

The sensitivity of the capacity performance for the optimum case is investigated by means of a narrow distance window, see Figure 6. The simulation is explored in the range of 0 m to 100 m, which is equivalent to a 100 m displacement range, refer to the optimal point $x = 0$ m. From this figure, it is clear that the capacity is relatively insensitive to small displacements from the optimum point. The reason is that the angle changes of θ and ω are very small due to short displacements. According to (16), the optimal interelement spacing is local optimum for the premise of $\sin(\theta)$ and $\sin(\omega)$ is basically invariable. So, the same reconfiguration antenna array used in a small regional is feasible.

4.2. ULA Azimuthal Orientation. There are some disadvantages for antenna array orientation in railway scenarios due

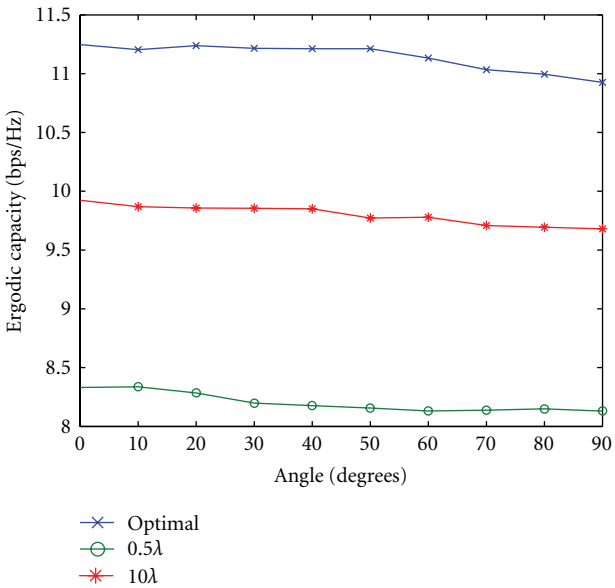

Figure 7: Ergodic capacity as a function of the angle deviation from the optimum angle ($\rho = 20$ dB).

to the fast moving of the train and the rapid change of the radio propagation environments. It is difficult to deal with this fast fading. On the other hand, it has some advantages that the route of the train is fixed and the path can be predicted. So, some special antenna types or programs can be chosen. It is clear that there is a dependence of the capacity to the azimuthal orientation of the two arrays (angles θ and ω) from the maximum capacity criterion of (16). This dependence is now examined using the same channel model as before.

The effect of ULA azimuthal orientation at MS ends on the capacity is shown in Figure 7. The units of angle in MS coordinate axes are degree. The ergodic channel capacity is obtained at $\rho = 20$ dB. Each point in Figure 7 stands for different MS azimuthal orientation and fixed BS azimuthal orientation at the optimal point $x = 0$. At each process of simulation, the antenna orientations of BS and the train are fixed. The results show a little sensitivity (in terms of capacity) to the orientation of the MS arrays. In detail, the channel capacity is seen to vary between the minimum ($C\min = 10.93$ bps/Hz) and the maximum ($C\max = 11.25$ bps/Hz) values about the curve for the optimal one. The results suggested that this sensitivity needs not focus too much on the design of any practical MIMO system.

(1) *Maximizing Capacity in Viaduct Scenarios Using Reconfigurable Antenna Arrays.* Now theory and methods for exploiting the potential of reconfigurable RF front-ends in high speed railway are not fully developed. The results of simulation offer a reference for reconfigurable antenna arrays on maximizing the capacity of MIMO wireless communication links in high speed railway scenarios. And there is measure data based on Propsound measurements, which is operated in viaduct scenarios [11]. Then, we put forward two proposals through a combination of simulation results and the measurement data.

Table 3: The parameters for optimum proposals.

	RA	TA	CA	AA
The region (X axis, m)	(0, 230)	(230, 320)	(320, 480)	(480, 500)
D for proposal 1 (m)	385	225	100	14
D for proposal 2 (m)	500	500	500	500
d_u for proposal 1 (m)	22.23	12.96	5.76	0.81
d_u for proposal 2 (m)	28.85	28.85	28.85	28.85

According to [11], the coverage area of the base station is divided into 4 regions as remote area (RA), toward area (TA), close area (CA), and arrival area (AA). We can design different regions in the area that are involved in different reconfigurable antenna arrays because of the rapidly change of separate distances and different small-scale fading characteristics. The maximum capacity criterion is introduced in the previous section, and then two practical optimum proposals are afforded.

Optimum Proposal 1. Select four midpoints of the four linear regions as the optimal locations and use them to calculate optimal interelement spacings for the different reconfiguration antenna arrays involved in the four regions. The interelement spacings of ULA are adjusted for different regions, when the train travels through the coverage area of base stations.

The maximum capacity criterion defines a number of MIMO architectures for systems with antenna arrays fixed at optimal locations. However, there is a need for high capacity over an area, rather than to a fixed point. In the simulations, to examine the sensitivity of the performance of maximum capacity architectures under high speed railway scenarios, we can determine the advantage of the optimal antenna array basically stable in the small displacements range.

Optimum Proposal 2. Select the edge point of base station coverage as the optimal location and obtain the optimal interelement spacing of the reconfigurable antenna array involved in all regions. The interelement spacing of ULA maintains invariable when the train travels through the linear coverage. This proposal maximizes the capacity of the coverage edge and minimizes the correlation of channel matrix in the coverage.

The corresponding parameters for optimum proposals are taken from Table 3.

4.3. Scattering. In the maximum LoS MIMO capacity criterion, only LoS component of the channel response is considered. In railway scenarios, some degrees of scatterings are always present in the radio channel, and, hence, their effects must be accounted for the design of the MIMO system.

In Figure 8, the ergodic capacity is plotted against the Ricean K-factor and compared with two reference geometries. It demonstrates again the superiority of the optimal design obtained by maximum capacity criterion.

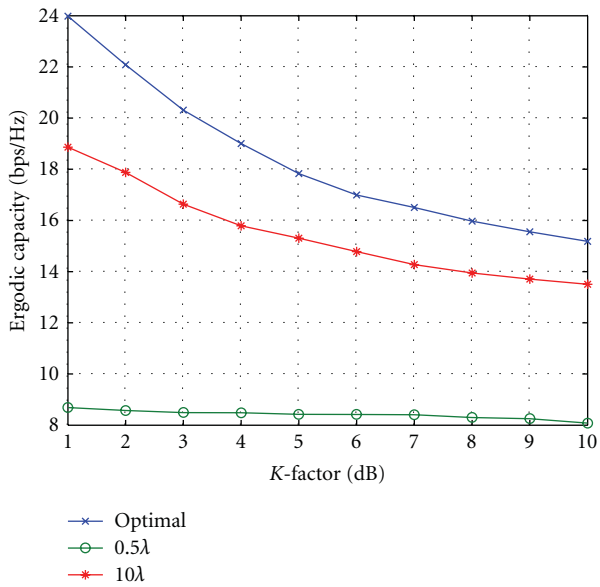

Figure 8: Ergodic capacity as a function of K-factor for different antenna spacings ($\rho = 10$ dB, $x = 500$ m).

And meanwhile we see the capacities for ULAs with different antenna spacings decrease when K-factor increases. The optimal design is not expected in this result because the curve for optimal interelement spacings should increase with the increment of K-factor, and the reason is high-rank channel for the optimal case [8]. And the unsatisfactory result can be attributed to the alterations of eigenvalue profiles, which are not full rank when K-factor changes. Meanwhile, UPA used in our investigation becomes quite suboptimal since an amount of power is wasted inevitably on the vanishing or relatively weak spatial dimensions.

5. Conclusion

In this paper, we study the validity of the maximum capacity criterion in real high speed railway environment, which is applied to realize high-rank LoS MIMO channels. D2a scenario of WINNER II channel model is adopted and it is a realistic high speed railway transmission multipath propagation channel. The ergodic capacity is used as the index to discuss the performance of reconfigurable antenna arrays. Numerical results demonstrate that significant capacity gains are achievable by simply adjusting antenna spacing according to the maximum capacity criterion. And we obtain relatively low sensitivity of the optimal antenna arrays to displacement from the optimal point and angle. So, we put forward two proposals for reconfigurable antenna arrays so as to maximize LoS MIMO capacity in the high speed railway scenarios. Then we find that the antenna array geometries obtained from the criterion are suboptimal, since the ergodic capacity decreases with the increment of K-factor. Thus, it is very necessary to carry on a more thorough research on this optimal methodology for constructing high-rank LoS MIMO channels in high speed railway communication system.

Acknowledgments

The authors would like to express their great thanks to the support from the National Natural Science Foundation of China under Grant 61222105, Beijing Municipal Natural Science Foundation under Grant 4112048, the Fundamental Research Funds for the Central Universities under Grant 2010JBZ008, Program for New Century Excellent Talents in University under Grant NCET-09-0206, and the Key Project of State Key Laboratory under Grant RCS2011ZZ008.

References

[1] Y. Li and L. J. Cimini Jr., "Bounds on the interchannel interference of OFDM in time-varying impairments," *IEEE Transactions on Communications*, vol. 49, no. 3, pp. 401–404, 2001.

[2] A. Grant, "Rayleigh fading multi-antenna channels," *Eurasip Journal on Applied Signal Processing*, vol. 2002, no. 3, pp. 316–329, 2002.

[3] M. Kang and M. S. Alouini, "Capacity of MIMO Rician channels," *IEEE Transactions on Wireless Communications*, vol. 5, no. 1, pp. 112–122, 2006.

[4] S. Jin, X. Gao, and X. You, "On the ergodic capacity of rank-1 Ricean-fading MIMO channels," *IEEE Transactions on Information Theory*, vol. 53, no. 2, pp. 502–517, 2007.

[5] F. Bøhagen, P. Orten, and G. E. Øien, "Construction and capacity analysis of high-rank line-of-sight MIMO channels," in *Proceedings of the IEEE Wireless Communications and Networking Conference (WCNC '05)*, pp. 432–437, March 2005.

[6] F. Bøhagen, P. Orten, and G. E. Øien, "Design of optimal high-rank line-of-sight MIMO channels," *IEEE Transactions on Wireless Communications*, vol. 6, no. 4, pp. 1420–1424, 2007.

[7] I. Sarris and A. Nix, "Design and performance assessment of maximum capacity MIMO architectures in line-of-sight," *IEE Proceedings on Communications*, vol. 153, no. 4, pp. 482–488, 2006.

[8] I. Sarris and A. R. Nix, "Design and performance assessment of high-capacity MIMO architectures in the presence of a line-of-sight component," *IEEE Transactions on Vehicular Technology*, vol. 56, no. 4, pp. 2194–2202, 2007.

[9] M. Matthaiou, D. I. Laurenson, and C. X. Wang, "Capacity study of vehicle-to-roadside MIMO channels with a Line-of-Sight component," in *Proceedings of the International ICST Conference on Communications and Networking in China (CHINACOM '10)*, pp. 1–5, 2010.

[10] L. Gao, Z. Zhong, B. Ai, and L. Xiong, "Estimation of the Ricean K factor in the high speed railway scenarios," in *Proceedings of the IEEE Wireless Communications and Networking Confenrence (WCNC '08)*, pp. 775–779, 2008.

[11] L. Liu, T. Cheng, Q. Jia-Hui, and C. Hou-Jin, "Research on small-scale fading characteristics of wireless channels in rural aera of high-speed railway," *Journal of the China Railway Society*, vol. 5, pp. 41–46, 2012.

[12] P. Kyosti et al., "WINNER II channel models, IST-WINNER D1.1.2," vol. 11, 2007.

[13] D. Tse and P. Vishwanath, *Fundamentals of Wireless Communications*, Cambridge University Press, Cambridge, UK, 2005.

Hindawi Publishing Corporation
International Journal of Antennas and Propagation
Volume 2012, Article ID 351487, 7 pages
doi:10.1155/2012/351487

Research Article

Influence of Training Set Selection in Artificial Neural Network-Based Propagation Path Loss Predictions

Ignacio Fernández Anitzine,[1] Juan Antonio Romo Argota,[1] and Fernado Pérez Fontán[2]

[1] *Department of Electronics and Telecommunications, University of the Basque Country, Alameda Urquijo s/n, 48013 Bilbao, Spain*
[2] *Department of Signal Theory and Communications, University of Vigo, Campus Universitario s/n, 36200 Vigo, Spain*

Correspondence should be addressed to Juan Antonio Romo Argota, juanantonio.romo@ehu.es

Received 26 July 2012; Accepted 19 October 2012

Academic Editor: César Briso Rodríguez

This paper analyzes the use of artificial neural networks (ANNs) for predicting the received power/path loss in both outdoor and indoor links. The approach followed has been a combined use of ANNs and ray-tracing, the latter allowing the identification and parameterization of the so-called dominant path. A complete description of the process for creating and training an ANN-based model is presented with special emphasis on the training process. More specifically, we will be discussing various techniques to arrive at valid predictions focusing on an optimum selection of the training set. A quantitative analysis based on results from two narrowband measurement campaigns, one outdoors and the other indoors, is also presented.

1. Introduction

The need for connectivity anywhere, added to the increment in the number of users, has triggered the development of various generations of mobile communication standards in the last decades. The demand for greater traffic capacity involving both voice and data transmission requires the planning of mobile communication networks comprised of smaller and smaller cells, thus making the number of base stations grow exponentially, and complicating the process of determining and optimizing the location of these stations. Because of this, accurate and fast prediction models are needed for making received signal level/path loss predictions prior to actual network deployment. In this paper, we analyze the performance achievable with an intermediate technique between purely empirical and purely deterministic, based on the use of artificial neural networks (ANNs).

2. Prediction Models

A great variety of methods [1] has been proposed for predicting the expected received electric field level or, alternatively, the path loss. These calculations can be made using empirical or deterministic models. An intermediate alternative is using artificial neural network-based (ANN) models.

Empirical models are based on measurement campaigns carried out in specific, representative environments. Regression techniques are then used for obtaining mathematical expressions describing the propagation loss as a function of the path length. The computational efficiency of these models is satisfactory, while having a limited accuracy. A typical example is the well-known Okumura-Hata model [2, 3].

On the other hand, deterministic models apply accurate electromagnetic techniques or simplified versions of them. These require accurate input information of the propagation environment: buildings, and so forth. Their main advantage is their precision, despite their lack of computational efficiency. It is quite common to see high frequency approximations of the full wave solutions which make use of ray-tracing techniques for identifying all possible paths between the transmitter and the receiver including multiple reflections, diffractions and transmissions through walls. The contribution of each ray is then calculated by using Fresnel's transmission and reflection coefficients, and GTD/UTD [4, 5] for diffracted contributions.

On the other hand, ANN-base models try to combine the advantages of empirical and deterministic models. ANNs are composed of several nodes or neurons divided into different levels with connections between them. The neurons may receive several input signals which are combined using appropriate weights and passed through specific transfer functions. To specify the various weights, the network must be trained. Training is carried out using measured data. Depending on the quality of the training process so will be the ability of the ANN to make predictions in unknown situations: generalization property.

In the literature, the most common choice is using feedforward networks, commonly referred to as multilayer perceptrons (MLPs) [6]. An alternative is to use the so-called radial basis function networks (RBFs) for their fast convergence, robustness, and small size [7].

Most implementations for our application use ANNs with two hidden layers. In the first, a number of neurons greater than the number of inputs is usually found [8]. However, other studies show that more complex networks do not necessarily increase the prediction accuracy. Moreover, it has been found that the generalization properties of ANNs may be reduced, that is, they may be more sensitive to the training set data [9].

In the hidden layers, nonlinear activation functions are normally used, for example, sigmoid-type functions. For the output level, linear functions are normally used. In the hidden layers, also wavelet functions can be found in received field prediction applications [10]. However, even though they show faster computation times, in contrast, they require much larger training data sets.

Different algorithms can be used for training an ANN. In [11], their efficiencies were analyzed showing that the best results are obtained with Bayesian regularization and Levenberg-Marquardt techniques, the latter being the most used option. Another algorithm also used [12, 13], which offers good performances is the resilient propagation algorithm.

ANNs can also be combined with other techniques for characterizing the effects of RF propagation. When simulation time is critical, the so-called "dominant path," selected by means of a ray-tracing tool, can be used to provide the necessary inputs to the AAN. This leads to acceptable results both in terms of time and accuracy. The dominant path is the propagation path between the transmitter and receiver showing the smallest loss. Thus, instead of searching for all possible ray combinations, the problem is simplified while an acceptable generalization performance may be achieved. The dominant path can be calculated using two main techniques: the recursive neighboring model [14] and the convex corners approach [15].

In the last few years, many researchers have applied ANNs for predicting the path loss in indoor [8, 16], outdoor urban [17, 18], and rural [9] environments. In the above references, extensive descriptions and optimizations of ANN architectures, trainings, and generalizations have been presented. However, special attention must still be paid to the repercussions of using different criteria for selecting the training data set. This is the main issue discussed in this paper.

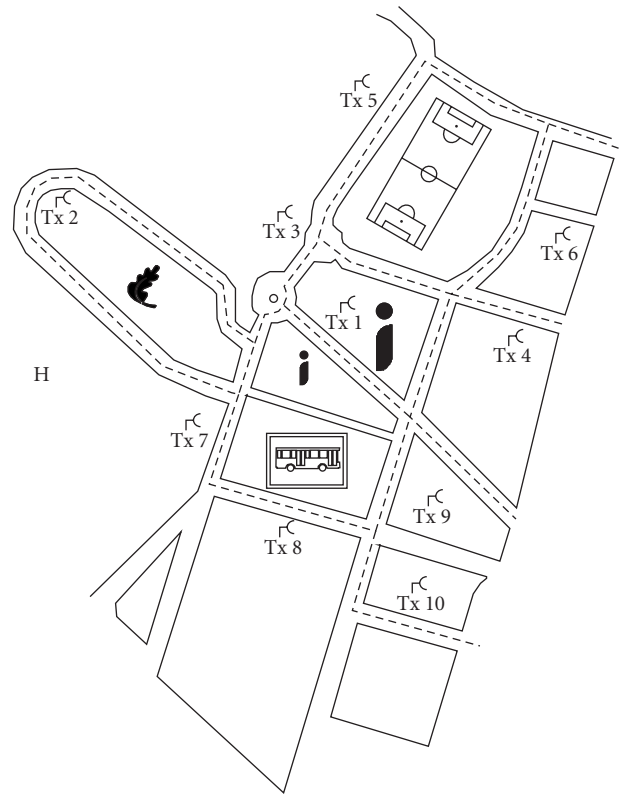

Figure 1: Outdoor measurement routes and transmitters.

3. Measurements and Tools

In this section, the main features of the measured data are presented, then we go on to present the developed ANN tool which operates in combination with a ray-tracing tool able to identify the dominant path between transmitter and receiver. Typically, a single transmitter is assumed while various receive locations can be defined as part of a route or a meshed grid. The route option is very well suited for the training process.

A continuous wave (CW) transmitter was set up at a number of sites, while the received power was measured at several points along a number of routes. Measurements were repeated several times so as to average out the signal cancellations and enhancements due to multipath. For each measurement point, information on its coordinates and the received power level in dBm were recorded. All the outdoor and indoor measurement routes and the transmit locations are shown in Figures 1 and 2, respectively. The CW measurements were made at the 900 and 1800 MHz bands, using in both cases a vertically polarized 4 dBi gain antenna and 35 dBm transmit power. The receiver was a spectrum analyzer connected to a PC. Measurements were triggered every 350 cm along the route. The receive antennas were also vertically polarized, with omnidirectional patterns and 0 dBi gains.

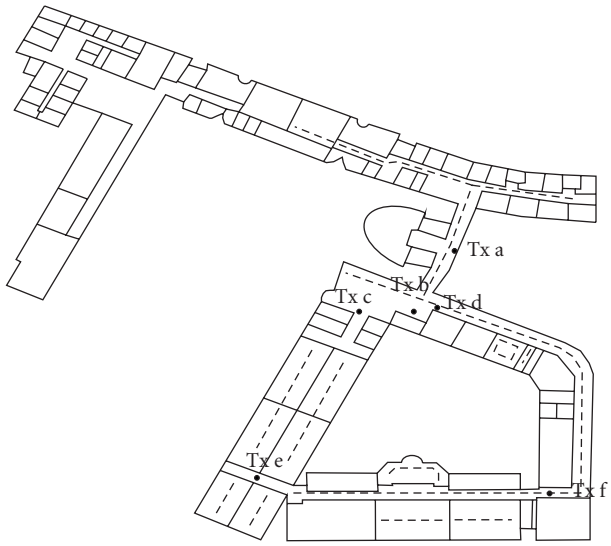

Figure 2: Indoor measurement routes and transmitters.

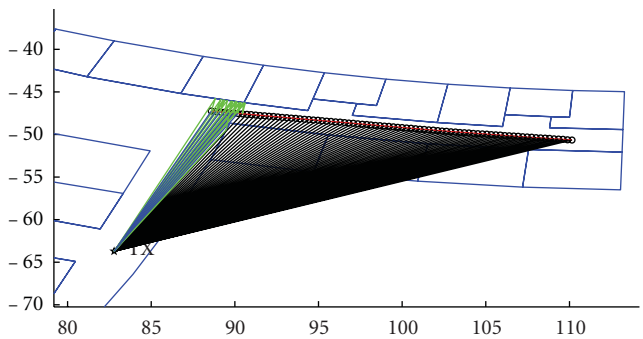

Figure 3: Example of dominant path calculation in the indoor case. Blue lines represent direct ray paths, Green lines represent reflection paths and black lines represent diffraction paths.

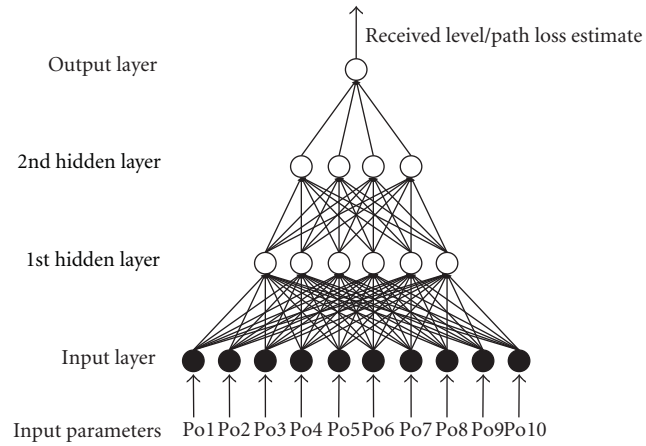

Figure 4: Architecture of the indoor neural network.

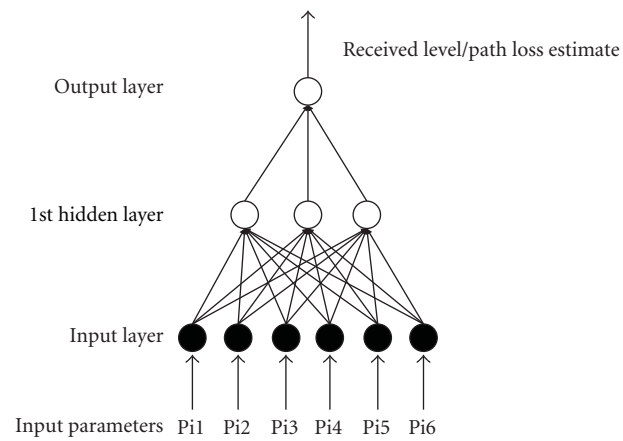

Figure 5: Architecture of the outdoor neural network.

Our ANN model works in combination with a simplified ray tracing tool. This performs CAD tasks as well as basic ray tracing for finding the dominant propagation path for each Tx-Rx pair, then it calculates this path's parameters.

For both outdoor and indoor links, the dominant path can belong to any of four different types: (a) direct ray paths, when the line-of-sight, LOS, path is not blocked, (b) wall-reflection paths, (c) corner-diffraction paths, and (d) propagation through-obstacle paths, when it is not possible to link the transmitter and receiver with one of other three path types. In this last case, a straight line is drawn from one end to the other. Each time this line crosses an obstacle, for example, a wall, the corresponding loss is added. Figure 3 illustrates this classification for the indoor case.

4. ANN-Based Model

Starting from an earlier version of the tool [16], we have implemented a new one using the dominant path approach. Then, this implementation has been trained with measurements. Finally, comparisons between predictions and measurements for data sets different from those used for training were carried out. Two different ANNs have been implemented for indoor and outdoor scenarios, respectively. Two different networks were necessary due to the significant differences in propagation conditions in the two scenarios.

The indoor ANN is a MLP network with pyramidal structure consisting of three main parts: an input layer with 8 neurons, each associated with one of the 8 selected input parameters, two hidden layers with 6 and 4 neurons, respectively, with sigmoid-type activation functions and, finally, an output layer with a single neuron with a linear function (Figure 4). The outdoor ANN uses fewer inputs resulting in a simpler structure (Figure 5).

The input parameters must characterize the propagation path between transmitter and receiver in the most faithful way. Numerous parameters could have been selected. After several trials, we selected the parameters listed below.

(a) Indoor Scenarios

(i) *Screen effect, Po1, Po2*. It occurs when there are walls near the transmitter or receiver blocking the direct ray.

Table 1: Classification of receive locations.

	Outdoor receivers	% Of total	Indoor receivers	% Of total
LOS direct ray	1352	20.2	572	16.7
NLOS reflection	526	7.8	—	—
NLOS diffraction	1972	29.4	635	18.6
NLOS obstacles	2861	42.6	2213	64.7
Total	6711	100	3420	100

Table 2: Distribution of measurement points in sets A and B according to their dominant paths.

Training routes	Set A	Set B
LOS direct ray	194	268
NLOS reflection	5	56
NLOS diffraction	250	494
NLOS obstacles	237	662
Total	686 (8.9% of 6711)	1480 (22% of 6711)

(ii) *Local reflections*, *Po3*, *Po4*. They exist when either the receiver or the transmitter are located close to a corner giving rise to multiple reflections.

(iii) *Waveguide effect*, *Po5*. It appears in corridors.

(iv) *Change of direction, Po6*. It occurs when diffraction takes place.

(v) *Transmission loss*, *Po7*. It is introduced when the signal must pass through an obstacle.

(vi) *Free space loss*, *Po8*. It depends on the distance between the transmitter and receiver, and the working frequency.

(b) Outdoor Scenarios

(i) *Distances L1* and *L2*, *Pi1*, *Pi2*. They are defined as the separations between the transmitter/receiver and the interaction point (reflection or diffraction point). The longer these distances are, the larger the loss will be.

(ii) *Incidence* and *scattering angles*, *Pi3*. They are defined with respect to a wall's normal.

(iii) *Reflection and diffraction coefficients*, *Pi4*, *Pi5*. Fresnel's reflection coefficients and UTD edge diffraction coefficients.

(iv) *Free space loss*, *Pi6*. It depends on the distance between the transmitter and receiver, and the working frequency.

The most critical step when designing an ANN-based model is the training process which will condition the achievable prediction accuracy. The *back-propagation* technique was selected as learning method, where the predicted power is compared with the actual measurement, and the difference (error) is fed back to the network for correcting the various network connection weights.

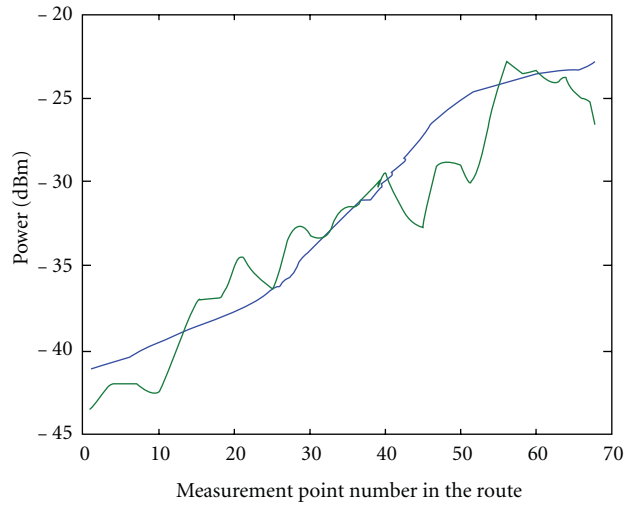

Figure 6: Example of prediction result and comparison with measurements.

The *Levenberg-Marquardt* algorithm was used for training the model. This method uses the evolution of the gradient changing the coefficient for each neuron connection in the direction that causes a larger error reduction. The chosen number of training cycles was one thousand. This is a tradeoff between error, and time. As said, the selection of the training set is the most critical issue and will be discussed in depth below.

After the ANNs were trained, we analyzed the prediction errors by comparing the results of the ANN-based model and the received power levels measured at points different from those used in the training phase. Figure 6 illustrates a measurement route and the obtained prediction. For each route, the mean error, mean squared error and standard deviation were calculated. In the figure we can observe how the prediction curve is much smoother than that of the measurement. This is because the ANN input parameters, obtained from the ray-tracer, are very similar for neighboring points along the route. The user of such a prediction tool must be aware of this limitation. Still, as observed, the average error and its spread are very small.

5. Selecting the Training Set

As discussed in previous sections, a wise selection of real propagation paths from which the neural network will learn how to calculate the received power is the most critical factor

Table 3: Error statistics for the outdoor case with the ANN trained with set A and with set B.

Test routes	Route 1	Route 2	Route 3	Route 4	Route 5
Network trained with training Set A					
Mean error	10.03	8.09	11.41	5.76	3.86
RMS error	14.17	10.11	13.26	8.29	5.15
std	10.01	6.07	6.76	5.97	3.41
Network trained with training Set B					
Mean error	6.66	6.70	5.40	4.26	1.77
RMS error	10.54	9.49	7.62	6.58	2.52
std	8.17	6.72	5.24	5.01	1.79

Table 4: Path types used in indoor trainings.

Training routes	Set C	Set D
LOS direct ray	399	406
NLOS diffraction	30	101
NLOS obstacles	219	390
Total	648 (17.5% of 3420)	897 (26% of 3420)

in the training phase. Those real situations form the so-called "training set."

To optimize the training set several routes with different characteristics must be selected so as to provide the ANN with all the propagation conditions (reflection paths, direct ray paths, etc.) likely to be encountered. In addition, the selected routes have to include received positions showing different ranges of input parameters. In this way, the network will learn to behave in many different situations and will be able to make correct generalizations when applied to new cases. After learning from a number of routes, the network must be tested with other data sets from different routes. Predictions for those test routes must show similar errors to those for the training routes. If this is the case, network will be correctly trained.

The first and essential step in the training process involves a suitable characterization of the measurements points in the training routes according to their dominant path type. The choice of training routes must be a planned process based on supplying a sufficient and balanced number of measured points belonging to the various propagation conditions to be expected. Based on the dominant path concept, we have to be careful when training the ANN to provide an appropriate mix of the four path types identified.

A total of 29 measurement routes were recorded, each with a different number of receive positions depending on its length. For outdoor links, a total of 50 routes were measured. Hence, the available measurements correspond to a total of 79 routes with 3420 sampling or receive points for the indoor case and 6711 for outdoor locations. As indicated earlier, each route was measured several times and, then, point-wise averages were calculated. The number of transmitter sites in the indoor case was 6, while for the outdoor case 5 sites were used. Table 1 presents a summary of all measurement locations according to their corresponding path types.

Two strategies have been analyzed in the selection of the training set. In the first, we selected entire routes while the second focused on selecting specific receive points according to the dominant path category to which they belonged.

We now analyze the first, that is, route-wise strategy. From the available measurements, a subset of the routes was used for training while the rest was used for testing. To illustrate the effect of the number of routes considered in the training process in relation to the achieved prediction accuracy, several training sets were used as discussed below, both for the indoor and outdoor cases.

To train the outdoor network, two different sets were used. Set A consisted of data gathered from a single transmit site and three different routes. In all, 686 data points: 194 corresponding to direct ray paths, 250 to diffraction paths, 5 to reflection paths, and 237 to through-obstacle paths. Set-B consisted of data from seven routes and 2 transmit sites, in all 1480 data points classified as follows: 268 were direct ray paths, 494 diffraction paths, 56 reflection paths and 662 through-obstacle paths, Table 2.

After training, measurements from 5 routes corresponding to a different transmit site were used to test the ANNs trained with sets A and B. Table 3 shows the results of this analysis. For set A, acceptable error levels were obtained when the test routes showed similar propagation characteristics to those used in the training process. However, for the other routes, all three error parameters (mean, RMS and standard deviation) were rather high, even over 10 dB. At some locations such as those corresponding to reflection paths, predictions were worse than those observed when training the network with set A. This is due to the fact that only 5 data points corresponding to this path type were used in the training. Thus, the network could not learn how to behave in reflection-dominated paths. It is clear that the training needed improvement for this type of paths. On the other hand, set B contained a more balanced mix of data points corresponding to all four classes. In this case, the error statistics are drastically reduced.

For training of the indoor network, two sets were also used. Set C consisted of data from two transmitters and four different routes. In all, 648 measurements were used: 399 points corresponded to direct-ray paths, 219 to through-obstacle paths and 30 to diffraction paths. Set D consisted of eight routes corresponding to four transmitters. Now, 897 training points were used (26.3% of a total of 3420). The distribution of path types is as follows: 406 were direct ray

Table 5: Numerical results of simulations, with two and four transmitters, for the indoor routes.

Test routes	Route 6	Route 7	Route 8	Route 9
		Network trained with set C		
Mean error	1.23	2.58	2.19	2.37
RMS error	1.72	3.46	3.14	3.27
std	1.20	2.31	2.25	2.25
		Network trained with set D		
Mean error	0.96	1.99	1.36	1.47
RMS error	1.48	2.84	1.99	2.60
std	1.13	2.03	1.45	2.15

Table 6: Errors for the path-type oriented analysis for the outdoor case.

Test routes	LOS direct ray	NLOS reflection	NLOS diffraction	NLOS obstacles
Mean error	5.77	7.49	8.78	7.32
RMS error	9.34	9.04	11.88	8.84
std	7.35	5.07	8.00	4.95

Table 7: Errors for the path-type oriented analysis for the indoor case.

Test routes	LOS direct ray	NLOS diffraction	NLOS obstacles
Mean error	1.77	3.26	2.15
RMS error	2.52	4.74	3.15
std	1.79	3.44	2.30

paths, 101 diffraction paths, and 390 through-obstacle paths, Table 4. For the test set four complete routes were used, Table 5.

Again, in the case of Set-D, the errors were much smaller than for the Set-C. With the new training, the same routes were simulated. Due to the path type mix in Set-C, routes with diffraction paths were badly predicted: the network so trained cannot properly simulate those measurement points where the dominating conditions are not sufficiently well represented in the training set. Training Set-D introduces more measurements and also covers a more balanced mix of propagation path types. Thus, the selected routes in Set-D encompass an appropriate assortment of paths from all types.

Now we analyze the second strategy to selecting the training set, that is, a path-type oriented selection. In this case, the training process was separately carried out for each type of propagation path. Training the ANN with separate receiver locations according to their propagation path types could, in principle, allow achieving a much better prediction accuracy. According to this approach, several routes were split into subsets, as a function of their dominant path, so that all receive points with a direct-ray predominant path were placed into the same subset. Then, some of those points were used to train the ANN and others for testing it. The same was done for reflection, diffraction, and through-obstacle paths.

As shown in Table 6, results for reflection, diffraction and through-obstacle paths show a similar error parameter range, in the order of 7-8 dB. Meanwhile, the variability of direct ray paths proved to be lower than in the other cases. A similar analysis was carried out for the indoor case, Table 7. Now, the error parameter range in through-obstacle and diffraction paths is in the order of 2-3 dB, whereas for direct ray paths it again shows a lower value. In any case, even though both in outdoor and indoor situations, the general performance is quite good, it does not seem to be much better than the one achieved in the previous analyses.

6. Conclusions

To create an effective ANN and properly make path loss predictions, a correct training strategy must be devised. The selection of the training sets is the most critical factor to ANN prediction performance in this application. An appropriate assortment of different propagation conditions represented by different types of propagation paths is required so the net can learn how to behave and make suitable generalizations in as many different situations as possible.

In this paper, we have focused on an implementation combining a simplified ray-tracing tool which takes care of identifying the so-called "dominant path" and calculating a number of propagation path-related parameters used as inputs to the ANN which, in turn, makes the final prediction.

When we indicate that there is a need for an appropriate assortment of paths with different propagation conditions, the selection has to be based on a classes defined according to the dominant path. Both for indoor and outdoor conditions, four different dominant path classes have been identified. When the above premises are fulfilled, ANNs may very well represent a good alternative to predict radio propagation with errors in a similar range to other, more complex methods with more computational load. From our experimental analyses the error parameters, mean, rms, and standard deviation were always below 7 dB.

To achieve these results in a training strategy oriented toward the dominant path, the training points need to be adequately selected so that they are representative of the ensemble of the possible types in the coverage area. This selection requires an in-depth knowledge of the propagation scenario, and hence an elevated cost for collating the data in the set which in practice is unfeasible.

In a complete route-oriented strategy, the accuracy of the achieved results will depend on the total number of routes in the training set. It was observed that as the number of samples is increased so does the accuracy, especially for a small number of routes. If the sample size is properly balanced, further increments will not produce significant performance improvements while the cost increases.

In this paper, the balanced size corresponds to a route selection approximately encompassing 25% of the foreseen coverage area. The selected routes should provide diversity of cases while they are validated through a simple process. Such a set produces similar results as with a set based on the dominant path types found in the coverage area. In summary, adopting this strategy will lead to the generation of a less complex training set at much smaller cost than using a path type-oriented strategy and achieving similar accuracies.

A word of caution must be said, however. As illustrated in Figure 6, ANN predictions for consecutive points belonging to the same route cannot follow some of the sharp variations encountered in the measurements, where the measurements are already the results of averaging over several repeated passes, that is, they contain the slow channel variations due to shadowing, but the multipath has been removed. This is because the inputs to the net provided by the ray-tracing plus dominant path tool do not change so drastically from point to point. This shortcoming needs to be born in mind when considering the application of this approach.

References

[1] S. Saunders and A. A. Aragon-Zavala, *Antennas and Propagation for Wireless Communications*, John Wiley & Sons, London, UK, 2nd edition, 2007.

[2] Y. Okumura, E. Ohmori, T. Kawano, and K. Fukuda, "Field strength and its variability in VHF and UHF land-mobile radio service," *Review of the Electrical Communications Laboratory*, vol. 16, no. 9-10, pp. 825–973, 1968.

[3] M. Hata, "Empirical formula for propagation loss in land mobile radio services," *IEEE Transactions on Vehicular Technology*, vol. 29, no. 3, pp. 317–325, 1980.

[4] J. H. Tarng, "Three-dimensional modeling of 900-MHz and 2.44-GHz radio propagation in corridors," *IEEE Transactions on Vehicular Technology*, vol. 46, no. 2, pp. 519–527, 1997.

[5] M. F. Cátedra and J. Pérez Arriaga, *Cell Planning For Wireless Communications*, Artech House, Norwood, Mass, USA, 1999.

[6] S. Haykin, *Neural Networks: A Comprehensive Foundation*, IEEE Press, McMillan College Publishing Co, 1994.

[7] Y. Sun, Y. Xu, and L. Ma, "The implementation of fuzzy RBF neural network on indoor location," in *Proceedings of the Pacific-Asia Conference on Knowledge Engineering and Software Engineering (KESE '09)*, pp. 90–93, December 2009.

[8] A. Nešković, N. Nešković, and D. Paunović, "Indoor electric field level prediction model based on the artificial neural networks," *IEEE Communications Letters*, vol. 4, no. 6, pp. 190–192, 2000.

[9] E. Ostlin, H. J. Zepernick, and H. Suzuki, "Macrocell path-loss prediction using artificial neural networks," *IEEE Transactions on Vehicular Technology*, vol. 59, no. 6, pp. 2735–2747, 2010.

[10] F. Cheng and H. Shen, "Field strength prediction based on wavelet neural network," in *Proceedings of the 2nd International Conference on Education Technology and Computer (ICETC '10)*, pp. V2255–V2258, June 2010.

[11] I. Vilović, N. Burum, and Z. Šipuš, "A comparison of neural network models for indoor field strength prediction," in *Proceedings of the 49th International Symposium ELMAR-2007 focused on Mobile Multimedia*, pp. 251–254, Zadar, Croatia, September 2007.

[12] I. Popescu, I. Naforniţă, Gh. Gavriloaia, P. Constantinou, and C. Gordan, "Field strenght prediction in indoor environment with a neural model," in *Proceedings of the 5th International Conference on Telecommunications in Modern Satellite, Cable and Broadcasting Service (TELSIKS '01)*, September 2001.

[13] B. Monteiro, G. P. S. Cavalcante, H. S. Gomes, D. M. Rosário, F. F. Lima, and H. A. Junior, "Evaluation of radio propagation parameters for field strength prediction using neural network," in *Proceedings of the SBMO/IEEE MTT-S International Microwave and Optoelectronics Conference (IMOC '07)*, pp. 888–892, November 2007.

[14] G. Wölfle and F. M. Landstorfer, "A recursive model for the field strength prediction with neural networks," in *Proceedings of the 20th International Conference on Antennas and Propagation*, vol. 2, pp. 174–1177, Edinburgh, UK, April 1997.

[15] G. Woelfle and F. M. Landstorfer, "Dominant paths for the field strength prediction," in *Proceedings of the 48th IEEE Vehicular Technology Conference (VTC '98)*, vol. 1, pp. 552–556, May 1998.

[16] J. A. Romo, I. F. Anitzine, and F. P. Fontán, "Application of neural networks to field strength prediction for indoor environments," in *Proceedings of the European Conference on Antennas and Propagation (EuCAP '06)*, November 2006.

[17] I. Popescu, D. Nikitopoulos, P. Constantinou, and I. Nafornita, "ANN prediction models for outdoor environment," in *Proceedings of the IEEE 17th International Symposium on Personal, Indoor and Mobile Radio Communications (PIMRC '06)*, September 2006.

[18] Z. Stankovic B, Milovanovic, M. Veljkovic, and A. Dordevic, "The hybrid-neural empirical model for the electromagnetic field level prediction in urban environments," in *Proceedings of the 7th Seminar Neural Network Applications Electrical Engineering*, Belgrade, Serbia, 2004.

Hindawi Publishing Corporation
International Journal of Antennas and Propagation
Volume 2012, Article ID 179378, 12 pages
doi:10.1155/2012/179378

Research Article

On the Statistical Properties of Nakagami-Hoyt Vehicle-to-Vehicle Fading Channel under Nonisotropic Scattering

Muhammad Imran Akram and Asrar U. H. Sheikh

Department of Electrical Engineering, King Fahd University of Petroleum and Minerals, Dhahran 31261, Saudi Arabia

Correspondence should be addressed to Muhammad Imran Akram, miakram@kfupm.edu.sa

Received 18 March 2012; Revised 14 July 2012; Accepted 19 September 2012

Academic Editor: Ai Bo

This paper presents the statistical properties of the vehicle-to-vehicle Nakagami-Hoyt (Nakagami-q) channel model under nonisotropic condition. The spatial time correlation function (STCF), the power spectral density (PSD), squared time autocorrelation function (SQCF), level crossing rate (LCR), and the average duration of Fade (ADF) of the Nakagami-Hoyt channel have been derived under the assumption that both the transmitter and receiver are nonstationary having nonomnidirectional antennas. A simulator that uses the inverse-fast-fourier-transform- (IFFT-) based computation method is designed for this model. The simulator and analytical results are compared.

1. Introduction

With passage of time, applications of wireless communication, their usefulness, and reliability are increasing. The recent applications where wireless communications is extensively used include wireless local area network (WLAN), multimedia messaging cellular telephone systems, satellite systems, femtocells, Bluetooth, and Zigbee devices. The wireless devices are also extensively used in in-car security systems equipment, home television systems private mobile systems, and so forth. In the conventional wireless communication systems, all the mobile stations communicate with each other via fixed base stations which are normally placed at elevated locations. Since mobile station is likely to be surrounded by objects having different shapes and orientations, the direct propagation path may not always present, and communication results from scattering that occurs near the mobile station. The channel between the transmitter and receiver is usually multipath fading channel; the signal fading occurs due to terminal mobility.

An in-depth knowledge leads to an accurate model of mobile propagation channel which is essential for a simulator design that provides dependable performance results. Over the past many years, several mobile channel models have been proposed for links between fixed base station and mobile station. These include short-term fading models like the well-known Rayleigh, Rice [1], Hoyt [2], Nakagami-m [3], and Weibull [4]. For long-term fading model, lognormal distribution has been used [5, 6]. Several composite fading models combining the effects of short- and long-term fading (Nakagami-lognormal [3], Suzuki [7], and Rice-lognormal [8]) have also been proposed.

Over the past decade, the research has been focused on vehicle-to-vehicle (V2V) or mobile-to-mobile (M2M) communication systems where no base station is present and both the transmitter Tx and the receiver Rx are in motion. The V2V communication finds applications in mobile ad-hoc wireless networks, intelligent highway systems, emergency, military, and security vehicles. The antennas are mounted on the top or on the side of vehicles, which move with different velocities and resulting in time varying channels. The buildings and other obstacles surrounding the terminals act as scatterers thereby generating multipaths. Depending upon the vehicular positions, the line of sight (LOS) may or may not be present.

During the past decade, a large number of research projects have been done on V2V communications [9–12]. Reference [13] presents a survey of the vehicular channel characterization under different environments (highway,

rural, urban, and suburban). It shows the path loss exponent, Root Mean Square (RMS) delay spread, and mean Doppler spread under these conditions. The statistical model for vehicle-to-vehicle communication was first proposed by Akki and Haber [14], and its statistical properties were reported in [15]. Based on the work of [15], many V2V simulators were designed and implemented. Reference [16] presented a discrete line spectrum-based approach to simulate the channel. The work reported in [17] is based on sum of sinusoids (SOS) approach for simulator design. In [18], the simulation of multiple input multiple output (MIMO) V2V is presented. The simulator proposed in [19] is based on Kullback-Leibler divergence which is compared with IFFT based approach of simulator design. Reference [20] uses Gaussian quadrature rule for simulator design. Reference [21] proposes an efficient SOS-based approach for V2V simulator design. All the simulator design approaches mentioned above were designed for V2V Rayleigh fading channels.

A small number of works have used non-Rayleigh fading channel models. The second order statistics of Nakagami-Hoyt channel have been derived in [22]. Reference [23] derives the statistical properties of double Nakagami-Hoyt channel.

In many real world scenarios, nonisotropic scattering is often experienced by both the mobile transmitter and receiver. It has been shown in [24–26] that in dense urban environments, non-isotropic scattering around the mobile station exists. Reference [27] derives the second order statistics of V2V Ricean fading channel under non-isotropic conditions and compares the theoretical results with the measured data. Reference [28] derives the autocorrelation function of Rice process under non-isotropic condition. Reference [29] presented V2V model for Rayleigh fading under non-isotropic condition. Many nonuniform distributions have been discussed for angle of arrival (AOA) and angle of departure (AOD). These include Gaussian, Laplacian, quadratic, and Von Misses distributions. Von Misses distribution (assumed in this paper), a generic case described in [24], covers the other distributions (Gaussian, Laplacian, cosine, and uniform distributions) as its special cases.

In this paper, a novel V2V Nakagami-Hoyt channel model under non-isotropic scattering condition is proposed. The existing channel models [2, 15, 30] are treated as its special cases. Analytical expressions for second order statistical properties including STCF, PSD, SQCF, LCR, and ADF of the envelop of the proposed model have also been derived. An IFFT based simulator has been developed to validate the first and second order statistical parameters of the proposed model. Mean Square Error (MSE) of autocorrelation function is also plotted to show the simulator accuracy. To the best of authors' knowledge, no work has been reported on the statistical parameters of the proposed model and its simulation.

The remainder of this paper is organized as follows. Section 2 presents details of the Nakagami-Hoyt V2V channel model and its first and second order statistics. Section 3 describes the simulation method, results of the simulator, and their comparison with the analytical results. Finally, Section 4 concludes the paper.

2. The Nakagami-Hoyt Channel Model

The Nakagami-Hoyt (also known as q) distribution is the distribution of the modulus of a complex Gaussian random variable whose components are uncorrelated with zero mean and unequal variances.

In this section, we briefly describe the proposed channel model along with its usefulness and derive the first and second order statistics of Hoyt fading channel under the assumptions that the channel is narrow band, and the receiver and transmitter are moving with velocities V_1 and V_2, respectively and the non-isotropic scattering (i.e, AOA and AOD have nonuniform distributions).

A Hoyt process, $R(t)$, is obtained by complex Gaussian random process as

$$\begin{aligned} \mu(t) &= \mu_1(t) + j\mu_2(t), \\ R(t) &= |\mu(t)|, \end{aligned} \tag{1}$$

where $j = \sqrt{-1}$, $\mu_1(t)$ and $\mu_2(t)$ are complex Gaussian random processes with zero means and variances σ_1^2 and σ_2^2, respectively. $|\cdot|$ indicates the L_2 norm.

The parameters q and a are defined as

$$\begin{aligned} q &= \frac{\sigma_1}{\sigma_2}, \\ a &= \frac{V_2}{V_1}. \end{aligned} \tag{2}$$

Reference [14] proposed a statistical model for the mobile-to-mobile Rayleigh fading channel. This model is modified for the Nakagami-Hoyt frequency flat fading channel. The baseband equivalent channel impulse response is given as

$$\mu_1(t) = \sum_{n=1}^{N} r_n \cos\big((w_{1n} + w_{2n})t + \phi_n\big). \tag{3}$$

Also

$$\mu_2(t) = \frac{1}{q}\sum_{n=1}^{N} r_n \sin\big((w_{1n} + w_{2n})t + \phi_n\big), \tag{4}$$

where N is the number of propagation paths; r_n and ϕ_n are the uniformly distributed amplitude and phase of nth path, respectively. w_{in} is given by

$$w_{in} = 2\pi f_{di} \cos(\alpha_{in}), \quad i = 1, 2, \tag{5}$$

where f_{d1} and f_{d2} are the maximum Doppler frequency due to the motion of receiver and transmitter, respectively. α_{1n} and α_{2n} are the AOA and AOD of the nth path with respect to the velocity vector of receiver and transmitter, respectively.

Assuming that α_{1n}, α_{2n}, and ϕ_n are independent for all n with α_{1n} and α_{2n} are non-uniformly distributed having Von Mises PDF described in [24]. The PDF of the Von Mises distribution is given by

$$p_\alpha(\alpha) = \frac{\exp[\kappa\cos(\alpha - \nu)]}{2\pi I_0(\kappa)}, \quad \kappa > 0, \tag{6}$$

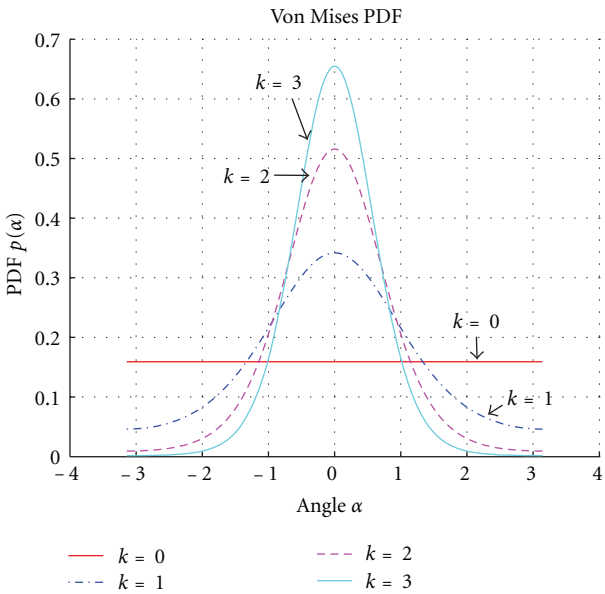

Figure 1: Von Mises PDF showing nonisotropic scattering.

where $I_0(\cdot)$ is the zero-order modified Bessel function of the first kind, ν is the mean direction of the AOD or AOA, and κ is the concentration parameter which controls the width of the scatterers. Figure 1 illustrates the PDF $p_\alpha(\alpha)$ with different values of κ for $\nu = 0$. If $\kappa = 0$, then the von Mises PDF reduces to a uniform distribution (isotropic scattering).

2.1. Usefulness of the Proposed Channel Model. The measurements made in the rural environment demonstrated that the channel is more accurately modeled only when the variance of the in-phase and the quadrature components are not identical [22]. This observation was further supported in [31] where the model matches the measured data for the cases of unequal variances. For V2V communication, reference [32] observed that when the distance between the vehicles exceeds 70 m, the Nakagami m-factor is observed to be less than unity, which corresponds to the case of unequal variances of the component of complex Gaussian process. Further as found from the V2V measurements [33, 34], the m value of each tap of the channel model described is found to be less than unity (0.75–0.89) which from [22] corresponds to the value of q (0.5–0.707).

The channel models described previously do not consider the following two scenarios simultaneously. First, when the antennas are not omnidirectional, and scatterers around the receiver and transmitter are not uniformly distributed. This is normally the case in V2V communications when transmit and receive antennas are present inside the vehicles. Second, when the fading is severe and the channel gains are no longer Rayleigh ie $q < 1$. The proposed model is a generalized model. IT is applicable to these cases for V2V when $a \neq 0$ and base to vehicle when $a = 0$ and covers the previously existing models as its special cases.

2.2. First Order Statistics. The probability density function of the envelope $R(t)$ is given by [2]

$$p_R(x) = \frac{x}{\sigma_1\sigma_2}\exp\left[-\frac{x^2}{4}\left(\frac{1}{\sigma_1^2}+\frac{1}{\sigma_2^2}\right)\right] \times I_0\left[\frac{x^2}{4}\left(\frac{1}{\sigma_1^2}-\frac{1}{\sigma_2^2}\right)\right], \quad x \geq 0, \tag{7}$$

where $I_0(\cdot)$ denotes the zeroth-order modified Bessel function of the first kind. The pdf of the corresponding phase process $\nu(t) = \arctan[\mu_2(t)/\mu_1(t)]$ is given by

$$p_\nu(\theta) = \frac{\sigma_1\sigma_2}{2\pi\left(\sigma_2^2\cos^2\theta + \sigma_1^2\sin^2\theta\right)}, \quad 0 \leq \theta < 2\pi. \tag{8}$$

Since the pdfs are independent of time so they will remain independent for V2V Nakagami-Hoyt channels. The mean m_μ and RMS R_{rms} values can be easily obtained as

$$\begin{aligned} m_\mu &= E[\mu(t)] = E[\mu_1(t)] + jE[\mu_2(t)] \\ &= 0 \\ R_{\text{rms}} &= \sqrt{E\left[\mu(t)^2\right]} = \sqrt{E\left[\mu_1(t)^2\right] + E\left[\mu_2(t)^2\right]} \\ &= \sqrt{\sigma_1^2+\sigma_2^2} \\ &= \sigma_2\sqrt{1+q^2}. \end{aligned} \tag{9}$$

2.3. Second Order Statistics. In this section, The STCF, PSD, SQCF, LCR and ADF of the Nakagami-Hoyt V2V fading process are derived. These quantities are useful in estimation of burst error, mobile velocity and Markov modeling of fading channels [35–37].

2.3.1. Spatial Time Correlation Function. For derivation of spatial time correlation function of *Nakagami-Hoyt* V2V channel, [14] is used as a reference, which describes the case for Rayleigh distribution. The results are obtained for more general case where $\sigma_1 \neq \sigma_2$.

The spatial time correlation function of the envelope is given by [38]

$$\mathbf{R}(x_1, x_2, t_1, t_2) = \frac{1}{2}\left\langle \mu_{x_2}(t_2)\mu_{x_1}^*(t_1)\right\rangle, \tag{10}$$

where $\langle\cdot\rangle$ is the statistical average $\mu_{x_1}(t_1)$ and $\mu_{x_2}(t_2)$ are the complex envelop received at positions x_1 and x_2 at time t_1 and t_2, respectively as given in [14]. It is shown in Appendix A that the general form of the spatial time correlation function is given by

$$\mathbf{R}(\Delta x, \Delta t) = \sum_{n=0}^{1}\frac{(1+q\cos(n\pi))^2}{4q^2}\sigma_1^2\prod_{i=1}^{2}\frac{I_0\left(\sqrt{\kappa_i^2 - K^2M_i^2 + j2\kappa_i K M_i\cos\nu_i\cos(n\pi)}\right)}{I_0(\kappa_i)}, \tag{11}$$

where

$$M_i(\Delta x, \Delta t) = V_i \Delta t + (2 - i)\Delta x \tag{12}$$

$K = 2\pi/\lambda$, $\Delta t = t_2 - t_1$ and $\Delta x = x_2 - x_1$.

$\mathbf{R}(\Delta x, \Delta t)$ is the correlation functions of two signal envelopes obtained at two locations Δx apart and at two time instant Δt apart.

The time correlation function is obtained by setting $\Delta x = 0$ in (11)

$$\mathbf{R}_\mu(\Delta t) = \mathbf{R}(0, \Delta t) = \sum_{n=0}^{1} \frac{(1 + q\cos(n\pi))^2}{4q^2} \sigma_1^2 \prod_{i=1}^{2} \frac{I_0\left(\sqrt{\kappa_i^2 - K^2(V_i\Delta t)^2 + j2\kappa_i K V_i \Delta t \cos\nu_i \cos(n\pi)}\right)}{I_0(\kappa_i)}. \tag{13}$$

For a more specific case (isotropic scattering), substituting $\kappa_i = 0$ and $\nu_i = 0$ in (11) and simplifying,

$$\mathbf{R}(\Delta x, \Delta t) = \frac{1 + q^2}{2q^2} \sigma_1^2 J_0(KV_2\Delta t) J_0(KV_1\Delta t + K\Delta x) \tag{14}$$

$J_0(\cdot)$ is the zero-order Bessel function. It can be shown that for $q = 1$, the space time correlation function for vehicle to vehicle Rayleigh fading channel is obtained.

$$\mathbf{R}(\Delta x, \Delta t) = \sigma_1^2 J_0(KV_2\Delta t) J_0(KV_1\Delta t + K\Delta x) \tag{15}$$

which matches with the result of [14]. Further by setting $V_2 = 0$ (i.e., transmitter stationary) in (15), we get Tx (stationary) and Rx (mobile) Rayleigh channel

$$\mathbf{R}(\Delta x, \Delta t) = \sigma_1^2 J_0(KV_1\Delta t + K\Delta x). \tag{16}$$

The time correlation is obtained by setting $\Delta x = 0$ in (15) as

$$\mathbf{R}_\mu(\Delta t) = \mathbf{R}(0, \Delta t) = \frac{1 + q^2}{2q^2} \sigma_1^2 J_0(KV_2\Delta t) J_0(KV_1\Delta t). \tag{17}$$

The spatial correlation function is obtained by setting $\Delta t = 0$ in (15) as

$$\mathbf{R}_\mu(\Delta x) = \mathbf{R}(\Delta x, 0) = \frac{1 + q^2}{2q^2} \sigma_1^2 J_0(K\Delta x). \tag{18}$$

Similarly, for Rayleigh fading, the time and spatial correlation functions are obtained as

$$\begin{aligned} \mathbf{R}_\mu(\Delta t) &= \sigma_1^2 J_0(KV_2\Delta t) J_0(KV_1\Delta t), \\ \mathbf{R}_\mu(\Delta x) &= \sigma_1^2 J_0(K\Delta x). \end{aligned} \tag{19}$$

2.3.2. Power Spectral Density. The power spectral density $S(f)$ of the wide sense stationary (WSS) process is obtained by taking the Fourier transform of the time autocorrelation function as

$$S(f) = \int_{-\infty}^{\infty} \mathbf{R}_\mu(\Delta t) e^{-j2\pi f \Delta t} d\Delta t. \tag{20}$$

For non-isotropic scattering ($\kappa_i \neq 0$, $\nu_i \neq 0$), the integral is evaluated using the Fourier transform of (13).

For isotropic scattering, the power spectral density is obtained by taking the Fourier transform of (17) as

$$S(f) = \frac{1 + q^2}{2q^2} \sigma_1^2 \int_{-\infty}^{\infty} J_0(KV_2\Delta t) J_0(KV_1\Delta t) e^{-j2\pi f \Delta t} d\Delta t. \tag{21}$$

The integral can be evaluated using [39]. From [14], the reduced form is

$$\begin{aligned} S(f) = {} & \frac{1 + q^2}{2q^2 \pi^2 f_{m1} \sqrt{a}} \sigma_1^2 \\ & \times K\left[\frac{(1 + a)}{2\sqrt{a}} \sqrt{1 - \left(\frac{f}{(1 + a) f_{m1}}\right)^2}\right], \end{aligned} \tag{22}$$

where $K(\cdot)$ is the elliptical integral function of first kind; f_{m1}, f_{m2} are the maximum Doppler shifts due to the motion of the receiver and transmitter, respectively with $f_{mi} = V_i/\lambda$. Therefore, $f_{m2} = a f_{m1}$.

Now, for the case $a = 0$, we have $V_2 = 0$. Hence, the PSD is obtained as

$$S(f) = \frac{1 + q^2}{2q^2} \sigma_1^2 \int_{-\infty}^{\infty} J_0(KV_1\Delta t) e^{-j2\pi f \Delta t} d\Delta t \tag{23}$$

which is evaluated in [39] as

$$S(f) = \frac{1 + q^2}{2q^2} \frac{\sigma_1^2}{\pi\sqrt{f_{m1}^2 - f^2}} \tag{24}$$

which is the expression for PSD of base to mobile Hoyt channel. Again the Rayleigh base to mobile PSD expression is obtained by setting $q = 1$ in (23) as

$$S(f) = \frac{\sigma_1^2}{\pi\sqrt{f_{m1}^2 - f^2}}. \tag{25}$$

2.3.3. Squared Time Autocorrelation Function. The squared time autocorrelation function is used in computation of carrier to noise ratio (CNR). For the proposed channel, it is defined as

$$\mathbf{R}_{\mu^2}(\Delta t) = E\left[\,|\mu(t)|^2 |\mu(t - \Delta t)|^2\right]. \tag{26}$$

In Appendix C, it is derived and the final form obtained is

$$\mathbf{R}_{\mu^2}(\Delta t) = \sigma_1^4 \frac{(1+q^2)^2}{q^4} + 2\left[\mathbf{R}_{11}^2(\Delta t) + \mathbf{R}_{22}^2(\Delta t) + 2\mathbf{R}_{12}^2(\Delta t)\right], \tag{27}$$

where $\mathbf{R}_{11}$ and $\mathbf{R}_{22}$ are the autocorrelation of in-phase and quadrature components, respectively, where $\mathbf{R}_{12}$ is cross-correlation between them.

2.3.4. Level Crossing Rate and Average Duration of Fade. The level crossing rate of the process $R(t)$ is obtained by solving the following integral:

$$N_R(r) = \int_0^\infty \dot{z} p_{R\dot{R}}(r, \dot{z}) d\dot{z}, \tag{28}$$

where $p_{R\dot{R}}$ is the joint PDF of $R(t)$ and its time derivative $\dot{R}(r)$. From [22], LCR for stationary to mobile Hoyt channel is given by

$$N_R(r) = \frac{r}{(2\pi)^{3/2}\sigma_1\sigma_2} \times \int_0^{2\pi} e^{[-(r^2/2\sigma_1^2\sigma_2^2)(\sigma_2^2\cos^2(\theta)+\sigma_1^2\sin^2(\theta))]} \times \sqrt{\beta_1\cos^2(\theta) + \beta_2\sin^2(\theta)}d\theta. \tag{29}$$

The expression will remain the same for V2V Nakagami-Hoyt channel. The only thing that will differ here will be the values of β_1 and β_2. These can be found in Appendix B using the relationship $\beta_i = -\ddot{\mathbf{R}}_\mu(0)$. Also, substituting $\beta_2 = \beta_1/q^2$ and $\rho = R/R_{\text{rms}}$, the LCR is obtained as

$$N_R(\rho) = \frac{\rho\sqrt{\beta_1(q^2+1)}}{(2\pi)^{3/2}q\sigma_1} \times \int_0^{2\pi} e^{[-(\rho^2(q^2+1)/2q^2)(\cos^2(\theta)+q^2\sin^2(\theta))]} \times \sqrt{q^2\cos^2(\theta) + \sin^2(\theta)}d\theta. \tag{30}$$

For isotropic scattering, from Appendix B, substituting the values of $\beta_1 = (\sqrt{2}\pi\sigma_1 f_{m1})^2(1+a^2)$, the expression becomes

$$N_R(\rho) = \frac{\sqrt{(1+a^2)(q^2+1)}f_{m1}\rho}{2q\sqrt{\pi}} \times \int_0^{2\pi} e^{[-(\rho^2(q^2+1)/2q^2)(\cos^2(\theta)+q^2\sin^2(\theta))]} \times \sqrt{q^2\cos^2(\theta) + \sin^2(\theta)}d\theta. \tag{31}$$

It is easy to show that by substituting $a = 0$ and $q = 1$, the above equation is reduced to the expression for base to mobile Rayleigh LCR given by [40].

The average duration of fade of a signal is defined as average duration of time for which the signal r spends below a specified threshold R_0. It is given by [41]

$$\overline{\tau} = \frac{P(r < R_0)}{N_R(r)}, \tag{32}$$

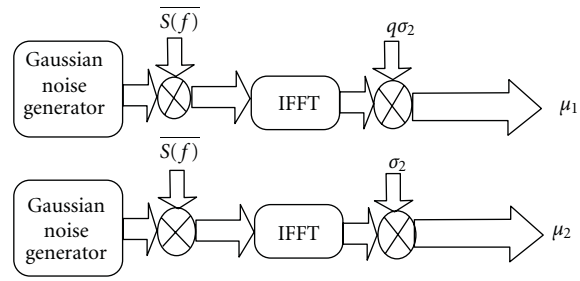

Figure 2: Block diagram of IFFT based simulator.

where $P(r < R_0)$ is the cumulative density function obtained by

$$P(r < R_0) = \int_0^{R_0} p_R(x)dx. \tag{33}$$

This is obtained by integrating (7). Hence substituting (31) and (33) in (32), ADF can be directly obtained.

3. Simulation and Results

The simulator described in this paper uses Smith spectrum method used in [42]. This method is IFFT based and was slightly modified to generate Hoyt Fading signal envelope. This method requires frequency domain generation and processing of random signal followed by inverse Fourier transform to obtain a time domain sequence with the desired properties. The block diagram of the proposed simulator is shown in Figure 2. To implement the simulator, the following steps are performed.

(1) Input number of frequency samples (N) and time samples (M).

(2) Specify maximum doppler frequency of the receiver f_{m1} in Hz.

(3) Specify the value of parameter a such that maximum Doppler frequency of transmitter $f_{m2} = af_{m1}$.

(4) Specify the value of q.

(5) Generate two $N/2$ samples Gaussian quadrature components of zero mean and unity variance. Generate the remaining $N/2$ components by conjugating them. This forms the negative frequency components.

(6) Generate N points spectrum $\sqrt{S(f)}$.

(7) The frequency spacing between the adjacent spectral lines is given by $\Delta f = 2f_{m1}(1+a)/N$.

(8) The time resolution is given by $1/\Delta f(M-1)$.

(9) Multiply the in-phase and quadrature components by $\sqrt{S(f)}$ and perform the IFFT of the resultant individual. Normalize both the resulting in-phase and quadrature to make their variance unity.

(10) Quadrature component will yield μ_2 while in-phase component after multiplying with q will yield μ_1.

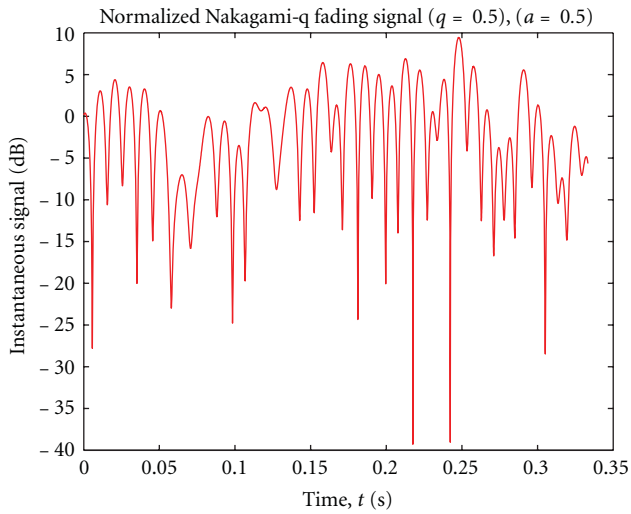

Figure 3: Output of the hoyt simulator.

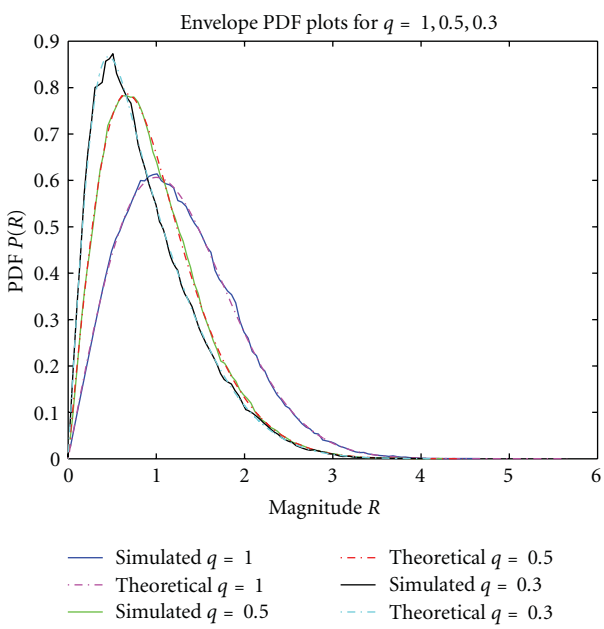

Figure 4: Hoyt amplitude PDF plot $q = 0.5$, $a = 0.5$, $k = 3$.

(11) The root of the sum of squared envelop of both will generate random variable Nakagami Hoyt distribution for the given value of q.

(12) The phase distribution is obtained by using the phase random variable $\tan^{-1}(\mu_1/\mu_2)$.

The simulation was run with the following parameters, carrier frequency $f = 900$ MHz, velocity of receiver $V_1 = 72$ km/hr which means $f_{m1} = 60$ Hz, three different values of $q = 1, 0.5, 0.3$ and three different values of $a = 1, 0.5, 0$. The simulator sample output for $q = 0.5$, $a = 0.5$ is shown in Figure 3. The amplitude and phase pdf plots are shown in Figures 4 and 5, respectively. The corresponding theoretical output of (7) and (8), respectively was also plotted for comparison.

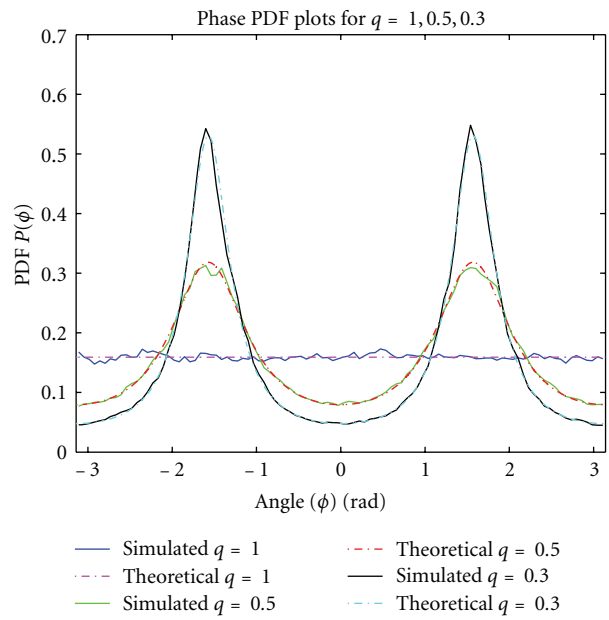

Figure 5: Hoyt phase PDF plot $q = 0.5$, $a = 0.5$, $k = 3$.

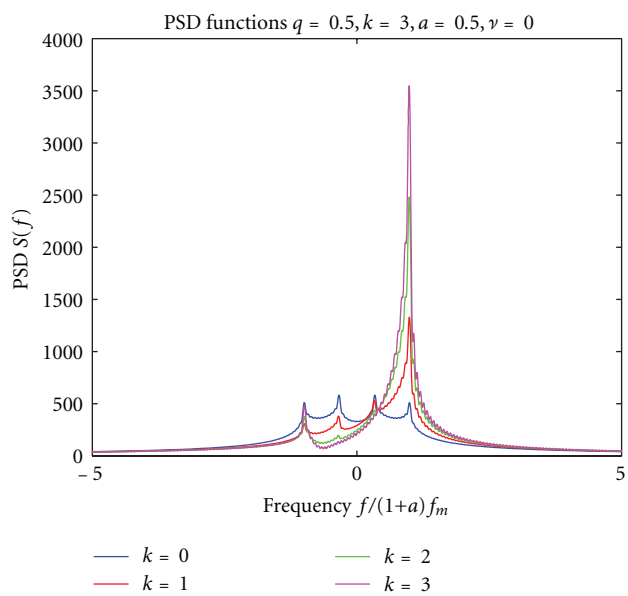

Figure 6: PSD plot for $q = 0.5$.

The power spectral density plots for $\kappa = (0, 1, 2, 3)$ are shown in Figure 6. The plots for other values of q are the scaled version of this and are not shown here. It has been evident from the plot that $S(f)$ has peaks at $f = \pm(f_{m1} - f_{m2})$. It has been shown that plot is symmetric for $\kappa = 0$ indicating isotropic scattering whereas $\kappa \neq 0$ results in asymmetric PSD (non-isotropic scattering).

The autocorrelation plots for $q = 0.5$ and $a = 0.5$ with 4 different values of $\kappa = (0, 1, 2, 3)$ are shown in Figure 7. Plot for $\kappa = 0$ indicates V2V isotropic scattering. The normalized autocorrelation functions plots have been shown in Figure 8. The plots for $a = 1, 0.5, 0$, $q = 0.5$, and $\kappa = 3$ are

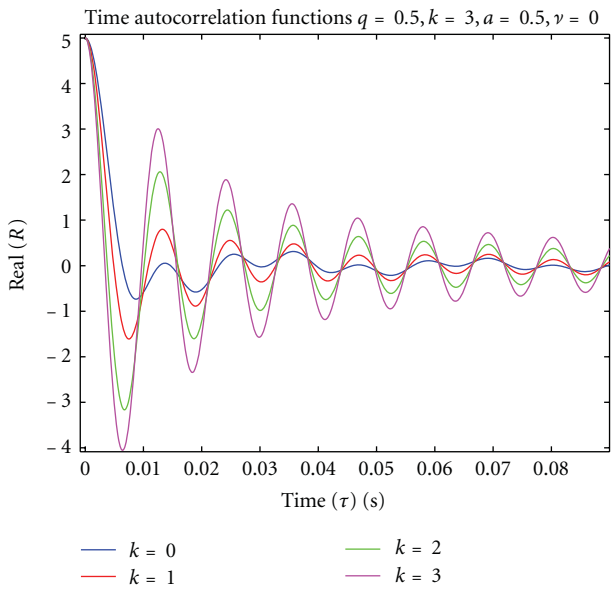

Figure 7: Time autocorrelation function of real part of envelope.

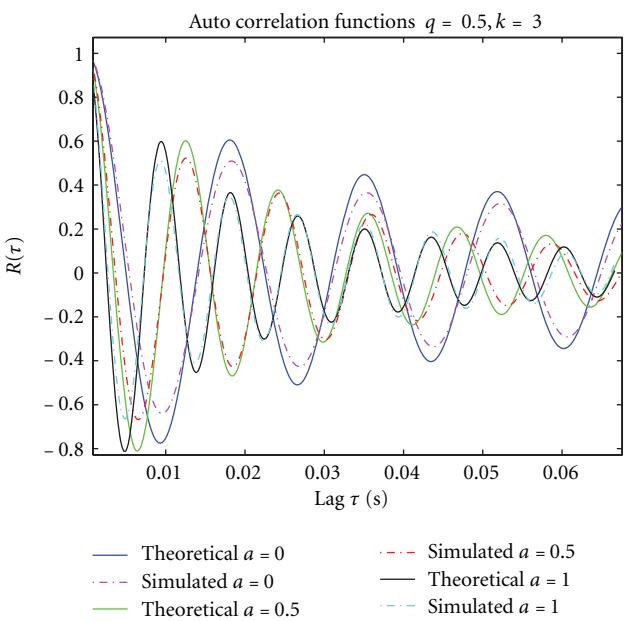

Figure 8: Time Autocorrelation function of Real part of Envelope for $q = 0.5,\ k = 3$.

compared with the theoretical expression given in (17). Since the real and imaginary components are Gaussian, it can be found from the plots that the normalized autocorrelation functions are still Bessel but with different shape than the one shown in [15]. Also the plots are function of κ and ν.

The normalized squared autocorrelation plots of real part for $q = 0.5$, $\kappa = 3$, $a = 0.5$ is shown in Figure 9. The plot is compared with the theoretical derived expression.

The LCR and ADF of envelop for $q = (1, 0.5, 0.3)$ and $\kappa = 3$ are plotted in Figures 10, 11, 12, 13, 14, and 15 for three different values of $a = (1, 0.5, 0)$. The curves are matched with their theoretical expressions given by (31) and (32). $q = 1$ shows the Rayleigh envelop whereas $a = 0$ indicates base to mobile communication plots for LCR and ADF.

The mean square error (MSE) of the time autocorrelation function is given by

$$\mathrm{MSE} = E\left[\left(\mathbf{R}_\mu \Delta t - \widehat{\mathbf{R}}_\mu \Delta t\right)^2\right], \tag{34}$$

where $\mathbf{R}_\mu \Delta t$ and $\widehat{\mathbf{R}}_\mu \Delta t$ are the theoretical and estimated autocorrelation functions, respectively. Figure 16 shows the mean square error of time autocorrelation function as a function of number of frequency sample points N. The figure is obtained for $q = 0.5$, $a = 0.5$, $\kappa = 3$, and varying N in power of 2 in the range 2048–32768. It is evident from the curve that the MSE reduces when the number of sample points is increased. Hence, more accurate simulator is obtained at the cost of increasing the complexity of simulator.

4. Conclusion

The second order statistical properties for vehicle to vehicle Nakagami-Hoyt channels, under the non-isotropic scattering conditions at both the transmitter and receiver, have been developed. These include expressions for space time correlation function, power spectral density, squared time autocorrelation, level crossing rates, and average duration of fade. The Nakagami-Hoyt V2V simulator has also been developed to verify the above mentioned theoretical expressions. It has been found that the theoretical results match closely with the simulated data verifying the validity of the model.

Appendices

A. Proof of the Spatial Time Correlation Function

The spatial time correlation function is given by

$$\mathbf{R}(x_1, x_2, t_1, t_2) = \frac{1}{2}\left\langle \mu_{x_2}(t_2)\mu^*_{x_1}(t_1)\right\rangle, \tag{A.1}$$

where $t_2 = t_1 + \Delta t$. Using [14] as a reference

$$\begin{aligned}\mu_{x_2}(t_2) &= \mu_{x_2}(t_1 + \Delta t)\\ &= \sum_{i=1}^{N} r_i \cos\left[(\omega_{1i} + \omega_{2i})(t_1 + \Delta t) + \phi_i + \psi_i\right]\\ &\quad + j\frac{1}{q}\sum_{i=1}^{N} r_i \sin\left[(\omega_{1i} + \omega_{2i})(t_1 + \Delta t) + \phi_i + \psi_i\right],\end{aligned} \tag{A.2}$$

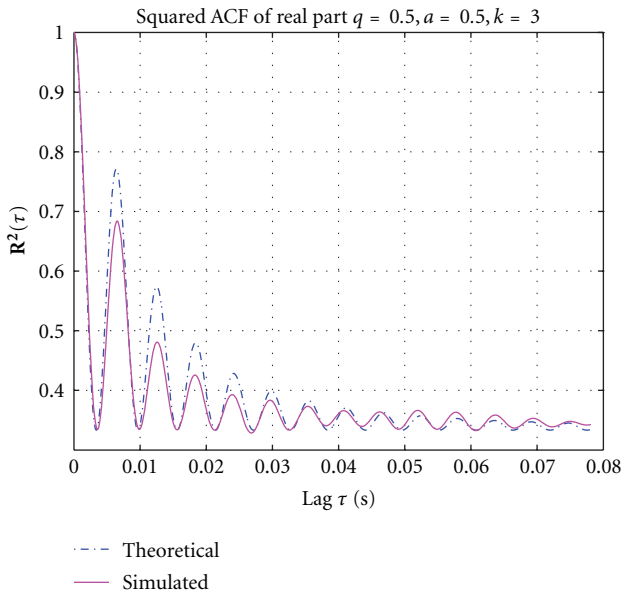

FIGURE 9: Squared Autocorrelation function of Real part for $q = 0.5,\ k = 3$.

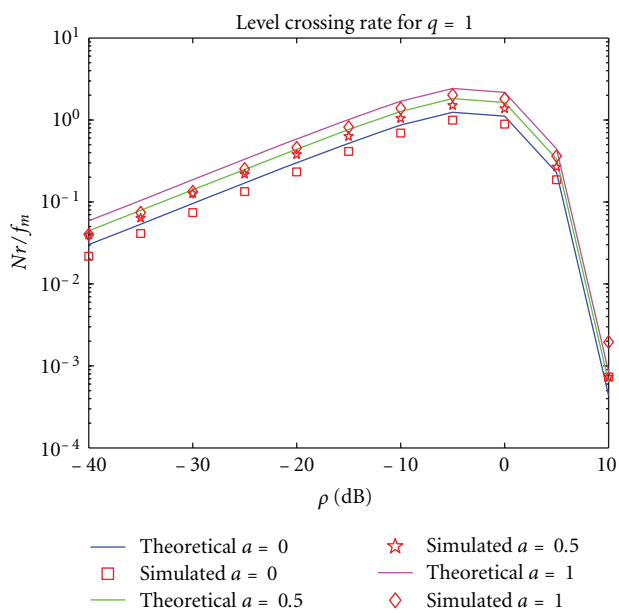

FIGURE 10: Level crossing rates for $q = 1, k = 3$.

where $\psi_i = (2\pi/\lambda)\Delta x \cos\alpha_{1i}$, $\omega_{li} = 2\pi f_{ml}\cos\alpha_{li}$, $l = 1, 2$, ϕ_i is the uniformly distributed phase, and α_{1i} is the AOA of the ith component. Also,

$$\mu_{x_1}(t_1) = \sum_{i=1}^{N} r_i \cos[(\omega_{1i} + \omega_{2i})t_1 + \phi_i] + j\frac{1}{q}\sum_{i=1}^{N} r_i \sin[(\omega_{1i} + \omega_{2i})t_1 + \phi_i]. \tag{A.3}$$

Therefore, we obtain,

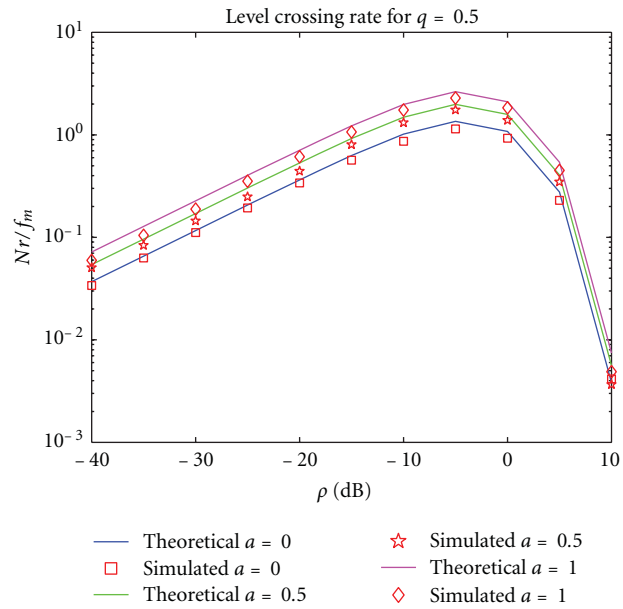

FIGURE 11: Level crossing rates for $q = 0.5, k = 3$.

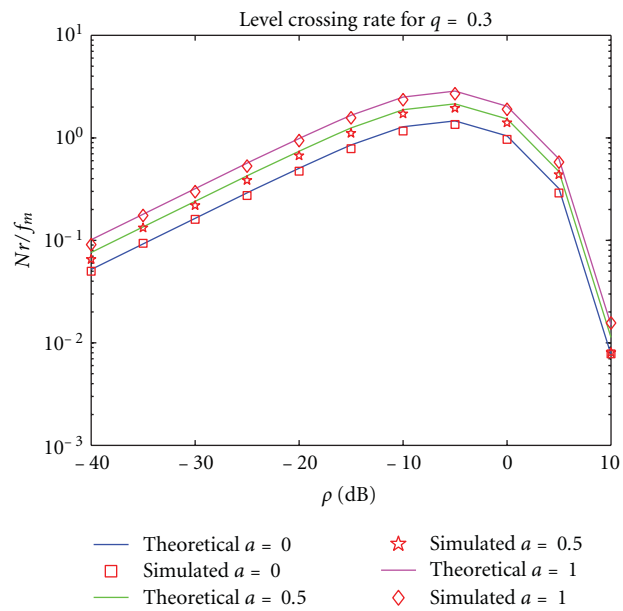

FIGURE 12: Level crossing rates for $q = 0.3, k = 3$.

$$\mathbf{R}(x_1, x_2, t_1, t_2) = \frac{1}{2}\left\langle \sum_{i=1}^{N} r_i r_j \sum_{j=1}^{N} r_i r_j \times \left\{ \cos[(\omega_{1i} + \omega_{2i})(t_1 + \Delta t) + \phi_i + \psi_i] \times \cos\left[\left(\omega_{1j} + \omega_{2j}\right)t_1 + \phi_j\right] \right.\right.$$

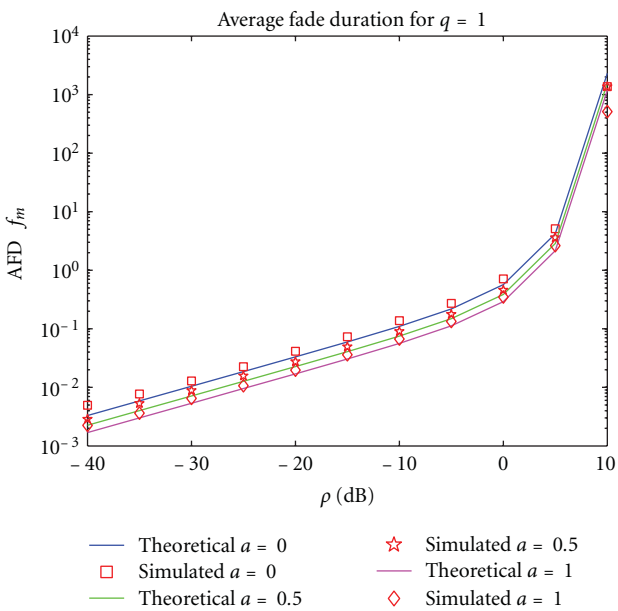

FIGURE 13: Average duration of fade for $q = 1, k = 3$.

$$+\frac{1}{q^2}\sin[(\omega_{1i}+\omega_{2i})(t_1+\Delta t)+\phi_i+\psi_i]$$
$$\times\sin\left[\left(\omega_{1j}+\omega_{2j}\right)t_1+\phi_j\right]$$
$$+j\frac{1}{q}\sin[(\omega_{1i}+\omega_{2i})(t_1+\Delta t)+\phi_i+\psi_i]$$
$$\times\cos\left[\left(\omega_{1j}+\omega_{2j}\right)t_1+\phi_j\right]$$
$$-j\frac{1}{q}\cos[(\omega_{1i}+\omega_{2i})(t_1+\Delta t)+\phi_i+\psi_i]$$
$$\times\sin\left[\left(\omega_{1j}+\omega_{2j}\right)t_1+\phi_j\right]\Bigg\}\Bigg\rangle. \tag{A.4}$$

Assuming ϕ_i, α_{1i}, α_{2i}, and r_i are mutually independent. Also, assume that α_{1i} and α_{2i} have same distributions for all i. Since ϕ_i is assumed to be uniformly distributed, therefore $E[e^{j(\phi_i-\phi_j)}] = 0$ for all $i \neq j$. Hence for $i = j$, $E[e^{j(\phi_i-\phi_j)}] = 1$ and we get

$$\mathbf{R}(\Delta x,\Delta t) = \frac{1}{2}\left\langle\sum_{i=1}^{N} r_i^2\right.$$
$$\times\left\{\left(1+\frac{1}{q^2}\right)\cos[(\omega_{1i}+\omega_{2i})\Delta t+\psi_i]\right.$$
$$\left.\left.+j\frac{2}{q}\sin[(\omega_{1i}+\omega_{2i})\Delta t+\psi_i]\right\}\right\rangle. \tag{A.5}$$

Also, assuming

$$\sigma_1^2 = \frac{1}{2}\left\langle\sum_{i=1}^{N} r_i^2\right\rangle. \tag{A.6}$$

Using the Euler identities for sine and cosine and the formula given in [29] for Von Mises distribution of α_i, we get

$$\begin{aligned} E\left[e^{jw_1\Delta t+(2\pi/\lambda)\Delta x\cos\alpha_1}\right] &= \frac{1}{2\pi I_0(\kappa_1)}\int_{-\pi}^{\pi} e^{\kappa_1\cos(\alpha_1-\nu_1)}e^{j(w_1\Delta t+(2\pi/\lambda)\Delta x\cos\alpha_1)}d\alpha_1 \\ &= \frac{I_0\left(\sqrt{\kappa_1^2+(\omega_1\Delta t+(2\pi/\lambda)\Delta x)^2+j\kappa_1(\omega_1\Delta t+(2\pi/\lambda)\Delta x)\cos\nu_1}\right)}{I_0(\kappa_1)} \end{aligned} \tag{A.7}$$

$$\begin{aligned} E\left[e^{jw_2\Delta t}\right] &= \frac{1}{2\pi I_0(\kappa_2)}\int_{-\pi}^{\pi} e^{\kappa_2\cos(\alpha_2-\nu_2)+j(w_2\Delta t)}d\alpha_2 \\ &= \frac{I_0\left(\sqrt{\kappa_2^2+\omega_2^2\Delta t^2+j2\kappa_2\omega_2\Delta t\cos\nu_2}\right)}{I_0(\kappa_2)}. \end{aligned} \tag{A.8}$$

Hence, after substituting $\omega_i = KV_i$ and further simplification, we obtain

$$\mathbf{R}(\Delta x,\Delta t) = \sum_{n=0}^{1}\frac{(1+q\cos(n\pi))^2}{4q^2}\sigma_1^2\prod_{i=1}^{2}\frac{I_0\left(\sqrt{\kappa_i^2-K^2M_i^2+j2\kappa_iKM_i\cos\nu_i\cos(n\pi)}\right)}{I_0(\kappa_i)}, \tag{A.9}$$

where

$$M_i(\Delta x,\Delta t) = V_i\Delta t+(2-i)\Delta x. \tag{A.10}$$

B. Values of Beta

The values of β_i are calculated from

$$\beta_i = -\ddot{\mathbf{R}}_{ii}(0), \tag{B.1}$$

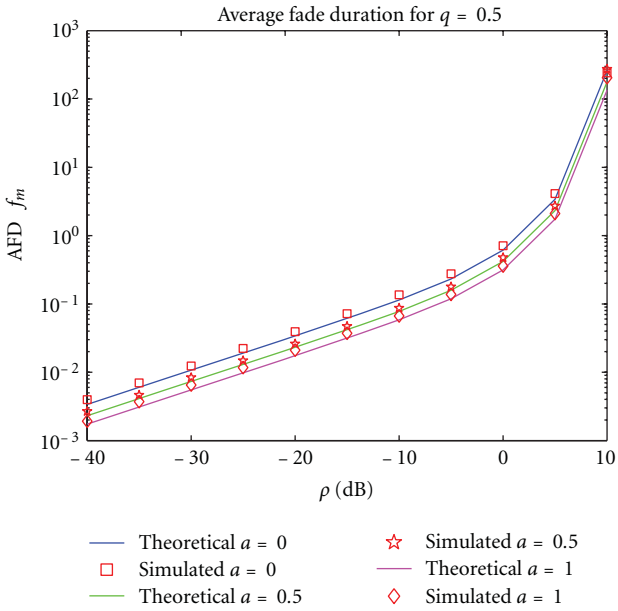

Figure 14: Average duration of fade for $q = 0.5, k = 3$.

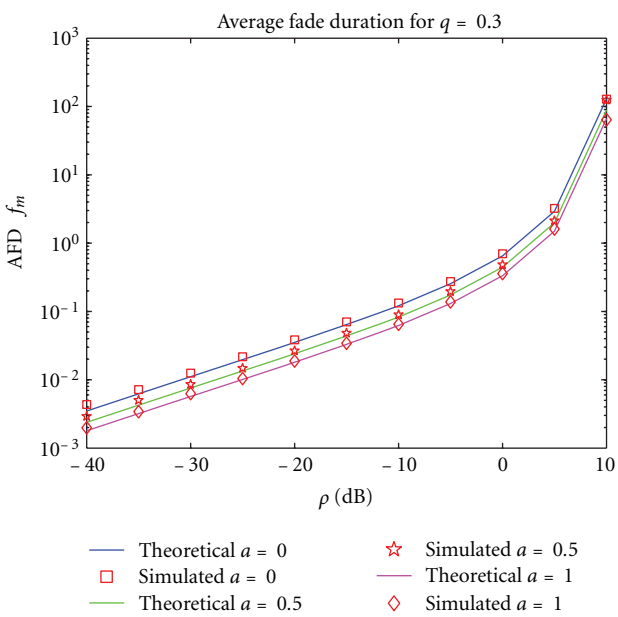

Figure 15: Average duration of fade for $q = 0.3, k = 3$.

where

$$\mathbf{R}_{ii}(\Delta t) = E[\mu_i(t+\Delta t)\mu_i(t)] \quad i = 1, 2$$

$$\mathbf{R}_{11}(\Delta t) = \sigma_1^2 \sum_{n=0}^{1}\prod_{i=1}^{2} \frac{I_0\left(\sqrt{\kappa_i^2 - (KV_i\Delta t)^2 + j2\kappa_i K V_i \Delta t \cos\nu_i \cos(n\pi)}\right)}{I_0(\kappa_i)}. \tag{B.2}$$

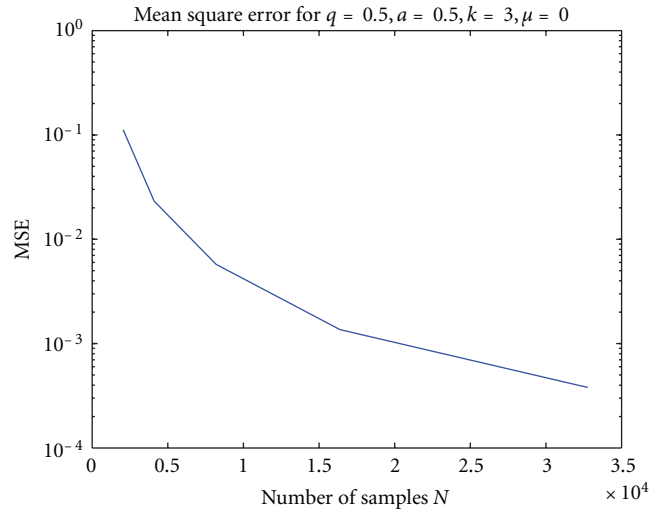

Figure 16: Mean square error of autocorrelation function $q = 0.5, a = 0.5, k = 3$.

Differentiating twice and substituting $\Delta t = 0$ yields

$$\begin{aligned}\beta_1 &= -\ddot{\mathbf{R}}_{11}(0) \\ &= \sigma_1^2 K^2 V_1^2 \Bigg[2a^2 \cos\nu_1 \cos\nu_2 \frac{I_1(\kappa_1)I_1(\kappa_2)}{I_0(\kappa_1)I_0(\kappa_2)} \\ &\quad - \frac{I_1(\kappa_1)\cos 2\nu_1}{\kappa_1 I_0(\kappa_1)} - a^2 \frac{I_1(\kappa_2)\cos 2\nu_2}{\kappa_2 I_0(\kappa_2)} \\ &\quad + \cos^2\nu_1 + a^2\cos^2\nu_2 \Bigg].\end{aligned} \tag{B.3}$$

Provided $\kappa_1, \kappa_2 \neq 0$.

Similarly, we get $\beta_2 = \beta_1/q^2$.

For the case of isotropic scattering ($\kappa_1 = \kappa_2 = \nu_1 = \nu_2 = 0$), differentiating (17) with respect to Δt twice and substituting $\Delta t = 0$, we get

$$\beta_1 = -\ddot{\mathbf{R}}_{11}(0) = \left(\sqrt{2}\pi\sigma_1 f_{m1}\right)^2 (1 + a^2). \tag{B.4}$$

C. Proof of the Squared Time Autocorrelation Function

The squared time autocorrelation function is given by (26) and can be written as

$$\begin{aligned}\mathbf{R}_{\mu^2}(\Delta t) &= E[\mu_1^2(t)\mu_1^2(t-\Delta t)] + E[\mu_2^2(t)\mu_2^2(t-\Delta t)] \\ &\quad + E[\mu_1^2(t)\mu_2^2(t-\Delta t)] + E[\mu_2^2(t)\mu_1^2(t-\Delta t)]\end{aligned} \tag{C.1}$$

For zero mean Gaussian random variable we have from Chapter 6 [43],

$$\begin{aligned}E[\mu_1^2(t)\mu_1^2(t-\Delta t)] &= E[\mu_1^2(t)]E[\mu_1^2(t-\Delta t)] \\ &\quad + 2E^2[\mu_1(t)\mu_1(t-\Delta t)] \\ &= \sigma_1^4 + 2\mathbf{R}_{11}^2(\Delta t).\end{aligned} \tag{C.2}$$

Similarly,

$$E[\mu_2^2(t)\mu_2^2(t-\Delta t)] = \sigma_2^4 + 2\mathbf{R}_{22}^2(\Delta t),$$
$$E[\mu_1^2(t)\mu_2^2(t-\Delta t)] = \sigma_1^2\sigma_2^2 + 2\mathbf{R}_{12}^2(\Delta t). \tag{C.3}$$

Hence substituting in (26) yields

$$\mathbf{R}_{\mu^2}(\Delta t) = \sigma_1^4 \frac{(1+q^2)^2}{q^4} + 2[\mathbf{R}_{11}^2(\Delta t) + \mathbf{R}_{22}^2(\Delta t) + 2\mathbf{R}_{12}^2(\Delta t)], \tag{C.4}$$

where

$$\mathbf{R}_{12}(\Delta t) = \frac{1}{q}\sigma_1^2 \left[\sum_{n=0}^{1} \cos(n\pi) \prod_{i=1}^{2} \frac{I_0\left(\sqrt{\kappa_i^2 - (KV_i\Delta t)^2 + j2\kappa_i KV_i\Delta t \cos\nu_i \cos(n\pi)}\right)}{I_0(\kappa_i)} \right]. \tag{C.5}$$

Acknowledgments

The authors would like to acknowledge the support provided by King Abdulaziz City for Science and Technology (KACST) through the Science and Technology Unit at King Fahd University of Petroleum and Minerals (KFUPM) for funding this work through Project no. NSTP08-ELEC42-4 as part of the National Science, Technology and Innovation Plan (NSTIP).

References

[1] S. O. Rice, "Statistical properties of a sine wave plus random noise," *Bell System Technical Journal*, vol. 27, pp. 109–157, 1948.

[2] R. S. Hoyt, "Probability functions for the modulus and angle of the normal complex variate," *Bell System Technical Journal*, vol. 26, pp. 318–359, 1947.

[3] M. Nakagami, "The m-distribution—a general formula of intensity distribution of rapid fading," in *Statistical Methods in Radio Wave Propagation*, W. G. Hoffman, Ed., pp. 3–36, Permagon Press, Oxford, UK, 1960.

[4] M. A. Taneda, J. Takada, and K. Araki, "A new approach to fading: weibull model," in *Proceedings of the IEEE International Symposium on Personal, Indoor, and Mobile Radio Communications*, pp. 711–715, Osaka, Japan, September 1999.

[5] G. L. Turin, F. D. Clapp, T. L. Johnston et al., "A statistical model of urban multipath propagation," in *Proceedings of the IEEE Transactions on Vehicular Technology*, vol. VT-21, p. 19, February 1972.

[6] F. Hansen and F. I. Meno, "Mobile fading—Rayleigh and lognormal superimposed," *IEEE Transactions on Vehicular Technology*, vol. VT-26, no. 4, pp. 332–335, 1977.

[7] H. Suzuki, "Statistical model for urban radio propagation," *IEEE Transactions on Communications*, vol. 25, no. 7, pp. 673–680, 1977.

[8] F. Vatalaro and G. E. Corazza, "Probability of error and outage in a rice-lognormal channel for terrestrial and satellite personal communications," *IEEE Transactions on Communications*, vol. 44, no. 8, pp. 921–924, 1996.

[9] Safe and Comfortable Driving Based Upon Inter-Vehicle Communication, 2001, http://www.cartalk2000.net/.

[10] Car2Car Communication Consortium, 2005, http://www.car-to-car.org/.

[11] Project MobiVip, 2005, http://www-sop.inria.fr/mobivip/.

[12] FleetNet project Internet on the road, 2000, http://www.neclab.eu/Projects/fleetnet.htm.

[13] C. F. Mecklenbraüker, A. F. Molisch, J. Karedal et al., "Vehicular channel characterization and its implications for wireless system design and performance," *Proceedings of the IEEE*, vol. 99, no. 7, pp. 1189–1212, 2011.

[14] A. S. Akki and F. Haber, "Statistical model of mobile-to-mobile land communication channel," *IEEE Transactions on Vehicular Technology*, vol. VT-35, no. 1, pp. 2–7, 1986.

[15] A. S. Akki, "Statistical properties of mobile-to-mobile land communication channels," *IEEE Transactions on Vehicular Technology*, vol. 43, no. 4, pp. 826–831, 1994.

[16] R. Wang and D. Cox, "Channel modeling for ad hoc mobile wireless networks," in *Proceedings of the IEEE Vehicular Technology Conference*, vol. 1, pp. 21–25, Birmingham, UK, May 2002.

[17] C. S. Patel, G. L. Stuber, and T. G. Pratt, "Simulation of Rayleigh faded mobile-to-miobile comimunication channels," in *Proceedings of the 58th IEEE Vehicular Technology Conference (VTC '03)*, pp. 163–167, Orlando, Fla, USA, October 2003.

[18] B. O. Hogstad, M. Pätzold, N. Youssef, and D. Kim, "A MIMO mobile-to-mobile channel model: part II—the simulation model," in *Proceedings of the IEEE 16th International Symposium on Personal, Indoor and Mobile Radio Communications (PIMRC '05)*, pp. 562–567, Berlin, Germany, September 2005.

[19] A. Petrolino, J. Gomes, and G. Tavares, "A mobile-to-mobile fading channel simulator based on an orthogonal expansion," in *Proceedings of the IEEE 67th Vehicular Technology Conference-Spring (VTC '08)*, pp. 366–370, Singapore, May 2008.

[20] K. C. Borries and D. D. Stancil, "Efficient simulation of mobile-to-mobile rayleigh fading using Gaussian quadrature," in *Proceedings of the IEEE 65th Vehicular Technology Conference (VTC '07)*, pp. 534–538, Dublin, Ireland, April 2007.

[21] A. G. Zajić and G. L. Stüber, "A new simulation model for mobile-to-mobile rayleigh fading channels," in *Proceedings of the IEEE Wireless Communications and Networking Conference (WCNC '06)*, pp. 1266–1270, Las Vegas, Nev, USA, April 2006.

[22] N. Youssef, C. X. Wang, and M. Pätzold, "A study on the second order statistics of Nakagami-Hoyt mobile fading channels," *IEEE Transactions on Vehicular Technology*, vol. 54, no. 4, pp. 1259–1265, 2005.

[23] N. Hajri, N. Youssef, and M. Pätzold, "A study on the statistical properties of double Hoyt fading channels," in *Proceedings of the 6th International Symposium on Wireless Communication Systems (ISWCS '09)*, pp. 201–205, Tuscany, Italy, September 2009.

[24] A. Abdi, J. A. Barger, and M. Kaveh, "A parametric model for the distribution of the angle of arrival and the associated correlation function and power spectrum at the mobile

station," *IEEE Transactions on Vehicular Technology*, vol. 51, no. 3, pp. 425–434, 2002.

[25] M. D. Austin and G. L. Stuber, "Velocity adaptive handoff algorithms for microcellular systems," *IEEE Transactions on Vehicular Technology*, vol. 43, no. 3, pp. 549–561, 1994.

[26] J. Salz and J. H. Winters, "Effect of fading correlation on adaptive arrays in digital mobile radio," *IEEE Transactions on Vehicular Technology*, vol. 43, no. 4, pp. 1049–1057, 1994.

[27] X. Cheng, C. X. Wang, D. I. Laurenson, and A. V. Vasilakos, "Second order statistics of non-isotropic mobile-to-mobile Ricean fading channels," in *Proceedings of the IEEE International Conference on Communications (ICC '09)*, Dresden, Germany, June 2009.

[28] A. Fayziyev, M. Pätzold, and N. Youssef, "On the autocorrelation function of rice processes for unsymmetrical Doppler power spectral densities," in *Proceedings of the International Conference on Advanced Technologies for Communications (ATC '10)*, pp. 118–123, Ho Chi Minh City, Vietnam, October 2010.

[29] Y. R. Zheng, "A non-isotropic model for mobile-to-mobile fading channel simulations," in *Proceedings of the Military Communications Conference (MILCOM '06)*, Washington, DC, USA, October 2006.

[30] M. I. Akram and A. U. H. Sheikh, "On the second order statistical properties of Nakagami Hoyt mobile to mobile fading channel," in *Proceedings of the Australasian Telecommunication Networks and Applications Conference (ATNAC '011)*, pp. 1–5, November 2011.

[31] A. K. Papazafeiropoulos and S. A. Kotsopoulos, "An extended generalized rice model for wireless communications," *IEEE Transactions on Vehicular Technology*, vol. 59, no. 5, pp. 2604–2609, 2010.

[32] A. F. Molisch, F. Tufvesson, J. Karedal, and C. F. Mecklenbräuker, "A survey on vehicle-to-vehicle propagation channels," *IEEE Wireless Communications*, vol. 16, no. 6, pp. 12–22, 2009.

[33] D. W. Matolak, I. Sen, and W. Xiong, "Channel modeling for V2V communications," in *Proceedings of the 3rd Annual International Conference on Mobile and Ubiquitous Systems, MobiQuitous*, pp. 1–7, San Jose, Calif, USA, July 2006.

[34] D. W. Matolak, I. Sen, W. Xiong, and N. T. Yaskoff, "5 GHZ wireless channel characterization for vehicle to vehicle communications," in *Proceedings of the Military Communications Conference (MILCOM '05)*, vol. 5, pp. 3016–3022, Atlantic City, NJ, USA, October 2005.

[35] K. Otani and H. Omori, "Distribution of burst error lengths in rayleigh fading radio channels," *Electronics Letters*, vol. 16, no. 23, pp. 889–891, 1980.

[36] K. Otani, K. Daikoku, and H. Omori, "Burst error performance encountered in digital land mobile radio channel," *IEEE Transactions on Vehicular Technology*, vol. VT-30, no. 4, pp. 156–160, 1981.

[37] H. S. Wang and N. Moayeri, "Finite-state Markov channel—a useful model for radio communication channels," *IEEE Transactions on Vehicular Technology*, vol. 44, no. 1, pp. 163–171, 1995.

[38] M. Schwartz, W. R. Bennet, and S. Stein, *Communication Systems and Techniques*, McGraw-Hill, New York, NY, USA, 1966.

[39] I. S. Gradshteyn and I. M. Ryzhik, *Tables of Integrals, Series and Products*, Academic Press, New York, NY, USA, 1994.

[40] W. C. Jakes, *Microwave Mobile Communications*, IEEE Press, Piscataway, NJ, USA, 2nd edition, 1993.

[41] S. O. Rice, "Mathematical analysis of random noise," *Bell System Technical Journal*, vol. 23, pp. 282–332, 1945.

[42] T. S. Rappaport, *Wireless Communications: Principle and Practice*, Printice Hall Communications Engineering and Emerging Techgnologies series, 2nd edition, 1996.

[43] A. Papoulis and S. U. Pillai, *Probability, Random Variables and Stochastic Processes*, McGrae-Hill Higher Education, 4th edition, 1996.

Hindawi Publishing Corporation
International Journal of Antennas and Propagation
Volume 2012, Article ID 891932, 10 pages
doi:10.1155/2012/891932

Research Article

Efficient Rank-Adaptive Least-Square Estimation and Multiple-Parameter Linear Regression Using Novel Dyadically Recursive Hermitian Matrix Inversion

Hsiao-Chun Wu,[1] Shih Yu Chang,[2] Tho Le-Ngoc,[3] and Yiyan Wu[4]

[1] *School of Electrical Engineering and Computer Science, Louisiana State University, 3183 Patrick F. Taylor Hall Baton Rouge, LA 70803, USA*
[2] *Department of Computer Science, National Tsing Hua University, Hsinchu 30013, Taiwan*
[3] *Department of Electrical and Computer Engineering, McGill University, Montreal, QC, Canada H3A 0G4*
[4] *Department of Television Networks and Transmission, Communications Research Centre, Ottawa, ON, Canada K2H 8S2*

Correspondence should be addressed to Hsiao-Chun Wu, wu@ece.lsu.edu

Received 27 July 2012; Accepted 3 October 2012

Academic Editor: Ai Bo

Least-square estimation (LSE) and multiple-parameter linear regression (MLR) are the important estimation techniques for engineering and science, especially in the mobile communications and signal processing applications. The majority of computational complexity incurred in LSE and MLR arises from a Hermitian matrix inversion. In practice, the Yule-Walker equations are not valid, and hence the Levinson-Durbin algorithm cannot be employed for general LSE and MLR problems. Therefore, the most efficient Hermitian matrix inversion method is based on the Cholesky factorization. In this paper, we derive a new dyadic recursion algorithm for sequential rank-adaptive Hermitian matrix inversions. In addition, we provide the theoretical computational complexity analyses to compare our new dyadic recursion scheme and the conventional Cholesky factorization. We can design a variable model-order LSE (MLR) using this proposed dyadic recursion approach thereupon. Through our complexity analyses and the Monte Carlo simulations, we show that our new dyadic recursion algorithm is more efficient than the conventional Cholesky factorization for the sequential rank-adaptive LSE (MLR) and the associated variable model-order LSE (MLR) can seek the trade-off between the targeted estimation performance and the required computational complexity. Our proposed new scheme can benefit future portable and mobile signal processing or communications devices.

1. Introduction

Least-square estimation (LSE) or multiple-parameter linear regression (MLR) is a crucial mathematical technique for science and engineering ubiquitously. A wide variety of applications in signal processing devices, mobile communications, computational physics, and statistics arise from the LSE or MLR. It has been adopted as a powerful tool in nuclear science [1, 2], system identification [3], data mining [4], linear system modeling [5], medical imaging analysis [6], and so forth. In particular, for signal processing and communications, least-square approach dominates a large majority of applications, such as the equalizations [7–16] as well as the interference estimation [17–19]. An overview of linear regression can be found in [20].

However, all of the aforementioned applications of LSE or MLR require the predetermined *model order* (the number of parameters to be estimated), and therefore the associated computational complexities are fixed and not flexible. In practice, the predetermined model order should be large enough to assure that the square error can be minimized due to the sufficient degree of freedom. Therefore, the model-order selection is essential to all LSE and MLR problems. Intuitively, we may adjust the model order such that an

appropriate model order can be achieved to satisfy a preset square-error requirement. In the meantime, the computational complexity can be variable and depends on the error tolerance using such an adjustable model order. Nevertheless, the computational complexity would augment tremendously during the model order adjustment. How to make the most use of the calculated estimates from the previous model order and estimate the new parameters thereupon draws the researchers' interest always.

Rank-one update scheme or iterative Levinson-Durbin algorithm is the well-known approach for computing the linear prediction coefficients with adjustable model orders [21]. The Levinson-Durbin algorithm is based on the Yule-Walker equations [22] and the strict assumption of *Hermitian Toeplitz correlation matrix* [21], but such an assumption is valid only when the multiple time series (the observed data) possess the exact temporal relationship (one is the delayed version of another) and the sample size approaches infinity under the ergodicity [23]. Besides, the Levinson-Durbin algorithm can only increase the model order by one at each iteration. A new class of extended Levinson-Durbin algorithms has been developed to achieve computational efficiency: in speech or audio coders, an adaptive multi-stage Levinson-Durbin algorithm was investigated in [24], and it was shown to be more robust than the conventional Levinson-Durbin algorithm when the input signal has large spectral dynamics; low-complexity approaches were also provided to determine the optimal delay and calculate the linear prediction filter coefficients in [7, 25]; iterative Levinson-Durbin algorithms were investigated for the frequency-domain decision feedback and MMSE equalizers in [8–12]. However, the Levinson-Durbin family of algorithms are still restricted by their limited model-order scalability due to their common rank-one update characteristics and Hermitian Toeplitz correlation matrix assumption.

For a general linear regression problem, the temporal relationship among multiple observed time series does not necessarily sustain. Hence, the Hermitian Toeplitz correlation matrix can exist only for some circumstances. To be more precise, the correlation matrix for a general linear regression problem should be Hermitian only [22, 26]. If the correlation matrix is Hermitian, the most efficient technique for the least-square solutions involves *Cholesky factorization* [21]. Recursion-based factorization methods were proposed to reduce the memory usage and computational complexity [27, 28]. However, they are not related to the direct Hermitian matrix inversion, which is the backbone of the linear estimation and the multiple-parameter linear regression. The existing Cholesky-factorization-based Hermitian matrix inversion procedure has to recalculate all the estimates when the model order is enlarged. In this paper, we present a novel *rank-adaptive Cholesky factorization scheme*, which can be employed to establish a low-complexity variable model-order LSE or MLR algorithm. In our newly derived LSE or MLR algorithm, the model order can be adjusted dyadically (model order is 2^m, $m = 1, 2, 3, \ldots$) while that in the Levinson-Durbin algorithm can be incremented one by one. To the best of our knowledge, our new algorithm is the only estimation or regression method which can adjust the model order dyadically. The magnificent dyadic-scalability property of our proposed LSE and MLR algorithm can well serve for the future signal processing or communications applications which demand the adaptability in both memory storage and computational complexity.

The rest of this paper is organized as follows. In Section 2, the problem formulation for the LSE and MLR is presented where the Wiener-Hopf equations will result in a Hermitian correlation matrix inversion. In Section 3, we derive the dyadic recursion formula for such a Hermitian matrix inversion. In Section 3.2, we design a novel dyadic rank-adaptive Hermitian matrix inversion algorithm based on the results in Section 3.1. The computational complexity analyses for the fixed model-order and rank-adaptive Hermitian matrix inversion using the conventional Cholesky factorization and our new dyadic recursion are manifested in Section 4. The frequent communications and signal processing applications using the sequential rank-adaptive LSE thereupon for channel estimation and equalization are introduced in Section 5. The numerical evaluations for the comparisons of the computational complexities and the least mean-square errors between our new dyadic recursion scheme and the conventional method are delineated in Section 6. Ultimate concluding remarks will be drawn in Section 7.

Notations: $\mathcal{N}$, $\mathcal{C}$ denote the sets of positive integers and complex numbers, respectively. $\vec{a}$ denotes a column vector and $\widetilde{A}$ denotes a matrix; $\widetilde{A}^T$, $\widetilde{A}^H$ denote the transpose and the Hermitian adjoint of $\widetilde{A}$, respectively. The symbols i, j, and k are reserved as the integer indices. The symbol $\widetilde{A}_k(i, j)$ represents a $k \times k$ square matrix with the dimensionality k, and this matrix is in a larger matrix which contains $\widetilde{A}_k(i, j)$ as its (i, j)-block. $\equiv$ represents the mathematical definition and $*$ denotes the complex-conjugate operator. The computational complexity function $\mathbb{C}_\bullet(N)$ specifies the number of complex multiplications incurred when $\bullet$ of dimension N is calculated.

2. Least-Square Estimation and Multiple-Parameter Linear Regression

The LSE and MLR can be formulated as follows: given the degree of freedom or model order $N \in \mathcal{N}$ and the N observed time series $x_i(n)$, $n = 0, 1, \ldots, M-1$ and the target time series (desired response) $d(n)$, $n = 0, 1, \ldots, M-1$ where M is the sample size for all time series, we want to search for the best-fitting coefficients w_i, for $i = 1, 2, \ldots, N$, such that $\sum_{n=0}^{M-1} \sum_{i=1}^{N} |d(n) - w_i^* x_i(n)|^2$ is minimized. In general, $x_i(n)$, $d(n)$, and w_i are complex-valued, $\forall n$, $\forall i$. Thereby, in matrix form, the LSE or MLR problem can be formulated as

$$\vec{w}_{\text{opt}} = \arg\min_{\vec{w}} \left(\sum_{n=0}^{M-1} \left| d(n) - \vec{w}^H \vec{X}(n) \right|^2 \right), \tag{1}$$

where

$$\vec{w} \equiv [w_1 w_2 \cdots w_N]^T, \tag{2}$$

$$\vec{X}(n) \equiv [x_1(n) x_2(n) \cdots x_N(n)]^T, \tag{3}$$

and $\vec{w}_{\text{opt}}$ is the collection of the best-fitting (optimal) coefficients. Equation (1) can be rewritten as

$$\vec{w}_{\text{opt}} = \arg\min_{\vec{w}}\left(\vec{w}^H\widetilde{R}_N\vec{w} - \vec{P}_N^H\vec{w} - \vec{w}^H\vec{P}_N\right), \tag{4}$$

where

$$\widetilde{R}_N \equiv \frac{1}{M}\sum_{n=0}^{M-1}\vec{X}(n)\vec{X}^H(n), \tag{5}$$

$$\vec{P}_N \equiv \frac{1}{M}\sum_{n=0}^{M-1}d^*(n)\vec{X}(n). \tag{6}$$

According to [22], the least-square solution to the LSE or MLR problem stated in (4) is given by the Wiener-Hopf equation as follows:

$$\vec{w}_{\text{opt}} = \widetilde{R}_N^{-1}\vec{P}_N, \tag{7}$$

and the least mean-squared error σ^2_{opt} is given by

$$\begin{aligned}\sigma^2_{\text{opt}} &\equiv \frac{1}{M}\sum_{n=0}^{M-1}\left|d(n) - \vec{w}^H_{\text{opt}}\vec{X}(n)\right|^2\\ &= \frac{1}{M}\sum_{n=0}^{M-1}|d(n)|^2 - \vec{P}_N^H\vec{w}_{\text{opt}}.\end{aligned} \tag{8}$$

It is noted from (7) that the major portion of the computational complexity for solving $\vec{w}_{\text{opt}}$ involves the calculation of $\widetilde{R}_N^{-1}$. Therefore, the computational complexity can be further reduced if the special mathematical properties of the *correlation matrix* $\widetilde{R}_N$ are exploited.

In particular, when the LSE or MLR is adopted for filter or equalizer design, the temporal relationship $x_i(n-1) = x_{i+1}(n)$, for $i = 1, 2, \ldots, N-1$, for all n, is assumed. Thus, as the sample size is large ($M \to \infty$), the correlation matrix $\widetilde{R}_N$ is both Hermitian and Toeplitz under the stationary and ergodic assumption [23]. However, very often, the multiple time series, $x_i(n)$, $i = 1, 2, \ldots, N$, specify the different observations generated from independent sources, or the sample size M is not large. Consequently,

$$\sum_{n=0}^{M-1}x_i(n)x^*_{i+q}(n) \neq \sum_{n=0}^{M-1}x_j(n)x^*_{j+q}(n), \quad \forall i \neq j, \tag{9}$$

$$1 \le i, \quad j \le N, \quad -N+1 \le q \le N-1,$$

$$1 \le i+q, \quad j+q \le N. \tag{10}$$

According to (9), the correlation matrix $\widetilde{R}_N$ is not necessarily Toeplitz. Based on (5), the only ever-sustaining property is that $\widetilde{R}_N$ is always Hermitian. Instead of employing the QR factorization to compute $\widetilde{R}_N^{-1}$ with high complexity [21], we can benefit from this Hermitian property to carry out. Since $\widetilde{R}_N$ is Hermitian, we can use the Cholesky factorization such that

$$\widetilde{R}_N = \widetilde{L}_N\widetilde{L}_N^H, \tag{11}$$

where $\widetilde{L}_N$ and $\widetilde{L}_N^H$ are the lower- and upper-triangular matrices, respectively. If $\widetilde{R}_N^{-1}$ exists, according to (11), we can calculate $\widetilde{R}_N^{-1}$ as

$$\widetilde{R}_N^{-1} = \widetilde{L}_N^{-H}\widetilde{L}_N^{-1}, \tag{12}$$

where $\widetilde{L}_N^{-H} \equiv \left(\widetilde{L}_N^{-1}\right)^H = \left(\widetilde{L}_N^H\right)^{-1}$, which is a more efficient procedure than the inversion based on the QR factorization [21].

3. Novel Dyadically Recursive Hermitian Matrix Inversion

3.1. Recursion of Hermitian Matrix Inversion Using Cholesky Outer Product. From the previous studies in Section 2, we cannot adopt the Levinson-Durbin algorithm for LSE or MLR when the correlation matrix $\widetilde{R}_N$ is not Toeplitz. To the best of our knowledge, no exiting literature had ever addressed any form of recursive formula for the procedure of Hermitian matrix inversion. In this section, we would like to introduce such a new procedure, which can dyadically extend the inverse of any Hermitian matrix from those of its submatrices with a half dimension. This novel dyadic recursion for Hermitian matrix inversion can reduce the computational complexity as we will analyze later on.

Any lower-triangular matrix $\widetilde{L}_N$ of dimension N can be decomposed as

$$\widetilde{L}_N = \begin{bmatrix}\widetilde{L}_{N/2}(1,1) & \widetilde{\mathbf{0}}_{N/2}\\ \widetilde{\psi}_{N/2} & \widetilde{L}_{N/2}(2,2)\end{bmatrix}, \tag{13}$$

where $\widetilde{\mathbf{0}}_{N/2}$ is the $(N/2)\times(N/2)$ matrix containing all zeros, $\widetilde{L}_{N/2}(1,1)$, $\widetilde{L}_{N/2}(2,2)$ are the two $(N/2)\times(N/2)$ submatrices both of which are lower-triangular, and $\widetilde{\psi}_{N/2}$ is the $(N/2)\times(N/2)$ submatrix. According to (11) and (13), we have

$$\widetilde{R}_N \equiv \begin{bmatrix}\widetilde{R}_{N/2}(1,1) & \widetilde{R}^H_{N/2}(2,1)\\ \widetilde{R}_{N/2}(2,1) & \widetilde{R}_{N/2}(2,2)\end{bmatrix} \tag{14}$$

$$= \begin{bmatrix}\widetilde{L}_{N/2}(1,1)\widetilde{L}^H_{N/2}(1,1) & \widetilde{L}^H_{N/2}(1,1)\widetilde{\psi}^H_{N/2}\\ \widetilde{\psi}_{N/2}\widetilde{L}^H_{N/2}(1,1) & \widetilde{\psi}_{N/2}\widetilde{\psi}^H_{N/2} + \widetilde{L}_{N/2}(2,2)\widetilde{L}^H_{N/2}(2,2)\end{bmatrix}, \tag{15}$$

where

$$\begin{aligned}\widetilde{R}_{N/2}(1,1) &\equiv \frac{1}{M}\sum_{n=0}^{M-1}\Big([x_1(n)x_2(n)\cdots x_{N/2}(n)]^T\\ &\qquad\times[x_1^*(n)x_2^*(n)\cdots x^*_{N/2}(n)]\Big)\\ &= \widetilde{L}_{N/2}(1,1)\widetilde{L}^H_{N/2}(1,1),\end{aligned} \tag{16}$$

$$\begin{aligned}\widetilde{R}_{N/2}(2,1) &\equiv \frac{1}{M}\sum_{n=0}^{M-1}\Big(\left[x_{(N/2)+1}(n)x_{(N/2)+2}(n)\cdots x_N(n)\right]^T \\ &\qquad \times \left[x_1^*(n)x_2^*(n)\cdots x_{N/2}^*(n)\right]\Big) \\ &= \widetilde{\psi}_{N/2}\widetilde{L}_{N/2}^H(1,1),\end{aligned} \tag{17}$$

$$\begin{aligned}\widetilde{R}_{N/2}(2,2) &\equiv \frac{1}{M}\sum_{n=0}^{M-1}\Big(\left[x_{(N/2)+1}(n)x_{(N/2)+2}(n)\cdots x_N(n)\right]^T \\ &\qquad \times \left[x_{(N/2)+1}^*(n)x_{(N/2)+2}^*(n)\cdots x_N^*(n)\right]\Big) \\ &= \widetilde{\psi}_{N/2}\widetilde{\psi}_{N/2}^H + \widetilde{L}_{N/2}(2,2)\widetilde{L}_{N/2}^H(2,2).\end{aligned} \tag{18}$$

According to (11)–(14), we obtain

$$\widetilde{L}_N^{-1} = \begin{bmatrix}\widetilde{L}_{N/2}^{-1}(1,1) & \widetilde{\mathbf{0}}_{N/2} \\ \widetilde{\phi}_{N/2} & \widetilde{L}_{N/2}^{-1}(2,2)\end{bmatrix}, \tag{19}$$

where

$$\widetilde{\phi}_{N/2} = -\widetilde{L}_{N/2}^{-1}(2,2)\widetilde{\psi}_{N/2}\widetilde{L}_{N/2}^{-1}(1,1). \tag{20}$$

3.2. New Efficient Dyadic Recursion for Hermitian Matrix Inversion. In this paper, we assume that the ill-posed problem can be neglected during the matrix inversion and no additional pivoting technique is required. Therefore, the computational complexity for the pivoting is not considered here. From the results in the previous subsection, we can design the following *efficient dyadic recursion algorithm* for any Hermitian matrix inversion.

Step 1 (Initialization). Set $N = 1$ and $\widetilde{R}_N(1,1) \equiv r_0 = (1/M)\sum_{n=0}^{M-1}|x_1(n)|^2$. $\widetilde{L}_N(1,1) \equiv l_1 = \sqrt{r_0}$. Hence, $\widetilde{L}_N^{-1}(1,1) = 1/l_1$.

Step 2. Construct the correlation matrix of dimension $2N$ such that

$$\widetilde{R}_{2N} = \begin{bmatrix}\widetilde{R}_N(1,1) & \widetilde{R}_N^H(2,1) \\ \widetilde{R}_N(2,1) & \widetilde{R}_N(2,2)\end{bmatrix}. \tag{21}$$

Step 3 (Dyadic Expansion). Compute

$$\widetilde{\psi}_N = \widetilde{R}_N(2,1)\widetilde{L}_N^{-H}(1,1). \tag{22}$$

Use the Cholesky factorization to calculate

$$\widetilde{L}_N(2,2)\widetilde{L}_N^H(2,2) = \widetilde{R}_N(2,2) - \widetilde{\psi}_N\widetilde{\psi}_N^H. \tag{23}$$

Then, calculate $\widetilde{L}_N^{-1}(2,2)$ accordingly.

Compute

$$\widetilde{\phi}_N = -\widetilde{L}_N^{-1}(2,2)\widetilde{\psi}_N\widetilde{L}_N^{-1}(1,1). \tag{24}$$

Step 4 (Dyadically Recursive Hermitian Matrix Inversion). Construct

$$\begin{aligned}\widetilde{L}_{2N} &= \begin{bmatrix}\widetilde{L}_N(1,1) & \widetilde{\mathbf{0}}_N \\ \widetilde{\psi}_N & \widetilde{L}_N(2,2)\end{bmatrix}, \\ \widetilde{L}_{2N}^{-1} &= \begin{bmatrix}\widetilde{L}_N^{-1}(1,1) & \widetilde{\mathbf{0}}_N \\ \widetilde{\phi}_N & \widetilde{L}_N^{-1}(2,2)\end{bmatrix}.\end{aligned} \tag{25}$$

Step 5. Repeat Steps 2–4 for $N = 2^p$, $p = 1,2,3,\ldots$ and stop at $N = 2^p$, which is determined by the preset square-error tolerance. Use the ultimate $\widetilde{L}_{2N}^{-1}$ to calculate $\widetilde{R}_{2N}^{-1} = \widetilde{L}_{2N}^{-H}\widetilde{L}_{2N}^{-1}$.

4. Computational Complexity Analyses for Hermitian Matrix Inversion

In this section, we will study the computational complexities of the two algorithms for the Hermitian matrix inversion, namely (i) conventional Cholesky factorization and (ii) our new dyadic recursion presented in Section 3.2. Since the correlation matrix assumption for the Levinson-Durbin method is different and it also has to be based on the Yule-Walker equations as previously discussed in Section 2, we cannot compare the Levinson-Durbin method with the two underlying schemes here on a fair ground. Without loss of generality, we assume that all of the observed time series are normalized with respect to their energies such that $\sum_{n=0}^{M-1}|x_i(n)|^2 = 1$, for $i = 1,2,\ldots,N$ in our subsequent analyses. Thus, the diagonal elements in the correlation matrices $\widetilde{R}_N$ of any dimension N are always 1.

4.1. Computational Complexity for Hermitian Matrix Inversion Using Conventional Cholesky Factorization. The Hermitian matrix inversion using the conventional Cholesky factorization has to be based on the predetermined model order N. Since the diagonal elements of $\widetilde{R}_N$ are 1, it yields

$$\begin{aligned}\widetilde{L}_N &= \begin{bmatrix}1 & 0 & \cdots & \cdots & \cdots & 0 \\ l_{21} & 1 & 0 & \cdots & \cdots & 0 \\ l_{31} & l_{32} & 1 & 0 & \cdots & 0 \\ \vdots & \vdots & \cdots & \ddots & \ddots & \vdots \\ \vdots & \vdots & \cdots & \cdots & \ddots & 0 \\ l_{N1} & l_{N2} & l_{N3} & \cdots & l_{N,(N-1)} & 1\end{bmatrix}, \\ \widetilde{R}_N &= \widetilde{L}_N\widetilde{L}_N^H.\end{aligned} \tag{26}$$

According to (26), the corresponding computational complexity $\mathbb{C}_{\widetilde{L}\widetilde{L}^H}(N)$ in terms of the total complex multiplications is

$$\mathbb{C}_{\widetilde{L}\widetilde{L}^H}(N) = \frac{N(N-1)(N-2)}{6}. \tag{27}$$

To compute $\widetilde{L}_N^{-1}$, we can write

$$\widetilde{L}_N^{-1} = \begin{bmatrix} 1 & 0 & \cdots & \cdots & \cdots & 0 \\ \lambda_{21} & 1 & 0 & \cdots & \cdots & 0 \\ \lambda_{31} & \lambda_{32} & 1 & 0 & \cdots & 0 \\ \vdots & \vdots & \cdots & \ddots & \ddots & \vdots \\ \vdots & \vdots & \cdots & \cdots & \ddots & 0 \\ \lambda_{N1} & \lambda_{N2} & \lambda_{N3} & \cdots & \lambda_{N,(N-1)} & 1 \end{bmatrix}, \tag{28}$$

where $\lambda_{ij} \in \mathcal{C}$, for $1 \le j < i \le N$, are the values to be determined from $\widetilde{L}_N$. Since $\widetilde{L}_N^{-1}\widetilde{L}_N = \widetilde{I}_N$ where $\widetilde{I}_N$ is the $N \times N$ identity matrix, the computational complexity $\mathbb{C}_{\widetilde{L}^{-1}}(N)$ for calculating $\widetilde{L}_N^{-1}$ is also

$$\mathbb{C}_{\widetilde{L}^{-1}}(N) = \frac{N(N-1)(N-2)}{6}. \tag{29}$$

Once $\widetilde{L}_N^{-1}$ is available, the inverse matrix $\widetilde{R}_N^{-1} = \widetilde{L}^{-H}(N)\widetilde{L}^{-1}(N)$ can be calculated accordingly and the corresponding computational complexity for this multiplication is

$$\mathbb{C}_{\widetilde{L}^{-H}\widetilde{L}^{-1}}(N) = \frac{N(N-1)(2N-1)}{6}. \tag{30}$$

Thus, from (27), (29), and (30), the *total computational complexity* $\mathbb{C}_{\widetilde{R}_{\text{Chol}}^{-1}}(N)$ for calculating $\widetilde{R}_N^{-1}$ using the conventional Cholesky factorization is

$$\begin{aligned} \mathbb{C}_{\widetilde{R}_{\text{Chol}}^{-1}}(N) &= \mathbb{C}_{\widetilde{L}\widetilde{L}^H}(N) + \mathbb{C}_{\widetilde{L}^{-1}}(N) + \mathbb{C}_{\widetilde{L}^{-H}\widetilde{L}^{-1}}(N) \\ &= \frac{4N^3 - 9N^2 + 5N}{6}. \end{aligned} \tag{31}$$

4.2. Computational Complexity for Hermitian Matrix Inversion Using New Efficient Dyadic Recursion. From the previous discussion in Section 3.2, we can calculate the computational complexity for our new scheme thereupon. First, let us focus on the incurred computational complexity in terms of complex multiplications when we apply the recursion in Section 3.2 to solve $\widetilde{R}_{2^p}^{-1}$ from the given $\widetilde{L}_{2^{p-1}}(1,1) = \widetilde{L}_{2^{p-1}}$ and $\widetilde{L}_{2^{p-1}}^{-1}(1,1) = \widetilde{L}_{2^{p-1}}^{-1}$, for $p \in \mathcal{N}$. According to (22), the computational complexity $\mathbb{C}_{\widetilde{\psi}}(2^{p-1})$ for computing $\widetilde{\psi}_{2^{p-1}} = \widetilde{R}_{2^{p-1}}(2,1)\widetilde{L}_{2^{p-1}}^{-H}(1,1)$ is

$$\mathbb{C}_{\widetilde{\psi}}(2^{p-1}) = \frac{4^{p-1}(2^{p-1}-1)}{2}. \tag{32}$$

Next, the calculation of $\widetilde{\psi}_{2^{p-1}}\widetilde{\psi}_{2^{p-1}}^H$ involves the computational complexity

$$\mathbb{C}_{\widetilde{\psi}\widetilde{\psi}^H}(2^{p-1}) = 8^{p-1}. \tag{33}$$

Then, we can compute $\widetilde{L}_{2p-1}(2,2)\widetilde{L}_{2^{p-1}}^H(2,2)$ according to (23); the corresponding computational complexity, similar to (27), is

$$\mathbb{C}_{\widetilde{L}_{2,2}\widetilde{L}_{2,2}^H}(2^{p-1}) = \frac{2^{p-1}(2^{p-1}-1)(2^{p-1}-2)}{6}. \tag{34}$$

In addition, similar to (29), the computational complexity for calculating $\widetilde{L}_{2^{p-1}}^{-1}(2,2)$ is also

$$\mathbb{C}_{\widetilde{L}_{2,2}^{-1}}(2^{p-1}) = \frac{2^{p-1}(2^{p-1}-1)(2^{p-1}-2)}{6}. \tag{35}$$

According to (24), we can calculate the computational complexity $\mathbb{C}_{\widetilde{\phi}}(2^{p-1})$ for $\widetilde{\phi}_{2^{p-1}} = -\widetilde{L}_{2^{p-1}}^{-1}(2,2)\widetilde{\psi}_{2^{p-1}}\widetilde{L}_{2^{p-1}}^{-1}(1,1)$ such that

$$\mathbb{C}_{\widetilde{\phi}}(2^{p-1}) = 4^{p-1}(2^{p-1}-1). \tag{36}$$

Thus, the computational complexity involved in the calculation of $\widetilde{L}_{2^p}^{-1}$ is equivalent to

$$\begin{aligned} \mathbb{C}_{\widetilde{L}^{-1}}(2^p) &= \mathbb{C}_{\widetilde{\psi}}(2^{p-1}) + \mathbb{C}_{\widetilde{\psi}\widetilde{\psi}^H}(2^{p-1}) \\ &\quad + \mathbb{C}_{\widetilde{L}_{2,2}\widetilde{L}_{2,2}^H}(2^{p-1}) + \mathbb{C}_{\widetilde{L}_{2,2}^{-1}}(2^{p-1}) + \mathbb{C}_{\widetilde{\phi}}(2^{p-1}). \end{aligned} \tag{37}$$

Consequently, according to the steps in Section 3.2 and (30), as well as (32)–(37), the *total computational complexity* $\mathbb{C}_{\widetilde{R}_{\text{new}}^{-1}}(2^p)$ for our new scheme in one dyadic recursion to solve $\widetilde{R}_{2^p}^{-1}$ can be calculated as

$$\begin{aligned} \mathbb{C}_{\widetilde{R}_{\text{new}}^{-1}}(2^p) &= \mathbb{C}_{\widetilde{L}^{-1}}(2^p) + \frac{2^p(2^p-1)(2^{p+1}-1)}{6} \\ &= \frac{11(8^p) - 18(4^p) + 8(2^p)}{16}. \end{aligned} \tag{38}$$

4.3. Computational Complexities for Sequential Rank-Adaptive Hermitian Matrix Inversions. From the studies in Sections 4.1 and 4.2, we have found that the asymptotical complexity ratio

$$\begin{aligned} \lim_{p\to\infty} \frac{\mathbb{C}_{\widetilde{R}_{\text{Chol}}^{-1}}(2^p)}{\mathbb{C}_{\widetilde{R}_{\text{new}}^{-1}}(2^p)} &= \lim_{p\to\infty}\left[\left(\frac{8}{3}\right)\frac{4(8^p) - 9(4^p) + 5(2^p)}{11(8^p) - 18(4^p) + 8(2^p)}\right] \\ &= \frac{32}{33} \approx 96.97\%, \end{aligned} \tag{39}$$

where $N = 2^p$. It is noted that from (39), our new dyadic recursion scheme does not possess any advantage over the conventional Cholesky method. The reason is quite obvious. The ratio presented in (39) involves the *fixed model order* for the conventional Cholesky factorization. If the model order $N = 2^m$ is predetermined as a constant, our new scheme described in Section 3.2 still needs to calculate all the intermediate matrices $\widetilde{L}_{2^p}$ and $\widetilde{L}_{2^p}^{-1}$, for all $p = 1, 2, \ldots, m$ while the conventional Cholesky factorization method does not.

However, in practice, the model order $N = 2^p$ should be variable and the sequential rank-adaptive LSE or MLR should take place. The least-square error will decrease when the model order $N = 2^p$ increases, that is, $p = 1, 2, 3, \ldots$. A *stop criterion* for the error tolerance (the maximum squared error which is allowed) can be introduced to terminate the model order enlargement. If such a *sequential rank-adaptive LSE or MLR* is considered, we need to recalculate the

corresponding computational complexities for the sequential computations of $\widetilde{R}_{2^p}^{-1}$, $p = 1, 2, 3, \ldots$. Assume that the stop criterion terminates the sequential computations of $\widetilde{R}_{2^p}^{-1}$ at $N = 2^m$. We can compute the total computational complexity $\mathbb{C}_{\widetilde{R}_{\text{Chol,seq}}^{-1}}(2^m)$ for such a sequential procedure using the conventional Cholesky factorization as

$$\begin{aligned}\mathbb{C}_{\widetilde{R}_{\text{Chol,seq}}^{-1}}(2^m) &= \sum_{p=1}^{m} \mathbb{C}_{\widetilde{R}_{\text{Chol}}^{-1}}(2^p) \\ &= \frac{16}{21}(8^m) - 2(4^m) + \frac{5}{3}(2^m) - \frac{3}{7}.\end{aligned} \tag{40}$$

On the other hand, if our new dyadic recursion scheme is used for the sequential calculations of $\widetilde{R}_{2^p}^{-1}$ up to $N = 2^m$, the corresponding computational complexity is

$$\begin{aligned}\mathbb{C}_{\widetilde{R}_{\text{new,seq}}^{-1}}(2^m) &= \mathbb{C}_{\widetilde{L}^{-1}}(2^m) + \sum_{p=1}^{m} \frac{1}{3}(8^p) - \frac{1}{2}(4^p) + \frac{1}{6}(2^p) \\ &= \frac{247}{336}(8^m) - \frac{31}{24}(4^m) + \frac{2}{3}(2^m) - \frac{1}{21},\end{aligned} \tag{41}$$

where $\mathbb{C}_{\widetilde{L}^{-1}}(2^m)$ is given by (37). Similarly, we may rederive the complexity ratio for the sequential calculations such that

$$\begin{aligned}&\lim_{m\to\infty} \frac{\mathbb{C}_{\widetilde{R}_{\text{Chol,seq}}^{-1}}(2^m)}{\mathbb{C}_{\widetilde{R}_{\text{new,seq}}^{-1}}(2^m)} \\ &= \lim_{m\to\infty} \frac{(16/21)(8^m) - 2(4^m) + (5/3)(2^m) - (3/7)}{(247/336)(8^m) - (31/24)(4^m) + (2/3)(2^m) - (1/21)} \\ &= \frac{256}{247} \approx 103.64\%.\end{aligned} \tag{42}$$

5. Applications of Sequential Rank-Adaptive Hermitian Matrix Inversions for Channel Estimation and Equalization

Based on the sequential rank-adaptive Hermitian matrix inversion approach in Section 4.3, we can design a new communication channel estimation and equalization scheme with model order adaptability. Other similar applications can be easily extended using our efficient dyadic Hermitian matrix inversion algorithm in Section 3.2. Here, we introduce this proposed new channel estimation and equalization method using our dyadic recursion for adjusting the model order.

A basic transmission model for communication systems can be formulated as

$$r(n) = s(n) \otimes h(n) + \xi(n), \quad n = 0, 1, \ldots, M' - 1, \tag{43}$$

where $\otimes$ denotes the linear convolution; $s(n)$, $r(n)$, $h(n)$, and $\xi(n)$ represent the transmitted training sequence, the received signal, the channel impulse response, and the background noise, respectively; M' is the sample size. Without loss of generality, the *windowing* of observed input data is assumed to comply with the *covariance* method [22]. For the *channel estimation* problem, the multiple time series can be set as

$$\begin{aligned}&x_i(n) \equiv s(n - i + 1), \\ &n = N - i, \\ &N - i + 1, \ldots, M' - i, \quad i = 1, 2, \ldots, N,\end{aligned} \tag{44}$$

where $x_1(n) \equiv s(n)$ and N is the *estimated channel filter length*. Thereby, the desired response is the received signal such that

$$d(n) \equiv r(n + N - 1), \quad n = 0, 1, \ldots, M' - N. \tag{45}$$

On the other hand, for the *equalization* problem, the multiple time series are set as

$$\begin{aligned}&x_i(n) \equiv r(n - i + 1), \\ &n = N - i, \\ &N - i + 1, \ldots, M' - i, \quad i = 1, 2, \ldots, N,\end{aligned} \tag{46}$$

where $x_1(n) \equiv r(n)$ and N is the *estimated equalizer length*. The desired response is therefore the transmitted training signal instead such that

$$d(n) \equiv s(n + N - 1), \quad n = 0, 1, \ldots, M' - N. \tag{47}$$

According to (43), we can acquire the data specified by (44) and (45) for channel estimation and that specified by (46) and (47) for equalization. Thus, setting $M \equiv M' - N + 1$, we can carry out $\widetilde{R}_N$, $\widetilde{P}_N$, $\vec{w}_{\text{opt}}$, σ_{opt}^2 according to (5)–(8). Note that the least mean-squared error σ_{opt}^2 given by (8) is a function of both M and N, and hence we can write

$$\sigma_{\text{opt}}^2 = \sigma_{\text{opt}}^2(M, N). \tag{48}$$

For a fixed sample size M, we can increase the model order N. For a sufficiently large N, we may achieve the *error floor* such that

$$\sigma_{\text{opt}}^2(M, N) \approx \sigma_{\text{opt}}^2(M, N + k), \quad \forall k \in \mathcal{N}. \tag{49}$$

We can design a simple threshold criterion to determine the minimum model order $N_{\min}$ for satisfying the condition in (49). For the dyadic model order adaptation, we propose a stop criterion

$$J(N) = \frac{\left|\sigma_{\text{opt}}^2(M, N) - \sigma_{\text{opt}}^2(M, 2N)\right|}{\sigma_{\text{opt}}^2(M, N)}. \tag{50}$$

Therefore, given a predetermined threshold τ_J, the minimum model order $N_{\min}$ for the dyadic adaptation is obtained as

$$N_{\min} = \inf_{N \in S_J} N, \tag{51}$$

where

$$S_J \equiv \{N \in \mathcal{N} : J(N) \le \tau_J\}, \tag{52}$$

and inf denotes the infimum operation [29]. Ultimately, we can apply (5)–(8) and (50)-(51) to build a sequential rank-adaptive LSE or MLR procedure which is capable of adapting the model order dyadically.

6. Numerical Evaluations

In this section, we would like to provide the numerical evaluations for the illustrations of the computational complexities associated with the two Hermitian matrix inversion algorithms (conventional Cholesky factorization and our new efficient dyadic recursion) and the LSE applications using the adaptive model order for channel equalization. Table 1 lists the comparison of the two methods for a few model orders. It is noted that when a Hermitian matrix inversion is carried out for a fixed model order, the conventional Cholesky factorization approach is more computationally efficient than our new dyadic recursion. However, in comparison of the total computational complexity for the sequential calculation of variable model order Hermitian matrix inversion, our new dyadic recursion is more efficient than the conventional Cholesky factorization when the same terminal model order is set, since the latter does not utilize any information from the previous calculation of the Hermitian inversion with a smaller model order.

6.1. Comparison of Computational Complexities. Figures 1 and 2 illustrate the total computational complexities in terms of complex multiplications for the Hermitian matrix inversion using the conventional Cholesky factorization and our new dyadic recursion method; they depict the complexities versus the model order for the fixed model order (one-time LSE or MLR) and the variable model order (sequential rank-adaptive LSE or MLR). According to Figures 1 and 2, it is clear that our dyadic recursion algorithm is more efficient than the conventional Cholesky factorization for sequent LSE (MLR) and vice versa. The computational complexity margin ratios in between for the two situations are also depicted in Figure 3. The *asymptotical complexity margin ratios* of around ±3% derived in (39) and (42) can be observed therein.

6.2. Sequential Rank-Adaptive LSE for Channel Equalization. Next, we would like to present some simulations for illustrating the application of our proposed sequential rank-adaptive Hermitian matrix inversions for channel equalization as discussed in Section 5. Assume that the modulation type of the transmitted signal is BPSK and the channel noise is additive white Gaussian noise (AWGN). The channel transfer function is arbitrarily chosen as $H(z) = 0.58 + 0.56z^{-1} + 0.55z^{-2} - 0.18z^{-3} - 0.12z^{-4}$, where the *channel gain* is normalized as unity such that $\sum_n |h(n)|^2 = 1$, and it complies with the LOS (light-of-sight) channel model such that the leading coefficient is the largest among all in magnitude. The received signals are generated by the computer using (43). The signal sample size is $M = 500$.

We carry out 200 Monte Carlo trials with randomly generated AWGN (various signal-to-noise ratios from 0 to 30 dB) and the aforementioned transmission model. The least mean-squared errors σ^2_{opt} on average are calculated using (8). Here, we compare three schemes, namely (i) one-time Hermitian matrix inversion using the Cholesky factorization with the fixed model order $N = 12$ (specified as "fixed $N = 12$"), (ii) one-time Hermitian matrix inversion using the Cholesky factorization with the fixed model order $N = 25$ (specified as "fixed $N = 25$"), and (iii) sequential rank-adaptive Hermitian matrix inversion using our proposed dyadic recursion with variable model order (specified as "Variable Model Order"). Two different threshold values are employed, namely $\tau_J = 1/200, 1/30$. It is noted that the

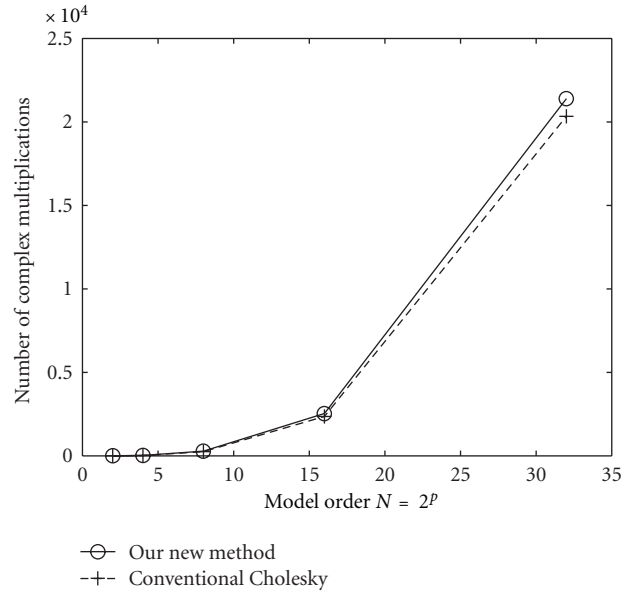

Figure 1: Computational complexity comparison (model order $N = 2^p$ is fixed for one-time LSE or MLR) for Hermitian matrix inversion using conventional Cholesky factorization ($\mathbb{C}_{\tilde{R}^{-1}_{\text{Chol}}}(N)$) and our proposed new dyadic recursion ($\mathbb{C}_{\tilde{R}^{-1}_{\text{new}}}(N)$).

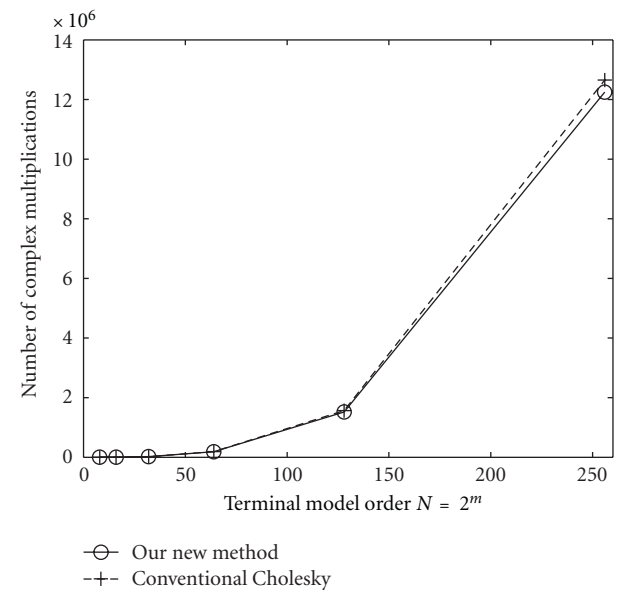

Figure 2: Computational complexity comparison (accumulated complexity for the sequential rank-adaptive LSE or MLR with terminal model order $N = 2^m$) for Hermitian matrix inversion using conventional Cholesky factorization ($\mathbb{C}_{\tilde{R}^{-1}_{\text{Chol,seq}}}(N)$) and our proposed new dyadic recursion ($\mathbb{C}_{\tilde{R}^{-1}_{\text{new,seq}}}(N)$).

Table 1: Computational complexities of hermitian matrix inversion algorithms in comparison.

$\mathbb{C}_{\tilde{R}^{-1}_{\text{chol}}}(N), \mathbb{C}_{\tilde{R}^{-1}_{\text{new}}}(N), \mathbb{C}_{\tilde{R}^{-1}_{\text{chol, seq}}}(N), \mathbb{C}_{\tilde{R}^{-1}_{\text{new, seq}}}(N)$	$N = 2^1$	$N = 2^2$	$N = 2^4$	$N = 2^6$
Conventional cholesky factorization (fixed model order)	1	22	2360	168672
Dyadic recursion (fixed model order)	2	28	2536	175648
Conventional cholesky factorization (variable model order)	1	23	2635	191643
Dyadic recursion (variable model order)	2	30	2691	187459

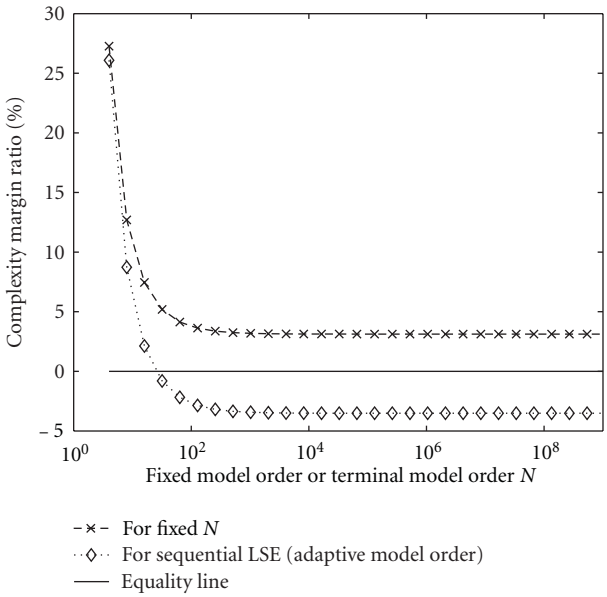

Figure 3: Computational complexity margin ratio versus model order N (fixed model order: $(\mathbb{C}_{\tilde{R}^{-1}_{\text{new}}}(N) - \mathbb{C}_{\tilde{R}^{-1}_{\text{Chol}}}(N))/(\mathbb{C}_{\tilde{R}^{-1}_{\text{Chol}}}(N))\%$, variable model order: $(\mathbb{C}_{\tilde{R}^{-1}_{\text{new,seq}}}(N) - \mathbb{C}_{\tilde{R}^{-1}_{\text{Chol,seq}}}(N))/(\mathbb{C}_{\tilde{R}^{-1}_{\text{Chol,seq}}}(N))\%$, equality line is for the margin ratio = 0%; N is the fixed or the terminal model order therein).

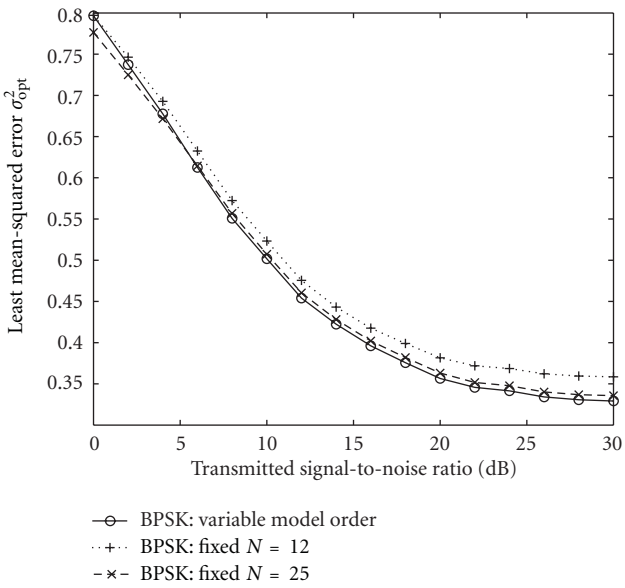

Figure 4: Various least mean-squared errors σ^2_{opt} versus signal-to-noise ratio (the threshold for our variable model scheme is $\tau_J = 1/200$).

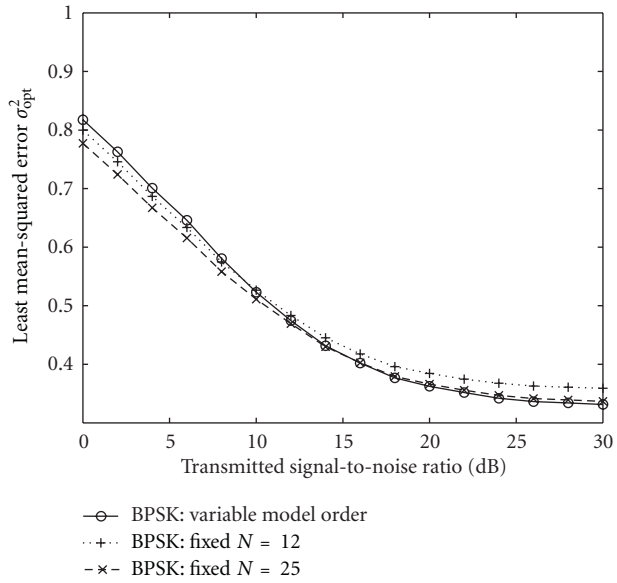

Figure 5: Various least mean-squared errors σ^2_{opt} versus signal-to-noise ratio (the threshold for our variable model scheme is $\tau_J = 1/30$).

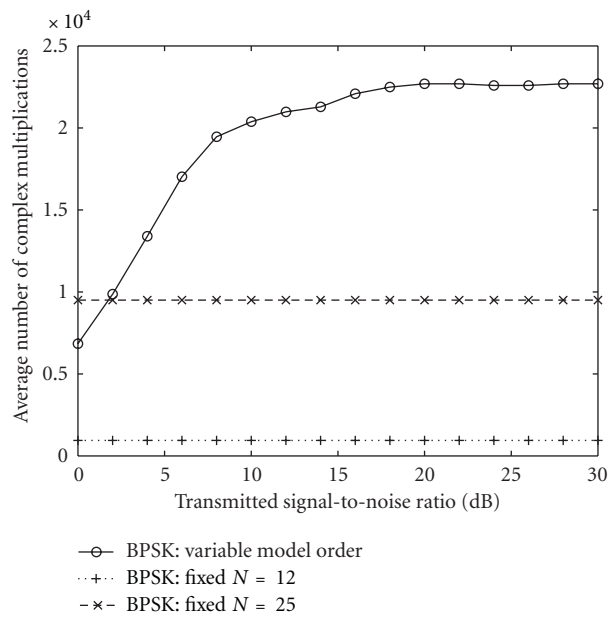

Figure 6: The corresponding computational complexities to Figure 4 versus signal-to-noise ratio (the threshold for our variable model scheme is $\tau_J = 1/200$).

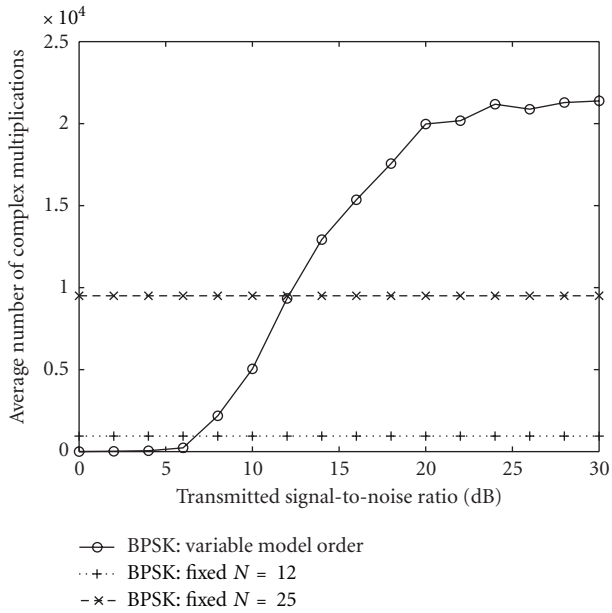

Figure 7: The corresponding computational complexities to Figure 5 versus signal-to-noise ratio (the threshold for our variable model scheme is $\tau_J = 1/30$).

allowed maximum model order for our dyadic recursion scheme is defaulted as $\lfloor (N - M + 1)/10 \rfloor$, where $\lfloor \quad \rfloor$ is the flooring operator.

Figures 4–7 show the simulation results. According to Figures 4 and 5, our proposed new dyadic recursion method achieves the smallest least mean-squared errors most of time especially for low threshold values. The trade-off of our scheme is the increased average computational complexities, which are shown in Figures 6 and 7. From Figures 6 and 7, it can be observed that we may save a huge computational burden for a bad channel condition (low signal-to-noise ratio) for a very slight equalization quality deterioration. According to Figures 1–7, we can justify that our dyadic recursion algorithm is more efficient than the conventional Cholesky factorization in the Hermitian matrix inversion for the sequential rank-adaptive LSE or MLR. Besides, the sequential rank-adaptive LSE or MLR with variable model orders using our recursion scheme can also seek the trade-off between the estimation performance and the required computational complexity.

7. Conclusion

Hermitian matrix inversion is the pivotal computation for least-square estimation and multiple-parameter linear regression. Conventional Cholesky factorization can be applied for one-time LSE and MLR with a predetermined fixed model order. In this paper, we decompose any Hermitian matrix into submatrices with a half of the original dimension and derive the new dyadic recursion algorithm for the Hermitian matrix inversion accordingly. Moreover, for the theoretical comparison, we elaborate the computational complexity analyses to derive the asymptotical complexity ratios for the Hermitian matrix inversion using the conventional Cholesky factorization and our new dyadic recursion scheme. We show that our new method can achieve the complexity margin ratio of −3.03% for the sequential rank-adaptive Hermitian matrix inversions and that of +3.64% for the one-time Hermitian matrix inversion over the conventional Cholesky factorization method. We also present the applications of the sequential rank-adaptive LSE with variable model order using our new dyadic recursion procedure for channel estimation and equalization in telecommunications. Our proposed new variable model order LSE scheme can seek the trade-off between the estimation performance and the computational complexity.

Acknowledgments

This work was supported by Information Technology Research Award for National Priorities (NSF-ECS 0426644) from National Science Foundation, Faculty Research Initiation Award from the Southeastern Center for Electrical Engineering Education, Research Enhancement Award from the Louisiana-NASA Space Consortium and Faculty Research Award from Louisiana State University.

References

[1] Y. Zhou, S. C. Huang, and M. Bergsneider, "Linear ridge regression with spatial constraint for generation of parametric images in dynamic positron emission tomography studies," *IEEE Transactions on Nuclear Science*, vol. 48, no. 1 I, pp. 125–130, 2001.

[2] Y. Zhou, S. C. Huang, and Y. I. Hser, "Generalized ridge regression versus simple ridge regression for generation of kinetic parametric images in PET," in *Proceedings of IEEE Nuclear Science Symposium*, vol. 3, pp. 1551–1555, 1999.

[3] B. J. Park, W. Pedrycz, and S. K. Oh, "Identification of fuzzy models with the aid of evolutionary data granulation," *IEE Proceedings: Control Theory and Applications*, vol. 148, no. 5, pp. 406–418, 2001.

[4] C. K. Mai, I. V. M. Krishna, and A. V. Reddy, "Polyanalyst application for forest data mining," in *Proceedings of IEEE International Geoscience and Remote Sensing Symposium (IGARSS '05)*, vol. 2, pp. 756–759, July 2005.

[5] G. N. Fouskitakis, "Pseudolinear estimation of fractionally integrated ARMA (ARFIMA) models with automotive application," *IEEE Transactions on Signal Processing*, vol. 47, no. 12, pp. 3365–3380, 1999.

[6] G. Sebastiani, F. Godtliebsen, R. A. Jones, O. Haraldseth, T. B. Müller, and P. A. Rinck, "Analysis of dynamic magnetic resonance images," *IEEE Transactions on Medical Imaging*, vol. 15, no. 3, pp. 268–277, 1996.

[7] L. Szczecinski, "Low-complexity search for optimal delay in linear FIR MMSE equalization," *IEEE Signal Processing Letters*, vol. 12, no. 8, pp. 549–552, 2005.

[8] T. Walzman and M. Schwartz, "Automatic equalization using the discrete frequency domain," *IEEE Transactions on Information Theory*, vol. 19, no. 1, pp. 59–68, 1973.

[9] D. K. Kim and P. G. Park, "Adaptive self-orthogonalizing pertone decision feedback equalizer for single carrier modulations," *IEEE Signal Processing Letters*, vol. 13, no. 1, pp. 21–24, 2006.

[10] F. Pancaldi and G. M. Vitetta, "Frequency-domain equalization for space-time block-coded systems," *IEEE Transactions on Wireless Communications*, vol. 4, no. 6, pp. 2907–2916, 2005.
[11] F. Pancaldi and G. M. Vitetta, "Block channel equalization in the frequency domain," *IEEE Transactions on Communications*, vol. 53, no. 3, pp. 463–471, 2005.
[12] F. Pancaldi and G. M. Vitetta, "Block equalization techniques in the frequency domain," in *Proceedings of IEEE Wireless Communications and Networking Conference (WCNC '04)*, vol. 4, pp. 2295–2300, 2004.
[13] J. G. Proakis, *Digital Communications*, McGraw-Hill, 4th edition, 2001.
[14] J. Salz, "Optimal mean-square decision feedback equalization," *Bell System Technical Journal*, vol. 52, no. 8, pp. 1341–1373, 1973.
[15] Y. Kojima, K. Takeda, and F. Adachi, "Polynomial prediction RLS channel estimation for DS-CDMA frequency-domain equalization," in *Proceedings of IEEE 70th Vehicular Technology Conference Fall (VTC '09) Fall*, pp. 1–5, September 2009.
[16] F. Chen, S. Kwong, and C. W. Kok, "Blind MMSE equalization of FIR/IIR channels using oversampling and multichannel linear prediction," *ETRI Journal*, vol. 31, no. 2, pp. 162–172, 2009.
[17] X. Huang and H. C. Wu, "Robust and efficient intercarrier interference mitigation for OFDM systems in time-varying fading channels," *IEEE Transactions on Vehicular Technology*, vol. 56, no. 5 I, pp. 2517–2528, 2007.
[18] H. C. Wu and Y. Wu, "Distributive pilot arrangement based on modified M-sequences for OFDM intercarrier interference estimation," *IEEE Transactions on Wireless Communications*, vol. 6, no. 5, pp. 1605–1609, 2007.
[19] H. C. Wu and Y. Wu, "A new ICI matrices estimation scheme using hadamard sequence for OFDM systems," *IEEE Transactions on Broadcasting*, vol. 51, no. 3, pp. 305–314, 2005.
[20] K. D. Concannon and W. J. Thompson, "Regression lines: more than meets the eye," *Computing in Science and Engineering*, vol. 2, no. 4, pp. 78–81, 2000.
[21] G. H. Golub and C. F. V. Loan, *Matrix Computations*, John Hopkins University Press, 2nd edition, 1991.
[22] S. Haykin, *Adaptive Filter Theory*, Prentice-Hall, 4th edition, 2001.
[23] S. M. Kay, *Modern Spectrum Estimation, Theory and Application*, Prentice-Hall, 1987.
[24] R. Yu, X. Lin, and C. C. Ko, "A multi-stage levinson-durbin algorithm," in *Proceedings of the 36th Asilomar Conference on Signals Systems and Computers*, vol. 1, pp. 218–221, usa, November 2002.
[25] L. M. Lee and H. C. Wang, "An extended Levinson-Durbin algorithm for the analysis of noisy autoregressive process," *IEEE Signal Processing Letters*, vol. 3, no. 1, pp. 13–15, 1996.
[26] B. Farhang-Boroujeny, *Adaptive Filters*, Wiley, 2003.
[27] I. F. Gustavson and I. Jonsson, "Minimal-storage high-performance Cholesky factorization via blocking and recursion," *IBM Journal of Research and Development*, vol. 44, no. 6, pp. 823–850, 2000.
[28] B. S. Andersen, J. Waśniewski, and F. G. Gustavson, "A recursive formulation of Cholesky factorization of a matrix in packed storage," *ACM Transactions on Mathematical Software*, vol. 27, no. 2, pp. 214–244, 2001.
[29] H. L. Royden, *Real Analysis*, Prentice-Hall, 3rd edition, 1988.

Hindawi Publishing Corporation
International Journal of Antennas and Propagation
Volume 2012, Article ID 184682, 6 pages
doi:10.1155/2012/184682

Research Article

Geometry-Based Stochastic Modeling for MIMO Channel in High-Speed Mobile Scenario

Binghao Chen and Zhangdui Zhong

State Key Laboratory of Rail Traffic Control and Safety, Beijing Jiaotong University, Beijing 100044, China

Correspondence should be addressed to Binghao Chen, bhchendo@gmail.com

Received 21 July 2012; Accepted 29 September 2012

Academic Editor: Ai Bo

The geometry-based stochastic channel models are proposed in this paper for the terrain cutting, suburb, and urban scenarios in high-speed railway. First, the special scenarios in high-speed railway are described. And the channel models based on the geometry scenarios are introduced. Some channel parameters are based on measurement data. Then, the space-time correlation functions in analytical form are obtained in suburb and urban scenarios. Finally, the space correlation characteristics in three scenarios are compared.

1. Introduction

High-speed railway is playing an important role in the transportation of China. The wireless train control system is essential for the train management and safety. The train control system CTCS3 (Chinese Train Control System) based on GSM-R (Global System for Mobile Communication Railway) is applied to the train with the speed above 300 km/h. There is a rising demand to transmit large amount of data for the train safety and passenger service. So the wireless communication system will have an evolution from narrowband to wideband in the future. However, the frequency bandwidth allocated for the railway is limited. Therefore, the MIMO (Multiple-input Multiple-output) technique can be used in railway for it can enhance the channel capacity without additional bandwidth.

It is reported that the MIMO system performance strongly depends on the propagation environment. The scenarios in high-speed railway, such as viaduct and cutting, are special and different from those in commercial cellar communication. So the spatial channel should be studied well before the MIMO application. Some pathloss and channel characteristics in high-speed railway have been discussed in literatures. Wei et al. in [1] give an analysis of the pathloss in viaduct and plain scenarios based on the measurement data of Zhengzhou-Xi'an passenger dedicated line with the maximum speed of 340 km/h. Two modified pathloss models are proposed and compared with Hata model. The Ricean K factors in viaduct and cutting scenarios are estimated in [2] based on the same measurement campaign. Lu et al. in [3] investigate the fitted pathloss model, shadow fading, and dynamic range of small-scale fading in viaduct and terrain cutting, which shows that the propagation environment of terrain cutting is worse than viaduct. The channel characteristics in high-speed railway for communication links based on Orthogonal Frequency Division Multiplexing (OFDM) are investigated in [4] using the ray-tracing tool. It seems that the researches mainly focus on the large-scale parameters and seldom refer to the small-scale channel characteristics and much less a MIMO channel model in high-speed railway. The geometry-based stochastic channel model (GSCM) is widely used in MIMO channel modeling [5]. The GSCM models can be classified into the regular-shaped GSCMs (RS-GSCMs) and irregular-shaped GSCMs (IS-GSCMs) [6]. It depends on whether the effective scatterers distribute on a regular shape, for example, one-ring, two-ring, and ellipses or an irregular shape determined by the environment. RS-GSCMs are mathematically tractable and used for theoretical analysis. However, the IS-GSCM can easily handle the nonstationarity

of mobile channel. Both the RS-GSCM and IS-GSCM models have been researched in Vehicle-to-Vehicle (VTV) scenario. In [7], a GSCM combining two-ring and one ellipse is proposed for mobile-to-mobile (M2M) scenario to study the space-time-frequency correlation, which is also the first model to take the vehicular traffic density into account. Then it is extended to a 3D M2M Ricean model [8]. And a wideband MIMO M2M model is proposed in [9]. It is assumed the scatterers are distributed in a set of concentric cylinders around the TX and RX. An IS-GSCM of VTV is proposed in [10], and the scatterers are distributed according to the environment geometry. A novel unified channel model for cooperative MIMO communication scenario is proposed in [11] with the ability to investigate the impact of the local scattering density on channel characteristics. Both the terminals in VTV and high-speed railway have a high speed, but the channel characteristics are different. In this paper, RS-GSCM and IS-GSCM are used to model the channels in terrain cutting, suburb, and urban scenarios.

The rest of this paper is organized as follows. The cutting scenario and the corresponding channel model are described in Section 2. The GSCMs in suburb and urban scenarios and the space-time correlation functions are introduced in Section 3. The simulations and compared results are shown in Section 4. Finally, Section 5 is the conclusion.

2. The Cutting Channel Model

2.1. Scenario Description. The terrain cutting scenario is shown in Figure 1. There are two slopes along the track. The height of the slope is about 13-14 m. The angle of inclination is 35–40 degrees. And the distance between the two slopes is 12-13 m. The slope is composed of concrete and stone with some grass on the surface.

2.2. Channel Model for Cutting Scenario. Based on the structure of cutting scenario, the channel model geometry is shown in Figure 2. The Base Stations (BSs) are built along the track. The distance between two BSs is about 3 km. The BS is 10 to 30 m away from the track. The height of BS tower is about 30 m. And the BS is built outside the cutting. The BS antennas face two directions along the track. Only the vertically polarized pattern field is considered. And the train antenna is 4.5 m high. The train is moving towards the BS. Only one BS is considered in simulation of this scenario.

The fitted pathloss model for cutting scenario is expressed as [3]:

$$\mathrm{PL}_{\mathrm{cutting}}\,(\mathrm{dB}) = 71.83 + 43\log_{10}\left(\frac{d}{100}\right) + X_{\sigma}. \qquad (1)$$

The pathloss exponent $n = 4.3$. d is the distance between the BS and the train. X_{σ} is a zero-mean Gaussian random variable (in dB) with standard deviation 3.5 dB.

The scatterers are assumed to distribute uniformly on the surface of the two slopes with a density χ_{DI}, stating the number of scatterers per meter. First, the scatterers can be generated in the x-y plane. The x coordinates of the scatterers follow the uniform distribution, that is, $x_s \sim U[x_{\min}, x_{\max}]$.

Figure 1: The cutting scenario in high-speed railway.

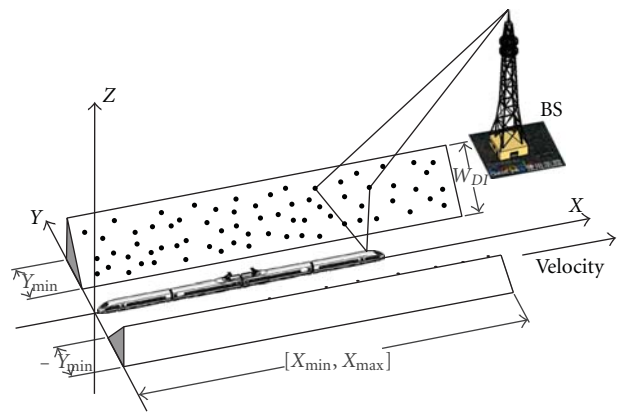

Figure 2: The channel model in terrain cutting.

And the y coordinates in two semiaxis parts are $y_s \sim U[y_{\min}, y_{\min} + W_{DI}]$ and $y_s \sim U[-y_{\min} - W_{DI}, -y_{\min}]$, where W_{DI} is the width of the slope area. Then the plane can be rotated to the angle of inclination to form the cutting slope.

The complex path gain of a diffuse scattering component in this GSCM is modeled as [10]:

$$a_s = G_{0,DI}^{1/2} \cdot c_s \cdot \left(\frac{d_{\mathrm{ref}}}{d_{T\to r} \times d_{r\to R}}\right)^{n_{DI}/2}, \qquad (2)$$

where c_s is the zero mean complex Gaussian variable. n_{DI} and $G_{0,DI}$ are pathloss exponent and the reference power, respectively. It is assumed that n_{DI} and $G_{0,DI}$ are the same for all diffuse scatterers. Only single-bounce path in this channel is considered. Since the slope is higher than the antenna on top of the train. Therefore, the power of paths from outside the cutting are neglected. In every time instant, the distance between the BS and the train is calculated. So are the distance from the BS to the scatterer and the distance from the scatterer to the train. The Angle-of-Arrival (AoA) and Angle-of-Departure (AoD) are considered in three dimensions.

The channel is composed of Line-of-Sight (LOS) part and NLOS part, that is, the contribution from the diffuse scatterers in the environment. The three-dimensional

double-directional channel impulse response for the diffuse components is expressed as:

$$H_s = \sum_{m=1}^{M} a_s \cdot \exp(j\Phi_m) \cdot \exp\left(jd_s \frac{2\pi}{\lambda} \overline{r}_s \cdot \overline{\Phi}_m\right) \cdot \exp\left(jd_u \frac{2\pi}{\lambda} \overline{r}_u \cdot \overline{\Psi}_m\right) \cdot \exp(j2\pi v_m t), \tag{3}$$

where M is the total number of diffuse paths. Φ_m is the random phase for each path and $\Phi \sim U[0, 2\pi]$. d_s, and d_u are the antenna spacing for the transmitter and receiver, respectively. λ is the carrier wavelength. The scalar product is defined as [12]:

$$\overline{r}_s \cdot \overline{\Phi}_m = x_s \cos\gamma_m \cos\phi_m + y_s \cos\gamma_m \sin\phi_m + z_s \sin\gamma_m, \tag{4}$$

where $\overline{r}_s$ is location vector of BS array element. x_s, y_s, z_s are the coordinates of $\overline{r}_s$ to x, y, and z-axis, respectively. $\overline{\Phi}_m$ is departure angle unit vector. ϕ_m and γ_m are the departure azimuth angle and departure elevation angle of the path m. And the scalar product $\overline{r}_u \cdot \overline{\Psi}_m$ is defined in the same way.

And v_m is Doppler frequency for each path. The train is running along the track, so the Doppler Effect is considered in x-y plane. v_m is written as [12]

$$v_m = \frac{\overline{v} \cdot \overline{\Psi}}{\lambda} = \frac{|v| \cos\theta_v \cos\gamma_m \cos\phi_m + |v| \sin\theta_v \cos\gamma_m \sin\phi_m}{\lambda}, \tag{5}$$

where θ_v is the mobile moving direction.

3. Channel Models for Suburb and Urban

The suburb and urban scenarios are kind of similar to those in commercial cell. So the RS-GSCM is used to model the channel in each scenario. Considering the narrowband system GSM-R used in high-speed railway, the spherical MIMO channel model is applied, which is appropriate for narrowband fading channel [13]. Also, the LOS and NLOS paths are considered separately.

The LOS case for 2×2 MIMO channel model is shown in Figure 3. And the train is in the center of the scatterer sphere.

In the channel model, D is the distance between BS and the train. R is the radius of the sphere and related to the delay spread in this scenario. According to the real case, it is assumed $D \gg R$. δ_{pq} and d_{lm} are the antenna spacing for BS and the train, with the antenna azimuth angles a_{pq} and β_{lm}, respectively. For ease of description, the distance between two points a and b is written as ξ_{ab}. The AoA ϕ_T^U and elevation angle of LOS path in train side can be obtained through simple geometrical calculation.

In NLOS case, the scatterers are located in a spherical surface around the train. It is assumed that only one-bounce scattering occurs. The scatterers locations are described by two random variables, that is, the azimuth AoA ϕ_i^U and the elevation angle from scatterers β.

The von Mises distribution [14] is used to describe the azimuth angle ϕ_i^U. The PDF (Probability Density Function) is written as

$$f\left(\phi^U\right) = \frac{\exp[\kappa \cos(\phi^U - \mu)]}{2\pi I_0(\kappa)}, \quad \phi^U \in [-\pi, \pi), \tag{6}$$

where $\mu \in [-\pi, \pi)$ is the mean angle of the paths from the scatterers. The parameter κ controls the spread around the mean angle. $I_0(\cdot)$ is the zero-order-modified Bessel function of the first kind.

The distribution of elevation angle from scatterers β is defined as [15]

$$f(\beta) = \begin{cases} \dfrac{\pi}{4|\beta|} \cos\left(\dfrac{\pi\beta}{2\beta_m}\right), & |\beta| \le |\beta_m| \le \dfrac{\pi}{2} \\ 0, & \text{otherwise}, \end{cases} \tag{7}$$

where β_m is the maximum elevation angle.

According to the definition of correlation function in [14], the space-time cross correlation between two arbitrary communication links $h_{lp}(t)$ and $h_{mq}(t)$ is expressed as

$$\rho_{lp,mq}(\tau, t) = \frac{E\left[h_{lp}(t) h_{mq}^*(t+\tau)\right]}{\sqrt{E\left[\left|h_{lp}(t)\right|^2\right] \cdot E\left[\left|h_{mq}(t)\right|^2\right]}}. \tag{8}$$

By referring to the assumptions above and skipping some geometrical and algebra manipulations, the LOS and NLOS space-time correlation functions can be written as:

$$\begin{aligned}
\rho_{lp,mq}^{\text{LOS}}(\tau) = {} & \frac{K}{K+1} \times \exp\left[jc_{pq} \frac{\cos\left(a_{pq}\right)}{\cos\beta} + jb_{lm} \frac{\cos(\phi^U - \beta_{lm})}{\cos\beta} - ja\cos\left(\phi^U - \gamma\right)\right] \\
\rho_{lp,mq}^{\text{DIF}}(\tau) = {} & \frac{1}{K+1} \cdot \frac{\pi}{4I_0(\kappa)|\beta_m|} \cdot \exp\left[\frac{jc_{pq}\cos\left(a_{pq}\right)}{\cos\beta_T}\right] \\
& \cdot \int_{-\beta_m}^{\beta_m} \cos\frac{\pi(\beta - \beta_T)}{2\beta_m} \\
& \cdot I_0\left(\left\{\kappa^2 - a^2 - \frac{b_{lm}^2}{\cos^2\beta} - \frac{c_{pq}^2 \Delta^2 \sin^2 a_{pq} \cos^2\beta}{\cos^2\beta_T} + \frac{2ab_{lm}\cos(\beta_{lm} - \gamma)}{\cos\beta} + \frac{2c_{pq}\Delta \sin a_{pq} \cos\beta}{\cos\beta_T} \cdot \left[a\sin\gamma - b_{lm}\frac{\sin\beta_{lm}}{\cos\beta}\right] - j2\kappa\left[a\cos(\mu - \gamma) - \frac{b_{lm}}{\cos\beta} \cdot \cos(\mu - \beta_{lm}) - \frac{c_{pq}\Delta \sin\left(a_{pq}\right)\sin\mu \cdot \cos\beta}{\cos\beta_T}\right]\right\}^{1/2}\right) d\beta,
\end{aligned} \tag{9}$$

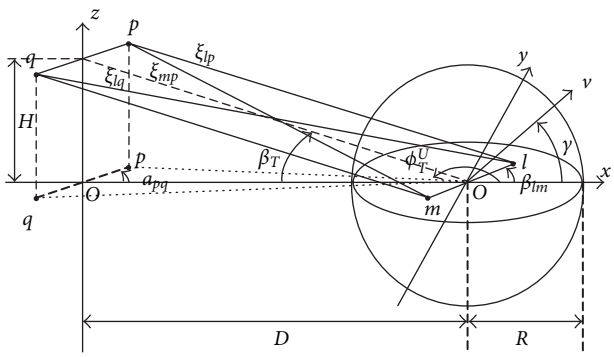

Figure 3: The 2×2 MIMO channel model with LOS path.

where $a = 2\pi f_D \tau$, $b_{lm} = 2\pi d_{lm}/\lambda$, and $c_{pq} = 2\pi\delta_{pq}/\lambda$. K is the Ricean factor, defined as the ratio of the LOS component power to the diffuse components power. f_D is the maximum Doppler frequency shift.

Finally, the total space-time cross correlation function $\rho_{lp,mq}$ is obtained by combining the (9):

$$\rho_{lp,mq}(\tau) = \rho_{lp,mq}^{\mathrm{LOS}}(\tau) + \rho_{lp,mq}^{\mathrm{DIF}}(\tau). \tag{10}$$

4. Simulation Results

4.1. Simulation of Cutting Channel Model. Some channel parameters are given as follows.

(i) The carrier frequency in high-speed railway is 900 MHz. So the carrier wavelength is 0.33 m. The velocity of the train is 360 km/h, equal to 100 m/s.

(ii) Both the BS and the train have two antenna elements. So it is a 2×2 MIMO link. And the broadside of antenna arrays in BS and train is along the track.

(iii) The scatterers are generated uniformly on the surface of two slopes with the density $\chi_{DI} = 2$ per meter. The pathloss exponent $n_{DI} = 3$ and the reference power $G_{0,DI} = 23$ [9].

(iv) The Ricean K factor in terrain cutting follows the log-normal distribution with the mean 0.94 dB and standard deviation 4.18 dB [2].

The model is generated in a deterministic approach. So the complex correlation coefficient in [10] is used. The correlation between two complex random variables u and v is defined as

$$\rho = \frac{E[uv^*] - E[u]E[v^*]}{\sqrt{\left(E\left[|u|^2\right] - |E[u]|^2\right)\left(E\left[|v|^2\right] - |E[v]|^2\right)}}, \tag{11}$$

where $(\cdot)^*$ is complex conjugation. The coefficient ρ denotes the space correlation between every two subchannels. The CDF (Cumulative Distribution Function) curves for different antenna spacing combinations are obtained.

According to the actual space limitation on top of the train, four combinations of BS and the train antenna spacing are chosen in the simulation. The correlation between the subchannels H_{11} and H_{22} is given in Figure 4. The curves of BS 4λ, the train λ case and BS 2λ, the train λ case are almost the same. It is shown that the antenna spacing of BS has little influence on the space correlation in railway scenario. However, when BS antenna spacing is fixed, as the train antenna spacing increases, the space correlation will change significantly.

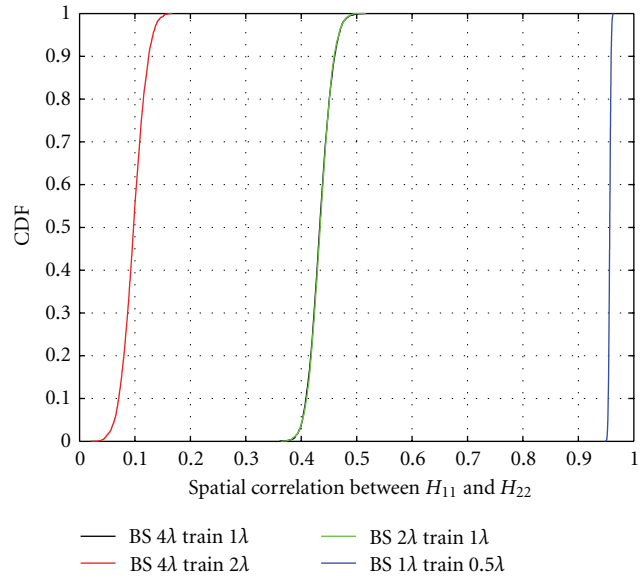

Figure 4: The space correlation in terrain cutting.

4.2. Simulation of Suburb and Urban Channel Models. The space-time correlation function is obtained using (10). The parameters of the model are set as: K (in dB) $\sim N(6.2, 2)$ [2], $D = 1000$ m, $R = 10$ m, $H = 30$ m, $\tau = 0$, $a_{pq} = 90°$, $\beta_{lm} = 90°$, the train moving direction $\gamma = 180°$, the velocity of the train $v = 360$ km/h $= 100$ m/s, $f_D = 300$ Hz. The scatterers in suburb scenario of high-speed railway are limited. Therefore, the azimuth angle distribution is more concentrated [14]. On the contrary, the scatterers in urban scenario are much richer and the AoA spread is large. So the control parameter κ for the azimuth angle spread is set as $\kappa = 3$ and $\kappa = 0$ for suburb and urban scenarios, respectively.

Figures 5 and 6 show the effect of antenna spacing on the space correlation under the two scenarios. The x- and y-axis denote the antenna spacing for the train and BS. For $\kappa = 0$, that is, the isotropic scattering, the minimum space correlation is lower than the correlation when $\kappa = 3$. It is clear that the space correlation fluctuation is decreasing when κ increases and the scattering components are getting more centralized. Therefore, the space correlation in suburb scenario is higher than that in urban area of high-speed railway under the same antenna spacing.

4.3. Space Correlations in Cutting, Suburb, and Urban. The channel modeling approach for terrain cutting is different from those in suburb and urban. So the space correlations

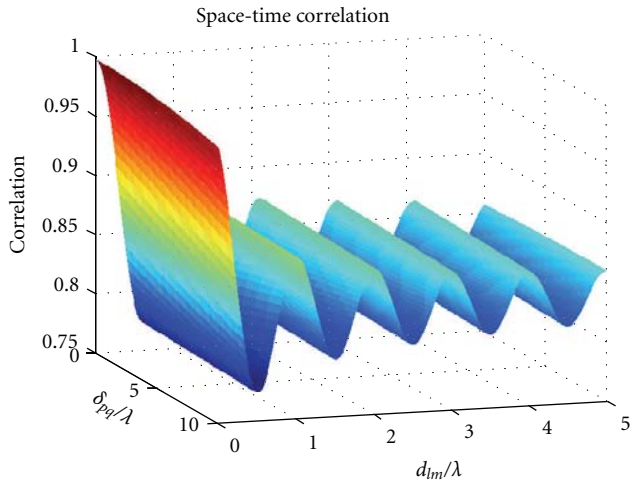

Figure 5: The space correlation when $\kappa = 0$.

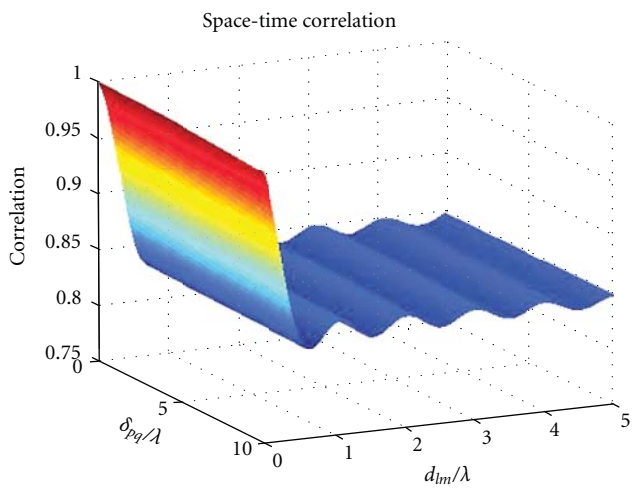

Figure 6: The space correlation when $\kappa = 3$.

in these three scenarios are compared by the means of CDF curves, which are shown in Figure 7.

In Figure 7, two antenna spacing combinations are given. When BS spacing is 1λ and the train spacing is 0.5λ, the space correlation is higher than those in suburb and urban. When BS spacing is changed into 2λ, the train spacing becomes 1λ, the space correlation changes more significantly than the other two scenarios. The reason is that the Ricean K factor in terrain cutting is much lower and has a larger change than the other two scenarios. For the cutting slope is high, there are even bridges across the cutting to block the LOS path which can be seen in Figure 1. Therefore, the diffuse components power is relatively high. So a low correlation can be obtained when the antenna spacing increases. In general, the space correlation dynamic range in terrain cutting is larger than those in the other two scenarios.

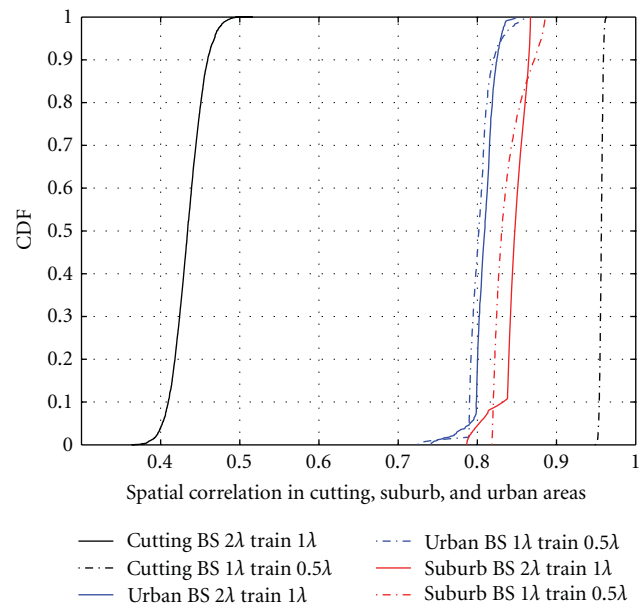

Figure 7: The CDF curves for the three scenarios.

5. Conclusions

In this paper, the MIMO channel modeling in high-speed railway is discussed including cutting, suburb, and urban scenarios. The IS-GSCM in cutting and RS-GSCM in suburb and urban scenarios are proposed. With the channel models, the space correlation coefficients in three scenarios are obtained. By comparing the simulation results, it shows that the train antenna spacing has a great impact on the space correlation. The space correlation in terrain cutting is more sensitive to the antenna spacing. And it has a greater dynamic range than the other two scenarios.

Acknowledgments

The project is supported by Program for New Century Excellent Talents in University under Grant NCET-09-0206; the National Natural Science Foundation of China under Grant 60830001; the Key Project of State Key Lab. of Rail Traffic Control and Safety under Grant RCS2011ZZ008; Program for Changjiang Scholars and Innovative Research Team in University under Grant no. IRT0949; the Project of State Key Lab. of Rail Traffic Control and Safety under Grant RCS2010ZT012; Beijing Natural Science Foundation (4112048), and "the Fundamental Research Funds for the Central Universities" under Grant nos. 2010JBZ008 and 2011YJS010.

References

[1] H. Wei, Z. Zhong, K. Guan, and B. Ai, "Path loss models in viaduct and plain scenarios of the high-speed railway," in *Proceedings of the 5th International ICST Conference on Communications and Networking in China (ChinaCom '10)*, pp. 1–5, August 2010.

[2] L. Gao, Z. Zhong, B. Ai, and L. Xiong, "Estimation of the Ricean K factor in the high speed railway scenarios," in *Proceedings of the 5th International ICST Conference on Communications and Networking in China (ChinaCom '10)*, pp. 1–5, August 2010.

[3] J. Lu, G. Zhu, and C. Briso-Rodriguez, "Fading characteristics in the railway terrain cuttings," in *Proceedings of the 73rd IEEE Vehicular Technology Conference (VTC Spring '11)*, pp. 1–5, 2011.

[4] S. Knörzer, M. A. Baldauf, T. Fügen, and W. Wiesbeck, "Channel modelling for an OFDM train communications system including different antenna types," in *Proceedings of the IEEE 64th Vehicular Technology Conference (VTC '06 Fall)*, pp. 213–217, September 2006.

[5] P. Almers, E. Bonek, A. Burr et al., "Survey of channel and radio propagation models for wireless MIMO systems," *Eurasip Journal on Wireless Communications and Networking*, vol. 2007, Article ID 19070, 2007.

[6] C. X. Wang, X. Cheng, and D. Laurenson, "Vehicle-to-vehicle channel modeling and measurements: recent advances and future challenges," *IEEE Communications Magazine*, vol. 47, no. 11, pp. 96–103, 2009.

[7] X. Cheng, C. X. Wang, D. I. Laurenson, S. Salous, and A. V. Vasilakos, "An adaptive geometry-based stochastic model for non-isotropic MIMO mobile-to-mobile channels," *IEEE Transactions on Wireless Communications*, vol. 8, no. 9, pp. 4824–4835, 2009.

[8] X. Cheng, C. X. Wang, Y. Yuan, D. I. Laurenson, and X. Ge, "A novel 3D regular-shaped geometry-based stochastic model for non-isotropic MIMO mobile-to-mobile channels," in *Proceedings of the IEEE 72nd Vehicular Technology Conference Fall (VTC '10-Fall)*, Ottawa, Canada, September 2010.

[9] A. G. Zajić, G. L. Stüber, T. G. Pratt, and S. T. Nguyen, "Wideband MIMO mobile-to-mobile channels: geometry-based statistical modeling with experimental verification," *IEEE Transactions on Vehicular Technology*, vol. 58, no. 2, pp. 517–534, 2009.

[10] J. Karedal, F. Tufvesson, N. Czink et al., "A geometry-based stochastic MIMO model for vehicle-to-vehicle communications," *IEEE Transactions on Wireless Communications*, vol. 8, no. 7, pp. 3646–3657, 2009.

[11] X. Cheng, C. X. Wang, H. Wang et al., "Cooperative MIMO channel modeling and multi-link spatial correlation properties," *IEEE Journal on Selected Areas in Communications*, vol. 30, no. 2, pp. 388–396, 2012.

[12] P. Kyosti, J. Meinila, L. Hentila et al., "WINNER II channel models, IST," Tech. Rep. IST-4-027756 WINNER II D1.1.2 v1.2, 2007.

[13] J. Gong, J. F. Hayes, and M. R. Soleymani, "The effect of antenna physics on fading correlation and the capacity of multielement antenna systems," *IEEE Transactions on Vehicular Technology*, vol. 56, no. 4 I, pp. 1591–1599, 2007.

[14] A. Abdi and M. Kaveh, "A space-time correlation model for multielement antenna systems in mobile fading channels," *IEEE Journal on Selected Areas in Communications*, vol. 20, no. 3, pp. 550–560, 2002.

[15] A. A. Al-Kheir, K. A. Qaraqe, and M. S. Alouini, "On the space-time correlation of MIMO fading channels in 3D scattering models," in *Proceedings of the 13th IEEE Symposium on Computers and Communications (ISCC '08)*, pp. 831–837, July 2008.

Hindawi Publishing Corporation
International Journal of Antennas and Propagation
Volume 2012, Article ID 815232, 7 pages
doi:10.1155/2012/815232

Research Article

Radio Wave Propagation Scene Partitioning for High-Speed Rails

Bo Ai, Ruisi He, Zhangdui Zhong, Ke Guan, Binghao Chen, Pengyu Liu, and Yuanxuan Li

State Key Laboratory of Rail Traffic Control and Safety, Beijing Jiaotong University, Beijing 100044, China

Correspondence should be addressed to Bo Ai, aibo@ieee.org

Received 11 July 2012; Revised 20 August 2012; Accepted 5 September 2012

Academic Editor: César Briso Rodríguez

Radio wave propagation scene partitioning is necessary for wireless channel modeling. As far as we know, there are no standards of scene partitioning for high-speed rail (HSR) scenarios, and therefore we propose the radio wave propagation scene partitioning scheme for HSR scenarios in this paper. Based on our measurements along the Wuhan-Guangzhou HSR, Zhengzhou-Xian passenger-dedicated line, Shijiazhuang-Taiyuan passenger-dedicated line, and Beijing-Tianjin intercity line in China, whose operation speeds are above 300 km/h, and based on the investigations on Beijing South Railway Station, Zhengzhou Railway Station, Wuhan Railway Station, Changsha Railway Station, Xian North Railway Station, Shijiazhuang North Railway Station, Taiyuan Railway Station, and Tianjin Railway Station, we obtain an overview of HSR propagation channels and record many valuable measurement data for HSR scenarios. On the basis of these measurements and investigations, we partitioned the HSR scene into twelve scenarios. Further work on theoretical analysis based on radio wave propagation mechanisms, such as reflection and diffraction, may lead us to develop the standard of radio wave propagation scene partitioning for HSR. Our work can also be used as a basis for the wireless channel modeling and the selection of some key techniques for HSR systems.

1. Introduction

Radio propagation environments may introduce multipath effects causing fading and channel time dispersion. Various propagation environments have different path loss and multipath effects, leading to the impossibility of radio wave propagation prediction in different propagation environment with the utilization of the same propagation channel model. Therefore, we should develop different wireless channel models according to radio propagation environments. That is to say, radio wave propagation scene portioning plays a very important role in wireless channel modeling. Scene partitioning is also the basis for the upper layer communication network design. Optimization with respect to radio wave propagation will greatly improve the planning of wireless networks for rails. Special railway structures such as cuttings, viaducts, and tunnels have a significant impact on propagation characteristics. However, these scenarios for high-speed rails (HSRs) have rarely been investigated, and few channel measurements have actually been carried out. Consequently, detailed and reasonable definitions for various scenarios in HSR are still missing. Therefore, a set of reasonable propagation scenarios for HSR environments needs to be defined so that statistical wireless channel models for HSR can be developed.

The main drawback of the current channel modeling approaches to railway communication is that the standard channel models used in the engineering implementation of HSR do not cover the special railway scenarios of cutting, viaducts, tunnels, and so on. For example, based on measurements obtained from the Zhengzhou-Xian passenger-dedicated line, operating at speeds of around 350 km/h, we have found that the Hata model (which is used for path loss prediction) might result in about 17 dB errors for wireless network coverage prediction, as it does not include the diffraction loss caused by the cuttings along the rails [1]. The recently proposed WINNER model [2, 3] treats rail structures as one species with no distinguishing characteristics between them, which may be unreasonable. In addition, the working frequency of the WINNER model is from 2 to 6 GHz, which is not suitable for GSM for railway (GSM-R) wireless network operating at 930 MHz.

This motivated us to carry out the research on radio wave propagation characteristics under the special scenarios for rails in order to obtain much more accurate path loss prediction results.

Several scene partitioning schemes for public wireless network communications are presented in Section 2. In Section 3, detailed descriptions about special scenarios in HSR are conducted. The scene partitioning scheme for HSR is proposed in Section 4, followed by the conclusions in Section 5.

2. Overview of Scene Partitioning Schemes

Several organizations and related standards should be mentioned when we refer to the scene partitioning. International Mobile Telecom System-2000 (IMT-2000) was proposed by International Telecommunication Union (ITU). It claims that [4] the purpose of defining distinct IMT-2000 radio operating environments is to identify scenarios that, from a radio perspective, may impose different requirements on the radio interface(s). It defines nine terrestrial scenarios and four satellite scenarios including business indoor, neighborhood indoor/outdoor, home, urban vehicular, urban pedestrian outdoor, rural outdoor, terrestrial aeronautical, fixed outdoor, local high bit rate environments, urban satellite, rural satellite, satellite fixed-mounted, and indoor satellite environments.

Universal Mobile Telecommunications System (UMTS) is developed by 3GPP. It claims that [5] a smaller set of radio propagation environments is defined which adequately span the overall range of possible environments. For practical reasons, these operating environments are an appropriate subset of the UMTS-operating environments described in Recommendation ITU-R M. 1034 [4].

WINNER project group in Europe was established in 2004. Based on UMTS and IMT-2000 scenario definitions, it defines four typical scenarios including in and around building, hot spot area, metropolitan, and rural scenarios. Eighteen detailed scenarios are defined on the basis of these four typical scenarios. The propagation scenarios listed above have been specified according to the requirements agreed commonly in the WINNER project [6]. The only one scenario appropriate for HSR defined in WINNER project is WINNER D2 model (rural moving network) [3]. However, the measurement environment for WINNER D2a is in European countries. These environments include no variable complicated HSR such as cuttings and viaducts. Moreover, as is mentioned in Section 1, the working frequency of WINNER D2a is at 2–6 GHz, which is not suitable for wireless network operating at 930 MHz.

Nowadays, more and more statistical wireless channel modeling approaches depend on Geographic Information System (GIS). Some GIS technology companieo define scenarios for wireless communications as well. These defined scenarios include inland water area, open wet area, open suburban, green land, forest, road, village, and tower.

Above all, the entire above-mentioned scene partitioning schemes include no special scenarios in HSR such as cuttings, viaducts, tunnels, and marshaling stations, which is not beneficial to wireless channel modeling for HSR. Therefore, it is necessary to establish the detailed scene partitioning scheme for HSR in order to improve the quality of dedicated wireless network planning and optimization.

3. Special Scenarios for High-Speed Rails

Based on our practical investigations on the Zhengzhou-Xian passenger-dedicated line, Wuhan-Guangzhou HSR, and some railway stations such as Beijing South Railway Station and Zhengzhou Railway Station, we obtained the valuable testing data for the HSR channels.

The actual measurements conditions are as follows [7, 8]: 930 MHz narrowband measurements along the Zhengzhou-Xian HSR of China, using GSM-R base stations (BSs). The cross-polarization directional antennas of BSs positioned 10–20 m away from the track are utilized, with 17 dBi gain, 43 dBm TX power. The height of BS antenna varies in different scenarios, ranging from 20 to 60 m. The omni-directional receiver antennas are placed in the middle of the train, mounted on the top with the height of 30 cm above the train roof and 4 dBi gain. The train moves at the speed up to 350 km/h. The samples are collected at 53 cm interval for large-scale analysis (the small scale effect is removed by averaging samples at the interval of 13 m) and 10 cm interval for small scale analysis [9, 10]. Note that our work uses the practical GSM-R network of HSR for measurement, at 930 MHz. Therefore, some of the channel parameters we present in the following may not be valid for other frequencies. However, our scene partitioning can be used in other communication systems for railways, such as GSM-R and long-term evolution for railway (LTE-R). In the following, we will describe the special propagation scenarios of HSR.

3.1. Viaducts. Viaduct is one of the most common scenarios in HSR (viaduct makes up 86.5% of the newly-opened Beijing Shanghai HSR of China).

Viaduct is a long bridge-like structure, typically a series of arches, carrying a railway across a valley or other uneven ground. In HSR constructions, it is difficult to lay the tracks on the uneven ground when the smoothness of rails is strictly required to ensure the high speed (350 km/h) of the train. To overcome this problem, viaducts with a height of 10 m to 30 m are quite necessary, as is shown in Figure 1. Generally, the transmitter antennas are usually 20–30 m higher than the surface of the track, and the receiver antennas are mounted on top of the high-speed trains. Under this condition, few scatterers are higher than the viaduct, and the direct ray dominates with regard to the radio wave propagation, which makes viaduct a typical LOS propagation scenario [8]. We defined two categories of viaducts according to line-of-sight (LOS) and none-line-of-sight (NLOS) conditions.

3.1.1. Viaduct-1a. Viaduct-1a corresponds to the scenario that has some scatterers (such as trees and buildings) higher than the surface of the viaduct, most of which are located

Figure 1: Viaduct scenario.

Figure 2: Cutting scenario.

Figure 3: Tunnel scenario.

within a range of 50 m from the viaduct. These scatterers introduce rich reflection and scattering components, resulting in great severity of shadow fading. The stochastic changes of these scatters (such as the swing of the trees caused by wind) may also lead to the changes of the fading distribution.

3.1.2. Viaduct-1b. Viaduct-1b corresponds to the scenario that most scatterers, located within a range of 50 m from the viaduct, are lower than the surface of the viaduct. Under this condition, LOS is rarely blocked, and the direct path makes the greatest contribution to the propagation compared with other reflected and scattered paths. The effects of these scatterers (lower than the viaduct, or 50 m far from the viaduct) on propagation characteristics are negligible.

3.2. Cuttings. Cutting is a common scenario in HSR environments, which helps to ensure the smoothness of rails and high speed of the train operation [1]. It is used in HSR construction on uneven ground and to pass or "cut" through large obstacles such as hills. The cutting sides are usually covered with vegetation and reinforced concrete in case of subsidence. The forms of cutting can be either regular, where the steep walls on both sides of the rails have almost the same depths and slopes, or irregular owing to the locations of irregular hills or mountains along the line. This special structure of cutting creates a big "container," with rich reflection and scattering.

Cutting usually can be described with three parameters: crown width, bottom width, and depth of cutting. In Chinese HSR constructions, the crown width of cutting mostly ranges from 48 to 63 m, while the bottom width ranges from 14 to 19 m [7]. The depth of cutting is usually 3–10 m. These parameters can greatly measure the goodness of a cutting to be a container, for example, whether the cutting is too "wide" or "open" to hold enough multipath components.

The most common cutting is the regular deep cutting, where the steep walls on both sides of the rails have almost the same depths and slopes, as is shown in Figure 2. Under this condition, the receiver antenna is mostly lower than the roof of the cutting, leading to much more multipath components at the receiver. Moreover, the cross-bridges built over the cuttings lead to NLOS propagation in a short distance and may cause extra large-scale loss due to diffraction or other radio wave propagation mechanisms. Consequently, cutting has a significant impact on radio wave propagation characteristics and so can be disruptive to wireless communication.

3.3. Tunnels. Tunnel is an artificial underground passage, especially one built through a mountain in HSR environment, as is shown in Figure 3. The presence of tunnel ensures the high speed of train operation in rolling terrain. The sectional view of tunnel in HSR is usually vaulted or semicircle, with a height of 5–10 m and a width of 10–20 m. The length of the tunnel in HSR mostly ranges from several to dozens of kilometers.

Generally, two main BSs are placed at the beginning and the end of the tunnel in HSR. Dependent on the length of the tunnel, several sub-BSs are placed inside the tunnel, installed in the wall. These sub-BSs help to provide great wireless coverage inside the tunnel. Due to the smooth walls and the close structure of the tunnel, there are rich reflections and scattering components inside the tunnel, which introduce the wave guide effect dominating the radio wave propagation inside the tunnel. This phenomenon makes the prediction of wireless signal in tunnel totally different from other propagation scenarios.

3.4. Railway Stations. Railway station is a railway facility where trains regularly stop to load or unload passengers. It generally consists of a platform next to the tracks and a depot providing related services such as ticket sales and waiting rooms. In the station scenario, the speed of the train is usually less than 80 km/h, while the speed of the crowd is 3–5 km/h. Due to the large number of users, high traffic requirements are expected in this environment. Moreover, the big awnings are usually utilized in stations to stop the rain from reaching the passengers and the trains, which may block

Figure 4: Medium- or small-sized station scenario.

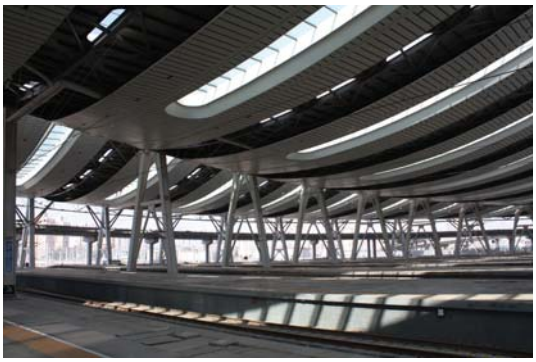

Figure 5: Large station scenario.

the LOS. Based on the capacity of the transportation, stations in HSR can be divided into three categories: medium- or small-sized station (4a), large station (4b), and marshaling station and container depot (4c).

3.4.1. Station-4a. Station-4a scenario indicates the medium or small-sized stations, as is shown in Figure 4. Mostly, there is not any awning on top of the trails, and the propagation could be both LOS and NLOS conditions. This scenario is similar to suburban environment. However, the passengers and platforms are usually close to the track so that the medium traffic requirements are expected in this environment.

3.4.2. Station-4b. Station-4b scenario indicates the quite large and busy stations in terms of daily passenger throughput. These stations are used by an average of more than 60 thousand people, or 6500 trains per day, such as Beijing South Railway station, Guangzhou South Railway Station, and Xian North Railway Station. In Station-4b, there are usually big awnings on top of the rails, as is shown in Figure 5, making Station-4b similar to some indoor propagation scenarios [6, 7]. The BSs are mostly located outside the awnings, sometimes inside the awnings. This special structure has a significant impact on radio wave propagation characteristics, especially when the train moves into or out of the railway station.

Figure 6: Marshaling station and container depot scenarios.

3.4.3. Station-4c. Station-4c scenario indicates the marshaling stations and container depots, where the carriages are marshaled before traveling, or the train stops to load or unload freight, as is shown in Figure 6. In this scenario, the great traffic requirements of train controlling signal are highly expected. In addition, a number of metallic carriages result in complex multipath structure and the rich reflection and scattering components.

3.5. Combination Scenarios. Considering the complex environments along the HSR, several propagation scenarios may exist in one communication cell. This combination of the propagation scenarios is a challenging task for prediction of wireless signal. There are usually two categories of combination scenarios in HSR: tunnel group (11a), and cutting group (11b).

3.5.1. Combination Scenario-11a. Tunnel groups are widely present when the train passes through multimountain environment. In this terrain, the train will not stay in tunnel all the time, but frequently moves in and moves out of the tunnel. Under this condition, the transition areas are usually viaduct scenario. The frequent changes of the propagation scenario from tunnel to viaduct will greatly increase the severity of fading at the beginning or the end of the tunnel, resulting in poor communication quality.

3.5.2. Combination Scenario-11b. In cutting scenario, the depth of the cutting changes frequently. Sometimes, the steep walls on both sides may transitorily disappear, where the transition areas can be considered as the rural scenario. The frequent changes of scenario among deep cutting, low cutting, and rural can be quite disruptive to wireless communication, making the wireless signal prediction a great challenge.

3.6. In-Carriage. In-carriage scenario corresponds to the radio wave propagation used to provide personal communications for passengers with high quality of service. We define two categories of in-carriage scenarios in HSR: relay transmission (12a), and direct transmission (12b).

Table 1: Radio wave propagation scene partitioning for HSR.

Scenarios	Definitions	Sub scenarios	LOS/NLOS	Speed (km/h)	Special propagation mechanisms	Notes
S1	Viaduct	Viaduct-1a	LOS	0–350		
		Viaduct-1b	LOS	0–350		
S2	Cutting		LOS	0–350		
S3	Tunnel		LOS	0–250	Guide effect	
S4	Station	Station-4a: medium- or small-sized station	LOS/NLOS	0–80		
		Station-4b: large station	LOS/NLOS	0–80		
		Station-4c: marshaling station and container depot	LOS	0–80		
S5	Water	Water-5a: river and lake areas	LOS	0–350		
		Water-5b: sea area	LOS	0–350		
S6	Urban		LOS	0–350		
S7	Suburban		LOS	0–350		
S8	Rural		LOS	0–350		
S9	Mountain	Mountain-9a: normal mountain	NLOS	0–150		
		Mountain-9b: far mountain	LOS	0–350		Long delay clutter
S10	Desert		LOS	0–350	Diffuse reflection	
S11	Combination scenarios	Combination scenario-11a: tunnel group	LOS	0–250		
		Combination scenario-11b: cutting group	LOS	0–350		
S12	In-carriage	In-carriage-12a: relay transmission	LOS/NLOS	0–5		
		In-carriage-12b: direct transmission	NLOS	0–350	Penetration loss	

Table 2: Predicted values of modeling parameters for HSR scenarios at 930 MHz.

Scenarios	Definitions	Sub scenarios	Path loss exponent	Standard deviation of shadowing (dB)	Fast fading distribution
S1	Viaduct	Viaduct-1a	2–4	3-4	Rice
		Viaduct-1b		2-3	
S2	Cutting		2.5–4	3–5	Rice
S3	Tunnel		1.8–3	5–8	Rice
S4	Station	Station-4a: medium- or small-sized station Station-4b: large station	3–5	3–5	Rice/Rayleigh
		Station-4c: marshaling station and container depot	2–4	2-3	Rice
S5	Water	Water-5a: river and lake areas Water-5b: sea area	2–4	2-3	Rice
S6	Urban		4–7	3–5	Rice
S7	Suburban		3–5	2-3	Rice
S8	Rural		2–5	2-3	Rice
S9	Mountain	Mountain-9a: normal mountain	5–7	3–5	Rayleigh
		Mountain-9b: far mountain	3–5	2–6	Rice
S10	Desert		2–4	2-3	Rice
S11	Combination scenarios	Combination scenario-11a: tunnel group Combination scenario-11b: cutting group	3–7	5–8	Rice
S12	In-carriage	In-carriage-12a: relay transmission	1.5–5	3–5	Rice/Rayleigh
		In-carriage-12b: direct transmission	5–8	4–7	Rayleigh

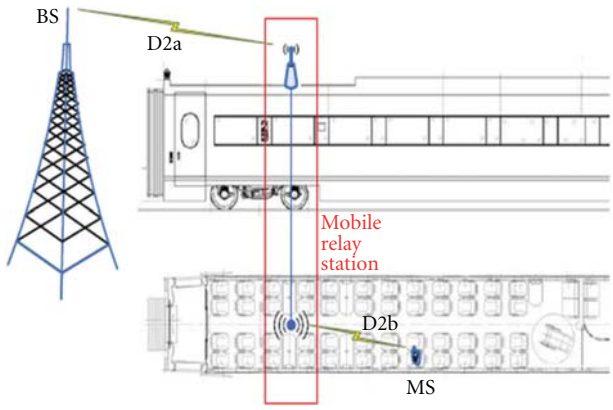

Figure 7: Relay transmission scenario in [3].

3.6.1. In-Carriage-12a. Relay transmission occurs in carriages of high-speed trains where wireless coverage is provided by the so-called moving relay stations which can be mounted to the ceiling [3], as is shown in Figure 7. Note that the link between the BS and the moving train is usually a LOS wireless link whose propagation characteristics are represented by other mentioned HSR propagation scenarios. Moreover, due to the great penetration loss of the carriage, the change of the environments outside the train has a negligible effect on radio wave propagation inside the train, and the propagation inside the carriage can be covered with the models for some typical indoor channels.

3.6.2. In-Carriage-12b. Direct transmission indicates the scenario that uses the wireless link between the BS and the user inside the carriage to provide the high-quality communications. Under this condition, the penetration loss of the carriage has a great effect on radio wave propagation. The wireless link between the BS and the moving train, together with the link inside the carriage and a reasonable value of the penetration loss, can be used to predict radio wave propagation in this scenario.

4. Scene Partitioning Scheme for High-Speed Rails

The proposed radio wave propagation scene partitioning scheme is presented in Table 1. The corresponding modeling parameters for each scenario are shown in Table 2. Detailed description and theoretical analysis based on reflection, scattering, and diffraction propagation mechanism will be given in our future work.

For the proposed scene partitioning scheme, we take comprehensive consideration of three categories attributes. The first one is physical attribute, which means variation of radio wave propagation mechanism between BS and mobile users, for example, direct wave and reflection wave, line-of-sight (LOS)/non-line-of-sight (NLOS), and the variation of multipath structure. Such physical attributes may lead to such special scenarios in HSR such as viaducts, cuttings, and tunnels. This attribute is clearly unfolded in Table 1.

The second one is user attribute, which is related with the user requirements of the provided services. It mainly takes the factor of transmission rate and moving speed into consideration. This attribute is unfolded in the scene partitioning scheme as the moving speed of users.

The third one is related with coverage of wireless network. It considers various wireless network covering approaches. For example, ribbon covering approach is commonly adopted along the rails currently. This attribute is unfolded in the scene partitioning scheme as the scene of marshaling stations. The traffic volume in railway marshaling station is much higher than that of the ordinary railway stations.

In accordance with the testing data, the scenarios are appropriate for 930 MHz working frequency. Note that the 10th scenario—desert—appears in Taiyuan-Yinchuan railway in China.

Note that the modeling parameters for scenarios S1 and S2 are based on our previous research results of [7, 8, 11, 12]. The parameters for scenario S3 are based on the results of [13, 14]. The parameters for scenarios S4, S6, S7, S8, and S9 are predicted based on our previous research results of [15]. The parameters for scenario S12 are based on the results of [6]. Moreover, the modeling parameters for each scenario are just the prediction values. Accurate parameters values could be obtained after accurate channel modeling.

5. Conclusions

Up till now, there is no any radio wave propagation scene partitioning scheme for HSR environments, which contains many special propagation scenarios, such as viaducts, cuttings, tunnels, and marshaling stations. Scene partitioning is very useful for wireless channel modeling, which is the basis for BS location, wireless network planning, and optimization. Only with the scene partitioning for HSR, the accurate path loss prediction models can be developed, which are the fundamental basis of wireless link budget and the basis of the position determination of the base stations for HSR network. In this paper, a series of propagation scenarios of HSR is reviewed based on the practical channel measurements in China, and the scene partitioning scheme is proposed. The results can be used for the propagation channel characterization in HSR environments. Our future work will focus on the theoretical analysis of these scenarios through such propagation mechanisms as reflection, diffraction and scattering. Corresponding wireless channel models for HSR on the basis of the scene partitioning will be studied as well. We will also pay attention to other working frequencies which could be used for railway communications in the future.

Acknowledgment

The authors are grateful to Hong Wei, Jing-hui Lu, Zi-mu Cheng, and other members of radio wave propagation and wireless channel modeling research group in Beijing Jiaotong University. They also express their many thanks

for the supports from the National Science Foundation of China under Grant 61222105, the Beijing Municipal Natural Science Foundation under Grant 4112048, the Program for New Century Excellent Talents in University of China under Grant NCET-09-0206, the NSFC under Grant 60830001, the Fundamental Research Funds for the Central Universities under Grant 2010JBZ008, and the Key Project of State Key Lab under Grant no. RCS2011ZZ008.

References

[1] B. Ai, "Interview," *Electronics Letters*, vol. 47, no. 21, article 1158, 2011.

[2] WINNER Group, "IST-4-027756 WINNER II D1. 1. 1 V1. 1, WINNER II Interim channel models," February 2007.

[3] WINNER Group and IST-WINNER II Deliverable 1. 1. 2 v. 1. 2, "WINNER II channel models," Tech. Rep. IST-WINNER2, 2008.

[4] I. T. U. . Rec, ITU-R M: 1034-1, Requirements for the radio interface(s) for international mobile telecommunications-2000, (IMT-2000).

[5] ETSI, TR 101 112 v3. 2. 0, Universal Mobile Telecommunications Systems (UMTS): selection procedures for the choice of radio transmission technologies of the UMTS, 1998.

[6] WINNER Group, "System assessment criteria specification," IST-2003-507581. WINNER, July 2004.

[7] R. He, Z. Zhong, B. Ai, and J. Ding, "Propagation measurements and analysis for high-speed railway cutting scenario," *Electronics Letters*, vol. 47, no. 21, pp. 1167–1168, 2011.

[8] R. He, Z. Zhong, B. Ai, and J. Ding, "An empirical path loss model and fading analysis for high-speed railway viaduct scenarios," *IEEE Antennas and Wireless Propagation Letters*, vol. 10, pp. 808–812, 2011.

[9] W. C. Y. Lee, "Estimate of local average power of a mobile radio signal," *IEEE Transactions on Vehicular Technology*, vol. 34, no. 1, pp. 22–27, 1985.

[10] B. Ai, Z. D. Zhong, G. Zhu, and M. Zhao, "Novel statistical criteria for local mean power estimation in wireless coverage perdiction," *IET Microwaves, Antennas and Propagation*, vol. 5, no. 5, pp. 596–604, 2011.

[11] H. Wei, Z. Zhong, L. Xiong, B. Ai, and R. He, "Study on the shadow fading characteristic in viaduct scenario of the high-speed railway," in *Proceedings of the IEEE 6th International ICST Conference on Communications and Networking in China (CHINACOM)*, pp. 1216–1220, Haerbin, China, August 2011.

[12] R. He, Z. Zhong, B. Ai, and J. Ding, "Measurements and analysis of short-term fading behavior for high-speed rail viaduct scenario," in *Proceedings of the IEEE ICC*, pp. 1–5, Ottawa, Canada, 2012.

[13] C. Nerguizian, C. L. Despins, S. Affès, and M. Djadel, "Radio-channel characterization of an underground mine at 2.4 GHz," *IEEE Transactions on Wireless Communications*, vol. 4, no. 5, pp. 2441–2453, 2005.

[14] Y. P. Zhang, "A hybrid model for propagation loss prediction in tunnels," in *Proceedings of the Millennium Conference on Antennas and Propagation*, Davos, Switzerland, 2000.

[15] R. He, Z. Zhong, and B. Ai, "Path loss measurements and analysis for high-speed railway viaduct scene," in *Proceedings of the 6th International Wireless Communications and Mobile Computing Conference (IWCMC'10)*, pp. 266–270, Caen, France, July 2010.

Hindawi Publishing Corporation
International Journal of Antennas and Propagation
Volume 2012, Article ID 913596, 4 pages
doi:10.1155/2012/913596

Research Article

NECOP Propagation Experiment: Rain-Rate Distributions Observations and Prediction Model Comparisons

J. S. Ojo and S. E. Falodun

Department of Physics, Federal University of Technology Akure, P.M.B. 704, Akure, Nigeria

Correspondence should be addressed to J. S. Ojo, josnno@yahoo.com

Received 15 February 2012; Accepted 20 May 2012

Academic Editor: Thomas Kürner

Empirical distribution functions for one-minute average rain-rate values were compiled for three station year of observations at Nigeria environmental and climatic observatory (NECOP) propagation experiment terminal sites. The empirical distribution functions were compared with cumulative distribution functions generated using four different rain-rate distribution models. It is found that although each of the models shows similar qualitative features at lower exceedance of time, the characteristic at higher time percentages shows quantitative difference from the experimental data except the improved version of Moupfouma model. The results further show that the rainfall rate and the microwave propagation characteristics in this region are out of accord with International Telecommunication Union predictions. This information is vital for predicting rain fading cumulative probability distributions over this region.

1. Introduction

The Nigeria environmental and climatic observatory (NECOP) experiment was designed for the following purposes among others: to generate data bank on the measured parameters for observatory and research purposes, to serve as a tool for planning acceptable terrestrial and satellite communication networks, as well as for the prediction of weather, hydrological purposes, and for agricultural usage. Among the parameters that were measured by the equipment in each site are the total rain accumulation and rain rate. This paper is based on the analysis of these two parameters, and comparisons were made with some existing rain-rate prediction models. The primary atmospheric phenomenon that contributed to degradation of satellite signals above 10 GHz is attenuation due to rain. The severity of rain impairments increases with frequency and varies with regional locations [1]. Hence, in order to successfully estimate rain attenuation along the link path, the point rainfall rate characteristic must be available in the location of interest. For such rainfall rate characteristics, information such as rainfall rate integration time, average rainfall cumulative distribution, and worst-month rainfall rate distributions are all required by a radio link planner in order to estimate path loss [2].

In this paper, continuous measurement of point rainfall rate data of 1-minute integration were used to find the best rainfall cumulative distribution model for three distributed sites: The Federal University of Technology, Akure, Ondo State (FUTA), University of Lagos, Lagos State (UNILAG), and University of Yola, Adamawa State (UNIYOLA).

Four different rain rate distribution models were considered in this study; the ITU rain-rate model as recommended by [3], the rain rate prediction model developed by Rice-Holmberg, RH [4], the modified version of the model developed by Moupfouma and Martin's [5, 6] and the Kitami's model [7]. The RH uses local climatological data to generate the two parameters needed to make prediction: the average annual precipitation, M, and the thunderstorm ratio β. The RH parameters may be calculated from the local long-term average annual precipitation accumulation, the number of thunderstorm days, and the maximum monthly precipitation in 30 years. The parameter may also be extrapolated from the maps presented by Rice and Holmberg [4]. Moupfouma and Martins also derived a very simple empirical model which provides a good description

Table 1: Site characteristics of the study locations.

Station	Latitude (°N)	Longitude (°E)	Height above sea level	Average annual rainfall (mm/year)	Observation period	Region climate
FUTA	7.17	5.18	358	1485.6	16 months (Jun. 2010–Sept. 2011)	Rain forest zone
UNILAG	6.27	3.24	40	1626.2	12 months (Oct. 2007–Nov. 2008)	Coastal region
UNIYOLA	9.14	12.28	174	948.5	14 months (Nov. 2009–Dec. 2010)	Semiarid

of the global distribution for cumulative rainfall rates above 2 mm/h. The model combines both log-normal and gamma distributions. The model also allows the prediction of the cumulative distribution of rainfall rate in temperate and tropical regions by using one-minute integration time of point rainfall in any location of interest. Details of the model are fully reported in [4].

Kitami's model was proposed by Ito and Hosoya, as reported in [7] to obtain 1-minute rain rate distribution using thunderstorm ratio and average annual precipitation as regional climatic parameter. The data used are the Kitami Institute of Technology data bank, which contains 290 datasets for 30 countries including the tropical region. The ITU P-837-6 model was based on the improved version of Salonen Baptisa [8] model. The method involves the use of a database of the following meteorological parameters: annual rainfall amount of convective-type rain M_c (mm), annual rainfall amount of stratiform-type rain M_s (mm), and probability of rainy 6 h periods P_{r6} (%). The parameters (P_{r6}, M_c, and M_s) are available from ITU's 3 M Group Web site, each of which is matched to a (latitude, longitude) pair [3].

2. Experimental Sites and Measurement

The rainfall rate data were collected at the Federal University of Technology, Akure campus in Ondo State (FUTA), University of Lagos campus, Lagos State (UNILAG), and University of Yola campus in Adamawa State (UNIYOLA). Detail characteristics of each of the measurement site are listed in Table 1.

Rainfall intensities measurements are made by a tipping bucket raingauge which stands 146 mm high as part of NECOP setup in all the sites. The rain gauge has sensitivity of about 0.1 mm and a data acquisition unit along with other sensors in unit that measured the following parameters: soil moisture content (volume of water), wind speed and wind direction, air temperature, and relative humidity among others. For the rain gauge measurement, the rain water is collected in a standard funnel and is converted into drops of equal sizes. The number of drops collected every 10 seconds is counted electronically and finally averaged over 1 minute. The AGC voltage of each channel is continuously sampled and stored in digital form, together with the date and time of each rain gauge tip. The calibration of the rain gauge is maintained by cleaning the capillary. The overall reliability of the gauge is extremely high due to the simple drop-forming mechanism. The reliability has to be ensured by keeping it clean, so that dust particles do not obstruct the free flow water [9].

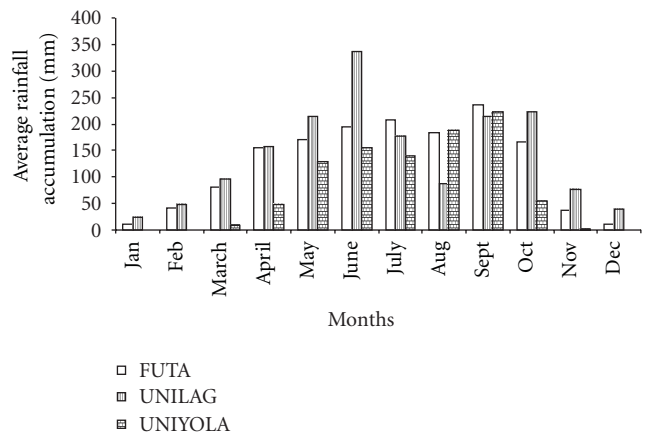

Figure 1: Average monthly rainfall accumulations during the observation period.

3. Results and Discussions

3.1. Distribution of Rain Rate. Figure 1 shows the average monthly rainfall accumulations during the observation period. The average monthly rainfall depends on the effects of movement of the Intertropical Convergence Zone (ITCZ). In summer, the ITCZ discontinuity follows the sun northward, as a result, more and more of the country comes under the influence of the moisture-laden tropical maritime air. As summer wanes, the zone shifts southward, bringing an end to the rainy season. Nigeria has two seasons, dry (Nov., Dec., Jan., and. Feb) season, and wet (the rest of the calendar year) season. Rainfall usually falls during the wet season and during this period the ITCZ moves across the country.

It could be observed that both the rain forest region (FUTA) and the semiarid region (UNIYOLA) recorded their peak average monthly rainfall accumulation in the month of September with 234 and 224 mm, respectively, while the coastal region has the wet month in June with average rainfall accumulation of about 336 mm. Due to ITCZ movement, rain continues to fall even during dry season in the rain forest and coastal regions.

3.2. Comparison of Measured and Model Data. The results of predictions by the four different rain rate-models when

Table 2: The composite comparison statistics for the different models.

Percentage of time		0.1%		0.01%	
Location	Model	Average relative error	Standard deviation	Average relative error	Standard deviation
FUTA	RH	125.0	15.0	4.6	27.2
	ITU	15.6	2.4	−22.0	12.9
	KITAMI	68.6	8.7	16.2	9.4
	Moupfouma	11.6	2.0	4.4	2.7
UNILAG	RH	9.5	2.5	23.0	16.2
	ITU	5.2	2.0	6.0	3.8
	KITAMI	4.5	6.1	−10.0	7.6
	Moupfouma	4.0	1.1	5.5	3.0
UNIYOLA	RH	88.0	9.9	34.1	26.0
	ITU	31.2	3.5	5.5	5.0
	KITAMI	22.9	2.6	14.7	7.9
	Moupfouma	30.0	3.0	4.4	4.7

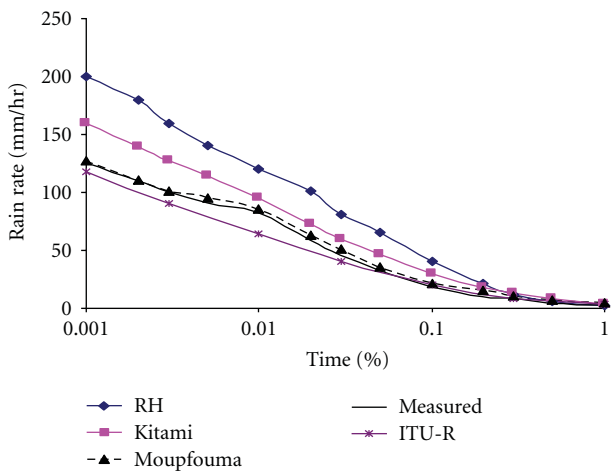

Figure 2: Comparison of measured FUTA rainfall data with model predictions.

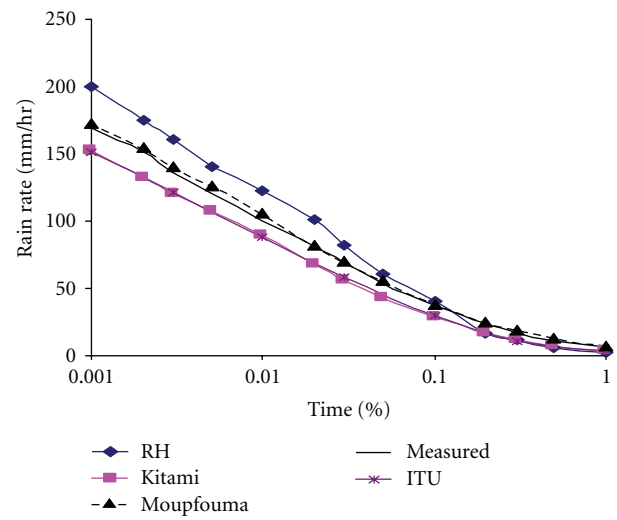

Figure 3: Comparison of measured UNILAG rainfall data with model predictions.

compared with the measured data from each location were considered to illustrate the differences in the expected rain-rate distributions for different locations and rain intensities. It is also needed to know how well a model performs statistically as compared with the measured values. Figures 2, 3, and 4 show the cumulative distribution of measured rainfall rate compared with each of the four predefined models, while Table 2 gives the composite comparison statistics for the different models.

It could be observed that the modified Moupfouma model shows the best prediction accuracy in all the measurement locations among the tested models based on the smaller absolute values of average relative error and standard deviation from the measured data (Table 2 referred). In addition to the statistical analysis, Moupfouma model combines the gamma and log-normal models by approximating a log-normal distribution at the low rain rates and a gamma distribution at high rain rate [10].

The ITU model is judged next suitable model for these locations apart from the statistical analysis because the

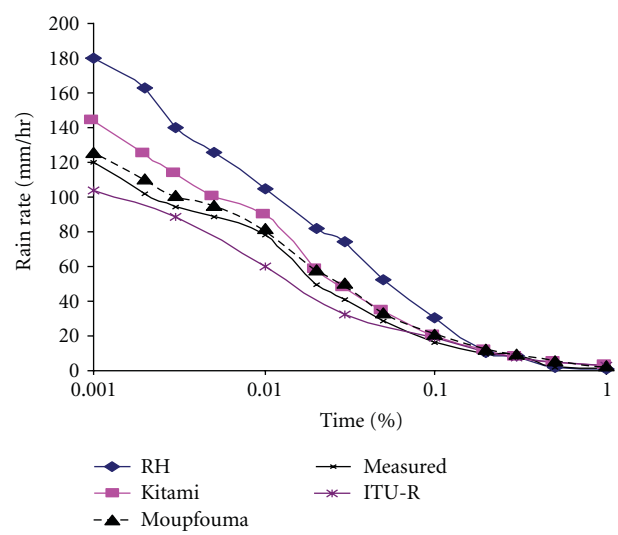

Figure 4: Comparison of measured UNIYOLA rainfall data with model predictions.

rainfall-rate model is based on the conversion to one-minute integration on long-term data of six hours rain accumulation.

The Kitami's model gives a good estimation for low rainfall rates but not fitted for high rainfall rates. The RH model is not suitable for use in tropical and equatorial climates judging from the statistical analysis, and because the model is based on the rainfall rate measurements in European countries where rainfall rates are moderate.

4. Conclusion

In this paper, comparison of rainfall rate was made with measured data and four preexisting models. It was found that Moupfouma model showed a close fit to the measured data for low, medium, and high rainfall rates based on the smaller values of average relative errors and standard deviation. The Moupfouma model is therefore judged suitable for use in predicting rain rates in these locations. The results are vital for system designer to estimate rain degradation along the satellite links over this region. It should be observed that the results are valid for this particular climates, and its applicability for other tropical regions requires further testing.

Acknowledgment

Authors are indebted to the Centre for Basic Space Science of NASRDA for providing NECOP equipment to each of the sites used for this research.

References

[1] G. O. Ajayi and E. B. C. Ofoche, "Some tropical rainfall rate characteristics at Ile-Ife for microwave and millimeter wave applications," *Journal of Climate & Applied Meteorology*, vol. 23, no. 4, pp. 562–567, 1984.

[2] P. A. Owolabi, T. J. Afullo, and S. B. Mallaga, "Effect of rainfall on millimeter wavelength radio in Gough and Marion Islands," *PIERS Online*, vol. 5, no. 4, pp. 328–335, 2009.

[3] International Telecommunication Union, "Characteristics of precipitation for propagation modeling," ITU-R Recommendations P.837-6, International Telecommunication Union, Geneva Switzerland, 2012.

[4] P. L. Rice and N. R. Holmberg, "Cumulative time statistics of surface-point rainfall rate," *IEEE Transactions on Communications*, vol. 21, no. 10, pp. 1131–1136, 1973.

[5] F. Moupfouma and L. Martin, "Modeling of the rainfall rate cumulative distribution for the design of satellite and terrestrial communication systems," *International Journal of Satellite Communications*, vol. 13, no. 2, pp. 105–115, 1995.

[6] J. S. Ojo, M. O. Ajewole, and L. D. Emiliani, "One-minute rain-rate contour maps for microwave-communication-system planning in a tropical country: Nigeria," *IEEE Antennas and Propagation Magazine*, vol. 51, no. 5, pp. 82–89, 2009.

[7] C. Ito and Y. Hosoya, "Worldwide 1 min rain rate distribution prediction method which uses thunderstorm ratio as regional climatic parameter," *Electronics Letters*, vol. 35, no. 18, pp. 1585–1587, 1999.

[8] E. T. Salonen and J. P. V. P. Baptista, "New global rainfall rate model," in *Proceedings of the 10th International Conference on Antennas and Propagation*, Pub N 14-176-436, pp. 2.182–2.185, April 1997.

[9] J. S. Ojo, "Rain rate statistics and fade distributions at Ka- and Ku band frequencies for microwave propagation in the tropical locations," *The Nigerian Journal of Space Research*, vol. 10, pp. 72–80, 2011.

[10] J. S. Mandeep and S. I. S. Hassan, "Comparison of 1-minute rainfall rate distributions for tropical and equatorial climates," *Space Communications*, vol. 19, no. 3-4, pp. 193–198, 2004.